DIVERGENT EVOLUTION OF ANIMAL EXCRETORY SYSTEMS: EVIDENCE FROM MOLECULAR AND FUNCTIONAL STUDIES IN PLANARIANS

by

Hanh Thi Kim Vu

A dissertation submitted to the faculty of
The University of Utah
in partial fulfillment of the requirements for the degree of

Doctor of Philosophy

Department of Neurobiology and Anatomy

The University of Utah

May 2015

The University of Utah Graduate School

STATEMENT OF DISSERTATION APPROVAL

The dissertation of **Hanh Thi Kim Vu**

has been approved by the following supervisory committee members:

Alejandro Sánchez Alvarado	, Chair	**12-04-2014** Date Approved
Charles L. Murtaugh	, Member	**12-04-2014** Date Approved
Tatjana Piotrowski	, Member	**12-04-2014** Date Approved
Yukio Saijoh	, Member	**12-04-2014** Date Approved
Monica L. Vetter	, Member	**12-04-2014** Date Approved

and by **Monica L. Vetter** , Chair/Dean of

the Department/College/School of **Neurobiology and Anatomy**

and by David B. Kieda, Dean of The Graduate School.

ABSTRACT

Animals have developed extraordinary capacities to maintain homeostasis in the face of severe osmoregulatory challenges from their environment. For instance, with respect to salt and water homeostasis, freshwater animals continuously eliminate excess water while conserving solutes, whereas land-dwelling organisms have to conserve water and solutes as much as possible. Comparative morphological studies suggest that animals have tackled the problems of excretion and osmoregulation by evolving a specialized structure: the excretory organ. Animal excretory organs are extremely diverse. Some are unicellular, such as the excretory cell in nematodes. Others are multicellular and highly specialized, such as the protonephridia/metanephridia in invertebrates or the kidneys in vertebrates. In light of such anatomical and functional diversity, the evolutionary origins of animal excretory systems pose an interesting question in biology. However, the hypotheses proposed thus far remain highly controversial for two main reasons. First, many evolutionary arguments are based solely on morphology in organisms for which no molecular data are available, precluding rigorous genetic comparisons. Second, while invertebrates are critical elements of this evolutionary puzzle, the molecularly tractable ones studied to date display highly derived excretory systems. *C. elegans* possesses a single excretory cell, while the ultrafiltration of nephrocytes is uncoupled from the absorption/secretion of Malpighian tubules in *D. melanogaster*.

Comparative morphological studies have demonstrated the existence of more complex excretory organs amongst many other invertebrates, including planarians. Planarians have a protonephridial excretory system in which each protonephridial unit consists of a tubule, opening distally via a nephridiopore at the surface of the animal and ending proximally in one or more terminal structures called flame cells. Protonephridia are commonly found amongst many invertebrates. Since protonephridia combine ultrafiltration with filtrate modification, planarians close an "invertebrate gap" in the study of excretory system biology. Taking advantage of a rapidly expanding list of molecular tools in recent years, this dissertation project aims to perform a comprehensive molecular and functional study of planarian protonephridia in order to provide new insights into the longstanding question on the evolutionary relationship between vertebrate and invertebrate excretory systems and gauge planarians' potential as a novel invertebrate model for human kidney development and disease.

TABLE OF CONTENTS

LIST OF FIGURES

ACKNOWLEDGEMENTS

First of all, I would like to express my deep gratitude to my mentor, Dr. Alejandro Sánchez Alvarado, for taking me on as his graduate student and providing outstanding guidance and support throughout these years. Thanks for giving me complete freedom to develop and follow my own ideas, a “luxury” that not all graduate students would have during their training. I have been inspired in multiple ways by Alejandro’s generosity, vision, and genuine passion for science.

I would like to thank Dr. Jochen Rink for being not only my friend, and my colleague, but also my second mentor in the lab. Jochen’s intelligence, critical eyes, and incredible skills as an experimentalist always have been and will be an inspiration. Thanks for always making sure that I am on the right track and also for being very critical with me for the past few years. His criticisms really shape my thinking about science.

I would like to thank Charles Murtaugh, Tatjana Piotrowski, Yukio Sajioh, and Monica Vetter for serving as my thesis committee members since the beginning of my graduate career. Thanks for so many insightful perspectives and so much thoughtful advice on my PhD projects.

I would like to thank all the past and present members of the Sánchez Lab, especially Sarah Elliott (my baymate), Li-chun Cheng (my dinner buddy), Carrie Adler, Kimberly Tu, and Alessandro Rossi. Thanks (to everybody!!!) for the help, and the lunch and coffee breaks!!! I consider myself an incredibly lucky person who got the chance to

work with them every day and to profit from the stimulating and creative atmosphere in this laboratory.

I would like to thank my family and friends, especially my husband, for their endless love and support. Without them, I would never have made it through the tough periods of this PhD.

And finally, I would like to thank the Vietnam Education Foundation for giving me a great opportunity not only to come to the University of Utah for graduate study but also to meet many awesome individuals whose friendships I will treasure for the rest of my life.

CHAPTER 1

OVERVIEW

"The regulation of its internal medium frees an animal from its external environment."

~ Claude Bernard ~

Living animals have a remarkable ability to adapt to their environments, majorly due to their amazing capacity to maintain homeostasis in the face of numerous osmoregulatory challenges posed by their environment. For instance, with respect to salt and water homeostasis, freshwater animals always have to confront the problems of water gain and salt loss while terrestrial organisms have to face the threat of desiccation. They therefore have developed different osmotic regulation strategies to maintain their internal milieus. Freshwater animals must continuously eliminate excess water while conserving solutes, whereas land-dwelling animals have to conserve water and solutes as much as possible. In safeguarding their internal homeostasis, animals must also deal with harmful by-products of metabolism, such as ammonia, the breakdown of nitrogenous molecules. Due to its toxicity, it is required to be continuously eliminated from the animal's body. In aquatic environments, ammonia can diffuse easily through the cell membrane due to its high solubility. However, in terrestrial environments, efficient elimination of ammonia by diffusion is not possible. Ammonia must instead be transformed into alternative nitrogenous substances with lower toxicity. This includes urea in amphibians and mammals and uric acid in insects and reptiles.

In pre-bilaterians like sponges, placozoans, cnidarians, and ctenophores, excretion and osmoregulation are performed by direct epithelial diffusion. No discrete excretory organs have evolved in these phyla. In contrast, most bilaterians (except Acoelomorpha and Xenoturbella) undergo excretion and osmoregulation in complex and specialized

structures – the excretory organs. Morphological studies suggest the existence of a variety of excretory systems. Some are unicellular, such as the excretory cell of nematodes. Others are multicellular and highly complex, such as the protonephridia in platyhelminths, metanephridia in annelids, Malphigian tubules in insects, and kidneys in vertebrates (Ruppert, 1994) (Fig. 1.1). Due to such functional and anatomical diversity, the evolutionary origin of excretory organs poses an interesting question in biology.

Kidneys constitute the excretory system in humans. The chief role of the kidney includes regulation of electrolyte concentrations, acid-base balance, and maintenance of extracellular fluid volume. This is achieved by hundreds of thousands of nephrons – the basic functional unit of the kidney through relatively simple mechanisms of filtration, reabsorption, and secretion. Due to its pivotal roles in maintaining body homeostasis, disturbance of kidney function poses a serious health threat. More than 10% of adults in the United States currently suffer from some type of chronic kidney disease (CDC, 2014). Basic kidney research, therefore, is essential for understanding kidney pathologies and developing effective strategies for prevention and treatment of kidney diseases. To set the research of this thesis in context, this chapter reviews our current knowledge of kidney biology and outstanding questions in the field. It discusses the potential of current invertebrate model systems in understanding kidney biology and their limitations. Finally, it introduces the planarian excretory system as a novel invertebrate model for studying kidney development, diseases, and evolution.

Figure 1.1. Cartoon representing the basic structural organization of excretory systems across animal kingdom. Despite the structural differences, animal excretory systems are composed of two principle components: filtration cells as mediators of ultrafiltration, and tubular cells that are responsible for filtrate modification by reabsorption and secretion (except for the unicellular excretory organ in *C. elegans*). Nephrons are excretory organs of vertebrates; protonephridia are excretory organs of amphioxus and planarians; metanephridia are excretory organs of annelids; nephrocytes and Malphigian tubules are excretory organs of flies; while an excretory cell is the unicellular excretory organ of *C. elegans*. Red branch indicating Ecdysozoa; green branch, Lophotrochozoa; blue branch, Deuterostomia; purple branch, Cnidaria.

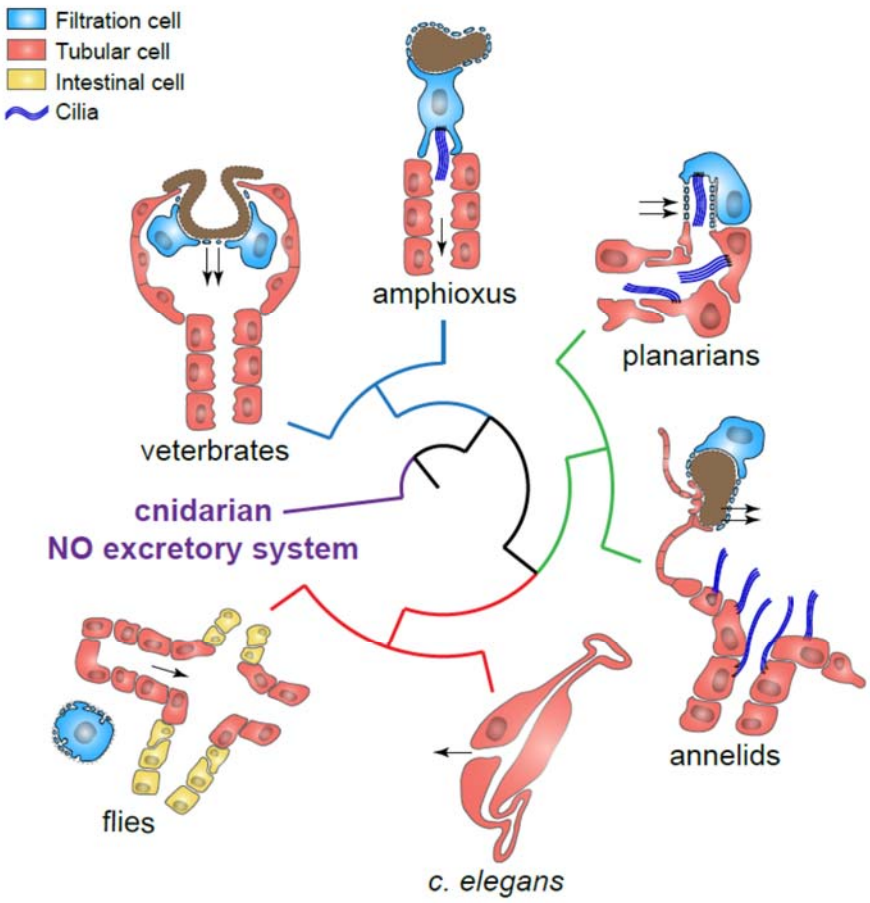
Filtration cell
Tubular cell
Intestinal cell
Cilia
amphioxus
planarians
veterbrates
cnidarian
NO excretory system
annelids
flies
c. elegans

A Brief Overview of Kidney Development

Anatomy of the Mammalian Kidney

The mammalian kidney is a bean-shape organ composed of hundreds of thousands of nephrons, the basic functional unit of the kidney. Each nephron comprises two functional components: a filtering component (the “glomerulus”) and a tubule specialized for reabsorption and secretion (the "renal tubule"). The glomerulus is formed at the most proximal end of the nephron, followed by the proximal convoluted tubule, the loop of Henle, and the distal convoluted tubule, which connects to the collecting duct (Fig. 1.2). Filtration of the blood occurs inside the glomerulus through the fenestrated structures formed by glomerular podocytes (reviewed in detail in (Quaggin and Kreidberg, 2008)). The filtrate is then concentrated by selective reabsorption and secretion along the different segments of the renal tubule. Glucose, amino acids, electrolytes, and peptides are reabsorbed in the proximal convoluted tubule, whereas water and electrolytes are taken up by loops of Henle and the distal convoluted tubule due to the segmental expression of distinct sets of solute transporters (reviewed in detail in (Fenton and Praetorius, 2011; Pannabecker, 2012; Staruschenko, 2012; Zhuo and Li, 2013). Waste and harmful substances are finally excreted out of the body as urine.

Embryology of Mammalian Kidney Development

The mammalian kidney derives from the intermediate mesoderm (IM), which produces three successive developmental fields: the pronephros, the mesonephros, and the metanephros (Fig. 1.3a) (Maezawa et al., 2011). The pronephros is formed first from the rostral-most region of the urogenital ridge. Later, the mesonephros forms more caudally,

Figure 1.2. Basic structural organization of the vertebrate nephron. A nephron is composed of two principle components: a glomerulus as mediator of ultrafiltration (blue), and a tubule that is responsible for filtrate modification. A tubule can be subdivided into 9 subdomains: S1, S2, and S3 segments of the proximal tubule; DTL, descending thin limb; ATL, ascending thin limb; TAL, thick ascending limb; DCT, distal convoluted tubules; CNT, connecting tubule; CD, collecting duct. Inset showing a schematic view of the podocyte, a key building block of the glomerulus. The podocyte wraps around the capillary wall on the outer surface of the glomerular basement membrane with its extended interdigitating foot processes. Podocyte foot processes are then bridged by a slit diaphragm. A close-up view of the glomerular filtration barrier consisting of three components: porous endothelium, glomerular basement membrane, and podocyte foot processes with the interposed slit diaphragm. The endothelial pores are not bridged by a diaphragm.

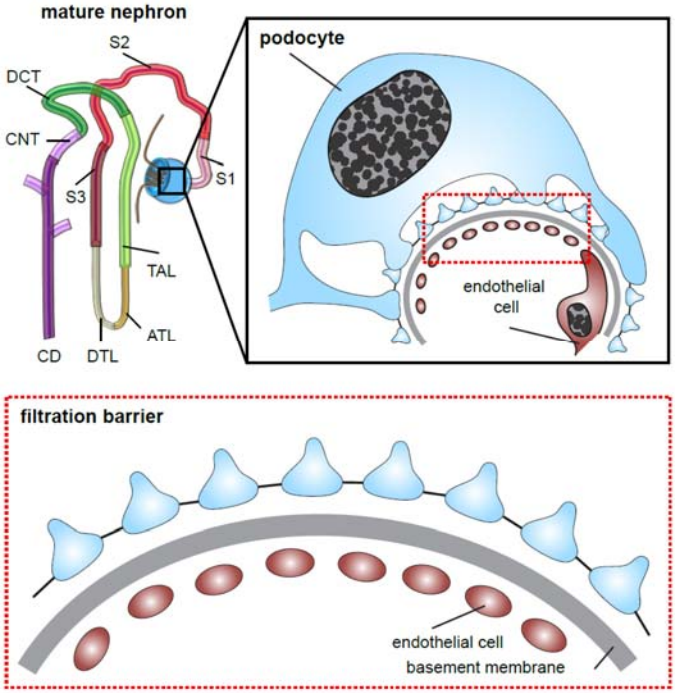
mature nephron
S2
DCT
CNT
S3
S1
TAL
ATL
CD
DTL
podocyte
endothelial cell
filtration barrier
endothelial cell
basement membrane

followed by the metanephros. The first two fields are transient in mammals. However, the mesonephros and possibly the pronephros perform excretory roles during embryogenesis. Both tissues are also required for the development of other organs, such as the adrenal gland and the gonads. Only the metanephros gives rise to the definitive adult kidney.

Kidney development is characterized by sequential inductive interactions and mesenchymal-to-epithelial transformations (Maezawa et al., 2011; Uhlenhaut and Treier, 2008). The formation of the nephric ducts or Wolffian ducts (WD) marks the earliest step in kidney development (Fig. 1.3b). Inductive interactions between the metanephric mesenchyme (MM) and the nephric ducts trigger the growth of the ureteric bud (UB) at the distal end of the nephric ducts. Upon the invasion of UB into the MM, signaling from the MM induces the UB to split into a T-tubule and undergo dichotomous branching. These branches subsequently form the collecting duct system that funnels urine into the bladder (Fig. 1.3b). Simultaneously, at the tips of the branching ureter, the MM is induced to condense, epithelialize, and differentiate into mature nephrons. The differentiation of nephrons occurs through a series of morphogenetic stages referred to as renal vesicles, comma-shape, and S-shape (Fig. 1.3c). These anlagen eventually connect with the collecting duct. This process of branching and differentiation is, remarkably, reiterated 600,000 to 1,000,000 times in each developing kidney. Although nephrogenesis is completed shortly after birth, functional maturation of the kidney continues into the postnatal period.

Figure 1.3. Development of the vertebrate kidney. a, Three stages of mammalian kidney development. The pronephros (P) and mesonephros (M) develop in a rostral-to-caudal direction, and the tubules are aligned adjacent to the Wolffian, or nephric duct (WD). The metanephros develops from an outgrowth of the distal end of the WD known as the ureteric bud (UB) epithelium and a cluster of cells known as the metanephric mesenchyme (MM). Cells migrate from the mesonephros (M) into the developing gonad (G), which develop in close association with one another (modified from (Maezawa et al., 2011)). **b,** Schematic diagram of UB growth and branching in response to inductive signals from the MM. See detailed explanation in the text. **c,** Schematic drawing of nephron development. Reciprocal interactions between the UB and the MM result in a series of well-defined morphologic stages, leading to formation of the nephron. See detailed explanation in the text.

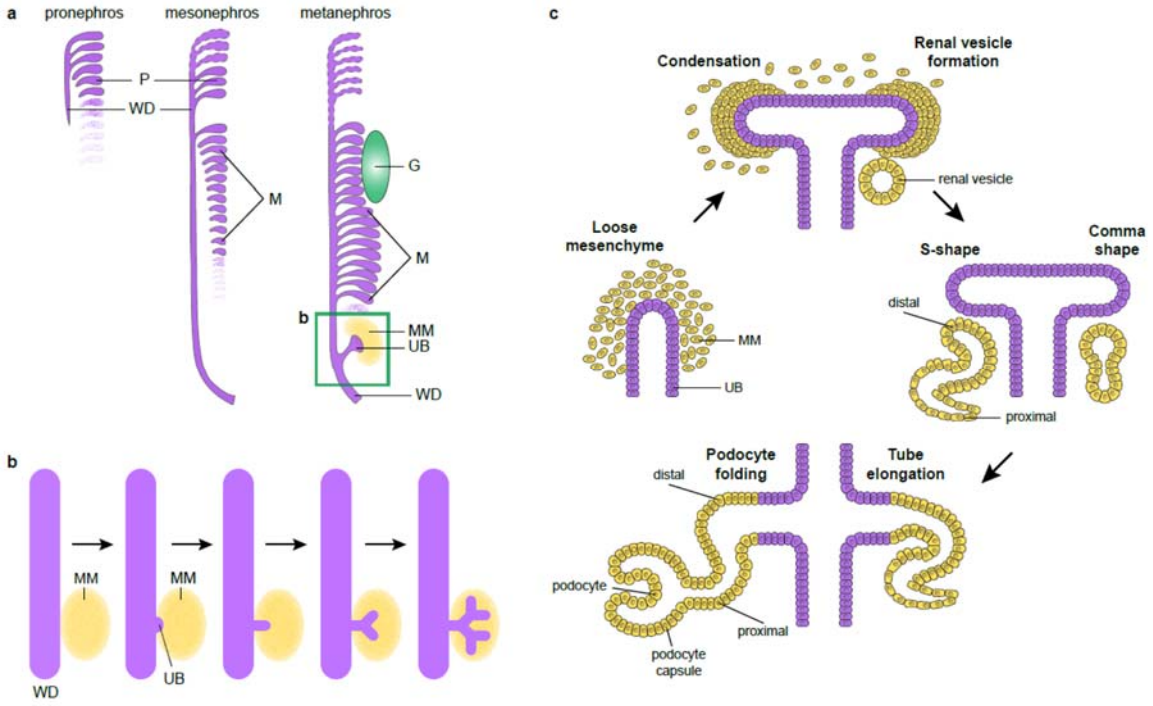
a
pronephros
mesonephros
metanephros
P
WD
M
G
M
b
MM
UB
WD
b
MM
MM
UB
WD
c
Condensation
Renal vesicle formation
renal vesicle
Loose mesenchyme
MM
UB
S-shape
Comma shape
distal
proximal
distal
Podocyte folding
Tube elongation
podocyte
proximal
podocyte capsule

Molecular Control of Mammalian Kidney Development

In the last two decades, a tremendous amount of knowledge has been gained regarding the molecular control of mammalian kidney development. However, many outstanding questions still must be addressed.

Early Lineage Determination of the Metanephric Kidney

The formation of the nephric duct marks the initiation of metanephric kidney formation (Fig. 1.3). This requires the cell-autonomous activity of either *Pax2* or *Pax8*, closely related PAX-family transcriptional regulators (Fig. 1.4a) (Bouchard et al., 2002). The LIM family member *Lhx1* later facilitates the caudal extension and development of the nephric duct (Fig. 1.4a) (Pedersen et al., 2005; Tsang et al., 2000). Consequently, no UB forms in these mouse mutants. At a later stage, *Pax2* and *Gata3* are required to establish the UB (Fig. 1.4a) (Grote et al., 2006; Lim et al., 2000; Torres et al., 1995). Normal specification of the MM, in turn, requires many key transcription factors, including *Osr1*, *Wt1*, *Hoxa11*, *Hoxc11*, *Hoxd11*, *Sall1*, *Six1*, and *Eya1* (Fig. 1.4a). Of these, *Osr1* and *Eya1* represent the earliest known determinants of the MM (James et al., 2006; Xu et al., 1999). *Osr1* mutants do not form the MM, nor do they express several other factors required for metanephric kidney formation, such as *Eya1*, *Six2*, *Pax2*, *Sall1*, or *Gdnf* (James et al., 2006). Similarly, *Eya1* and *Six1* mutants fail to induce the MM, suggesting that *Eya1* acts together with *Six1* to determine MM cell fate (Sajithlal et al., 2005; Xu et al., 1999). *Wt1* instead acts broadly and early within the IM, at least in part as an anti-apoptotic factor to support MM development (Kreidberg et al., 1993). Although the functions of many aforementioned genes during early MM specification are well

understood, their roles within specific compartments of the kidney at later stages have not been thoroughly investigated. Furthermore, the analysis of numerous factors within the MM is complicated by their expression in multiple kidney compartments. For example, *Pax2* acts in the UB, but its expression is also present in the MM. To date, a MM-specific function for *Pax2* has not yet been examined.

Regulating of Ureteric Bud Outgrowth and Branching Morphogenesis

The GDNF/RET pathway is a key regulator of UB outgrowth and branching morphogenesis through its inductive interactions with the nephric ducts (Fig. 1.4a). GDNF, secreted by the MM, activates a GFRA1/RET receptor-tyrosine kinase (RTK) complex that is expressed by cells of the UB. This initiates a signaling cascade that upregulates expression of the RET receptor and triggers outgrowth of RET^{+} cells from the nephric duct toward the GDNF signal (Fig. 1.4a) (reviewed by (Costantini and Kopan, 2010)). Disruption of *Gdnf*, *Ret*, or *Gfra1* in the mouse results in the complete failure of UB outgrowth and kidney agenesis (Jain, 2009). A number of transcription factors have been shown to regulate expression of *Gdnf*, including *Eya1*, *Pax2*, *Sall1*, and the *Hox11* paralog group (Fig. 1.4a). Targeted deletion of any one of these genes leads to renal agenesis and a failure of *Gdnf* expression. As mentioned previously, *Eya1* mutants fail to form metanephric mesenchyme. In *Pax2* null mutants, *Eya1*, *Six1*, and *Sall1* are still expressed, indicating that the *Eya1/Six1* pathway is not downstream but may be upstream of *Pax2* (Dressler et al., 1990). Meanwhile, mice carrying mutations in any one of the *Hox11* paralogs, including *Hoxa11*, *Hoxc11*, and *Hoxd11*, do not have kidney abnormalities; yet, mice with triple mutations in these genes demonstrate a complete

Figure 1.4. Genetic networks controlling early lineage determination of the metanephric kidney, ureteric bud branching, nephron induction, and segmentation. **a,** Genetic network controlling early lineage determination of the metanephric kidney and ureteric bud branching (see text for details). Dashed arrow indicates uncertain regulatory effects. Modified from (Costantini and Kopan, 2010; Maezawa et al., 2011). **b-c,** Genetic network controlling nephron induction (b) and segmentation (c) (see text for details). NP, nephron progenitors; UB, ureteric bud; PTA, pretubular aggregate; red arrow in (b) represents promotion of self-renewal. Modified from (O'Brien and McMahon, 2014).

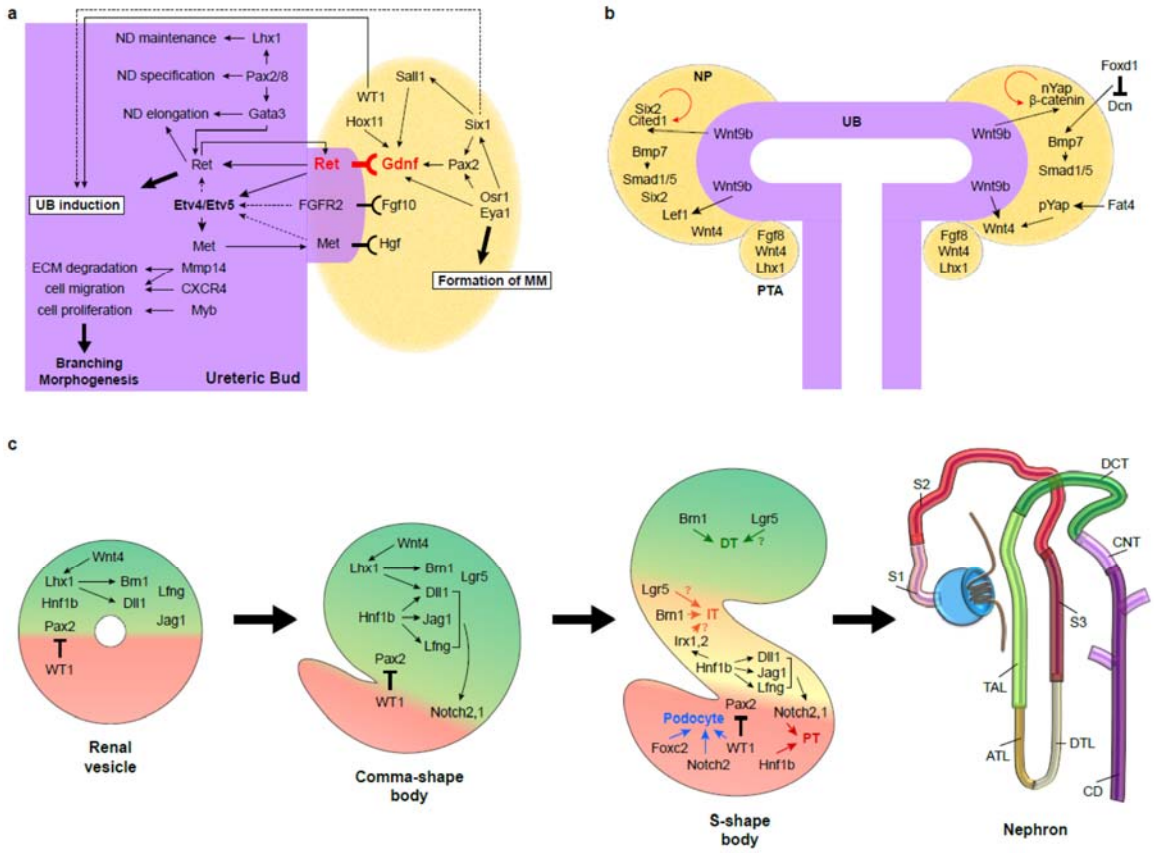
a
ND maintenance
Lhx1
ND specification
Pax2/8
ND elongation
Gata3
Ret
Ret
Gdnf
Pax2
WT1
Sall1
Hox11
Six1
UB induction
Etv4/Etv5
FGFR2
Fgf10
Osr1
Eya1
Met
Met
Hgf
ECM degradation
Mmp14
cell migration
CXCR4
cell proliferation
Myb
Formation of MM
Branching Morphogenesis
Ureteric Bud
b
NP
Six2
Cited1
Wnt9b
UB
Bmp7
Smad1/5
Six2
Lef1
Wnt4
Fgf8
Wnt4
Lhx1
PTA
Foxd1
Dcn
nYap
β-catenin
Wnt9b
Bmp7
Smad1/5
pYap
Fat4
Wnt4
Fgf8
Wnt4
Lhx1
c
Wnt4
Lhx1
Brn1
Lfng
Hnf1b
Dll1
Jag1
Pax2
WT1
Renal vesicle
Wnt4
Lhx1
Brn1
Lgr5
Dll1
Hnf1b
Jag1
Lfng
Pax2
WT1
Notch2,1
Comma-shape body
Brn1
Lgr5
DT
Lgr5
Brn1
IT
Irx1,2
Hnf1b
Dll1
Jag1
Lfng
Pax2
Notch2,1
Podocyte
Foxc2
WT1
PT
Notch2
Hnf1b
S-shape body
S2
DCT
CNT
S1
S3
TAL
ATL
DTL
CD
Nephron

absence of metanephric kidney induction (Wellik et al., 2002). Interestingly, in these triple mutants, the formation of condensing MM and the expression of *Eya1*, *Pax2*, and *Wt1* remain unperturbed, suggesting that *Hox11* is not upstream of these factors.

GDNF/RET is not the sole RTK pathway that mediates branching (Fig. 1.4a). Many other RTK signaling pathways are involved in regulating UB outgrowth and morphogenesis. These include FGF/FGFR (Bates, 2011), EGF/EGFR (Ishibe et al., 2009), VEGFA/VEGFR2 (Marlier et al., 2009; Tufro et al., 2007), and HGF/MET (Ishibe et al., 2009). Furthermore, Angiotensin I/II binding to AGTR1/AGTR2 in the ureteric tips induces tyrosine phosphorylation of EGFR (Yosypiv et al., 2006) and RET (Song et al., 2010), which then stimulates branching. In contrast to factors deriving from the MM that promote UB branching, a number of signals produced by the MM or stroma inhibit this process, including BMP4 and other TGFβ family members (Cain et al., 2008). Together, these inhibitory inputs ensure the outgrowth of a single UB from the nephric duct at the right time and place. RTKs then activate the PI3K-AKT and RAS/ERK MAP kinase signaling pathways, which leads to changes in gene expression of many transcriptional regulatory factors that control branching morphogenesis, including *Etv4*, *Etv5*, *Sox8*, and *Sox9* (detailed review by (Costantini and Kopan, 2010)).

Nephron Induction

As mentioned in the previous section, nephrogenesis requires a sequential inductive interaction between the UB and the MM (Fig. 1.4b). This triggers a subpopulation of *Six2*$^{+}$ cap mesenchyme (CM) to undergo mesenchymal epithelial transition (MET) and generate the renal vesicle (RV) (O'Brien and McMahon, 2014).

Canonical Wnt signaling directed by *Wnt9b/β-catenin* has emerged as the key pathway initiating this process. *Wnt9b* is expressed in the entire UB, except the very tips. Genetic analysis has demonstrated that *Wnt9b* is not required for nephron progenitor specification nor UB outgrowth, but is essential for mediating RV commitment through the stabilization of β-CATENIN (Carroll et al., 2005). *Wnt9b* also activates expression of secondary signals including *Fgf8* and *Wnt4* within pretubular aggregates to regulate RV formation (Carroll et al., 2005; Grieshammer et al., 2005; Kispert et al., 1998; Mugford et al., 2009; Perantoni et al., 2005; Stark et al., 1994). The observation that *Six2* is required to maintain the CM, while *Wnt9b* commits a subset of this population to an RV fate, raises an interesting question. How is Wnt signaling regulated to restrict RV induction in only a subset of the *Six2*$^{+}$ CM population? In the absence of *Six2*, all nephron progenitors undergo rapid and premature differentiation, resulting in ectopic formation of RVs (Self et al., 2006). These data suggest that *Six2* might be involved in the suppression of RV differentiation within nephron progenitors. *Six2* and *Wnt9b* double mutants lack RVs, which bear a resemblance to *Wnt9b* single mutants. This indicates that *Six2* counters *Wnt9b's* nephron-inducing activity (Kobayashi et al., 2008). However, the mechanism for this remains to be addressed.

Recent studies have revealed an additional nephrogenic contribution from the *Foxd1*$^{+}$ interstitial progenitors surrounding *Six2*$^{+}$ nephron progenitors (Fig. 1.4b). Depleting this population leads to an expansion of the nephron progenitors and a marked delay in the inductive process (Das et al., 2013). Furthermore, stromal *Fat4* and the Hippo/Warts pathway were demonstrated to modulate β-CATENIN activity in nephron progenitors (Fig. 1.4b) (Das et al., 2013; Reginensi et al., 2013). Uninduced nephron

progenitors retain nuclear TAZ/YAP, and deletion of these components within the nephron progenitor population significantly reduces the number of differentiated structures. This suggests that nuclear TAZ/YAP cooperates with β-CATENIN to promote progenitor self-renewal. However, the mechanistic details of crosstalk between the Hippo and Wnt signaling pathways in nephron progenitors remains to be determined. Additionally, BMP7/SMAD signaling promotes nephron induction based upon the analysis of *Foxd1* mutants, although this might be an indirect effect (Das et al., 2013). *Foxd1*$^{+}$ stromal cells activate BMP7/SMAD signaling in nephron progenitors by repressing *Dcn*, an antagonist of *Bmp7*. This subsequently promotes the commitment of nephron progenitors to an RV fate. *Bmp7* has also been shown to play an important role in the maintenance of nephron progenitors (Dudley et al., 1999; Dudley et al., 1995; Luo et al., 1995). How these dual roles for *Bmp7* in maintenance and induction are differentially regulated remains elusive.

Interestingly, nephron induction is a temporally regulated process. Nephron progenitors are lost by P2-3 in the mouse (Hartman et al., 2007; Rumballe et al., 2011) and around 36 weeks of gestation in humans (Hinchliffe et al., 1991). Once lost, the capacity for *de novo* nephrogenesis ceases, even in injured kidneys. However, what causes the cessation of nephrogenesis is not understood. Is it the result of a complete loss of nephron progenitor self-renewal? Or is it due to perturbations in the balance between self-renewal and commitment to differentiation? An improved understanding about the limits to nephrogenesis undoubtedly holds great promise for future clinical treatments of kidney disease and injury.

Patterning, Segmentation, and Morphogenesis of the Nephrons

After nephron progenitors commit to the RV fate, the RV forms a lumen and begins to "'unwind" to form comma-shaped and S-shaped bodies (Fig. 1.3c). The neo-nephron then connects with the ureteric tip shortly after undergoing MET, forming the mature nephron. During this process, cells in the RV acquire polarity and initiate a patterning program that leads to the determination of specific cell types along the proximal-distal axis of the nephron. How the lumen forms in the RV and what initiates polarity in the RV are poorly understood processes. However, some aspects of patterning processes after lumen formation are known. The distal expression of Notch (*Dll1*, *Lfng*, and *Jag1*), Bmp (*Bmp2*), and Wnt (*Wnt4*, *Lef1*, and *Dkk1*) pathway genes implies different cellular identity and activity along the proximal-distal axis (Fig. 1.4c) (Cheng et al., 2007; Dressler, 2009; Georgas et al., 2009; Mugford et al., 2009). Notch signaling is critical for the specification of proximal cell fates including the podocyte and proximal tubule (Chen and Al-Awqati, 2005; Cheng et al., 2007; Georgas et al., 2009; Heliot et al., 2013; Piscione et al., 2004), whereas *Lrg5*, *Lhx1*, and *Brn1* regulates patterning of distal tubule structures (Georgas et al., 2009; Kobayashi et al., 2005; Nakai et al., 2003) (Fig. 1.4c). *Wt1* also promotes proximal identity by antagonizing *Pax2* and cooperating with the Notch pathway and *Foxc2* to specify the podocyte (Fig. 1.4c) (Georgas et al., 2009; Moore et al., 1999; Ryan et al., 1995). *Hnf1b* promotes proximal and intermediate/medial fate through regulation of Notch ligand expression and *Irx1/2* (Heliot et al., 2013). After establishing proximal-distal polarity, the nephron continues to elongate and segment to produce a functioning nephron composed of many specialized regions. Proximal segments give rise to the glomerulus and S1-S3 segments of the proximal tubule. Intermediate segments form the

loop of Henle. Distal segments establish the distal tubule, which joins the collecting duct through a connecting segment (Fig. 1.4c).

Although many of the genes involved in the establishment of nephron polarity have been identified, little is known about how terminal differentiation of the various segments is accomplished. Additionally, regulation of tubule length, elongation, and shape are critical for normal renal function. However, this remains poorly understood and under-investigated. Disrupted tubular patterning and morphogenesis lead to kidney diseases, most notably cystic kidney diseases (CKDs). Exploring the biophysics and molecular mechanisms of tubule elongation and morphogenesis are crucial for better understanding kidney pathologies and developing new therapies.

Invertebrate Model Systems for Kidney Development and Diseases

Due to their experimental accessibility, invertebrate models have provided incredible insights into understanding human kidney development and diseases (Igarashi, 2005). One of the best examples is the discovery of the link between cilia and autosomal dominant polycystic kidney disease (ADPKD), first made in *C. elegans*. ADPKD, one of the most common inherited diseases in humans, is caused by a mutation in *PKD1* and *PKD2*, genes encoding POLYCYSTIN-1 and POLYCYSTIN-2, respectively (Wilson and Goilav, 2007). *C. elegans* has homologues of *Polycystin-1* and *Polycystin-2*, named *lov-1* and *pkd-2*, which are expressed in the primary cilia of sensory neurons and required for mating behavior (Barr, 2005; Barr and Sternberg, 1999). Additionally, comparative genomic studies in *C. elegans* have revealed the important function of other CKD genes in the primary cilia, including Bardet-Biedl syndrome and nephronophthisis (Barr, 2005).

These results suggest that many CKD genes encode ciliary proteins that are involved in cell sensing, and therefore establish ciliary hypothesis as the unifying disease mechanism of CKDs. In addition to *C. elegans*, *D. melanogaster's* renal (Malpighian) tubule has been recognized as a useful model to study branching tubular morphogenesis, stem cell-mediated regeneration, and podocyte biology (Dow and Romero, 2010).

While both of these invertebrate model systems have yielded key insights into kidney physiology and diseases, there are many aspects of kidney biology that cannot be modeled in *C. elegans* or *D. melanogaster*. For instance, both organisms have highly derived excretory organs in which ultrafiltration is either entirely lacking (*C. elegans*) or uncoupled from reabsorption/secretion (*D. melanogaster*). This makes it impossible to study important classes of human cyst pathologies that arise from tubular segments disconnected from the influx of glomerular filtrate and tubular flow. Furthermore, the excretory cells of both *C. elegans* and *D. melanogaster* lack cilia. Therefore, ciliary dysfunction – the major cause of CKDs – cannot be studied in either of these invertebrates. Since renal cilia in the mammalian kidney are very difficult to visualize *in vivo*, other model organisms with experimentally accessible ciliated excretory organs will be instrumental for improving our understanding of human CKDs.

The Planarian Protonephridial Excretory System

Protonephridia are a self-contained ciliated excretory system found in a wide range of invertebrate groups, including Platyhelminthes, Nemertea, Rotifera, Acanthocephala, Entoprocta, Kinorhyncha, Gastrotricha, Priapulida, Annelida, Mollusca, and Cephalochordata (Ruppert and Smith, 1988; Wilson and Webster, 1974). Planarian

flatworms, members of the Platyhelminthes, possess protonephridal excretory systems, a network of tubules distributed along the body length of the animals (Fig. 1.5a). The protonephridium consists of a tube or tubule opening distally via nephridiopore at the surface of the animal and ending proximally in one or more terminal structures (Fig. 1.5a'-a'') (Wilhelmi, 1906; Wilson and Webster, 1974). Like many invertebrates, the morphology of the planarian excretory system has been extensively investigated by histochemical and ultrastructural techniques (Ishii, 1980a, b; McKanna, 1968a, b; Pedersen, 1961; Wetzel, 1962).

Morphology of Planarian Protonephridia

Planarian flame cell is a single cell comprised of a blindly ending nucleated tube of cytoplasm in which lies the tuft of flagella (Wilson and Webster, 1974). In *Dugesia tigrina*, the flame cell is cylindrical, forming a thin-walled "basket" open to the lumen of a nonciliated collecting duct (Wetzel, 1962). The cytoplasm is concentrated at the basal pole (the closed end of the "basket"), which supports a bundle of cilia (Fig. 1.5b-c). These abundant cilia resemble the appearance of a fire's flames when visualized histologically, providing the inspiration for naming these cells. The cell body and its nucleus can reside at the proximal pole or anywhere along the length of the flame bulb. There are about 35-90 cilia forming the "flame" in the lumen of the flame cell surrounded by numerous microvilli in the regions of the fenestrae (Fig. 1.5c). The flame cells are connected to the cells of a nonciliated tubule and to a ciliated collecting duct by septate junctions, the homologous structure to the tight junctions in vertebrates. The cilia of the "flame" terminate several micrometers into the tubules (McKanna, 1968a). Meanwhile, in the

Figure 1.5. The planarian protonephridial excretory system. a, Distribution of protonephridial excretory system in the planarian *Dendrocoelum lacteum* (after (Hyman, 1951)). **a'-a'',** Part of flatworm protonephridium consists of multiple flame cells (a'') connected to the tubule (after (Hyman, 1951)). **b,** Schematic diagram of protonephridial system in the planarian *Dugesia tigrina* (after (McKanna, 1968b)). **c-e,** electron micrographs showing cross sections of protonephridial cell types showing in b: (c) flame cell; (d) tubule cell; and (d) collecting duct (after (McKanna, 1968b)).

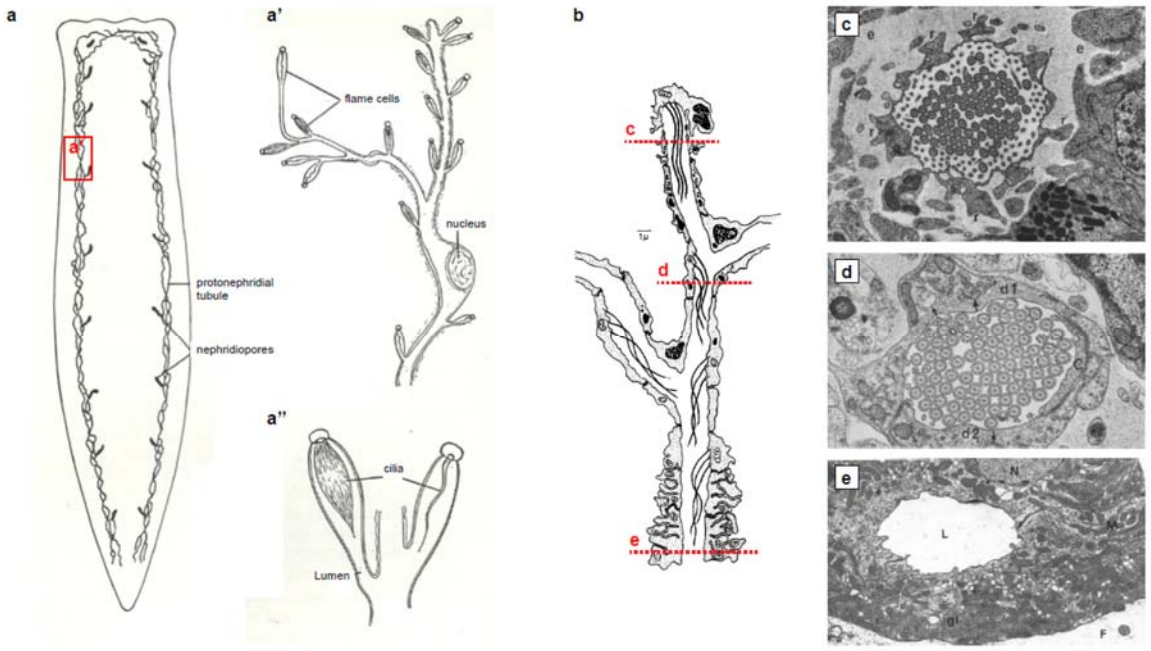
a
a'
a''
flame cells
nucleus
protonephridial tubule
nephridiopores
cilia
Lumen
b
c
d
e
d1
d2
N
L
M
F

planarian *Bdellocephala brunnea*, the flame cell was described as an elongated ellipsoidal shape and could be divided into two parts by the position of the cell body: a larger proximal part and a smaller distal part that appears narrower (Ishii, 1980a). In this study, the fenestrated structure of the planarian flame cell was also described as the result of the interdigitation of luminal microvilli on its peripheral margin.

Distal to the terminal structures of protonephridia is a tubular network. These tubules have been described as single-layer cuboidal or flattened epithelial canals leading from the flame cells to the surface epithelium (Wilson and Webster, 1974). The tubule walls in the planarian *Dugesia tigrina* are made up of two cells, approximately half of the lumen being bounded by each cell. Desmosomes are present where the cells meet and the cytoplasm of each cell contains an irregular nucleus, Golgi complexes, and many vesicles (Fig. 1.5d-e) (McKanna, 1968b; Pedersen, 1961). Wetzel described tubules of protonephridia as being thrown into folds that penetrated between the surrounding parenchymal cells. The presence of these folds, together with numerous mitochondria in the cytoplasm, were taken as evidence that the excretory fluid was modified by the tubules (Wetzel, 1962). Cilia are sometimes present in the lumen of the large collecting ducts, presumably to assist the flow of fluid towards the nephridiopore (McKanna, 1968b). The number of flame cells and tubule distribution may vary greatly from group to group. Some worms have a simple system in which ducts from a few protonephridia fuse before emptying on the surface of the worm. In more complex systems, there are many terminal and lateral flame cells with highly convoluted tubules that fuse before entering a large collecting duct with a nephridiopore on the surface of the worm. However, the location

and structure of the nephridiopore remain unknown in planarians (Ishii, 1980b; McKanna, 1968b).

Proposed Functions of Planarian Protonephridia

Functions of planarian protonephridia in excretion and osmoregulation have been proposed mainly on the basis of ultrastructural analyses. First of all, the flame cells of protonephridia were argued to be the site of filtration because they satisfied two necessary criteria for filtration. This includes 1) the presence of a filter separating two fluid compartments and 2) a pressure gradient across the filter. The interdigitations between the flame cell and tubule cell have been postulated to be a region where filtration of interstitial fluid occurs. Meanwhile, the beating cilia have been suggested to draw fluid from interstitial spaces into the lumen of the organ, propelling it down the tubule (Ishii, 1980a; McKanna, 1968a; Pedersen, 1961; Wetzel, 1962). Secondly, in the proximal tubules, there is a distribution gradient of elements interpreted as participating in protein absorption, such as vacuoles and dense vesicles and granules. These are most numerous in the flame cell and gradually decrease distally. These features closely resemble the proximal convoluted tubule cell of the mammalian kidney (Ishii, 1980a; McKanna, 1968a; Pedersen, 1961; Wetzel, 1962). Finally, there is evidence for morphological similarity of "osmoregulatory cells" in the distal tubules and collecting tubes of planarian protonephridia to various epithelia in the distal convoluted tubules of vertebrate nephrons (Ishii, 1980b; McKanna, 1968b).

Research Summary

The recent revival of planarians as a molecularly tractable model system and their phylogenetic position within the scarcely sampled Lophotrochozoa superphylum has provided a unique opportunity to close the "invertebrate gap" in kidney model systems. As mentioned above, planarians provide a representative invertebrate protonephridial excretory system. They also offer a rapidly expanding list of experimental tools, including a sequenced genome for the species *Schmidtea mediterranea*, RNA-mediated genetic interference (RNAi), and various histological protocols (Elliott and Sanchez Alvarado, 2013). Additionally, planarians have the fascinating ability to regenerate not only all organ systems, but complete animals from minute tissue fragments. Thus, amputation-induced organogenesis provides a unique experimental paradigm to study excretory system ontogeny. As such, for the first time, planarians provide a unique opportunity to systematically characterize a protonephridial excretory system at the molecular level.

This thesis research aims to perform a comprehensive functional and molecular characterization of planarian protonephridia in order to provide new insights into the long-debated question of the evolutionary relationship between vertebrate and invertebrate excretory systems as well as to gauge planarians' potential as a novel invertebrate model for human kidney development, diseases, and evolution. To achieve these goals, this thesis has focused on answering three key questions:

1) **What are the molecular and functional identities of the protonephridial cell types in planarians, and how do they compare to the vertebrate nephron?**

2) **Does protonephridia regeneration resemble morphogenetic events during kidney ontogeny? Do they share common genetic regulators?**

3) **Can planarian protonephridia model pathologies of the human kidney?**

References

Barr, M.M. (2005). Caenorhabditis elegans as a model to study renal development and disease: Sexy cilia. J Am Soc Nephrol *16*, 305-312.

Barr, M.M., and Sternberg, P.W. (1999). A polycystic kidney-disease gene homologue required for male mating behaviour in c. Elegans. Nature *401*, 386-389.

Bates, C.M. (2011). Role of fibroblast growth factor receptor signaling in kidney development. Pediatr Nephrol *26*, 1373-1379.

Bouchard, M., Souabni, A., Mandler, M., Neubuser, A., and Busslinger, M. (2002). Nephric lineage specification by pax2 and pax8. Genes Dev *16*, 2958-2970.

Cain, J.E., Hartwig, S., Bertram, J.F., and Rosenblum, N.D. (2008). Bone morphogenetic protein signaling in the developing kidney: Present and future. Differentiation *76*, 831-842.

Carroll, T.J., Park, J.S., Hayashi, S., Majumdar, A., and McMahon, A.P. (2005). Wnt9b plays a central role in the regulation of mesenchymal to epithelial transitions underlying organogenesis of the mammalian urogenital system. Dev Cell *9*, 283-292.

CDC (2014). 2014 national chronic kidney disease fact sheet (Atlanta, GA: National Center for Chronic Disease Prevention and Health Promotion).

Chen, L., and Al-Awqati, Q. (2005). Segmental expression of notch and hairy genes in nephrogenesis. Am J Physiol Renal Physiol *288*, F939-952.

Cheng, H.T., Kim, M., Valerius, M.T., Surendran, K., Schuster-Gossler, K., Gossler, A., McMahon, A.P., and Kopan, R. (2007). Notch2, but not notch1, is required for proximal fate acquisition in the mammalian nephron. Development *134*, 801-811.

Costantini, F., and Kopan, R. (2010). Patterning a complex organ: Branching morphogenesis and nephron segmentation in kidney development. Dev Cell *18*, 698-712.

Das, A., Tanigawa, S., Karner, C.M., Xin, M., Lum, L., Chen, C., Olson, E.N., Perantoni, A.O., and Carroll, T.J. (2013). Stromal-epithelial crosstalk regulates kidney progenitor cell differentiation. Nat Cell Biol *15*, 1035-1044.

Dow, J.A., and Romero, M.F. (2010). Drosophila provides rapid modeling of renal development, function, and disease. Am J Physiol Renal Physiol *299*, F1237-1244.

Dressler, G.R. (2009). Advances in early kidney specification, development and patterning. Development *136*, 3863-3874.

Dressler, G.R., Deutsch, U., Chowdhury, K., Nornes, H.O., and Gruss, P. (1990). Pax2, a new murine paired-box-containing gene and its expression in the developing excretory system. Development *109*, 787-795.

Dudley, A.T., Godin, R.E., and Robertson, E.J. (1999). Interaction between fgf and bmp signaling pathways regulates development of metanephric mesenchyme. Genes Dev *13*, 1601-1613.

Dudley, A.T., Lyons, K.M., and Robertson, E.J. (1995). A requirement for bone morphogenetic protein-7 during development of the mammalian kidney and eye. Genes Dev *9*, 2795-2807.

Elliott, S.A., and Sanchez Alvarado, A. (2013). The history and enduring contributions of planarians to the study of animal regeneration. Wiley Interdiscip Rev Dev Biol *2*, 301-326.

Fenton, R.A., and Praetorius, J. (2011). Molecular physiology of the medullary collecting duct. Compr Physiol *1*, 1031-1056.

Georgas, K., Rumballe, B., Valerius, M.T., Chiu, H.S., Thiagarajan, R.D., Lesieur, E., Aronow, B.J., Brunskill, E.W., Combes, A.N., Tang, D.*, et al.* (2009). Analysis of early nephron patterning reveals a role for distal rv proliferation in fusion to the ureteric tip via a cap mesenchyme-derived connecting segment. Dev Biol *332*, 273-286.

Grieshammer, U., Cebrian, C., Ilagan, R., Meyers, E., Herzlinger, D., and Martin, G.R. (2005). Fgf8 is required for cell survival at distinct stages of nephrogenesis and for regulation of gene expression in nascent nephrons. Development *132*, 3847-3857.

Grote, D., Souabni, A., Busslinger, M., and Bouchard, M. (2006). Pax 2/8-regulated gata 3 expression is necessary for morphogenesis and guidance of the nephric duct in the developing kidney. Development *133*, 53-61.

Hartman, H.A., Lai, H.L., and Patterson, L.T. (2007). Cessation of renal morphogenesis in mice. Dev Biol *310*, 379-387.

Heliot, C., Desgrange, A., Buisson, I., Prunskaite-Hyyrylainen, R., Shan, J., Vainio, S., Umbhauer, M., and Cereghini, S. (2013). Hnf1b controls proximal-intermediate nephron segment identity in vertebrates by regulating notch signalling components and irx1/2. Development *140*, 873-885.

Hinchliffe, S.A., Sargent, P.H., Howard, C.V., Chan, Y.F., and van Velzen, D. (1991). Human intrauterine renal growth expressed in absolute number of glomeruli assessed by the disector method and cavalieri principle. Lab Invest *64*, 777-784.

Hyman, L.H. (1951). Invertebrates: Platyhelminthes and rhynchocoela (New York: Mcgraw-Hill).

Igarashi, P. (2005). Overview: Nonmammalian organisms for studies of kidney development and disease. J Am Soc Nephrol *16*, 296-298.

Ishibe, S., Karihaloo, A., Ma, H., Zhang, J., Marlier, A., Mitobe, M., Togawa, A., Schmitt, R., Czyczk, J., Kashgarian, M.*, et al.* (2009). Met and the epidermal growth factor receptor act cooperatively to regulate final nephron number and maintain collecting duct morphology. Development *136*, 337-345.

Ishii, S. (1980a). The ultrastructure of the protonephridial flame cell of the freshwater planarian bdellocephala brunnea. Cell Tissue Res *206*, 441-449.

Ishii, S. (1980b). The ultrastructure of the protonephridial tubules of the freshwater planarian bdellocephala brunnea. Cell Tissue Res *206*, 451-458.

Jain, S. (2009). The many faces of ret dysfunction in kidney. Organogenesis *5*, 177-190.

James, R.G., Kamei, C.N., Wang, Q., Jiang, R., and Schultheiss, T.M. (2006). Odd-skipped related 1 is required for development of the metanephric kidney and regulates formation and differentiation of kidney precursor cells. Development *133*, 2995-3004.

Kispert, A., Vainio, S., and McMahon, A.P. (1998). Wnt-4 is a mesenchymal signal for epithelial transformation of metanephric mesenchyme in the developing kidney. Development *125*, 4225-4234.

Kobayashi, A., Kwan, K.M., Carroll, T.J., McMahon, A.P., Mendelsohn, C.L., and Behringer, R.R. (2005). Distinct and sequential tissue-specific activities of the lim-class homeobox gene lim1 for tubular morphogenesis during kidney development. Development *132*, 2809-2823.

Kobayashi, A., Valerius, M.T., Mugford, J.W., Carroll, T.J., Self, M., Oliver, G., and McMahon, A.P. (2008). Six2 defines and regulates a multipotent self-renewing nephron progenitor population throughout mammalian kidney development. Cell Stem Cell *3*, 169-181.

Kreidberg, J.A., Sariola, H., Loring, J.M., Maeda, M., Pelletier, J., Housman, D., and Jaenisch, R. (1993). Wt-1 is required for early kidney development. Cell *74*, 679-691.

Lim, K.C., Lakshmanan, G., Crawford, S.E., Gu, Y., Grosveld, F., and Engel, J.D. (2000). Gata3 loss leads to embryonic lethality due to noradrenaline deficiency of the sympathetic nervous system. Nat Genet *25*, 209-212.

Luo, G., Hofmann, C., Bronckers, A.L., Sohocki, M., Bradley, A., and Karsenty, G. (1995). Bmp-7 is an inducer of nephrogenesis, and is also required for eye development and skeletal patterning. Genes Dev *9*, 2808-2820.

Maezawa, Y., Kreidberg, J., and Quaggin, S.E. (2011). Embryology of the kidney. In Brenner and Rector's the kidney, M. Taal, G. Chertow, P. Marsden, K. Skorecki, A. Yu, and B. Brenner, eds. (USA: Elsevier), 2-30.

Marlier, A., Schmidt-Ott, K.M., Gallagher, A.R., Barasch, J., and Karihaloo, A. (2009). Vegf as an epithelial cell morphogen modulates branching morphogenesis of embryonic kidney by directly acting on the ureteric bud. Mech Dev *126*, 91-98.

McKanna, J.A. (1968a). Fine structure of the protonephridial system in planaria. I. Flame cells. Z Zellforsch Mikrosk Anat *92*, 509-523.

McKanna, J.A. (1968b). Fine structure of the protonephridial system in planaria. Ii. Ductules, collecting ducts, and osmoregulatory cells. Z Zellforsch Mikrosk Anat *92*, 524-535.

Moore, A.W., McInnes, L., Kreidberg, J., Hastie, N.D., and Schedl, A. (1999). Yac complementation shows a requirement for wt1 in the development of epicardium, adrenal gland and throughout nephrogenesis. Development *126*, 1845-1857.

Mugford, J.W., Yu, J., Kobayashi, A., and McMahon, A.P. (2009). High-resolution gene expression analysis of the developing mouse kidney defines novel cellular compartments within the nephron progenitor population. Dev Biol *333*, 312-323.

Nakai, S., Sugitani, Y., Sato, H., Ito, S., Miura, Y., Ogawa, M., Nishi, M., Jishage, K., Minowa, O., and Noda, T. (2003). Crucial roles of brn1 in distal tubule formation and function in mouse kidney. Development *130*, 4751-4759.

O'Brien, L.L., and McMahon, A.P. (2014). Induction and patterning of the metanephric nephron. Semin Cell Dev Biol *36*, 31-38.

Pannabecker, T.L. (2012). Structure and function of the thin limbs of the loop of henle. Compr Physiol *2*, 2063-2086.

Pedersen, A., Skjong, C., and Shawlot, W. (2005). Lim 1 is required for nephric duct extension and ureteric bud morphogenesis. Dev Biol *288*, 571-581.

Pedersen, K.J. (1961). Some observation on the fine structure of planarian protonephridia and gastrodermal phagocytes. Zeitschrift fiir Zellforschung *53*, 609-628.

Perantoni, A.O., Timofeeva, O., Naillat, F., Richman, C., Pajni-Underwood, S., Wilson, C., Vainio, S., Dove, L.F., and Lewandoski, M. (2005). Inactivation of fgf8 in early mesoderm reveals an essential role in kidney development. Development *132*, 3859-3871.

Piscione, T.D., Wu, M.Y., and Quaggin, S.E. (2004). Expression of hairy/enhancer of split genes, hes1 and hes5, during murine nephron morphogenesis. Gene Expr Patterns *4*, 707-711.

Quaggin, S.E., and Kreidberg, J.A. (2008). Development of the renal glomerulus: Good neighbors and good fences. Development *135*, 609-620.

Reginensi, A., Scott, R.P., Gregorieff, A., Bagherie-Lachidan, M., Chung, C., Lim, D.S., Pawson, T., Wrana, J., and McNeill, H. (2013). Yap- and cdc42-dependent nephrogenesis and morphogenesis during mouse kidney development. PLoS Genet *9*, e1003380.

Rumballe, B.A., Georgas, K.M., Combes, A.N., Ju, A.L., Gilbert, T., and Little, M.H. (2011). Nephron formation adopts a novel spatial topology at cessation of nephrogenesis. Dev Biol *360*, 110-122.

Ruppert, E.E. (1994). Evolutionary origin of the vertebrate nephron. Amer. Zool *34*, 542-553.

Ruppert, E.E., and Smith, P.R. (1988). The functional organization of filtration nephridia. Biol Rev *63*, 231-258.

Ryan, G., Steele-Perkins, V., Morris, J.F., Rauscher, F.J., 3rd, and Dressler, G.R. (1995). Repression of pax-2 by wt1 during normal kidney development. Development *121*, 867-875.

Sajithlal, G., Zou, D., Silvius, D., and Xu, P.X. (2005). Eya 1 acts as a critical regulator for specifying the metanephric mesenchyme. Dev Biol *284*, 323-336.

Self, M., Lagutin, O.V., Bowling, B., Hendrix, J., Cai, Y., Dressler, G.R., and Oliver, G. (2006). Six2 is required for suppression of nephrogenesis and progenitor renewal in the developing kidney. EMBO J *25*, 5214-5228.

Song, R., Spera, M., Garrett, C., and Yosypiv, I.V. (2010). Angiotensin ii-induced activation of c-ret signaling is critical in ureteric bud branching morphogenesis. Mech Dev *127*, 21-27.

Stark, K., Vainio, S., Vassileva, G., and McMahon, A.P. (1994). Epithelial transformation of metanephric mesenchyme in the developing kidney regulated by wnt-4. Nature *372*, 679-683.

Staruschenko, A. (2012). Regulation of transport in the connecting tubule and cortical collecting duct. Compr Physiol *2*, 1541-1584.

Torres, M., Gomez-Pardo, E., Dressler, G.R., and Gruss, P. (1995). Pax-2 controls multiple steps of urogenital development. Development *121*, 4057-4065.

Tsang, T.E., Shawlot, W., Kinder, S.J., Kobayashi, A., Kwan, K.M., Schughart, K., Kania, A., Jessell, T.M., Behringer, R.R., and Tam, P.P. (2000). Lim1 activity is required for intermediate mesoderm differentiation in the mouse embryo. Dev Biol *223*, 77-90.

Tufro, A., Teichman, J., Banu, N., and Villegas, G. (2007). Crosstalk between vegf-a/vegfr2 and gdnf/ret signaling pathways. Biochem Biophys Res Commun *358*, 410-416.

Uhlenhaut, N.H., and Treier, M. (2008). Transcriptional regulators in kidney disease: Gatekeepers of renal homeostasis. Trends Genet *24*, 361-371.

Wellik, D.M., Hawkes, P.J., and Capecchi, M.R. (2002). Hox11 paralogous genes are essential for metanephric kidney induction. Genes Dev *16*, 1423-1432.

Wetzel, B.K. (1962). Contributions to the cytology of dugesia tigrina (turbellaria) protonephridia. In: Breese, S.S. eds. Proc. 5th Int. Congr. Electron Microscopy (New York: Academic Press), Q10.

Wilhelmi, J. (1906). Untersuchungen über die excretionsorgane der sübwassertricladen. Zeitschrift für wissenschartliche Zoologie *80*, 544-575.

Wilson, P.D., and Goilav, B. (2007). Cystic disease of the kidney. Annu Rev Pathol *2*, 341-368.

Wilson, R.A., and Webster, L.A. (1974). Protonephridia. Biol Rev Camb Philos Soc *49*, 127-160.

Xu, P.X., Adams, J., Peters, H., Brown, M.C., Heaney, S., and Maas, R. (1999). Eya1-deficient mice lack ears and kidneys and show abnormal apoptosis of organ primordia. Nat Genet *23*, 113-117.

Yosypiv, I.V., Schroeder, M., and El-Dahr, S.S. (2006). Angiotensin ii type 1 receptor-egf receptor cross-talk regulates ureteric bud branching morphogenesis. J Am Soc Nephrol *17*, 1005-1014.

Zhuo, J.L., and Li, X.C. (2013). Proximal nephron. Compr Physiol *3*, 1079-1123.

CHAPTER 2

THE MAINTENANCE AND REGENERATION OF THE PLANARIAN EXCRETORY SYSTEM IS REGULATED BY EGFR SIGNALING

Jochen C. Rink[+], Hanh Thi-Kim Vu[+], and Alejandro Sánchez Alvarado

[+] Authors contributed equally to this work

Published as:

Rink, J.C., Vu, H.T., and Sanchez Alvarado, A. (2011). The maintenance and regeneration of the planarian excretory system are regulated by EGFR signaling. Development 138, 3769-3780.

Abstract

The maintenance of organs and their regeneration in case of injury are critical to the survival of all animals. High rates of tissue turnover and nearly unlimited regenerative capabilities make planarian flatworms an ideal system to investigate these important processes, yet little is known about the cell biology and anatomy of their organs. Here we focus on the planarian excretory system, consisting of internal protonephridial tubules. We find that these assemble into complex branching patterns with a stereotyped succession of cell types along their length. Organ regeneration likely originates from a precursor structure arising in the blastema, which undergoes extensive branching morphogenesis. In an RNAi-screen of signaling molecules, we identified an EGF-Receptor (*Smed-EGFR-5*) as a critical regulator of branching morphogenesis and maintenance. Overall, our characterization of the planarian protonephridial system establishes a new paradigm for regenerative organogenesis and provides a platform for exploring its functional and evolutionary homologies with vertebrate excretory systems.

Introduction

Planarian flatworms have astonishing regenerative abilities (Reddien and Sanchez, 2004). Arbitrary tissue fragments originating from almost any body plan position can regenerate into complete and perfectly proportioned animals. This ability is even more fascinating in the face of the anatomical complexity of planarians. As members of the Lophotrochozoa, they contain a set of organ systems typically associated with higher animals, including a central nervous system (bi-lobed brain and ventral nerve cords), a muscle layer surrounding the body wall, a highly branched gut cavity, an

excretory system (protonephridia), and complex arrays of sensory systems (*e.g.*, chemo-, rheo- and photoreceptors). In order to restore the anatomical complexity of newly formed tissues, the regeneration of a complete animal from a random tissue fragment necessitates organogenesis on a massive scale. Regenerative organogenesis shares a number of problems with embryonic organogenesis (*e.g.*, cell differentiation and morphogenesis), but raises further intriguing questions: Does organogenesis in regenerated tissues proceed *de novo* or by templated biogenesis from organ remnants? How is the regenerative response tuned to replace exactly the missing organ mass? How are functional and morphological integration between regenerated and preexisting organ fragments achieved? Similar questions pertain to the limited, but medically important regenerative abilities of vertebrate organs (*e.g.*, liver) (Pahlavan et al., 2006) and are generally not well understood.

In terms of organ regeneration, the planarian CNS has so far received the most attention (Agata and Umesono, 2008; Cebria, 2007). However, a multitude of cell types indicated by the rich and varied gene expression patterns and cell morphologies described to date make a mechanistic understanding of planarian brain regeneration a daunting endeavor (Cebria et al., 2002; Collins et al.; Nishimura et al., 2007; Nishimura et al.; Nishimura et al., 2008; Umesono et al., 1999). In search of a simpler structure to develop as a regenerative organogenesis model, we decided on the planarian excretory system. The latter consists of epithelial tubules that appear to end blindly in the mesenchyme. This feature defines the planarian excretory system as protonephridial in contrast to metanephridial systems like the vertebrate nephron, in which one terminus is located in an extracellular fluid compartment (Wilson and Webster, 1974). Protonephridia are

found throughout the animal kingdom. Their evolutionary relationship with metanephridial systems such as the mammalian kidney remains a subject of intense debate and considerable interest due in great part to the limited suitability of traditional invertebrate model systems for studying kidney pathologies (Hyman, 1951; Ruppert, 1994; Wilson and Webster, 1974).

However, the anatomy of planarian protonephridia is not well understood. According to Hyman (Hyman, 1951), who remains the most comprehensive author on invertebrate anatomy, the planarian excretory system consists of anastomosing "main tubules" along the lateral body margins and their ciliated side branches. The lumen of the tubules is thought to be continuous with the outside via dorsally located nephridiopores. However, substantial disagreements in the underlying light microscopic observations from the late 19th and early 20th century reveal considerable uncertainty regarding this view (Chichkoff, 1888; Wilhelmi, 1906). On the ultrastructural level, electron microscopy studies described protonephridia as having the following components: 1) cylindrical cells located at the tip of the ciliated side branches, with narrowly apposed strands of cytoplasm forming a fenestrated barrel around a central bundle of cilia, whose flickering movements gave rise to the term "flame cell" (Ishii, 1980a; McKanna, 1968a); 2) an initial ciliated tubule segment connected to the lumen of the flame cell barrel and purportedly composed of squamous epithelial cells; and 3) nonciliated "main tubules" composed of a cuboidal epithelium (Ishii, 1980b; McKanna, 1968b; Pedersen, 1961).

Functional studies on protonephridia in planarians or other invertebrates are extremely scarce, but it is generally assumed that the concerted beating of the flame cell cilia bundle creates a pressure gradient to force tissue fluid across the fenestrations into

the lumen of the tubule, where the lining epithelial cells modify the ultrafiltrate by absorption and secretion during its proximo-distal passage and eventual release to the outside (Wilson and Webster, 1974). Likewise, knowledge regarding the molecular or functional identity of protonephridial cell types remains largely elusive (Finken-Eigen and Kunz, 1997; Pedersen, 1961; Skelly and Shoemaker, 2001).

We report here a systematic analysis of protonephridial structure and function with modern molecular biology tools. Our visualization of protonephridial architecture in planarians and the concomitant identification of specific markers for flame cells, proximal and distal tubule cells reveal a complex, branched epithelial organ consisting of multiple cell types. We found that protonephridia regenerate in a stereotypic sequence of events and we identified EGF-signaling as a crucial regulator of protonephridial branching morphogenesis.

Results

Anatomy and Ultrastructure of the *Schmidtea mediterranea* Protonephridial System

Sections of the planarian protonephridial system are known to be ciliated, and it has been reported that antibodies against tubulin, a major structural component of cilia, may label flame cells (Cebria and Newmark, 2005). We therefore used α–Tubulin staining of whole-mounted animals to gauge the general organization of protonephridia in planarian. Even though α–Tubulin staining also labeled other anatomical features (Fig. 2.1A, C), protonephridia were by far the brightest structures, allowing unambiguous tracing of their course through the tissue. The club-shaped cilia bundles of flame cells

Figure 2.1. Distribution of protonephridia. **A**: Whole-mount α–Tubulin antibody staining. Magnified head and tail regions are shown to the lower left and right, respectively. Flame cells appear as brightly staining club-shaped structures. Other anatomical features labeled by α-Tub staining are: Ventral nerve cord (VNC); Pharynx (Prx); Eye cups (Ey); peripheral nerves (*e.g.*, arrows). Blue frame: Magnified inset shown in B. Images are maximum projections of confocal Z-sections. Scale bars: 200 μm. **B**: Depth-coded maximum projection. Superficial structures appear in red, structures deep in the tissue as blue. Dotted outlines: Single protonephridial units. f: Examples of flame cells. Proximal units in the tail are depicted. Scale bars: 20 μm. **C**: Top: Transverse cross sections of α–Tubulin stained whole-mount animals, at the level of the photo receptors (left), pharynx (center), and half-way between pharynx and tail tip (right). Flame cells appear as bright dots (*e.g.*, f: top center and bottom right). Scale bar: 200 μm. Bottom: Magnification of red-framed area above. Left: Nuclei (DAPI); Center: α–Tubulin; Right: Merge. e: Surface epithelium; bm: Basement membrane; m: Mesenchyme; dct: Nonprotonephridial ductules of mucus-secreting cells.

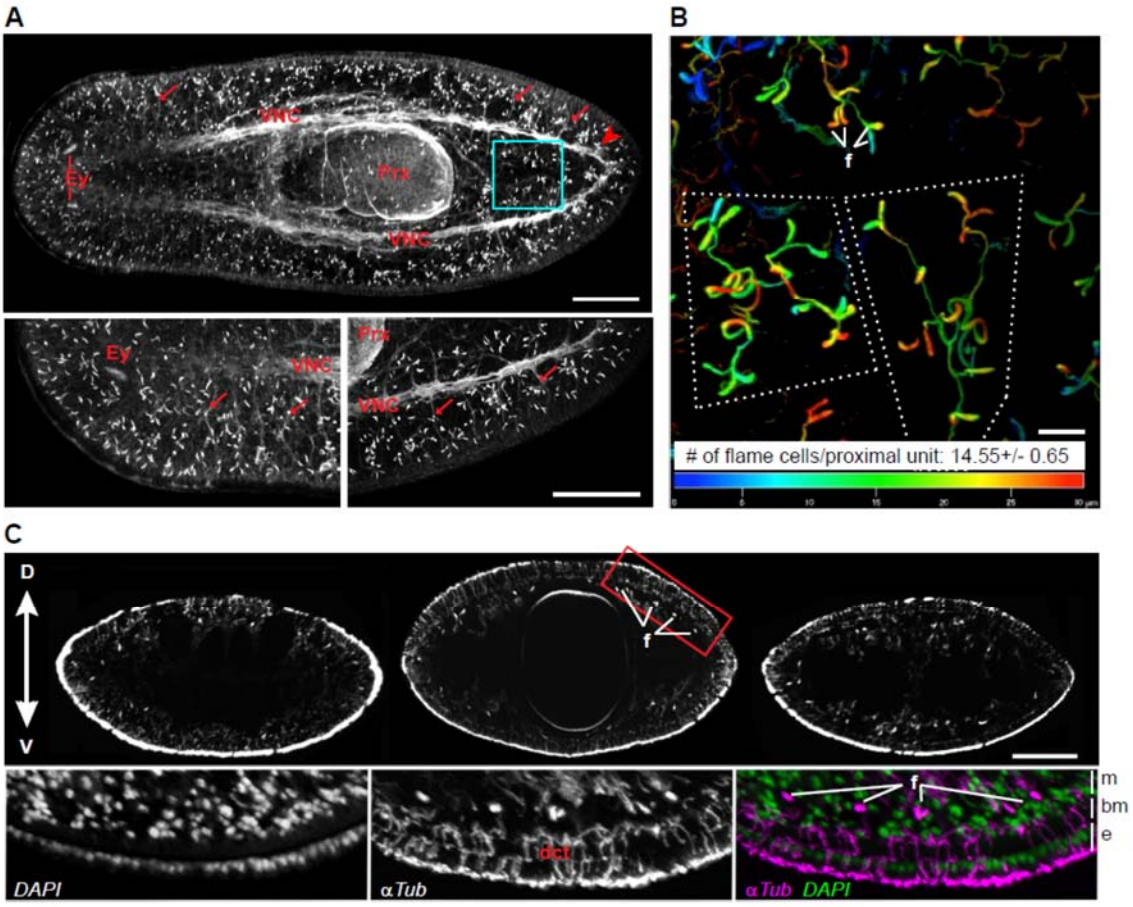
A
VNC
Ey
Pha
VNC
Ey
VNC
Pha
VNC
B
f
# of flame cells/proximal unit: 14.55+/- 0.65
C
D
V
f
DAPI
dcf
αTub
f
m
bm
e
αTub DAPI

were readily apparent (Fig. 2.1A). Flame cells were highly abundant throughout the entire animal and appeared to be specifically aligned along the head margins (Fig. 2.1A, bottom left). At higher magnification, flame cells could be seen to connect to an α–Tubulin positive network, likely corresponding to the ciliated tubule segments described in prior electron microscopy studies (McKanna, 1968b; Pedersen, 1961). Our whole-mount stains revealed a stereotypic organization of planarian protonephridia into tree-like units, whereby a common highly coiled "stem" splits into several thinner branches, each carrying one or two flame cells at its end. At least in the caudal regions of planarians, this arrangement results in a remarkably consistent number of 14 or 15 flame cells/unit (14.55 +/- 0.65), possibly indicating a stereotyped developmental sequence of protonephridia (Fig. 2.1B). Transverse sections showed protonephridial units to be entirely embedded in the mesenchyme and distributed without appreciable dorso-ventral bias. Flame cells were mostly located immediately below the muscular layer that surrounds the planarian mesenchyme (Fig. 2.1C). The tubule stems usually faded out deeper into the mesenchyme, suggesting a transition into a nonciliated tubule section undetectable by α-Tubulin stainings. Although some protonephridial units were found deep in the mesenchyme (near CNS elements, between the two posterior gut branches and within the pharynx), the ciliated sections of the planarian protonephridia system appeared to mostly form a loose network around the surface of the mesenchyme (Fig. 2.1A, C).

In parallel, we optimized high pressure freezing methods for planarians, a method that can yield better tissue preservation for electron microscopy than traditional chemical fixatives (Fig. 2.2A-H) (Dernburg et al., 1998; Salvenmoser et al., 2010). A notable

feature of high pressure frozen specimens were large volumes of extracellular space between cells in the mesenchyme (Fig. 2.2B). The suggested loose organization is consistent with the almost instantaneous dissociation of the planarian mesenchyme upon removal of the epithelium (not shown). Readily identifiable ciliation and other criteria previously established in chemically fixed material (Ishii, 1980a, b; McKanna, 1968a, b) provided a set of morphological features for the identification of protonephridial structures. Flame cells were defined by the "filtration weir" consisting of closely apposed strands of cytoplasm surrounding a central cilia bundle and by numerous microvilli between weir and cilia (Fig. 2.2C, D). The flame cells were often attached to a muscle fibre (not shown), and were always surrounded by a comparatively large volume of extracellular space (Fig. 2.2C), which in past studies using chemically fixed material appears to have occasionally been misinterpreted as "fixed parenchymal cells" (Ishii, 1980b; Pedersen, 1961). Cross sections through ciliated tubule sections were much more frequent than flame cell sections and tended to occur in clusters, consistent with the tortuous course of ciliated trunk and side branches (Fig. 1.1B). Interestingly, clusters of ciliated profiles were almost invariably accompanied by clusters of nonciliated tubular cross sections (Fig. 2.2B). Both types of lumens were formed by intercellular junctions between two cells, which in the case of nonciliated tubules often showed dramatic folding of their cytoplasm, appearing as mitochondria-rich "loops" in cross section (Fig. 2.2B, H). Due to their spatial co-occurrence with ciliated profiles, the nonciliated profiles likely correspond to a similarly sinusoidal continuation of the ciliated tubules. In both ciliated- and nonciliated tubule sections, we observed morphological subtypes of the bounding cells (Fig. 2.2E, F, G, H), consistent with functional differentiation of

Figure 2.2. Ultrastructure of protonephridial cell types in high-pressure frozen specimens. **A**: Cartoon showing approximate location of indicated section planes. Question marks indicate uncertainty with respect to the exact position. **B:** Overview image, showing ciliated tubule lumens (ctl) and nonciliated tubule lumens (nctl). Lumens are formed by intercellular tight junctions (tj) between two tubule cells with laterally positioned nuclei (n). The cytoplasm of distal tubule cells is thrown into extensive folds (f), rich in Mitochondria (m). Scale bar: 1 μm. **C**: Coronal cross section through a flame cell. The bundle of 9+2 cilia (c) is surrounded by a barrel of thick cytoplasmic processes (*e.g.*, tcp), which support the filtration diaphragm (fd). Filaments (fl) inside the barrel have been interpreted as structural support. bb: Basal body, es: Extracellular space. Red frame: High magnification of the filtration diaphragm (arrowhead). Scale bar: 1 μm. **D**: Longitudinal cross section through a flame cell, annotations as before. Scale bar: 1 μm. **E, F**: Cross sections through two types of ciliated proximal tubule lumens, bounded by squamous (D) or more cuboidal (E) cells. Scale bars D-E: 2 μm. **G, H**: Cross sections through two types of nonciliated distal tubule lumina, bounded by cuboidal (F) or extensively folded (G) cells. Scale bars F-G: 2 μm.

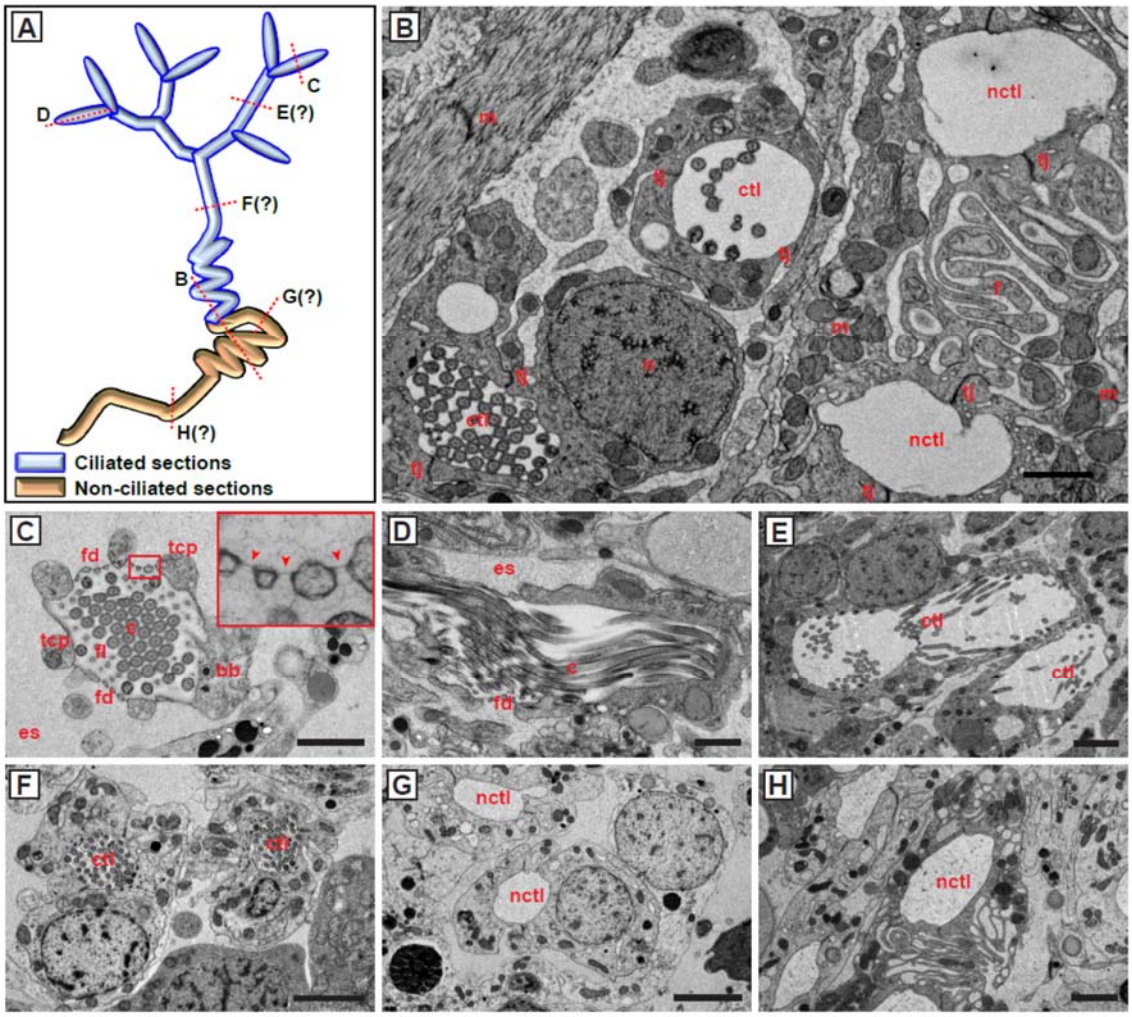
A
C
D
E(?)
F(?)
B
G(?)
H(?)
Ciliated sections
Non-ciliated sections
B
nctl
ctl
n
ctl
nctl
C
fd
tcp
tcp
fl
c
bb
fd
es
D
es
c
fd
E
ctl
ctl
F
ctl
ctl
G
nctl
nctl
H
nctl

constituent cell types inferred previously (ciliated “ductule” and ciliated “collecting duct” (McKanna, 1968b); nonciliated “trunk” and “distal tubule” (Ishii, 1980b), or “transitional region” or “osmoregulatory duct” (McKanna, 1968b)). Jointly, these experiments provide strong evidence to support the existence of multiple protonephridial cell types.

Protonephridia Are Complex Epithelial Organs

In order to identify molecular markers for the suspected diversity of protonephridial cell types, we screened whole-mount gene expression patterns for partial recapitulation of the α–Tubulin staining pattern (Fig. 2.3A). The gap junction gene *Smed-innexin-10* (short hand *inx10)* (Oviedo and Levin, 2007), and a carbonic anhydrase gene (H.14.9d = *Smed-CAVII-1;* short hand *CAVII-1*) (Sanchez Alvarado et al., 2002), were both expressed in branching patterns, whereby *CAVII-1* branches appeared less complex and tended to terminate farther away from the body margins. The ciliary dynein heavy chain *Smed-DNAH-β3* (short hand *DNAH-β3*) was expressed in punctate foci with a similarly uniform distribution as flame cells, yet with additional expression domains in the pharynx and along the body margins. All three genes indeed marked specific sections of protonephridia, as shown by colocalization with α–Tubulin immunostaining and double *in situ* experiments (Fig. 2.3B, C; supplemental movies 1, 2). Together, these markers permit the following molecular description of protonephridial anatomy (Fig. 3D): *DNAH–β3*-positive flame cells connect to *inx10*-expressing, ciliated tubules, which transition into *CAVII-1*-positive tubules. The tightly coiled *CAVII-1*-positive tubules are no longer ciliated, thus very likely corresponding to the nonciliated tubule profiles seen in EM (Fig. 2.2B, G, H) (Ishii, 1980b; McKanna, 1968b). *CAVII-1*-

Figure 2.3. Molecular anatomy of protonephridia. **A:** Whole-mount expression patterns of indicated marker genes by *in situ* hybridization (NBT/BCIP development). Anterior is to the top. Prx: Pharynx. Bottom: Magnification of red-framed area. Scale bars: 500 μm (top), 100 μm (bottom). **B:** Fluorescent overlay of indicated *in situ* patterns (green; right) with anti-α–Tubulin staining (pink and left). Images are maximum projections of confocal Z-sections. Scale bars: 20 μm. **C:** Fluorescent overlay of double *in situ* patterns (red and green) with anti-α–Tubulin staining (blue). Marker identity as indicated. Images are maximum projections of confocal Z-sections. Scale bars: 20 μm. **D:** Cartoon of protonephridial molecular anatomy. See text for details. **E:** Cross sections of double-labelled whole-mount animals (red: *inx10* and green: *CAVII-1*) and overlayed with anti-α–Tubulin staining (blue). Sections were taken at the level of the photoreceptors (top), pharynx (center), and half-way between pharynx and tail tip (bottom). Arrows: Examples of *inx10* positive transverse tubules. Scale bar: 200 μm.

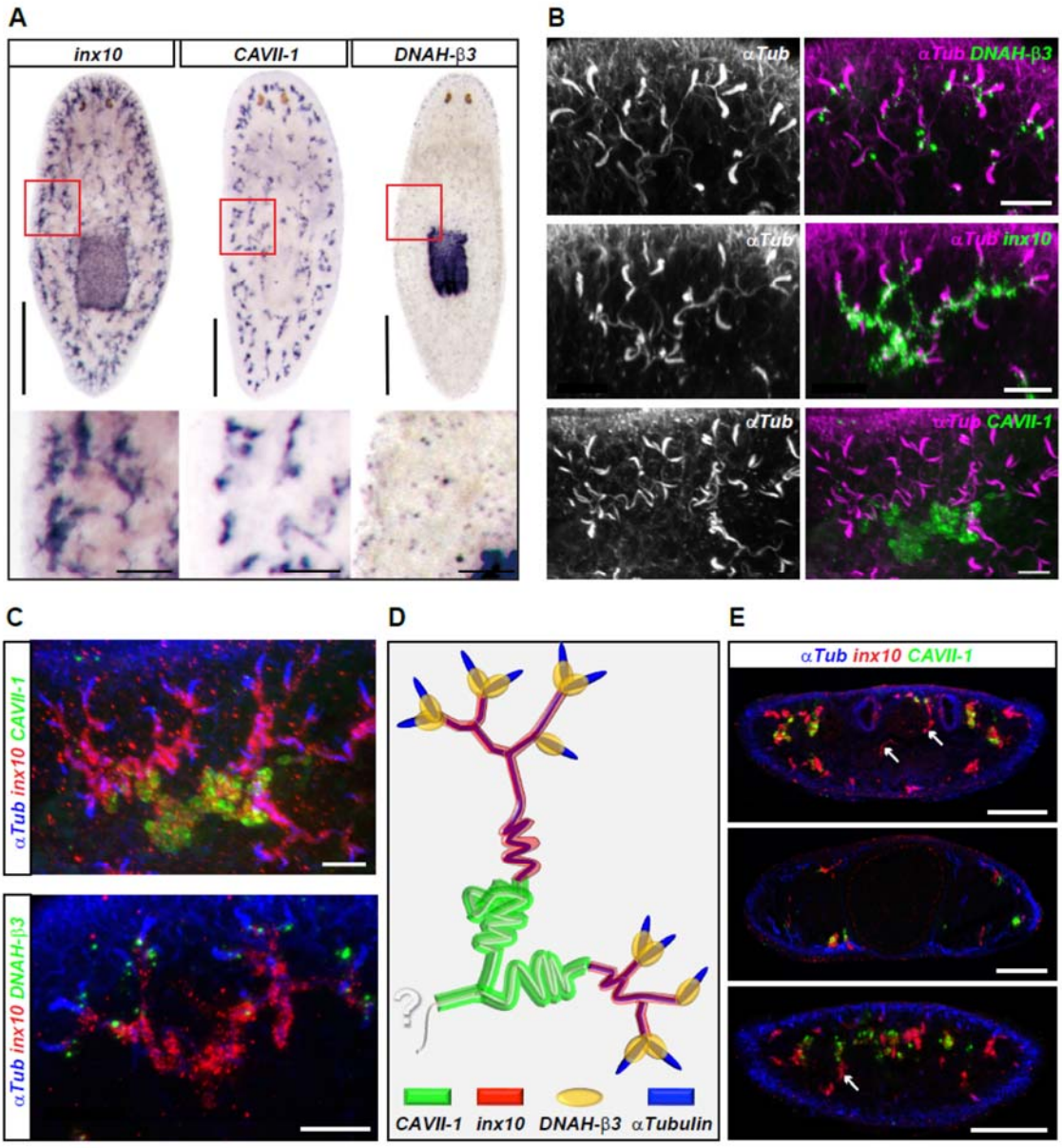
A
inx10
CAVII-1
DNAH-β3
B
αTub
αTub DNAH-β3
αTub
αTub inx10
αTub
αTub CAVII-1
C
αTub inx10 CAVII-1
αTub inx10 DNAH-β3
D
CAVII-1
inx10
DNAH-β3
αTubulin
E
αTub inx10 CAVII-1

positive segments often connected two neighboring proximal units, continuing the convergence trend of many proximal elements into fewer and fewer distal structures. Based on our molecular markers and Ishii's previous efforts to clarify the confusing nomenclature (Ishii, 1980b), we refer to the ciliated and *inx10*-expressing segments as "proximal tubules" and nonciliated *CAVII-1*-expressing segments as "distal tubules". Unlike the uniformly distributed proximal units, distal tubules showed a clear bias towards the dorsal side in transverse sections (Fig. 2.3E). The connection to ventral proximal units was maintained via long *inx10*-positive tubule segments transgressing the mesenchyme (Fig. 2.3E). However, distal tubules still appeared to terminate abruptly in the mesenchyme. Hence, markers for yet more distal segments remain to be discovered, which should also reveal whether protonephridia really drain via dorsal nephridiopores or possibly into the gut instead. Together, our ultrastructural and molecular marker analyses indicate that planarian protonephridia are a complex epithelial organ system, consisting of multiple cell types organized into an intricate branching pattern.

Protonephridia Regeneration

Having characterized markers for protonephridial cell types, we next explored how the cellular and morphological complexity of these organs is restored in the course of regeneration. Using multicolor *in situ* experiments at defined time points after amputation, we examined the temporal sequence and morphology of marker expression in head and tail blastemas (Fig. 2.4A, B). At day 1 post amputation, the flame cell marker (*DNAH-β3*) and the proximal marker *inx10* produced diffuse and grainy signals at the wound margin. The small volume of new tissue at this early time point did not allow

unambiguous differentiation between old and new tissues and the variability of signal observed between different animals could indicate background staining. However, 2 days after amputation, the proximal marker was prominently expressed in a rod-shaped structure embedded within the blastema, which was also associated with punctate flame cell marker expression. Even in high magnification confocal Z-stacks, we could not detect proximal marker-positive connections between this rod and protonephridia in the old tissue. Moreover, the morphology and temporal appearance of the structure was highly stereotyped, invariably occurring as a size-matched pair on either side of the midline in both head and tail blastema. Interestingly, the temporal snapshots of the regeneration time course experiments suggested that this structure may be the precursor of all protonephridia regeneration in the new tissue, which is why we refer to it as the proto-tubule. The distal marker *CAVII-1* was first expressed on the 3rd day after amputation, its initial expression domain invariably bisecting the proto-tubule. Beginning on day 3, the *inx10* positive proximal segments underwent extensive branching morphogenesis. Branching became first evident on day 3 (see also dispersal of *DNAH-β3* signal), and branch elongation towards the blastema margins was especially prominent on day 4. Even though branching appeared to be slightly delayed in tail blastemas as compared to head blastemas, protonephridia morphology in both cases became practically indistinguishable from uncut animals by day 6 after amputation, suggesting that organ regeneration as assessable with the present set of markers was complete by this time point. Overall, the highly stereotyped regeneration of protonephridia from a precursor structure argues in favor of *de novo* organogenesis in regenerating tissues.

Figure 2.4. Protonephridia regeneration. **A**: Magnified view of left-anterior and left-posterior blastema of regenerating trunk fragments at indicated time points after amputation. Dotted lines demarcate boundary between old and new tissue, inferred from autofluorescence in the infra-red channel (not shown). In addition to anti-α–Tubulin antibody staining (blue), the top two rows were hybridized with the proximal marker probe (*inx10*; red) and the distal marker probe (*CAVII-1*; green). The bottom two rows were hybridized with the flame cell probe (*DNAH-β3*, red). Images are maximum projections of confocal Z-sections. Scale bars: 100 μm. **B**: Cartoon representation of regeneration sequence.

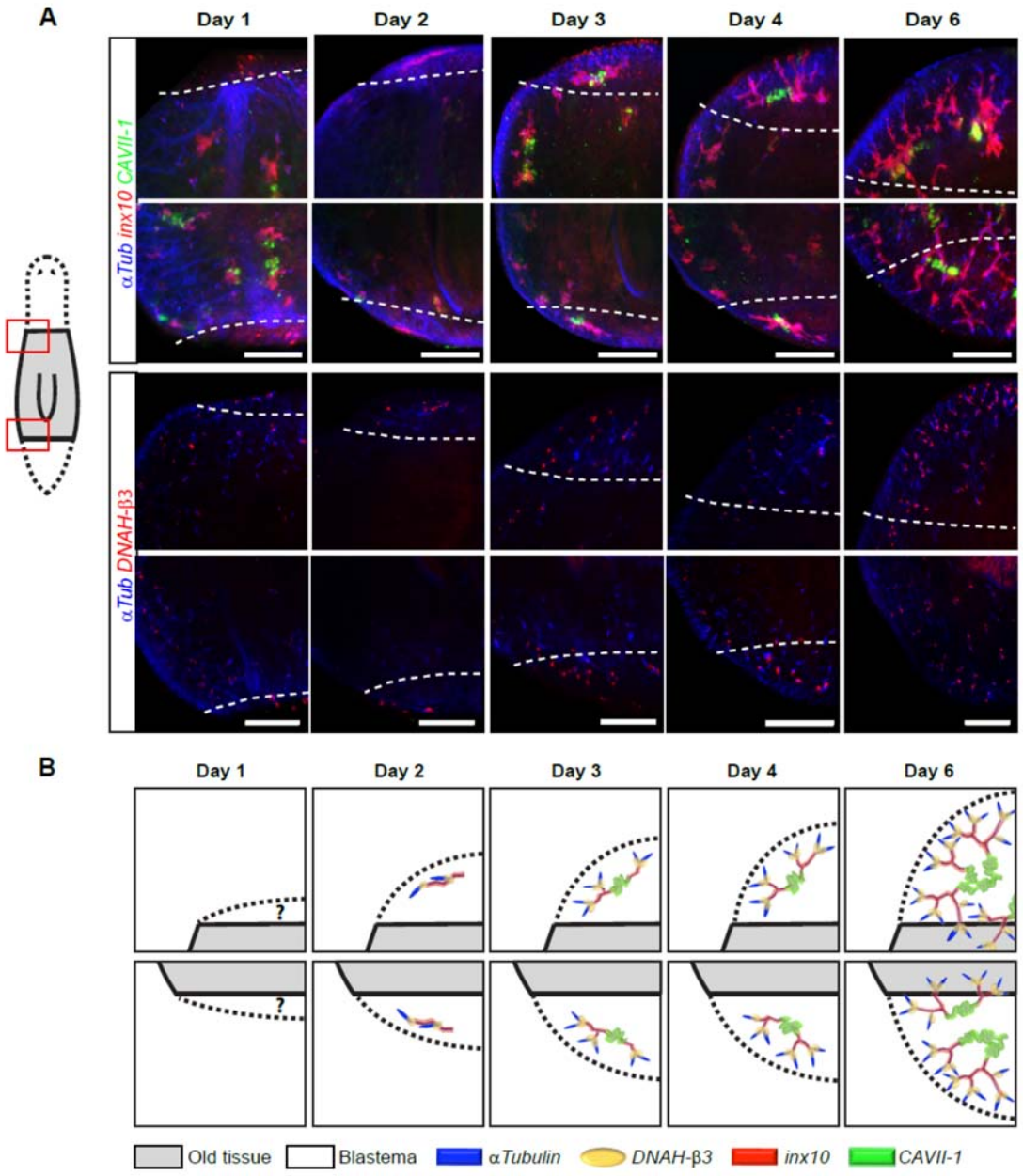
A
Day 1
Day 2
Day 3
Day 4
Day 6
αTub inx10 CAVII-1
αTub DNAH-β3
B
Day 1
Day 2
Day 3
Day 4
Day 6
?
?
Old tissue
Blastema
αTubulin
DNAH-β3
inx10
CAVII-1

An Epidermal Growth Factor Receptor Is Required for Protonephridial Function

In order to identify components of the signaling network orchestrating protonephridia differentiation and morphogenesis, we performed an RNAi-screen of a candidate library comprising ~400 planarian homologues of conserved signaling pathway components (Rink J.C. and Gurley K.A.; unpublished). Previous studies have reported massive bloating of animals fed RNAi against cilia components (Reddien et al., 2005; Rink et al., 2009), or the proximal marker gene *inx10* (Oviedo and Levin, 2007). In osmotic shock experiments and accompanying histological sections, we observed that such bloating is in fact caused by severe edema formation upon functional impairment of the ciliated and *inx10*-expressing proximal tubule (Fig. 2.5). Edema formation also provided a readily apparent screening phenotype for potential protonephridia genes. Our screen identified the Epidermal Growth Factor Receptor (EGFR) homologue *Smed-EGFR-5* (short hand *EGFR-5*) that, when knocked down, led to edema formation in intact and regenerating animals similar to *inx10(RNAi)* (Fig. 2.6A, Fig. 2.7). Even though planarians have 5 EGFR-family members (Rink J.C., unpublished), which represents an unusual expansion of this gene family amongst invertebrates (Stein and Staros, 2006), only RNAi of *Smed-EGFR-5* led to edema formation. The first indication of a phenotype in uncut *EGFR-5(RNAi)* animals was an apparent depigmentation in the anterior half of the animals ("Pale"; beginning at day 5 after the last RNAi-feed; Fig. 2.6B). Within 3 days, "pale" animals progressed to tail edema formation as in *inx10(RNAi)* animals. Starting at day 14 after the last RNAi feeding, lesions became apparent which progressed to eventual lysis and death of all *EGFR-5(RNAi)* animals. Consistent with a direct role

Figure 2.5. Proximal tubule defects cause edema formation. A: Knockdown of *inx10* or the cilia component *IFT172* cause severe bloating in uncut RNAi-fed animals 14 days after the last feed. Scale bar: 500 μm. **B:** 10-fold increase of environmental osmolarity for 24 hours phenotypically rescues *inx10(RNAi)* induced bloating (bottom right), without noticeable effects on control animals (top right). Randomly selected animals are shown. Scale bar: 1000 μm. **C:** Transverse cross sections through the tail region stained with the protein dye Toluidine Blue. The drastically lowered cell density in bloated *inx10(RNAi)* animals in regular environment (center) nearly returned to control levels (left) after 24 hours exposure to high external osmolarity (right). VNC: Ventral nerve chords. g: Gut. Scale bar: 50 μm.

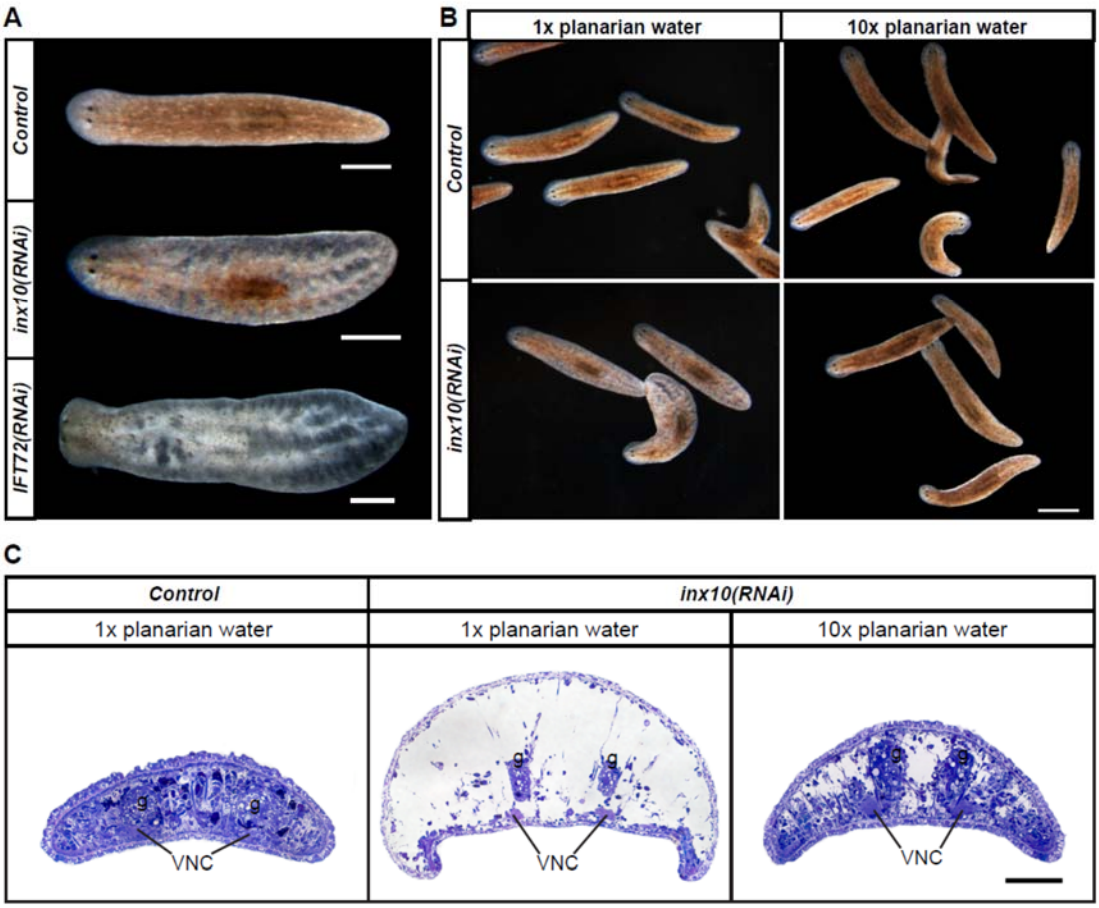
A
Control
inx10(RNAi)
IFT72(RNAi)
B
1x planarian water
10x planarian water
Control
inx10(RNAi)
C
Control
inx10(RNAi)
1x planarian water
1x planarian water
10x planarian water
g
g
VNC
g
g
VNC
g
g
VNC

Figure 2.6. *Smed-EGFR-5* is required for protonephridia function and expressed in flame cells. **A:** Gross morphological consequences of *EGFR-5* knockdown in uncut animals (left, 14 days after last feed) and regenerated fragments (right, 14 days after amputation). Scale bars: 500 μm (right), 300 μm (right). **B**: Temporal succession of indicated phenotypes in a cohort of *EGFR-5(RNAi)*-fed animals. N = 42. **C**: Whole-mount expression pattern of *EGFR-5* by *in situ* hybridization (NBT/BCIP development). Bottom: Magnification of red-framed areas. Scale bars: 500 μm. **D:** Fluorescent overlay of *EGFR-5 in situ* pattern (green) with indicated proximal markers. Images are maximum projections of confocal Z-sections. Scale bars: 50 μm. **E:** High magnification views of EGFR-5 expression together with indicated markers in early head and tail blastemas. Images are maximum projections of confocal Z-sections. Scale bars: 20 μm.

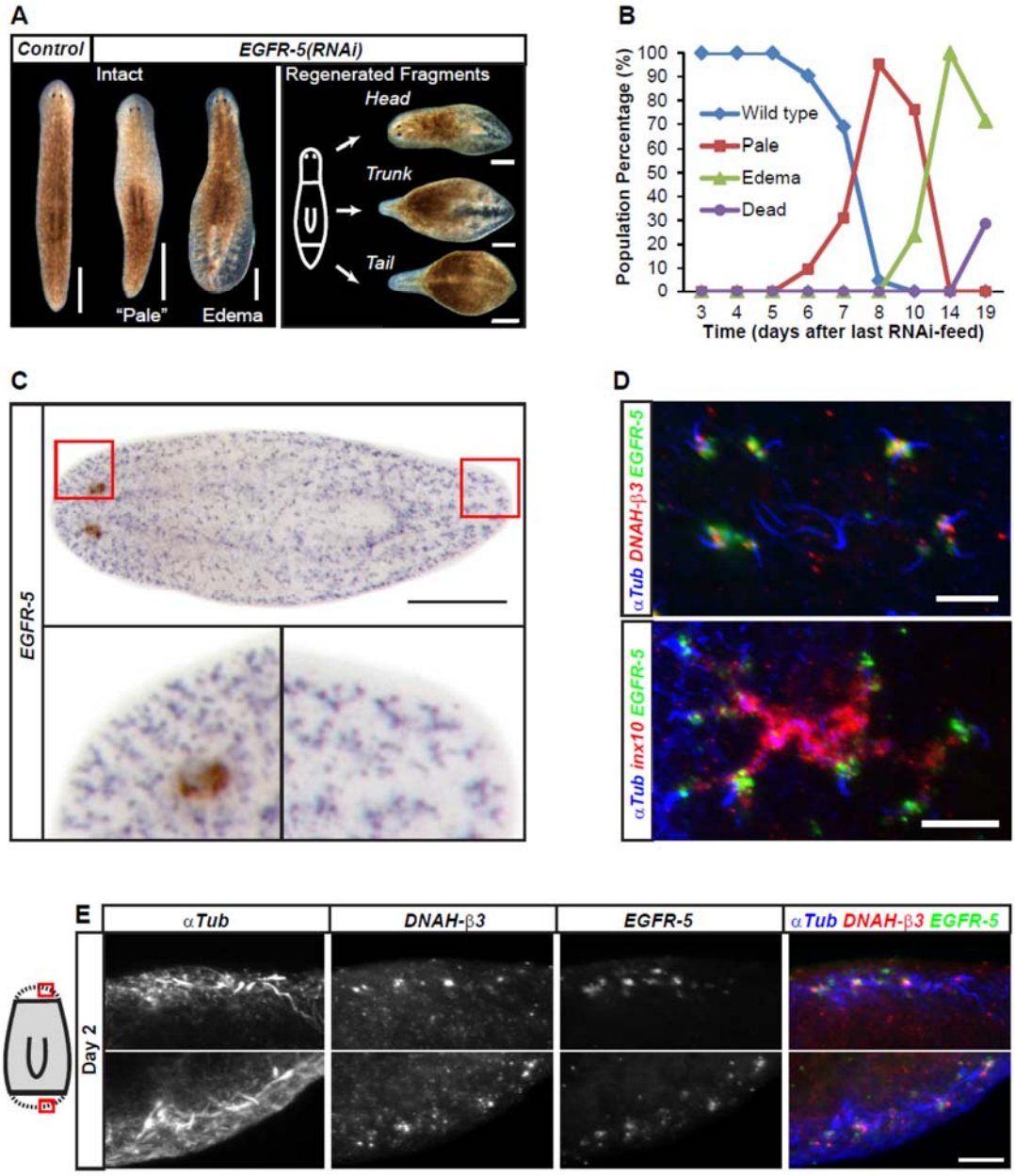
A
Control
EGFR-5(RNAi)
Intact
Regenerated Fragments
Head
Trunk
Tail
"Pale"
Edema
B
Population Percentage (%)
Wild type
Pale
Edema
Dead
Time (days after last RNAi-feed)
C
EGFR-5
D
αTub DNAH-β3 EGFR-5
αTub inx10 EGFR-5
E
αTub
DNAH-β3
EGFR-5
αTub DNAH-β3 EGFR-5
Day 2

Figure 2.7. EGFR-5 structure and sequence analysis. A: Domain structure (SMART: http://smart.embl-heidelberg.de/) of SMED-EGFR-5 and its two closest human- or fly homologues, HS-ERBB4 and DM-EGFR, respectively. Note that the N-terminus of the SMED-EGFR-5 sequence is truncated. Fu: Furin-like repeats, TyrKc: Tyrosine Kinase domain. Dark blue bar: Transmembrane domain, which is obscured in HS-ERBB4 due to overlap with a Fu- prediction. Pink rectangles: Disordered regions. Scale bar: Amino acids. **B:** Blast e-values, obtained by blasting the SMED-EGFR-5 sequence against human (H.s.) or *Drosophila melanogaster* (D.m) nonredundant protein sequences. The top hits in both cases were EGFR-homologues. Despite the high e-value, SMED-EGFR-5 is likely not an orthologue of vertebrate ERBB4. Preliminary sequence analysis (JCR, unpublished) suggests that the 5 planarian EGFR-homologues arose from an independent expansion of this gene family. **C:** Amino acid sequence alignment (Clustal-W) between Hs-ERBB4, Dm-EGFR, and SMED-EGFR-5, the N-termini of Hs-ERBB4 and Dm-EGFR were cropped to the length of SMED-EGFR-5. Identical, conserved or similar residues are indicated by *****, **:**, or **.**, respectively. The tyrosine kinase domain is highlighted in orange, the individual transmembrane domain predictions (SMART) in gray. The regions corresponding to the 5 Furin-like repeats in the SMED-EGFR-5 sequence are underlined in blue.

A

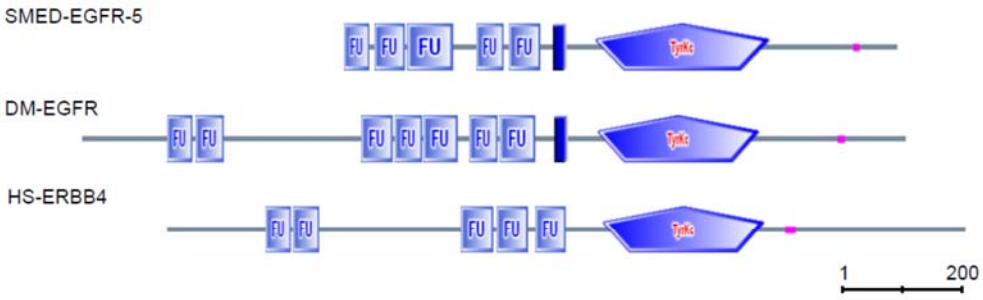

B

	H.s. ERBB4	H.s. EGFR	H.s. ERBB2	H.s. ERBB3	D.m. EGFR
SMED-EGFR-5	$1e^{-100}$	$7e^{-88}$	$1e^{-85}$	$2e^{-81}$	$1e^{-115}$

Figure 2.7. Continued

in protonephridial function, EGFR-5 was expressed seemingly exclusively in Y-shaped branches reminiscent of proximal protonephridia segments (Fig. 2.6C). Multicolor *in situ* hybridizations confirmed co-expression with the proximal marker *inx10* and revealed particularly high expression levels in *DNAH-β3* positive flame cells (Fig. 2.6D). Consistently, *EGFR-5* expression became detectable along with the flame cell marker already at 48-hour of regeneration at the proto-tubule stage (Fig. 2.6E). Taken together, these data identify *EGFR-5* not only as a second marker for flame cells and the adjacent terminal proximal branches, but also as a molecule with an important role in maintaining the functional integrity of the proximal segment of protonephridia.

EGFR-5 Is Required for Flame Cell Maintenance and Branching Morphology

In order to understand how *EGFR-5* might influence protonephridia function, we examined protonephridia regeneration in *EGFR-5(RNAi)* animals. A first survey of regenerated heads and tails 14 days after amputation demonstrated that all three cell-type markers were present, indicating that the respective cell types had differentiated (Fig. 2.8A). However, the expression patterns, especially those of the proximal markers, were severely disturbed. Multicolor confocal imaging experiments (Fig. 2.9A) demonstrated abnormal thickening of proximal branches and misdirected branch extension towards the posterior in head fragments. In tail fragments, however, the few remaining proximal segments were coiled into tight balls (Fig. 2.9A). Regeneration time course experiments provided insights into the ontogenesis of these defects (Fig. 2.8B, Fig. 2.9B; refer to Fig. 2.4A for control). The proto-tubule appeared to form normally in regenerating

Figure 2.8. *EGFR-5(RNAi)* regeneration phenotypes. **A**: Indicated protonephridial marker gene expression in regenerated *control* and *EGFR-5(RNAi)* animals, 14 days after amputation. Each pair was developed under identical conditions. Only regenerated heads and tails are shown. Scale bars: 100 μm. **B**: Magnified view of left-anterior and left-posterior blastema of regenerating trunk fragments of *EGFR-5(RNAi)* animals at indicated time points after amputation. Refer to Fig. 2.4 as control. Dotted lines demarcate boundary between old and new tissue, as inferred from autofluorescence in the infra-red channel (not shown). α–Tubulin antibody staining (blue) was combined with the flame cell probe (*DNAH-β3*, red). Images are maximum projections of confocal Z-sections. Scale bars: 100 μm. **C:** Representative examples of regenerating *EGFR-5(RNAi)* animals, hybridized with the *EGFR-5* antisense probe, at the indicated day of regeneration. *EGFR-5* expression was below the detection threshold on day 1, but clearly detectable at day 6. The hazy staining at intermediate time points is likely background. The fragments were all treated and developed in an identical manner, except for day 14 animals, which were from a separate experiment. Scale bar: 100 μm.

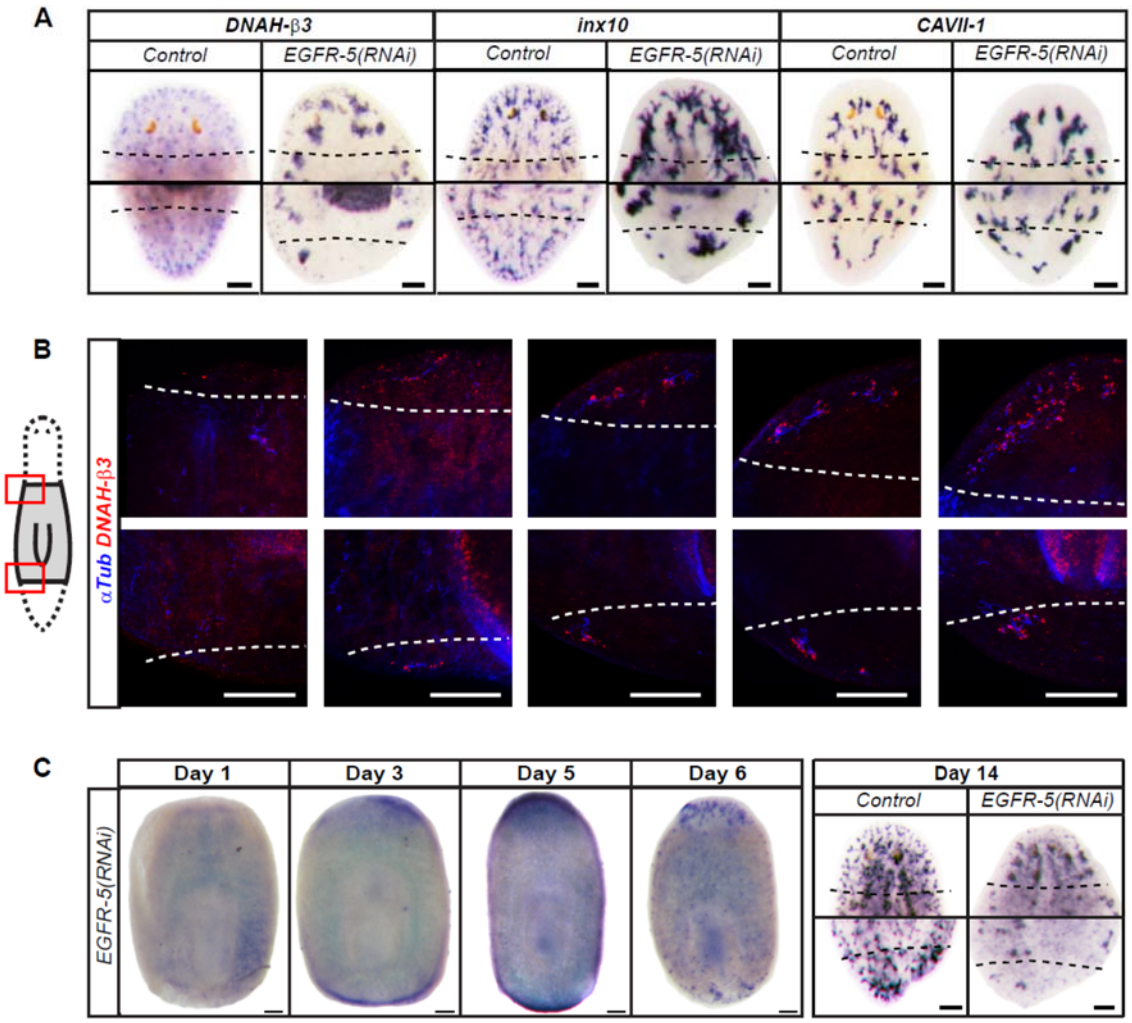
A
DNAH-β3
inx10
CAVII-1
Control
EGFR-5(RNAi)
Control
EGFR-5(RNAi)
Control
EGFR-5(RNAi)
B
αTub DNAH-β3
C
EGFR-5(RNAi)
Day 1
Day 3
Day 5
Day 6
Day 14
Control
EGFR-5(RNAi)

Figure 2.9. *EGFR-5(RNAi)* phenotype ontogeny in regeneration. **A**: Late stage morphological defects of regenerated protonephridia in *EGFR-5(RNAi)* animals (right half), compared to control (left half) at 14 days post amputation. Head (top row) and tail (bottom) of representative animals are shown, magnifications show the boxed region in the respective overview images. Color coding of markers as indicated, monochrome magnifications: α–Tubulin staining. Images are maximum projections of confocal Z-sections. Scale bar: 100 μm. **B**: Magnified view of left-anterior and left-posterior blastema of regenerating trunk fragments of *EGFR-5(RNAi)* animals at indicated time points after amputation. Refer to Fig. 4 as control. Dotted lines demarcate boundary between old and new tissue, as inferred from autofluorescence in the infra-red channel (not shown). α–Tubulin antibody staining (blue) was combined with the proximal marker probe (*inx10*; red) and the distal marker probe (*CAVII-1*; green). Images are maximum projections of confocal Z-sections. Scale bars: 100 μm. **C:** Left: Flame cell quantification in 14-day *EGFR-5(RNAi)* regenerates having received either the standard RNAi-dosage used throughout this manuscript ("Feeding") or an additional injection of *EGFR-5* dsRNA on the 3rd day of regeneration ("Feeding + Injection"). 3 proximal units in 6 animals were scored for each time point. Error bars represent the standard error of the mean. Right: Example illustrating the flame cell counting procedure using the indicated markers. For greater sensitivity, the flame cell marker *DNAH-β3* was developed with the nonfluorescent substrate NBT/BCIP. Flame cells (labeled) were defined as the spatial coincidence of an NBT/BCIP focus with a terminal tubule segment in image Z-stacks. The images shown are maximum projections of a Z-stack, the NBT/BCIP brightfield image was brightness-inverted and pseudo-colored green. Scale bar: 100 μm.

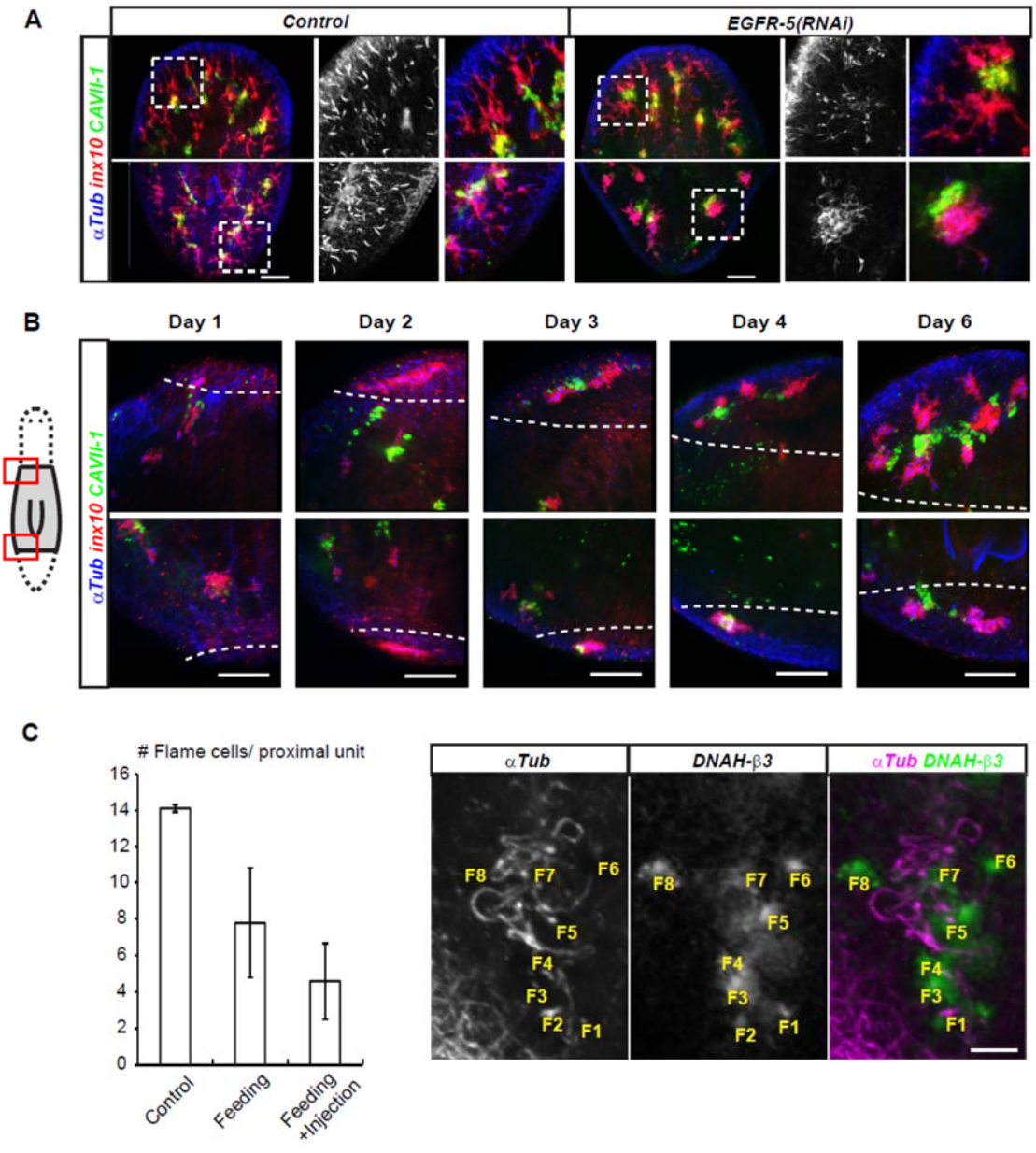
A
Control
EGFR-5(RNAi)
αTub inx10 CAVll-1
B
Day 1
Day 2
Day 3
Day 4
Day 6
αTub inx10 CAVll-1
C
Flame cells/ proximal unit
16
14
12
10
8
6
4
2
0
Control
Feeding
Feeding +Injection
αTub
DNAH-β3
αTub DNAH-β3
F8
F7
F6
F5
F4
F3
F2
F1

EGFR-5(RNAi) animals, but severe branching and branch extension defects became apparent from day 3 onwards. The sprouting and peripherally directed extension of proximal branches from the proto-tubule was severely inhibited, such that by day 6, when control animals had regenerated the complete proximal arborizations, *EGFR-5(RNAi)* animals displayed only short, partly posteriorly misoriented *inx10*-positive bundles in the head, but hardly any signs of branch extension in tails. A further abnormality of protonephridia regenerated under *EGFR-5(RNAi)* were less prominent flame cell cilia bundles in the α-Tubulin channel (Fig. 2.9A). Also the flame cell marker expression pattern was affected (Fig. 2.8A, B), suggesting possible defects in flame cell specification or maintenance. Indeed, quantification of flame cells numbers in *EGFR-5(RNAi)* animals 14 days after amputation (Fig. 2.9C) revealed a decrease to an average of 8 flame cells/proximal unit. An additional injection of *EGFR-5* dsRNA on the 3rd day of regeneration, administered in order to boost the lessening knockdown efficiency (Fig. 2.8C), resulted in a further decrease to approximately 5 flame cells/proximal unit. Thus, regeneration of protonephridia under *EGFR-5(RNAi)* caused both morphological defects of proximal arborizations and a reduced number of flame cells/proximal unit.

The same spectrum of phenotypes was also observed in nonregenerating animals. Expression of the flame cell marker was severely reduced 14 days after the last RNAi-feed (Fig. 2.10A). A quantification of flame cell numbers/proximal unit revealed a rapid decline in response to *EGFR-5(RNAi),* reducing their numbers to 2/unit around day 14 (Fig. 2.10B). Such loss of flame cells likely explains edema formation and eventual lysis in *EGFR-5(RNAi)* animals. In addition, proximal arborizations were also severely affected under *EGFR-5(RNAi)* (Fig. 2.10C). However, in contrast to the disorganized

Figure 2.10. *EGFR-5(RNAi)* phenotype ontogeny in intact animals. **A**: Indicated protonephridial marker gene expression in *control*- and *EGFR-5(RNAi)* animals, 14 days after last RNAi-feed. Each pair was developed under identical conditions. Bottom: Magnification of the red framed area above. Scale bars: 500 μm (top), 100 μm (bottom). **B**: Time course quantification of average flame cell numbers per proximal unit. Diamonds: *EGFR-5(RNAi)* animals, triangles: controls. Flame cells were counted in confocal Z-stacks of α–Tubulin/DNAH-β3 double-labeled whole-mount animals. 3 proximal units in 5 animals were scored for each time point. Error bars represent the standard error of the mean. **C:** Morphological defects of protonephridia in *EGFR-5(RNAi)* animals (right half), compared to control (left half) at 14 days post last RNAi feed. Head (top row) and tail (bottom) of representative animals are shown, magnifications show the boxed region in the respective overview image. Color coding of markers as indicated, monochrome magnifications: α–Tubulin staining. Images are maximum projections of confocal Z-sections. Scale bar: 100 μm.

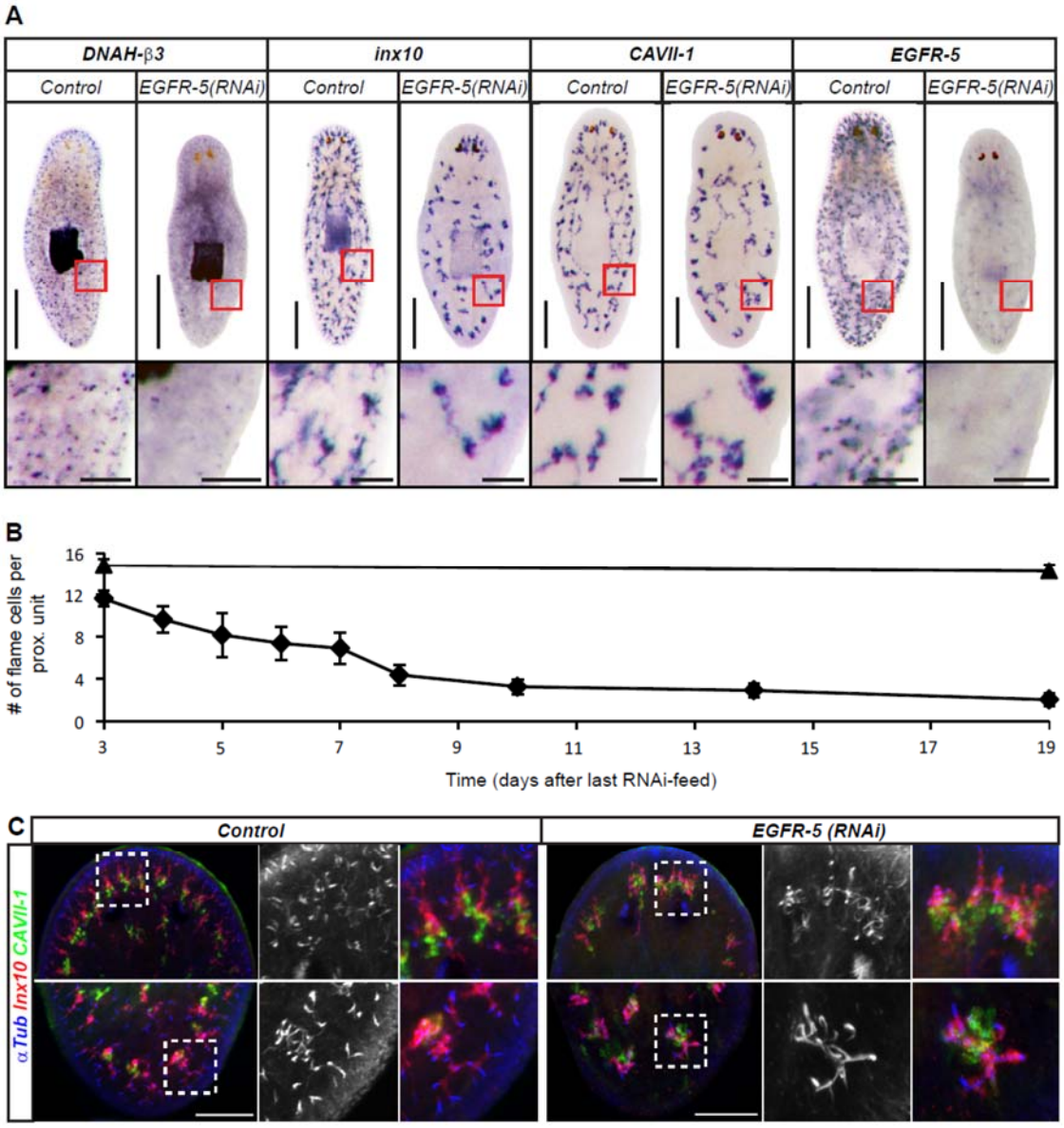
A
DNAH-β3
inx10
CAVII-1
EGFR-5
Control
EGFR-5(RNAi)
Control
EGFR-5(RNAi)
Control
EGFR-5(RNAi)
Control
EGFR-5(RNAi)
B
# of flame cells per prox. unit
16
12
8
4
0
3
5
7
9
11
13
15
17
19
Time (days after last RNAi-feed)
C
Control
EGFR-5 (RNAi)
αTub Inx10 CAVII-1

and misdirected branching patterns observed in regenerating animals (Fig. 2.8A), proximal arborizations were severely shortened to a few, short coils, especially in caudal regions.

Interestingly, the gradual loss of flame cells (Fig. 2.10B) was paralleled by a collapse of proximal arborizations (Fig. 2.11). Thus, our data indicate that *EGFR-5* is required both for flame cell maintenance and for guiding branch extension of protonephridia. The close association between the two phenotypes further suggests that they may be mechanistically linked.

Discussion

Our results establish the planarian protonephridia as a *bona fide* epithelial organ system. A variety of cell types assemble into complex tubular arbors with stereotypic proximo-distal organization, in which abundant proximal elements converge into fewer and fewer distal structures. Such complexity at the architectural and morphological level place planarian protonephridia *en par* with other branched organ systems such as trachea in insects and lungs, mammary glands, blood vessels, and the kidney in vertebrates (Beyenbach et al., 2010; Costantini and Kopan, 2010; Lu and Werb, 2008). All of the above examples rely critically on branching morphogenesis to establish the specific morphology necessary for proper organ function. It is, therefore, not too surprising that our screen of signaling components required for protonephridia-mediated tissue fluid homeostasis identified a gene with functions in branching morphogenesis.

The first phenotype resulting from *Smed-EGFR-5(RNAi)* was dramatic effect on the branching pattern of protonephridia. In nonregenerating RNAi-fed animals, the

Figure 2.11. Gradual collapse of proximal units in nonregenerating *EGFR-5(RNAi)* animals. Representative examples of protonephridial units in the tail region from the data set used to quantify the progressive flame cell loss depicted in Fig. 7C. For each of the indicated day, one control unit and three separate examples of proximal units in *EGFR-5(RNAi)* animals are shown. The images are confocal maximum projections of α-Tubulin staining. Scale bar: 20 μm.

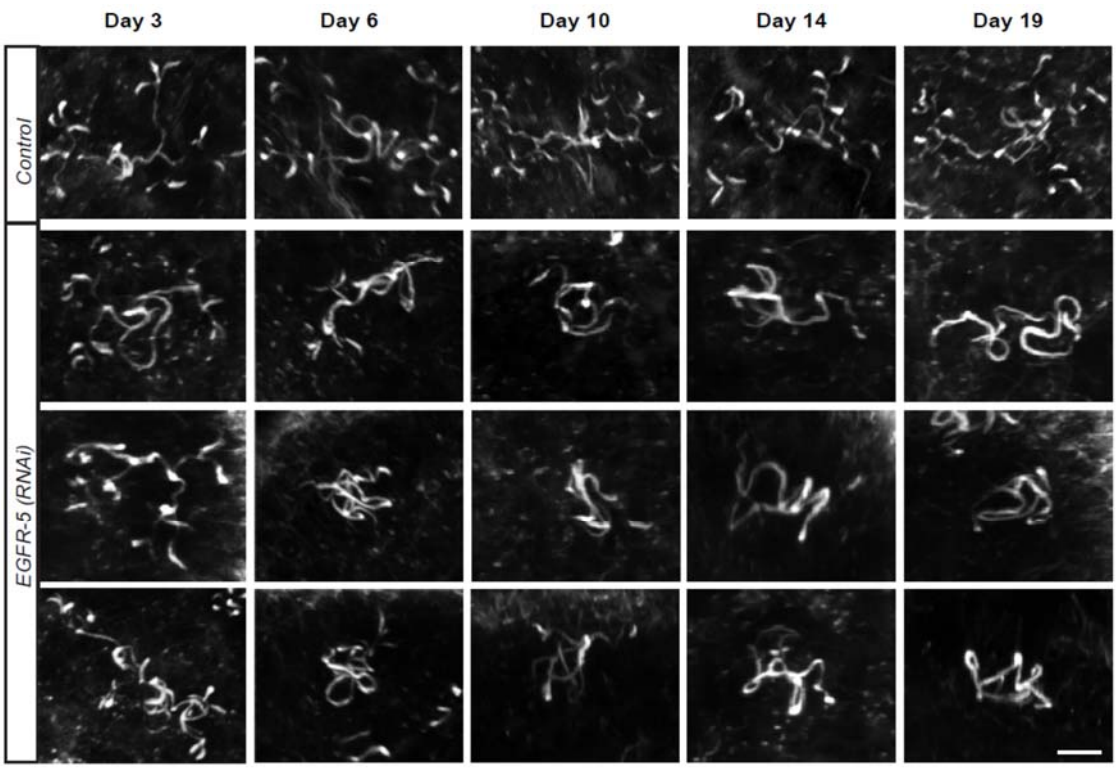
Day 3
Day 6
Day 10
Day 14
Day 19
Control
EGFR-5 (RNAi)

fanned-out organization of proximal branches collapsed until only short scrawl-like structures remained (Fig. 2.10C). In regenerating RNAi animals, by contrast, we observed misorientation of the branches in the head and dramatic coiling of proximal tubules into tight balls in the tail region (Fig. 2.8A). Time course experiments provided insights into the ontogeny of these seemingly disparate phenotypes. In intact animals, the collapse of proximal arborizations correlated with the loss of flame cells (see below). In regenerating animals, the misdirected branch extension phenotypes appeared to develop in two phases. Until regeneration day 6, *EGFR-5(RNAi)* animals displayed markedly reduced branching and branch extension in comparison to control animals (Fig. 2.8B, 4A). In order to generate the striking coils in tails or disorganized branch patterns in heads of 14-day regenerates (Fig. 2.8A), a burst of misguided proximal branch extension must consequently occur between day 6 and 14. The reason for the distinct outcomes in heads versus tails involves differential RNAi-sensitivities: Both misguided branch extension and coil formation were part of a phenotypic series, but for unknown reasons, tail tissues responded more strongly to a given dose of RNAi than head tissues (Fig. 2.12A-C). This effect may also contribute to edema formation preferentially in tails of *EGFR-5(RNAi)* animals (Fig. 2.6A). Moreover, we noticed that the switch in branch extension capabilities around regeneration day 6 coincided with lessening knockdown efficiency of *EGFR-5* (Fig. 2.9C). The misdirected branch extension between day 6 and 14 therefore likely involved inappropriate levels or timing of *EGFR-5* expression, whereas the early inhibition of branch extension correlated with low EGFR-5 receptor levels. Similarly, the collapse and shortening of proximal branches observed in nonregenerating *EGFR-5(RNAi)* animals occurred under low and sustained knockdown

Figure 2.12. Differential RNAi effects in regenerating fragments. A: Representative examples out of a batch of *EGFR-5(RNAi)* animals 14 days after amputation, showing the 4 indicated classes of branching phenotypes. *inx10 in situ* hybridization was used to visualize proximal branching. "Defective branching" was defined by abnormal thickening of branches or projections away from the head margin, blastemas displaying at least one extended branch were scored as "minimal branching". Scale bar: 100 μm. **B, C:** Color-coded population frequency of the above phenotypic categories in 14-day regenerates exposed to 4 different RNAi-dosage regimes. In order to dilute the RNAi-dosage, *EGFR-5* dsRNA expressing bacteria were diluted with bacteria expressing an irrelevant control dsRNA, such that the absolute amount of dsRNA was constant in all cases. "4x" corresponded to the standard RNAi-dosage used throughout this manuscript, "1x" is ¼ thereof. The number of animals in the cohort is listed below each bar. Head and tail blastemas were scored separately and the results are graphed in B and C, respectively. **D, E:** Morphological phenotype assessment of the two RNAi dosage regimes used in Fig. 6C. The population frequencies of the phenotypic categories as defined and color-coded above were scored in the batch of 14-day regenerates used for the flame cell count. The number of animals in each cohort is listed below the bar. Head and tail blastemas were scored separately and the results are graphed in D and E, respectively.

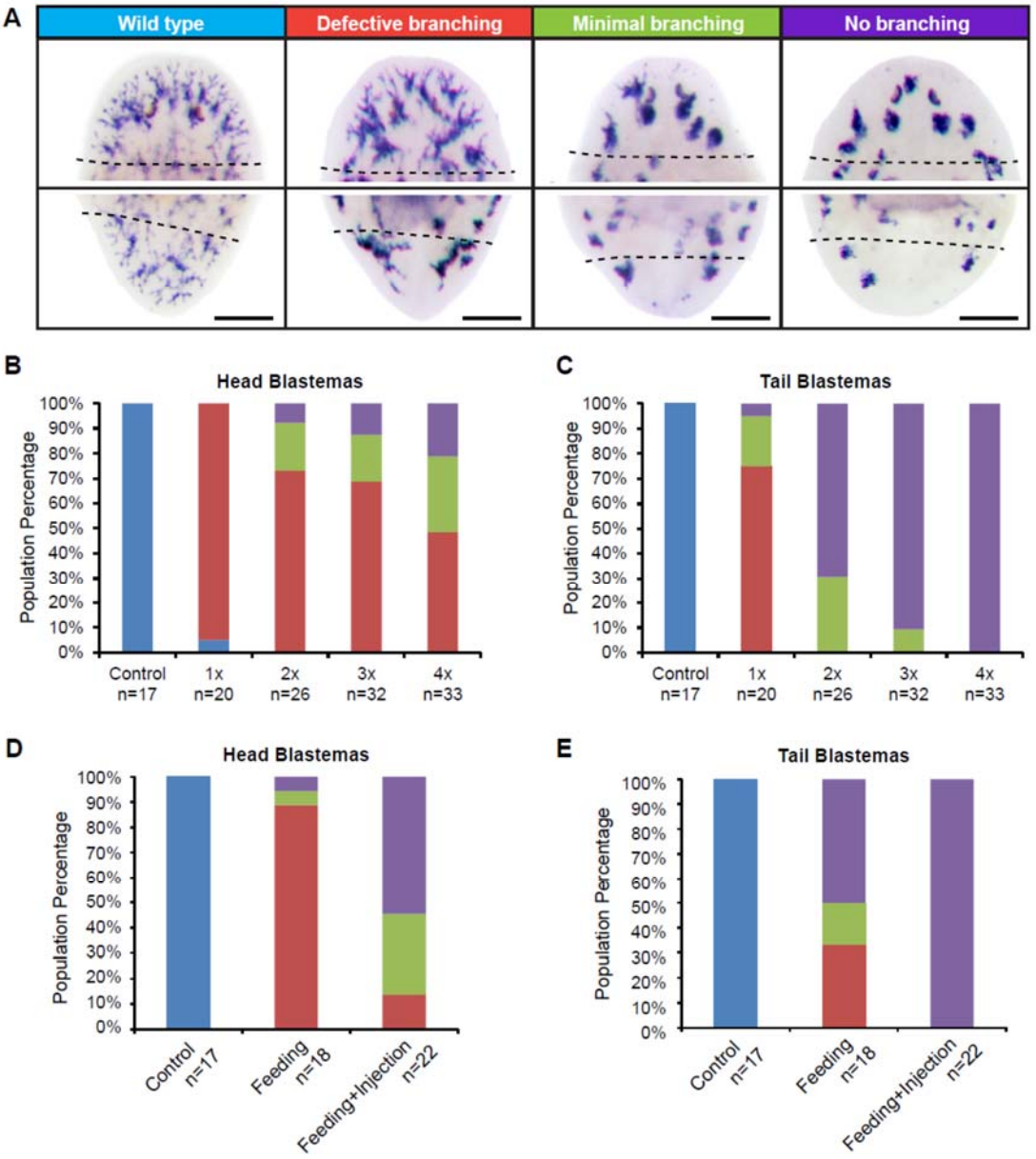
A
Wild type
Defective branching
Minimal branching
No branching
B
Head Blastemas
Population Percentage
100%
90%
80%
70%
60%
50%
40%
30%
20%
10%
0%
Control n=17
1x n=20
2x n=26
3x n=32
4x n=33
C
Tail Blastemas
Population Percentage
Control n=17
1x n=20
2x n=26
3x n=32
4x n=33
D
Head Blastemas
Population Percentage
Control n=17
Feeding n=18
Feeding+Injection n=22
E
Tail Blastemas
Population Percentage
Control n=17
Feeding n=18
Feeding+Injection n=22

of *EGFR-5* (Fig. 2.10A). Hence, a shared feature between intact and regeneration phenotypes is, therefore, a requirement for EGFR-5 in causing and maintaining branch extension.

Second, RNAi-mediated knockdown of *Smed-EGFR-5* caused a loss of flame cells, the cell type at the tip of protonephridial branches. These cells are thought to represent the entry point of interstitial fluid into the protonephridial system by means of ultrafiltration, analogous to the role of the glomerulus in the human kidney (Pedersen, 1961). Hence, the dramatic edema formation in *EGFR-5(RNAi)* animals likely results primarily from a loss of flame cells, rather than the altered branching morphology of protonephridia. In intact animals, the number of flame cells per proximal unit declined rapidly in response to *EGFR-5(RNAi)* from 14-15/unit at the onset of RNAi-feeding to only 2/unit at the lysis-stage (Fig. 2.10B). In regenerating animals, we could also measure an RNAi-dose-dependent decrease of flame cells/proximal unit 14 days post amputation (Fig. 2.9C). These data establish a definite role of EGFR-5 in maintaining flame cells (and possibly the adjacent proximal branches). Whether EGFR-5 is also required for flame cell differentiation during regeneration and/or homeostasis is currently difficult to ascertain. Flame cell marker expression was detectable early on in regenerating *EGFR-5(RNAi)* animals (Fig. 2.8B), but the tools to determine whether their numbers are normal and whether or not the differentiation process might be affected are presently lacking. Moreover, the seemingly regeneration-induced decrease in *EGFR-5* RNAi-efficiency (Fig. 2.8C) represents a second experimental obstacle for addressing early roles of EGFR-5 in flame cell differentiation.

Regardless of the specific role of EGFR-5 in flame cells, the strong correlation between flame cell phenotypes and proximal branching morphology remains an important observation. In intact animals, we observed a gradual collapse of arborizations concomitantly with the loss of flame cells. In regenerating animals, the severity of the branching defects at day 14 post amputation correlated with the number of flame cells (Fig. 2.9C; Fig. 2.12D,E). Hence, a mechanistic link between flame cells and the establishment and maintenance of proximal branching patterns seems likely.

Interestingly, branching morphogenesis generally depends on specialized cells at the tubule tips (Lu and Werb, 2008). Tip cells specified by and responding to FGF-signaling guide the extension and morphogenesis of Drosophila tracheal tubules (Ghabrial and Krasnow, 2006). Vertebrate kidney development relies on tip cells specified via differential RET-Receptor signaling to guide branch outgrowth from the ureteric bud (Chi et al., 2009), and vertebrate blood vessel development represents yet another example in which migratory tip cells act as "motor" for elongation and positioning of a tubular network (Hellstrom et al., 2007; Siekmann and Lawson, 2007). By analogy and in light of our data, flame cells may act as tip cells in protonephridia morphogenesis, besides their roles in organ physiology. Further, EGFR-5 may carry out the widespread requirement for RTK-signaling in specifying and guiding the "tip motor" (Andrew and Ewald). The collapse of proximal arborizations concomitant with the loss of flame cells in intact *EGFR-5(RNAi)* animals (Fig. 2.11) indicates a persisting tip cell function, which may reflect the anchoring of tubule ends to the muscular layer via the prominent flame cell filopodia visible in electron micrographs (Ishii, 1980a; McKanna, 1968a).

Altogether, the branching morphogenesis of planarian protonephridia revealed by our studies represents fascinating examples of biological pattern formation on several levels (Fig. 2.1A,B). First, individual protonephridial units tile in a nonoverlapping manner. Second, within units, branches extend in a spatially efficient manner. Third, proximal units contain a remarkably consistent number of 14.55 +/- 0.65 flame cells, amounting to 14 or 15 flame cells/proximal unit in caudal regions. The mechanistic basis of these patterns, in particular the hypothesis that limiting quantities of an EGFR-5 ligand may be involved, represents an interesting area for future exploration. Further, the striking food supply-dependent variations in planarian body size raise questions regarding the scaling of protonephridial capacity with animal size. The animals used in this study ranged between 0.8 and 2.5 mm in length, hence it appears likely that the number of 14 or 15 flame cells/unit remains constant irrespective of animal size. The consequence of capacity adjustments via the addition or removal of entire protonephridial units seems also in agreement with the mechanism of protonephridial regeneration in forming tissues.

Our data strongly suggest that protonephridia regenerate *de novo*, rather than by growth and extension from preexisting units. A proximal marker expressing structure, which we called the proto-tubule, appears to initiate organ regeneration. The rod-shaped proto-tubule emerged at around hour 36 embedded within the blastema (Fig. 2.4A). Besides the fact that we could not detect connections to preexisting protonephridia, the remarkable consistency in timing of appearance, position, size, and symmetry between right and left blastema halves strongly suggests *de novo* formation of the proto-tubule. We cannot exclude a contribution of preexisting protonephridia to the final organ complement in the new tissue, for example by dynamic reorientation of proximal

branches near the blastema boundary. However, the temporal snapshots of our time course experiments suggest that the majority of protonephridia in the new tissue originate from the morphogenetic remodeling of the proto-tubule. One interesting aspect of this remodeling is the invariable bisection of the proto-tubule by distal marker expressing cells on day 3 (Fig. 2.4A), which likely represents the ontogenetic cause for the convergence of two proximal units into one distal unit (Fig. 2.3). Besides the mechanisms driving branching and branch extension, the origin of the proto-tubule raises further fascinating problems. In analogy with epithelial tube formation in other systems (Lubarsky and Krasnow, 2003), both invagination from the overlying epithelium or condensation of blastema cells are plausible mechanisms. The intermittent ciliation within 48-hour proto-tubules (Fig. 2.6E) might indicate a focal mode of lumen formation typical of solid precursor structures (Dong et al., 2009). Moreover, a study in the polyclad flatworm species *Imogine mcgrathi* suggests embryonic protonephridia formation from mesodermal cells (Younossi-Hartenstein and Hartenstein, 2000), which is why we currently tend to favor a condensation mechanism. The relatively poor preservation of cell boundaries by our *in situ* hybridization protocol is one of the current obstacles in further addressing the cell biology of such a fascinating example of non-embryonic organogenesis.

Altogether, our ultrastructural, molecular, and functional dissection of planarian protonephridia define a novel experimental paradigm for studying both the various processes involved in the assembly, morphogenesis, and maintenance of an epithelial organ, as well as its evolution. The cellular complexity of the planarian protonephridia revealed by our work suggests that studies of this organ system will not only complement

studies from other molecularly tractable, yet highly derived excretory systems (*e.g.*, the single excretory cell of *C. elegans*, or the uncoupling between ultrafiltration and absorption/secretion in the Malpighian tubules of *Drosophila*), but also may help elucidate the functional and evolutionary relationships defining invertebrate and vertebrate excretory systems.

Materials and Methods

Planarian Maintenance

The CIW4 clonal line of *Schmidtea mediterranea* was maintained as described (Cebria and Newmark, 2005). 1-week starved animals were used for all experiments.

Gene Identification and Cloning

All genes were cloned from an 8-day regeneration time course cDNA library prepared as described previously (Gurley et al., 2008). EGFR-5 was identified by performing BLAST analyses of the planarian genome against a panel of vertebrate and invertebrate EGFR-sequences followed by reverse BLAST of the resulting hits against the human and *Drosophila melanogaster* genomes to ensure EGFR-homology. The following primers were used:

DNAH-β3f: TAGCTGACCAAGAAGAAGAAGTGG

DNAH-β3r: CACAGACTTTAATGGATCGACACC

CAVII-1f: TTATTTCTTGTCTCATCTCTTGATCTG

CAVII-1r: CAGGCACATGAAAATTGCAC

inx10f: ATGGTTCTTTCGGAATTCATAG

inx10r: AAATAAAATCATCTTTCAGTGGTAAAGTGGA

EGFR-5f-1: AGTGTGAACAACGATTAGGATG

EGFR-5r-1: TCAGCAGGTTTCTCACATAC

The 3'-end of the EGFR-5 sequence, which was exclusively used for the sequence analysis purposes of Supp. Fig. 2, was cloned with

EGFR-5f-2: TCTTTTACGGAATTGAG and a poly-T reverse primer.

In situ Hybridization and Immunohistochemistry

Whole-mount and fluorescent *in situ* hybridizations were performed as previously described (Pearson et al., 2009). Following fluorescent or NBT/BCIP development, animals were incubated with anti-α-Tubulin antibody (1:300, NeoMarkers) or anti-acetylated-Tubulin antibody (1:500, Sigma) to detect ciliated sections of protonephridia. Primary antibodies were detected with alexa-fluor-labelled anti-Mouse secondary antibodies (1:500; Invitrogen). For documenting NBT/BCIP developed whole-mount *in situ* specimens, animals were mounted in 80% glycerol and photographed using a Zeiss SteREO Lumar.V12 equipped with an AxioCam HRc. Whole-mount specimens stained with fluorescent markers were mounted in 2:1 Benzyl benzoate:Benzyl alcohol after dehydration in methanol and imaged on a Zeiss LSM510-Live Laser Scanning Microscope. Flame cell quantifications were carried out independently by two observers. For sectioning, fluorescently stained whole-mounted animals were dehydrated in a graded series of ethanol, incubated for ~2 hours in 1:1 ethanol:Immuno-bed (Poly-sciences), and subsequently immersed in 100% Immuno-bed supplemented with catalyst according to the manufacturer's suggestions. Sections (10 µm) were collected on a Leica

Microtome equipped with a glass knife. Sections were mounted in Fluoromount-G (SouthernBiotech) and photographed using a Zeiss LSM510-Live Laser Scanning Microscope.

Histology

Specimens were prepared as following: 1) animals were fixed overnight at 4ºC in 2.5% glutaraldehyde in 0.1M sodium cacodylate, 1mM $CaCl_2$; 2) animals were washed in wash buffer of 0.1M sodium cacodylate (supplemented with 1mM $CaCl_2$ and 1% w/v) for 1 hour at room temperature (3-4 exchanges) and in distilled water for 1 hour at room temperature (3-4 exchanges); 3) specimens were dehydrated in acetone 30% (20 minutes), 50% (20 minutes), 70% (overnight), 90% (20 minutes, 2 times), and 100% (20 minutes, 3 times); 4) specimens were embedded in epon-araldite (30% resin/acetone for 5 hours, 70% resin/acetone for 6 hours, 90% resin/acetone overnight, and fresh 100% resin for 8 hours, curing at 60ºC for 2 days); and 5) thin sections (1 µm) were collected using an Ultracut UCT microtome (Leica), stained with Toluidine Blue, mounted in Cytoseal XYL (Richard-Allan Scientific), and photographed using a Zeiss Axiovert microscope.

Electron Microscopy

Specimens were prepared for electron microscopy using high pressure freezing/freeze substitution, as previously described (Pellettieri, Fitzgerald et al. 2010). Ultra-thin 50 nm sections were collected using an Ultracut UCT microtome (Leica). TEM specimens were stained with 2.5% uranyl acetate for 4 minutes prior to imaging on a Hitachi H-7100 electron microscope equipped with a Gatan Orius CCD camera.

RNAi

RNAi feedings were performed as described previously (Gurley et al., 2008; Rink et al., 2009). 6 feedings 2-3 days apart were used in the unsuccessful attempt to elicit *DNAH-β3(RNAi)* and *CAVII-1(RNAi)* phenotypes. For *inx10(RNAi)* and *EGFR-5(RNAi)* experiments, animals were fed 3 times every 2–3 days. For regeneration time series experiments, animals were amputated 3 days after the last feeding. For Fig. 5C and Supp. Fig. 5D,E, RNAi-fed animals were additionally injected with *EGFR-5* dsRNA, 200 ng/ul, 3 days after amputation. dsRNA was prepared with a Megascript RNAi-kit (Ambion).

References

Agata, K., and Umesono, Y. (2008). Brain regeneration from pluripotent stem cells in planarian. Philos Trans R Soc Lond B Biol Sci *363*, 2071-2078.

Andrew, D.J., and Ewald, A.J. (2010). Morphogenesis of epithelial tubes: Insights into tube formation, elongation, and elaboration. Dev Biol *341*, 34-55.

Beyenbach, K.W., Skaer, H., and Dow, J.A. (2010). The developmental, molecular, and transport biology of malpighian tubules. Annu Rev Entomol *55*, 351-374.

Cebria, F. (2007). Regenerating the central nervous system: How easy for planarians! Dev Genes Evol *217*, 733-748.

Cebria, F., Kudome, T., Nakazawa, M., Mineta, K., Ikeo, K., Gojobori, T., and Agata, K. (2002). The expression of neural-specific genes reveals the structural and molecular complexity of the planarian central nervous system. Mech Dev *116*, 199-204.

Cebria, F., and Newmark, P.A. (2005). Planarian homologs of netrin and netrin receptor are required for proper regeneration of the central nervous system and the maintenance of nervous system architecture. Development *132*, 3691-3703.

Chi, X., Michos, O., Shakya, R., Riccio, P., Enomoto, H., Licht, J.D., Asai, N., Takahashi, M., Ohgami, N., Kato, M.*, et al.* (2009). Ret-dependent cell rearrangements in the wolffian duct epithelium initiate ureteric bud morphogenesis. Dev Cell *17*, 199-209.

Chichkoff, G.D. (1888). Recherches sur les dendrocoeles d'eau douce (triclades). Thèse de doctorat : Université de Genève.

Collins, J.J., 3rd, Hou, X., Romanova, E.V., Lambrus, B.G., Miller, C.M., Saberi, A., Sweedler, J.V., and Newmark, P.A. Genome-wide analyses reveal a role for peptide hormones in planarian germline development. PLoS Biol *8*, e1000509.

Costantini, F., and Kopan, R. (2010). Patterning a complex organ: Branching morphogenesis and nephron segmentation in kidney development. Dev Cell *18*, 698-712.

Dernburg, A.F., McDonald, K., Moulder, G., Barstead, R., Dresser, M., and Villeneuve, A.M. (1998). Meiotic recombination in c. Elegans initiates by a conserved mechanism and is dispensable for homologous chromosome synapsis. Cell *94*, 387-398.

Dong, B., Horie, T., Denker, E., Kusakabe, T., Tsuda, M., Smith, W.C., and Jiang, D. (2009). Tube formation by complex cellular processes in ciona intestinalis notochord. Dev Biol *330*, 237-249.

Finken-Eigen, M., and Kunz, W. (1997). Schistosoma mansoni: Gene structure and localization of a homologue to cysteine protease er 60. Exp Parasitol *86*, 1-7.

Ghabrial, A.S., and Krasnow, M.A. (2006). Social interactions among epithelial cells during tracheal branching morphogenesis. Nature *441*, 746-749.

Gurley, K., Rink, J., and Sanchez, A.A. (2008). Beta-catenin defines head versus tail identity during planarian regeneration and homeostasis. Science *319*, 323-327.

Hellstrom, M., Phng, L.K., Hofmann, J.J., Wallgard, E., Coultas, L., Lindblom, P., Alva, J., Nilsson, A.K., Karlsson, L., Gaiano, N.*, et al.* (2007). Dll4 signalling through notch1 regulates formation of tip cells during angiogenesis. Nature *445*, 776-780.

Hyman, L.H. (1951). The invertebrates: Platyhelminthes and Rhynchocoela (New York: McGraw-Hill).

Ishii, S. (1980a). The ultrastructure of the protonephridial flame cell of the freshwater planarian bdellocephala brunnea. Cell Tissue Res *206*, 441-449.

Ishii, S. (1980b). The ultrastructure of the protonephridial tubules of the freshwater planarian bdellocephala brunnea. Cell Tissue Res *206*, 451-458.

Lu, P., and Werb, Z. (2008). Patterning mechanisms of branched organs. Science *322*, 1506-1509.

Lubarsky, B., and Krasnow, M.A. (2003). Tube morphogenesis: Making and shaping biological tubes. Cell *112*, 19-28.

McKanna, J.A. (1968a). Fine structure of the protonephridial system in planaria. I. Flame cells. Z Zellforsch Mikrosk Anat *92*, 509-523.

McKanna, J.A. (1968b). Fine structure of the protonephridial system in planaria. Ii. Ductules, collecting ducts, and osmoregulatory cells. Z Zellforsch Mikrosk Anat *92*, 524-535.

Nishimura, K., Kitamura, Y., Inoue, T., Umesono, Y., Sano, S., Yoshimoto, K., Inden, M., Takata, K., Taniguchi, T., Shimohama, S., *et al.* (2007). Reconstruction of dopaminergic neural network and locomotion function in planarian regenerates. Dev Neurobiol *67*, 1059-1078.

Nishimura, K., Kitamura, Y., Taniguchi, T., and Agata, K. Analysis of motor function modulated by cholinergic neurons in planarian dugesia japonica. Neuroscience *168*, 18-30.

Nishimura, K., Kitamura, Y., Umesono, Y., Takeuchi, K., Takata, K., Taniguchi, T., and Agata, K. (2008). Identification of glutamic acid decarboxylase gene and distribution of gabaergic nervous system in the planarian dugesia japonica. Neuroscience *153*, 1103-1114.

Oviedo, N.J., and Levin, M. (2007). Smedinx-11 is a planarian stem cell gap junction gene required for regeneration and homeostasis. Development *134*, 3121-3131.

Pahlavan, P.S., Feldmann, R.E., Jr., Zavos, C., and Kountouras, J. (2006). Prometheus' challenge: Molecular, cellular and systemic aspects of liver regeneration. J Surg Res *134*, 238-251.

Pearson, B.J., Eisenhoffer, G.T., Gurley, K.A., Rink, J.C., Miller, D.E., and Sanchez Alvarado, A. (2009). Formaldehyde-based whole-mount in situ hybridization method for planarians. Dev Dyn *238*, 443-450.

Pedersen, K.J. (1961). Some obserfations on the fine structure of planarian protonephridia and gastrodermal phagocytes. Z. Zellforsch. *53*, 609-628.

Reddien, P., and Sanchez, A.A. (2004). Fundamentals of planarian regeneration. Annu Rev Cell Dev Biol *20*, 725-757.

Reddien, P.W., Bermange, A.L., Murfitt, K.J., Jennings, J.R., and Sanchez Alvarado, A. (2005). Identification of genes needed for regeneration, stem cell function, and tissue homeostasis by systematic gene perturbation in planaria. Dev Cell *8*, 635-649.

Rink, J.C., Gurley, K.A., Elliott, S.A., and Sanchez Alvarado, A. (2009). Planarian hh signaling regulates regeneration polarity and links hh pathway evolution to cilia. Science *326*, 1406-1410.

Ruppert, E. (1994). Evolutionary origin of the vertebrate nephron. Amer. Zool. *34*, 542-553.

Salvenmoser, W., Egger, B., Achatz, J.G., Ladurner, P., and Hess, M.W. (2010). Electron microscopy of flatworms: Standard and cryo-preparation methods. Methods Cell Biol *96*, 307-330.

Sanchez Alvarado, A., Newmark, P.A., Robb, S.M., and Juste, R. (2002). The schmidtea mediterranea database as a molecular resource for studying platyhelminthes, stem cells and regeneration. Development *129*, 5659-5665.

Siekmann, A.F., and Lawson, N.D. (2007). Notch signalling limits angiogenic cell behaviour in developing zebrafish arteries. Nature *445*, 781-784.

Skelly, P.J., and Shoemaker, C.B. (2001). Schistosoma mansoni proteases sm31 (cathepsin b) and sm32 (legumain) are expressed in the cecum and protonephridia of cercariae. J Parasitol *87*, 1218-1221.

Stein, R.A., and Staros, J.V. (2006). Insights into the evolution of the erbb receptor family and their ligands from sequence analysis. BMC Evol Biol *6*, 79.

Umesono, Y., Watanabe, K., and Agata, K. (1999). Distinct structural domains in the planarian brain defined by the expression of evolutionarily conserved homeobox genes. Dev Genes Evol *209*, 31-39.

Wilhelmi, J. (1906). Untersuchungen über die excretionsorgane der sübwassertricladen. Z Wiss Zool *80*, 544-575.

Wilson, R.A., and Webster, L.A. (1974). Protonephridia. Biol Rev Camb Philos Soc *49*, 127-160.

Younossi-Hartenstein, A., and Hartenstein, V. (2000). The embryonic development of the polyclad flatworm imogine mcgrathi. Dev Genes Evol *210*, 383-398.

CHAPTER 3

STEM CELLS AND FLUID FLOW DRIVE CYST FORMATION IN AN INVERTEBRATE EXCRETORY SYSTEM

Hanh Thi-Kim Vu, Jochen C. Rink, Sean A. McKinney, Melainia McClain, Naharajan Lakshmanaperuma, Richard Alexander, and Alejandro Sánchez Alvarado

This chapter was prepared using the style guide from Cell. It will be submitted for publication as:

Vu H. T., Rink J. C., McKinney S. A., McClain M., Lakshmanaperuma N., Alexander R., and Sánchez Alvarado A. (2014). Stem cells and fluid flow drive cyst formation in an invertebrate excretory system.

Abstract

Cystic kidney diseases (CKDs) are the most commonly inherited causes of kidney failure that affect millions of people worldwide. The defining features of the pathology are fluid-filled cysts developing from nephric tubules due to defective flow sensing, cell proliferation, and differentiation. The underlying molecular mechanisms remain poorly understood. Compounding this problem is that the simplified excretory systems of *C. elegans* and *D. melanogaster* cannot recapitulate disease ontology. We report here a systematic characterization of the protonephridial excretory system of planarians. Our extensive structure/function comparisons with the vertebrate nephrons reveal that planarian protonephridia retain the combination of ultrafiltration and flow-associated filtrate modification that is a central element in the ontology of CKDs. Consistently, the inhibition of tubule flow led to cystic enlargements of proximal tubules that share many features with vertebrate CKDs, including lumen occlusions and the overproliferation of protonephridial progenitors. The recapitulation of the phenotype by RNAi-mediated knockdown of orthologues of human CDK genes demonstrated deep mechanistic conservation of cyst ontogeny. Altogether, our results therefore establish a uniquely accessible invertebrate model system for the elucidation of human kidney pathologies.

Introduction

The vertebrate kidney plays a pivotal role in the maintenance of organismal homeostasis in face of changing external and internal conditions. Its myriad individual functions, including the removal of metabolic waste products, regulation of ion concentrations, or acid/base balance, are all tied to two basic physiological processes: first,

the pressure-driven ultrafiltration of blood plasma across the glomerulus, whereby molecular sieves prevent the passage of large macromolecules (*e.g.*, plasma proteins); and second, the subsequent modification of the resulting filtrate during its passage through the epithelial nephron tube (Ruppert, 1994; Ruppert and Smith, 1988). The parallel operation of many millions of glomerulus/nephron units allows formidable filtration rates, amounting to 170 liters of primary filtrate/day in a healthy human adult. In line with the pivotal homeostatic roles of the kidney, kidney diseases pose a serious health problem. The most common human kidney disorders are cystic kidney diseases (CKDs), affecting 12 million people worldwide (Priolo and Henske, 2013). CKDs refer to a wide range of hereditary, developmental, and acquired conditions (Bisceglia et al., 2006) that all share the pathological hallmark of fluid-filled cysts developing in the kidney. This has led to the suggestion that the molecular mechanisms causing cyst formation are similar or, at least, share a common pathway (Watnick and Germino, 2003). The molecular cloning of multiple CKD mutations and the realization that the affected genes all function at the primary cilia, basal bodies, or centrosomes has given rise to the ciliary hypothesis as unifying disease mechanism of CKDs (Fliegauf et al., 2006; Mollet et al., 2005; Yoder et al., 2002). Accordingly, the primary cilia of tubule cells are thought to act as flow sensors, eliciting intracellular calcium fluxes through stretch sensitive polycystin channels in response to flow-driven bending (Nauli et al., 2003; Praetorius et al., 2004; Praetorius and Spring, 2001, 2003). These signals are thought to constitutively dampen cell proliferation, such that loss of filtrate flow or interruptions in the signal transduction process precipitate chronic overproliferation and consequent cyst formation (Deane and Ricardo, 2012). However, major mechanistic components of the ciliary hypothesis remain poorly

understood, including the integration of the calcium signal with downstream transcriptional regulation of cell behavior (Deane and Ricardo, 2012; Kotsis et al., 2013; Uhlenhaut and Treier, 2008; Wilson and Goilav, 2007), the extent by which cyst development can be understood as chronic activity of endogenous repair mechanisms (Deane and Ricardo, 2012) or identity and origins of the ectopically overproliferating cells (Lodi et al., 2012; Murer et al., 2002; Weimbs, 2007). Further, these questions present an investigative challenge, given the poor experimental accessibility of the kidney as an internal and essential organ. The *Xenopus* pronephros and zebrafish pro- and metanephric kidneys are therefore increasingly explored as model systems for human kidney disease (Igarashi, 2005). Compounding this problem is that the power of invertebrate models in solving fundamental cell biological processes could so far not be applied to the analysis of human kidney disease (Dow and Romero, 2010; Igarashi, 2005). Both *C. elegans* and *D. melanogaster* have highly derived excretory organs in which ultrafiltration is either entirely lacking (*C. elegans;* (Buechner, 2002)) or uncoupled from reabsorption/secretion (*D. melanogaster;* (Dow and Romero, 2010)). Furthermore, the excretory cells of both organisms are lacking cilia as a further requirement for modeling CKDs. However, *C. elegans* or *Drosophila* are but two of myriad invertebrate species and multiple studies have documented the existence of more complex excretory systems outside the *Ecdysozoa* (Ruppert and Smith, 1988). One such example is the excretory system of planarian flatworms. We and others have previously reported on intriguing similarities between planarian protonephridia and the vertebrate nephron (Rink et al., 2011; Scimone et al., 2011). Here, we carried out a systematic structure function comparison to systematically gauge the potential of planarian protonephridia as a model system for human kidney

diseases. Our results demonstrate the structural coupling of cilia-driven ultrafiltration and filtrate modification in planarian protonephridia, as well as extensive topological homology of solute carrier expression domains with the vertebrate nephron. These structure/function homologies extend to common pathologies, including shared requirements of nephrin in the maintenance of the ultrafiltration barrier or of nephrocystins in preventing the development of tubular cysts. Our results therefore establish planarian protonephridia as a unique invertebrate model for studying human kidney development and diseases.

Results

Protonephridia Are Ultrafiltration Devices in Planarian

The planarian excretory system consists of branched epithelial tubules (protonephridia) distributed throughout the entire body plan (Fig. 3.1a) (Rink et al., 2011). The barrel-shaped flame cells capping the proximal tubule ends have been proposed to act as unicellular ultrafiltration devices solely on the basis of morphological evidence (Fig. 3.1b) (Wilhelmi, 1906; Wilson and Webster, 1974). To functionally test this premise, we adapted an assay previously used to demonstrate the ultrafiltration capacity of *Drosophila* nephrocytes (Weavers et al., 2009; Zhuang et al., 2009). We co-injected two inert and differentially labeled tracer molecules of different sizes into the anterior planarian mesenchyme (10 kDa and 500 kDa molecular weight dextrans). Already at 2-hour post injection, we found robust tracer accumulation in protonephridia throughout the body, confirming their active role in extracellular fluid processing. Interestingly, only the small molecular weight tracer produced intense and continuous protonephridial labeling, whereas

Figure 3.1. Protonephridia are ultrafiltration devices in planarians. a, Whole-mount AcTub staining. Scale bars: 500 μm. Inset showing depth-coded projection of AcTub staining. Superficial structures are in blue and deeper structures are in red. Scale bars: 50 μm. **b**, Cross section through a flame cell. Inset showing a high magnification of filtration diaphragm. Scale bar: 1 μm. **c-d**, Ultrafiltration assay assessing ultrafiltration capacity in the planarian protonephridia. (c) Fluorescent overlay showing dextran uptake in the animals that co-injected with 10 kDa and 500 kDa fluorescently labeled dextran. Inset showing a high magnification of tubule structure labeled by dextran. Scale bar: 100 μm. (d) Quantification of small and large dextran uptake.

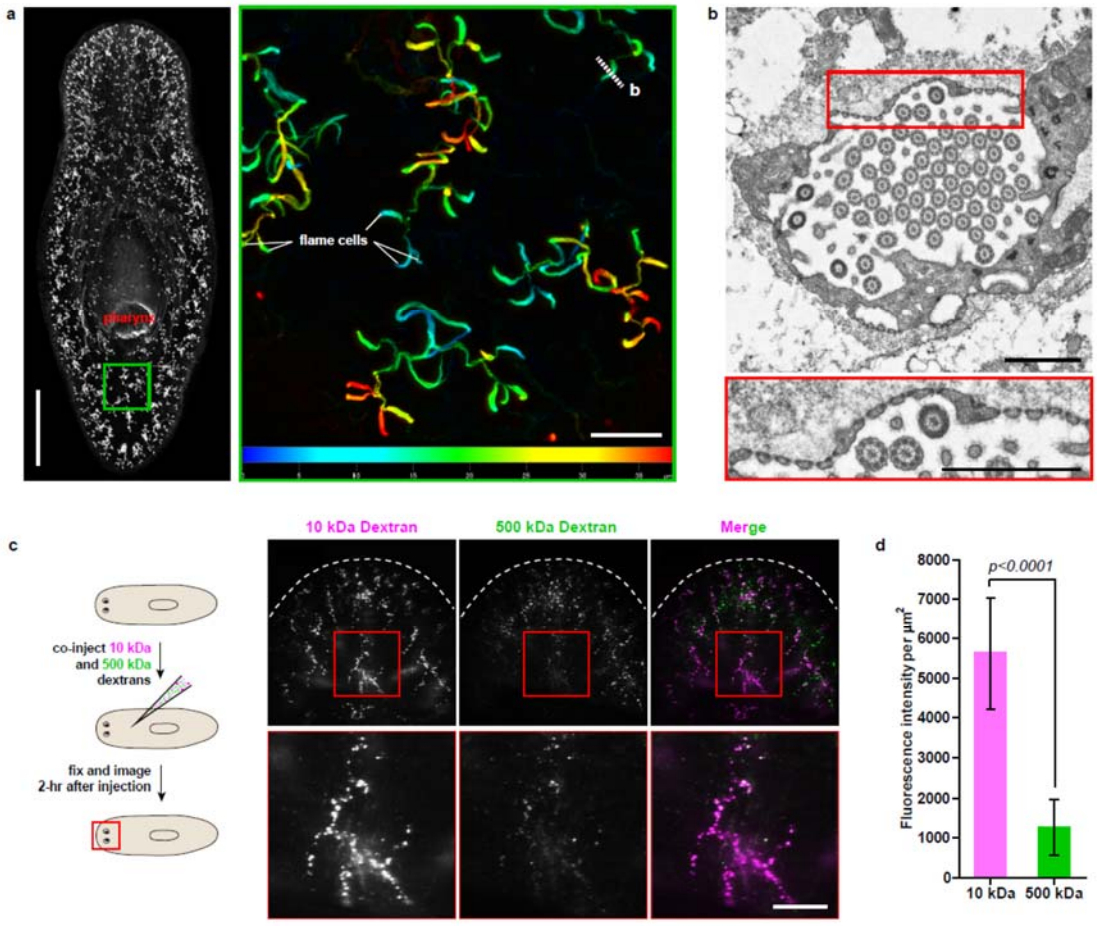
a
pharynx
flame cells
b
b
c
co-inject 10 kDa
and 500 kDa
dextrans
fix and image
2-hr after injection
10 kDa Dextran
500 kDa Dextran
Merge
d
p<0.0001
Fluorescence intensity per µm²
8000
7000
6000
5000
4000
3000
2000
1000
0
10 kDa
500 kDa

the large dextran displayed weak and patchy labeling (Fig. 3.1c-d). Since the two tracer molecules in the injection mix carried equal numbers of fluorophores, the preferential accumulation of the small over the large dextran demonstrates molecular size filtration upon entry into the protonephridial system. Therefore, like the vertebrate nephron, the planarian protonephridia combine ultrafiltration with filtrate modification in the same structure.

Unexpected Complexity of Protonephridial Tubules

We next sought to investigate the filtrate modification capacities of the planarian protonephridial system. In the vertebrate nephron, the expression of a large number of solute carrier (slc) transporters recovers essential molecules from the primary filtrate or secretes waste products into the tubule lumen (Landowski, 2008; Raciti et al., 2008). The known substrate specificity of slc families together with their restricted expression in specific nephron segments establishes a structure/function topology of filtrate modification processes along the nephron. Towards the dual goal of identifying and mapping solute modification processes in planarian protonephridia, we set out to identify, clone, and expression-map all solute carriers in the planarian genome. A systematic sequence homology search of the planarian *Schmidtea mediterranea* (*S. mediterranea*) genome identified 318 *slc* genes. Reciprocal BLAST analysis and sequence alignments revealed that *S. mediterranea* slcs represent 43 slc families (Fig. 3.2, Appendix A). Expression patterns of all *slc* genes were analyzed by *in situ* hybridization in intact asexual planarians. We obtained expression patterns of 287 genes in various tissues (Fig. 3.3) and thereof, 49 genes showed putative protonephridial expression.

Figure 3.2. Solute carrier gene families in the planarian *Schmidtea mediterranea*. a, *slc* gene families in planarian. **b-v,** Schematic representation of the seven major phylogenetic clusters, the α-, β-, δ-, γ-groups of *slcs* (panel g, h, c, b, respectively); the Tim barrel-, IT-, Drug/Metabolite transporter clans of *slcs* (panel d, e, f, respectively), and selected slc families, including slc1a (i), *slc5a* (j), *slc22a* (k), *slc6a* (l), *slc4a* (m), *slc7a* (n), *slc12* (o), *slc15* (p), *slc20* (q), *slc23* (r), *slc26* (s), *slc28* (t), *slc30* (u), and *slc42* (v). Planarian homologs are colored in red.

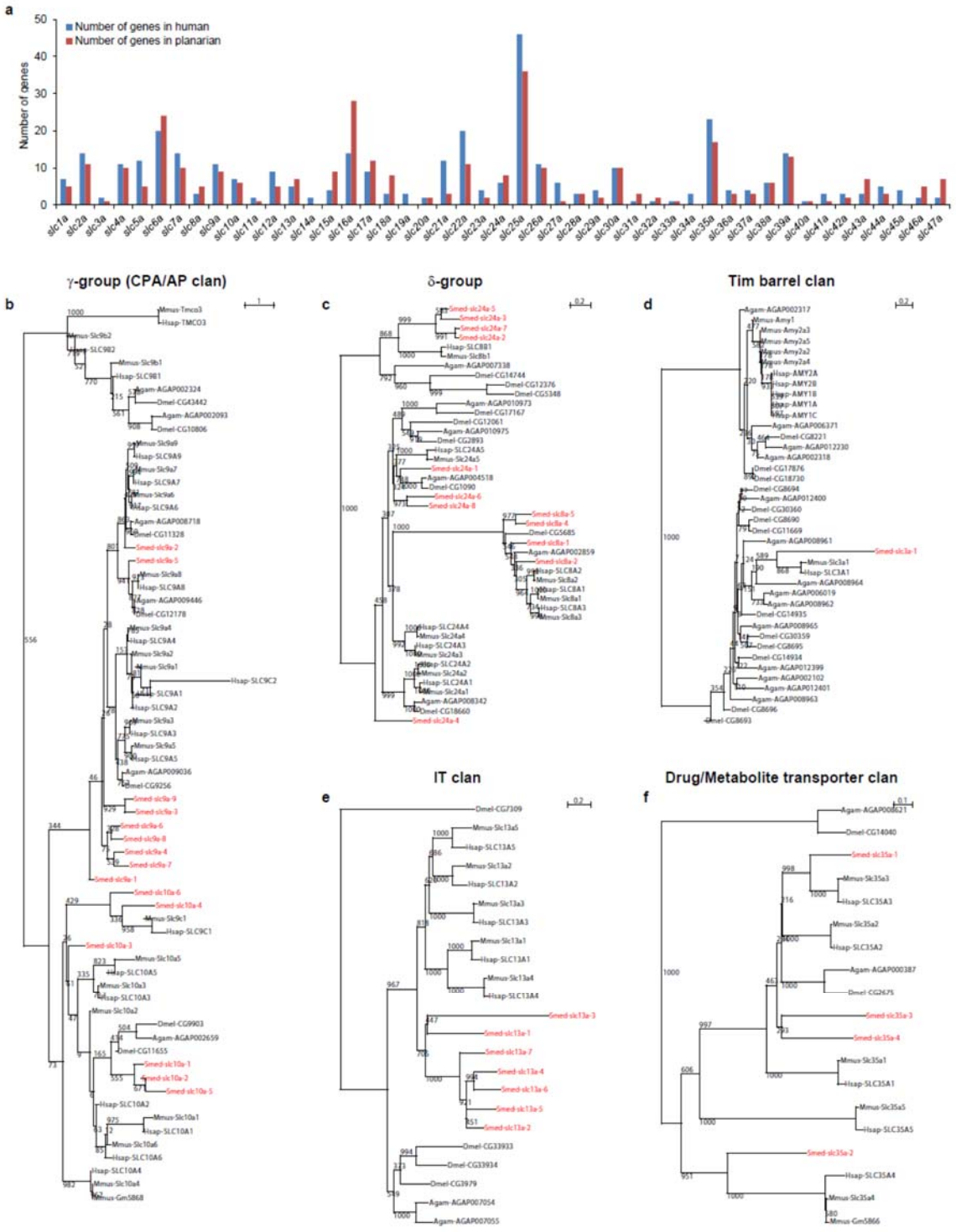
a
Number of genes in human
Number of genes in planarian
Number of genes
slc1a slc2a slc3a slc4a slc5a slc6a slc7a slc8a slc9a slc10a slc11a slc12a slc13a slc14a slc15a slc16a slc17a slc18a slc19a slc20a slc21a slc22a slc23a slc24a slc25a slc26a slc27a slc28a slc29a slc30a slc31a slc32a slc33a slc34a slc35a slc36a slc37a slc38a slc39a slc40a slc41a slc42a slc43a slc44a slc45a slc46a slc47a
γ-group (CPA/AP clan)
δ-group
Tim barrel clan
IT clan
Drug/Metabolite transporter clan
b
c
d
e
f

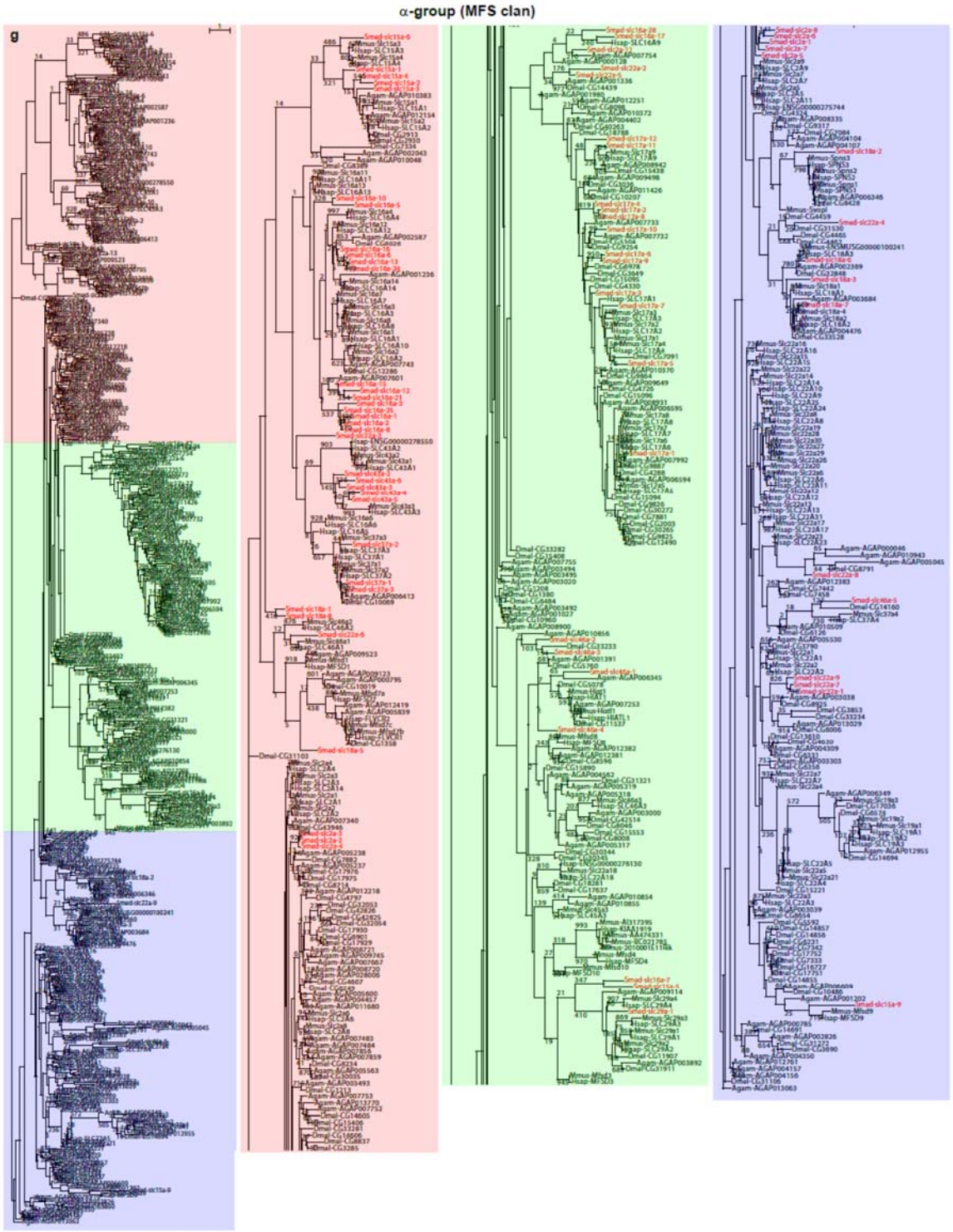

Figure 3.2. Continued

Figure 3.2. Continued

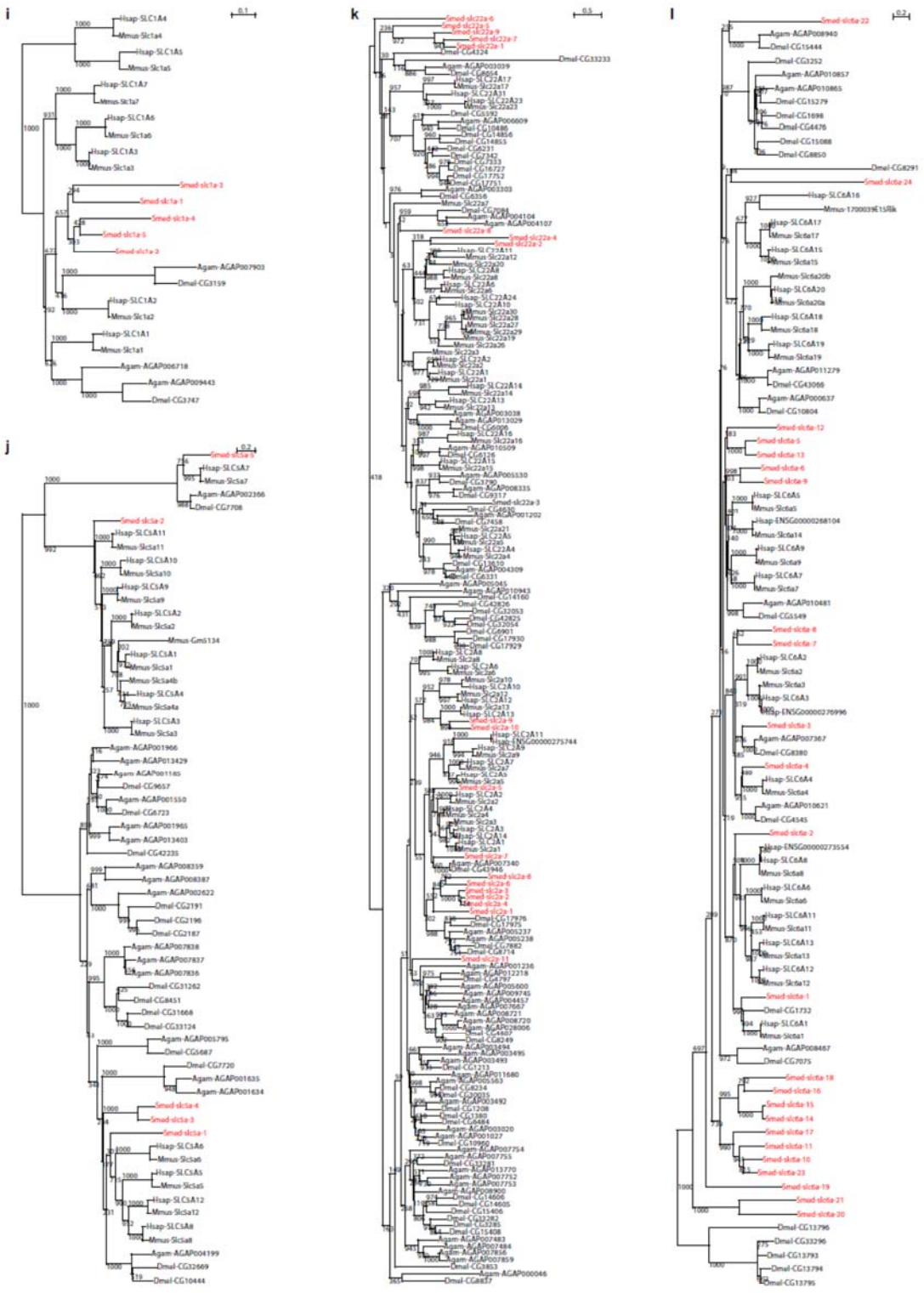

Figure 3.2. Continued

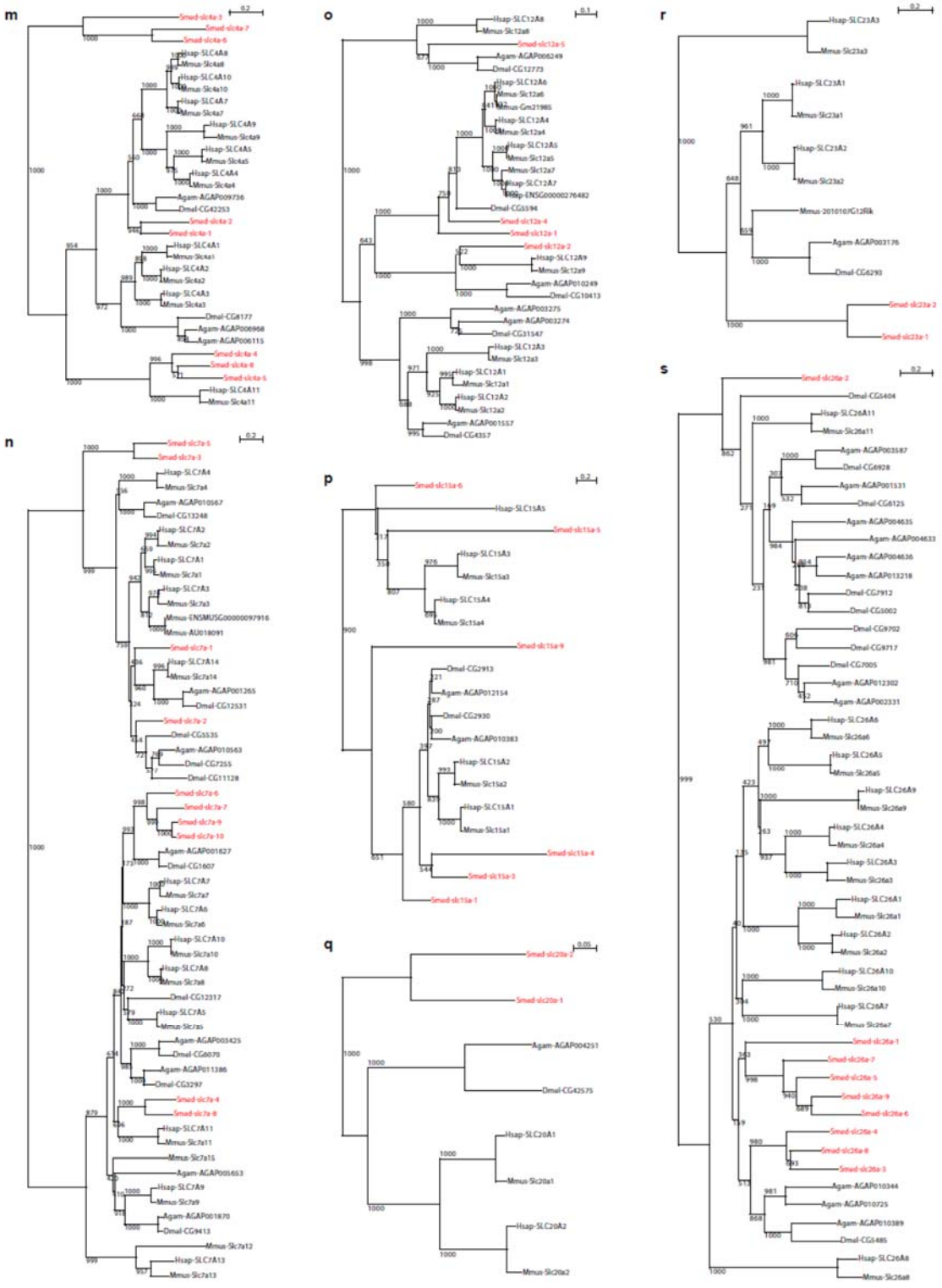

Figure 3.2. Continued

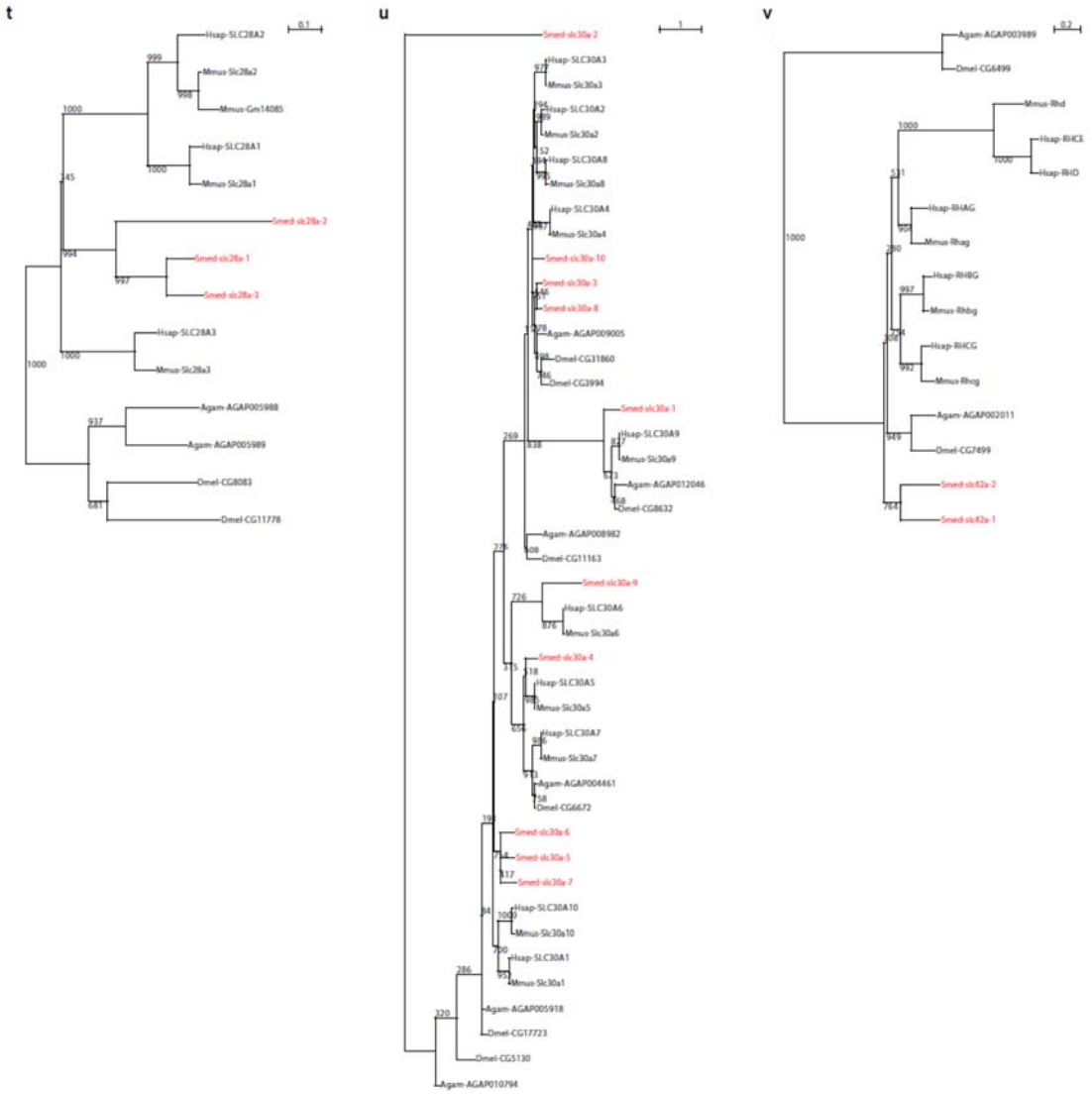

Figure 3.2. Continued

Figure 3.3. Expression patterns of *slc* genes in an asexual strain of the planarian *Schmidtea mediterranea*. Whole-mount expression patterns of *slc* genes by *in situ* hybridization (NBT/BCIP development). Scale bars: 500 μm.

Solute carrier family 1: High-affinity glutamate and neutral amino acid transporter family

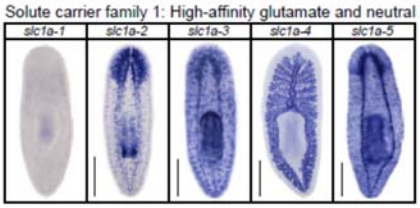

Solute carrier family 2: Facilitative GLUT transporter family

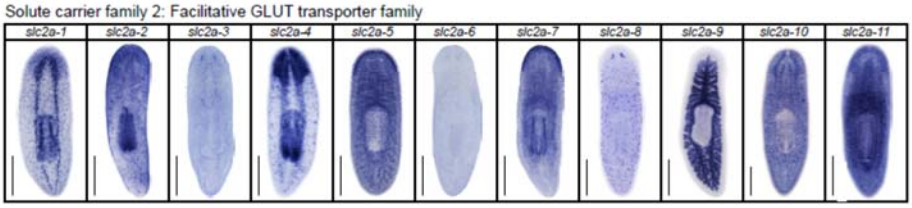

Solute carrier family 3: Heavy subunits of heterodimeric amino acid transporters

Solute carrier family 4: Bicarbonate transporter family

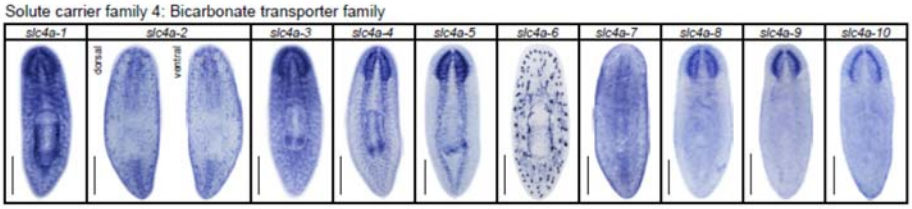

Solute carrier family 5: Sodium glucose cotransporter family

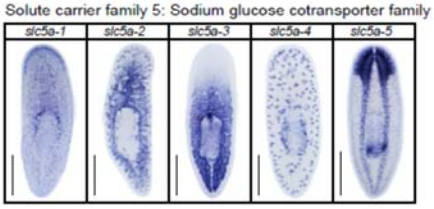

Solute carrier family 6: Sodium- and chloride-dependent sodium:neurotransmitter transporter family

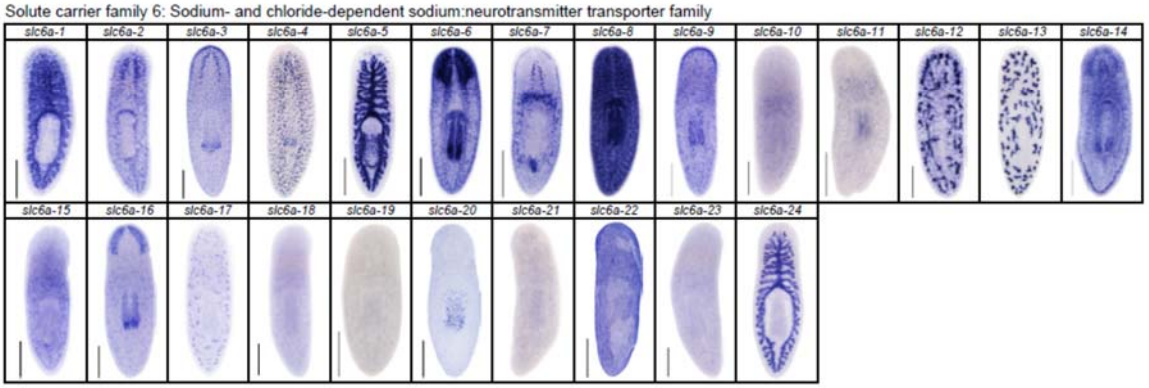

Figure 3.3. Continued

Figure 3.3. Continued

Figure 3.3. Continued

Figure 3.3. Continued

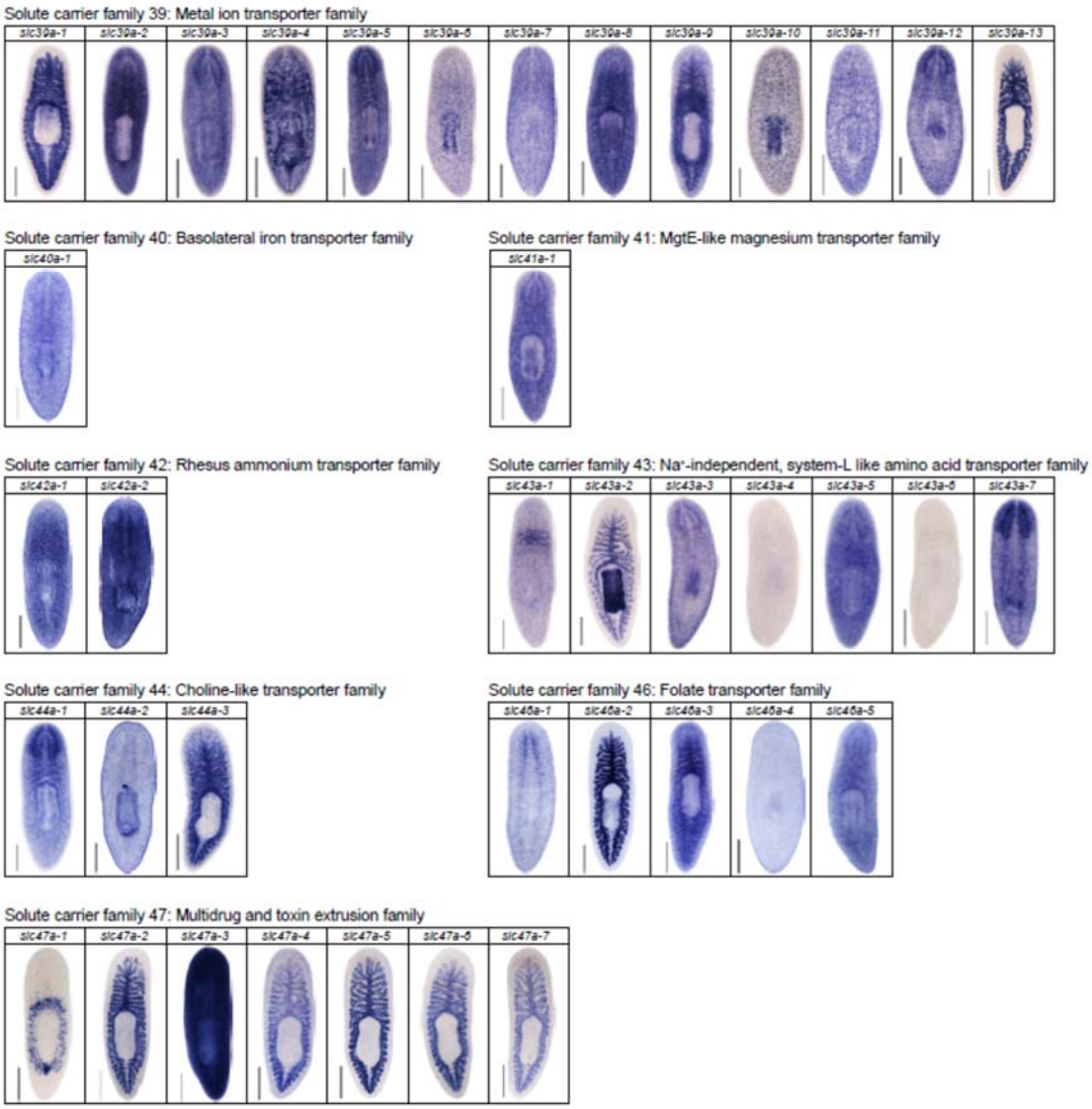

Figure 3.3. Continued

The expression of such a large fraction of *slc* genes in protonephridial tubules already indicated a rich potential for solute modifications.

Towards our goal of establishing a comprehensive structure-function map of protonephridia, we next mapped the expression domain of each protonephridial *slc* relative to two previously characterized markers (Fig. 3.4a, top; Appendix B): 1) acetylated tubulin (AcTub) antibody staining, which marks flame cells and the adjoining proximal tubule (PT) segment; 2) *Smed-CAVII-1*, which is expressed in the adjacent distal tubule (DT) segment (Rink et al., 2011). Markers for the domains distal to *CAVII-1* expression were not available at the beginning of this study. Fluorescent *in situ* hybridization (FISH) mapping of putative protonephridial *slc* genes against the two markers and general tubule anatomy (*e.g.*, branched versus coiled PT segments) revealed a significantly greater complexity of protonephridial cell types than previously appreciated (Fig. 3.4a; Fig. 3.5-3.11). *slc* expression domains define at least three subdomains within the PT (PT1, PT2, and PT3; Fig. 3.4a-d) and the nonoverlapping expression of representative *slc* genes in 3-color FISH experiments demonstrates the significance of the inferred PT subdivisions (Fig. 3.5-3.8). Similarly, we found that *slc* expression domains divide the DT into 2 subdomains (DT1 and DT2; Fig. 3.4a, d-f; Fig. 3.9f). Interestingly, the *slc12a-4* expression domain extended beyond *CAVII-1* expression, where it was co-expressed with further 14 *slc* genes, including *Smed-slc24a-3* (Fig. 3.4a, g, (Scimone et al., 2011)). Together, these 14 *slc* genes therefore define the so-far unknown continuation of protonephridia beyond *CAVII-1* expression domain, which for reasons detailed below we refer to as “Collecting Duct” (CD). Interestingly, CD marker expressing segments were exclusively located close to the dorsal body surface, supporting early reports suspecting the protonephridial terminus in the

dorsal epithelium (Wilhelmi, 1906). Consistently, sagittal sections revealed occasional CD segments crossing the basal lamina and appearing to terminate in the single-layered outer epithelium (*e.g.*, *Smed-slc12a-1*, Fig. 3.4h). To further confirm this finding, we performed electron microscopy (EM) on serial thin sections and succeeded in visualizing multiple examples of ducts connecting into the dorsal epithelium and opening directly to the exterior (Fig. 3.4i, Supplementary movie 1). The presence of mitochondria and numerous small vesicles are ultrastructural characteristics of this region, similar to that of type B intercalated cells in the vertebrate CD.

Thus, our results for the first time trace the complete course of protonephridial tubules from the ultrafiltrating flame cells as proximal entry point to their terminus in the dorsal epithelium. Further, our systematic mapping of expression domains of *slc* genes defined 6 molecularly distinct segments along the proximal-distal axis of protonephridia.

Extensive Functional Homology between Planarian Protonephridia and Vertebrate Nephrons

We next took advantage of our expression data and the known transport activities of slc families to infer possible functional specializations of the 6 protonephridial segments. Clustering a subset of slc genes with known substrate specificity by substrate class and site of expression revealed a striking segregation of similar transport activities into similar regions of the protonephridial tubule, thus demonstrating the functional specialization of different segments (Fig. 3.4j, top). Because this subset of slc genes was intentionally chosen due to its known representation for transport activities of specific segments of the nephron (Raciti et al., 2008), this map afforded a basis for direct structure/function

Figure 3.4. Extensive structural and functional homology between protonephridia and nephrons. **a**, Cartoon showing previous segmentation model of protonephridial tubule and expression map of *slc* genes along protonephridial tubule. **b-g,** Representative images showing expression domains of selected *slc* genes in (b) PT1, PT2, and PT3, (c) PT2 and PT3, (d) PT3, (e) DT1, DT2, and CD, (f) DT2 and CD and (g) CD. Fluorescent overlay of indicated gene (red) with PT marker (AcTub) and DT marker (*CAVII-1*). A color-coded scheme of protonephridial tubule at the end of each panel showing expression domain of indicated gene. Images are maximum projections of confocal Z-sections. Scale bars: 50 μm. **h**, Longitudinal-section through a worm showing dorsal-bias expression of *slc12a-1*. Scale bars: 200 μm. **i**, TEM image showing CD connected to the dorsal epithelia. Inset showing a magnification of CD connected to the dorsal epithelia. e, epithelia; bm, basement membrane; m, mesenchyme; sj, septate junction; l, lumen; ms, muscle. Scale bars: 5 μm. **j**, Tables summarize expression domains of selected *slc* genes in planarian protonephridia and rodent metanephros. Cartoons showing segmental organization of planarian protonephridia and rodent metanephros are on the left. Gray color in the tables indicates expression domain of *slc* in planarian protonephridia and rodent metanephros. Planarian *slc* sequence nomenclature (*e.g., slc1a-3*) does not reflect direct orthology to the mammalian counterparts. Abbreviations for segments of protonephridia are as follows: PT1, PT2, and PT3, segments of proximal tubule; DT1 and DT2, segments of distal tubule; CD, collecting duct. Abbreviations for segments of metanephros are as follows: S1, S2, and S3, segments of proximal tubule; DTL, descending thin limb; ATL, ascending thin limb; TAL, thick ascending limb; DCT, distal convoluted tubules; CNT, connecting tubule; CD, collecting duct. **k**, Fluorescent overlay of reabsorbed dextran with proximal tubule marker (AcTub). **l**, pH_i reporter assay using SNARF-5F-AM in *control(RNAi)* and *slc4a-6(RNAi)*.

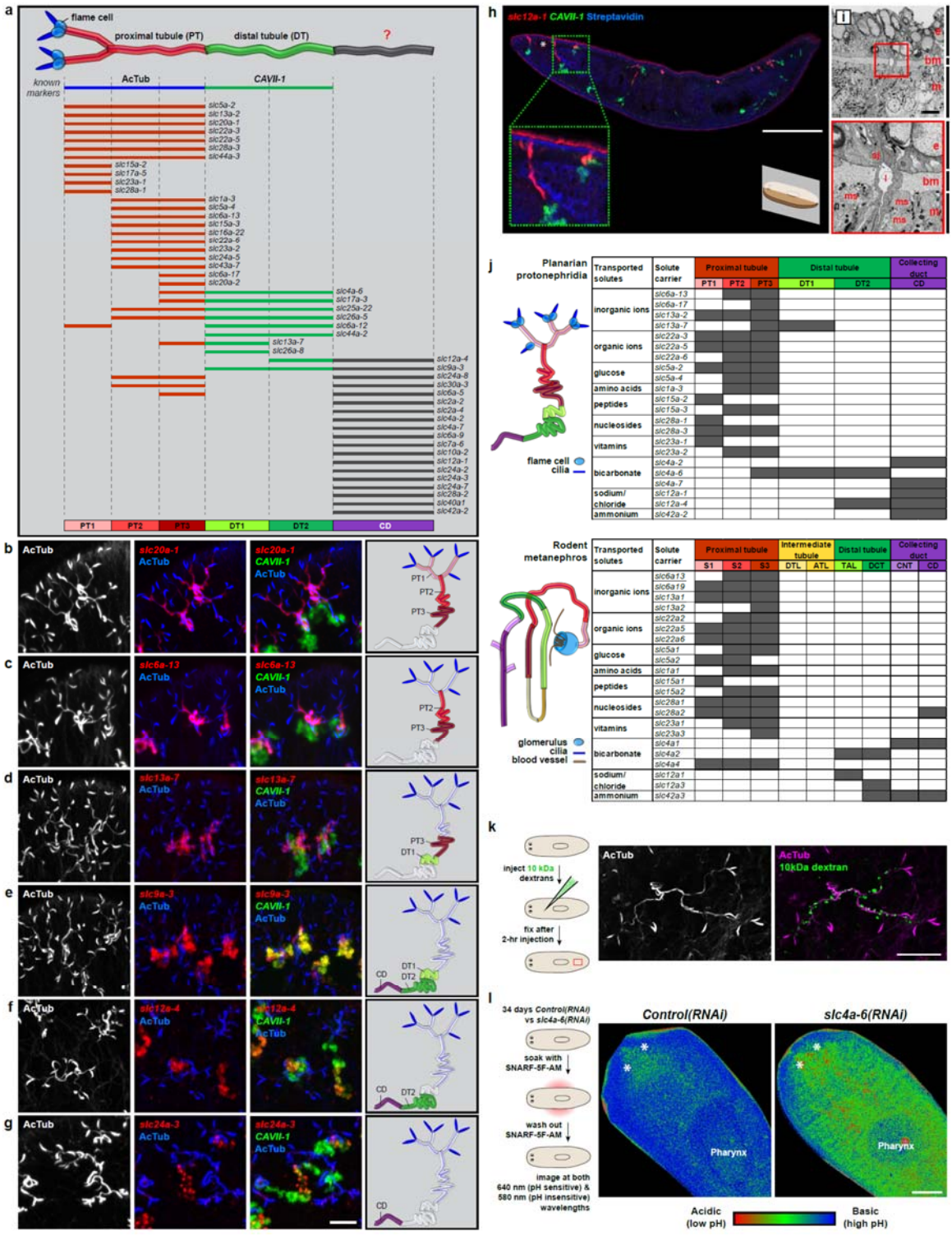
a
flame cell
proximal tubule (PT)
distal tubule (DT)
?
known markers
AcTub
CAVII-1
slc5a-2
slc13a-2
slc20a-1
slc22a-3
slc22a-5
slc28a-3
slc44a-3
slc15a-2
slc17a-5
slc23a-1
slc28a-1
slc1a-3
slc5a-4
slc6a-13
slc15a-3
slc16a-22
slc22a-6
slc23a-2
slc24a-5
slc43a-7
slc6a-17
slc20a-2
slc4a-6
slc17a-3
slc25a-22
slc26a-5
slc6a-12
slc44a-2
slc13a-7
slc26a-8
slc12a-4
slc9a-3
slc24a-8
slc30a-3
slc6a-5
slc2a-2
slc2a-4
slc4a-2
slc4a-7
slc6a-9
slc7a-6
slc10a-2
slc12a-1
slc24a-2
slc24a-3
slc24a-7
slc28a-2
slc40a1
slc42a-2
PT1
PT2
PT3
DT1
DT2
CD
b
AcTub
slc20a-1
AcTub
slc20a-1
CAVII-1
AcTub
PT1
PT2
PT3
c
AcTub
slc6a-13
AcTub
slc6a-13
CAVII-1
AcTub
PT2
PT3
d
AcTub
slc13a-7
AcTub
slc13a-7
CAVII-1
AcTub
PT3
DT1
e
AcTub
slc9a-3
AcTub
slc9a-3
CAVII-1
AcTub
CD
DT1
DT2
f
AcTub
slc12a-4
AcTub
slc12a-4
CAVII-1
AcTub
CD
DT2
g
AcTub
slc24a-3
AcTub
slc24a-3
CAVII-1
AcTub
CD
h
slc12a-1 CAVII-1 Streptavidin
i
e
bm
m
sj
i
ms
mv
j
Planarian protonephridia
flame cell cilia
Transported solutes
Solute carrier
Proximal tubule
PT1
PT2
PT3
Distal tubule
DT1
DT2
Collecting duct
CD
inorganic ions
slc6a-13
slc6a-17
slc13a-2
slc13a-7
organic ions
slc22a-3
slc22a-5
slc22a-6
glucose
slc5a-2
slc5a-4
amino acids
slc1a-3
peptides
slc15a-2
slc15a-3
nucleosides
slc28a-1
slc28a-3
vitamins
slc23a-1
slc23a-2
bicarbonate
slc4a-2
slc4a-6
slc4a-7
sodium/ chloride
slc12a-1
slc12a-4
ammonium
slc42a-2
Rodent metanephros
glomerulus
cilia
blood vessel
Transported solutes
Solute carrier
Proximal tubule
S1
S2
S3
Intermediate tubule
DTL
ATL
Distal tubule
TAL
DCT
Collecting duct
CNT
CD
inorganic ions
slc6a13
slc6a19
slc13a1
slc13a2
organic ions
slc22a2
slc22a5
slc22a6
glucose
slc5a1
slc5a2
amino acids
slc1a1
peptides
slc15a1
slc15a2
nucleosides
slc28a1
slc28a2
vitamins
slc23a1
slc23a3
bicarbonate
slc4a1
slc4a2
slc4a4
sodium/ chloride
slc12a1
slc12a3
ammonium
slc42a3
k
inject 10 kDa dextrans
fix after 2-hr injection
AcTub
AcTub
10kDa dextran
l
34 days Control(RNAi) vs slc4a-6(RNAi)
soak with SNARF-5F-AM
wash out SNARF-5F-AM
image at both 640 nm (pH sensitive) & 580 nm (pH insensitive) wavelengths
Control(RNAi)
slc4a-6(RNAi)
Pharynx
Pharynx
Acidic (low pH)
Basic (high pH)

Figure 3.5. Expression of *slc* genes in the proximal tubule. Fluorescent overlay of indicated gene (in red) with PT2 and PT3 marker (*slc6a-13*), DT marker (*CAVII-1*), and AcTub staining. Images are maximum projections of confocal Z-sections. Scale bars: 50 μm. A color-coded scheme of protonephridial tubule at the end of each panel showing expression domain of indicated gene.

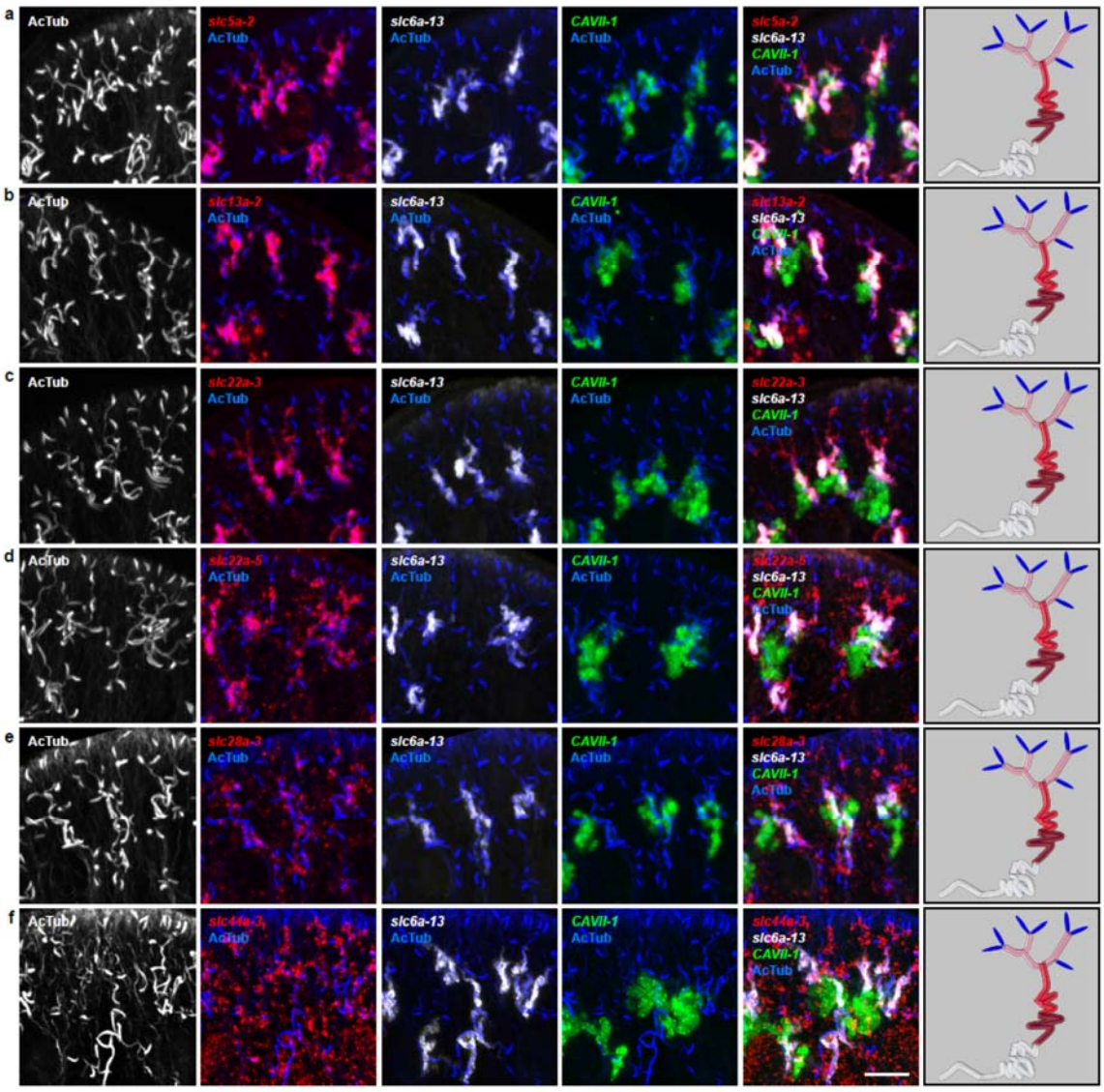
a
AcTub
slc5a-2
AcTub
slc6a-13
AcTub
CAVII-1
AcTub
slc5a-2
slc6a-13
CAVII-1
AcTub
b
AcTub
slc13a-2
AcTub
slc6a-13
AcTub
CAVII-1
AcTub
slc13a-2
slc6a-13
CAVII-1
AcTub
c
AcTub
slc22a-3
AcTub
slc6a-13
AcTub
CAVII-1
AcTub
slc22a-3
slc6a-13
CAVII-1
AcTub
d
AcTub
slc22a-5
AcTub
slc6a-13
AcTub
CAVII-1
AcTub
slc22a-5
slc6a-13
CAVII-1
AcTub
e
AcTub
slc28a-3
AcTub
slc6a-13
AcTub
CAVII-1
AcTub
slc28a-3
slc6a-13
CAVII-1
AcTub
f
AcTub
slc44a-3
AcTub
slc6a-13
AcTub
CAVII-1
AcTub
slc44a-3
slc6a-13
CAVII-1
AcTub

Figure 3.6. Expression of *slc* genes in the PT1 segment of the proximal tubule. **a**, Fluorescent overlay of indicated gene (in red) with PT1 and PT2 marker (*CUBN1*), PT2 and PT3 marker (*slc6a-13*), and AcTub staining. **b**, Fluorescent overlay of indicated gene (in red) with PT2 and PT3 marker (*slc6a-13*), DT marker (*CAVII-1*), and AcTub staining. Images are maximum projections of confocal Z-sections. Scale bars: 50 μm. A color-coded scheme of protonephridial tubule at the end of each panel showing expression domain of indicated gene.

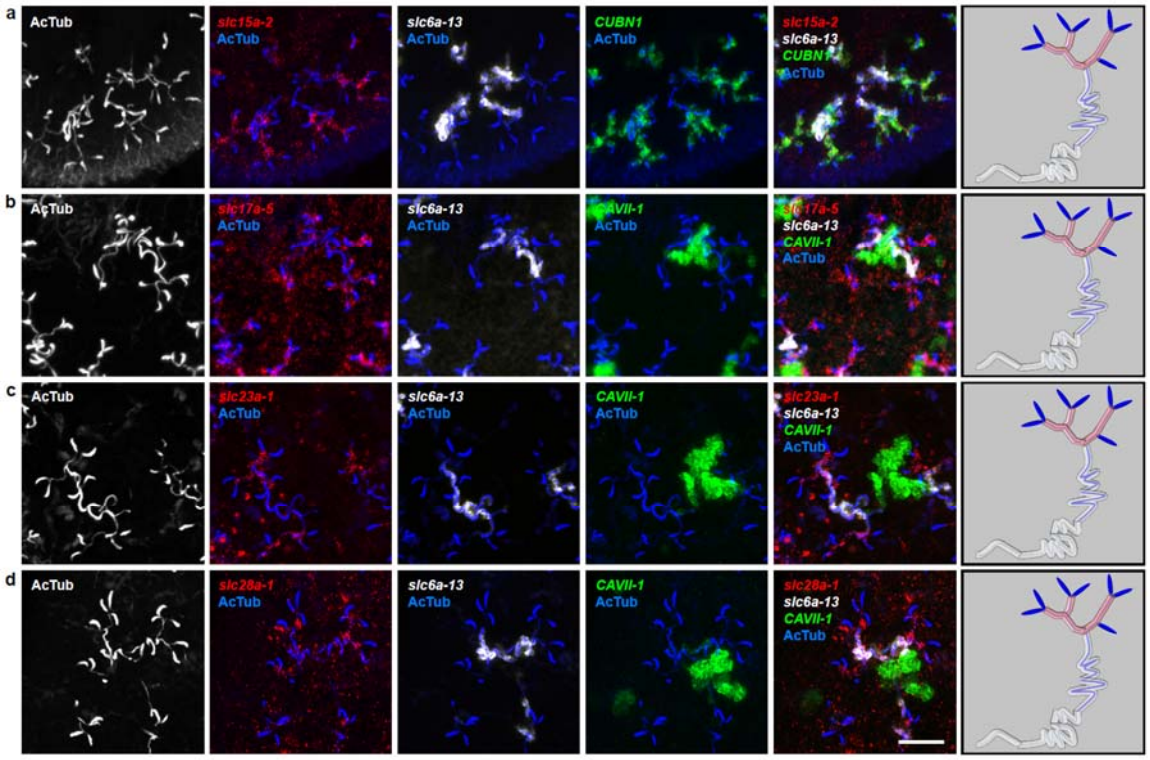
a
AcTub
slc15a-2
AcTub
slc6a-13
AcTub
CUBN1
AcTub
slc15a-2
slc6a-13
CUBN1
AcTub
b
AcTub
slc17a-5
AcTub
slc6a-13
AcTub
CAVII-1
AcTub
slc17a-5
slc6a-13
CAVII-1
AcTub
c
AcTub
slc23a-1
AcTub
slc6a-13
AcTub
CAVII-1
AcTub
slc23a-1
slc6a-13
CAVII-1
AcTub
d
AcTub
slc28a-1
AcTub
slc6a-13
AcTub
CAVII-1
AcTub
slc28a-1
slc6a-13
CAVII-1
AcTub

Figure 3.7. Expression of *slc* genes in PT2 and PT3 segments of the proximal tubule. Fluorescent overlay of indicated gene (in red) with PT2 and PT3 marker (*slc6a-13*), DT marker (*CAVII-1*), and AcTub staining. Images are maximum projections of confocal Z-sections. Scale bars: 50 μm. A color-coded scheme of protonephridial tubule at the end of each panel showing expression domain of indicated gene.

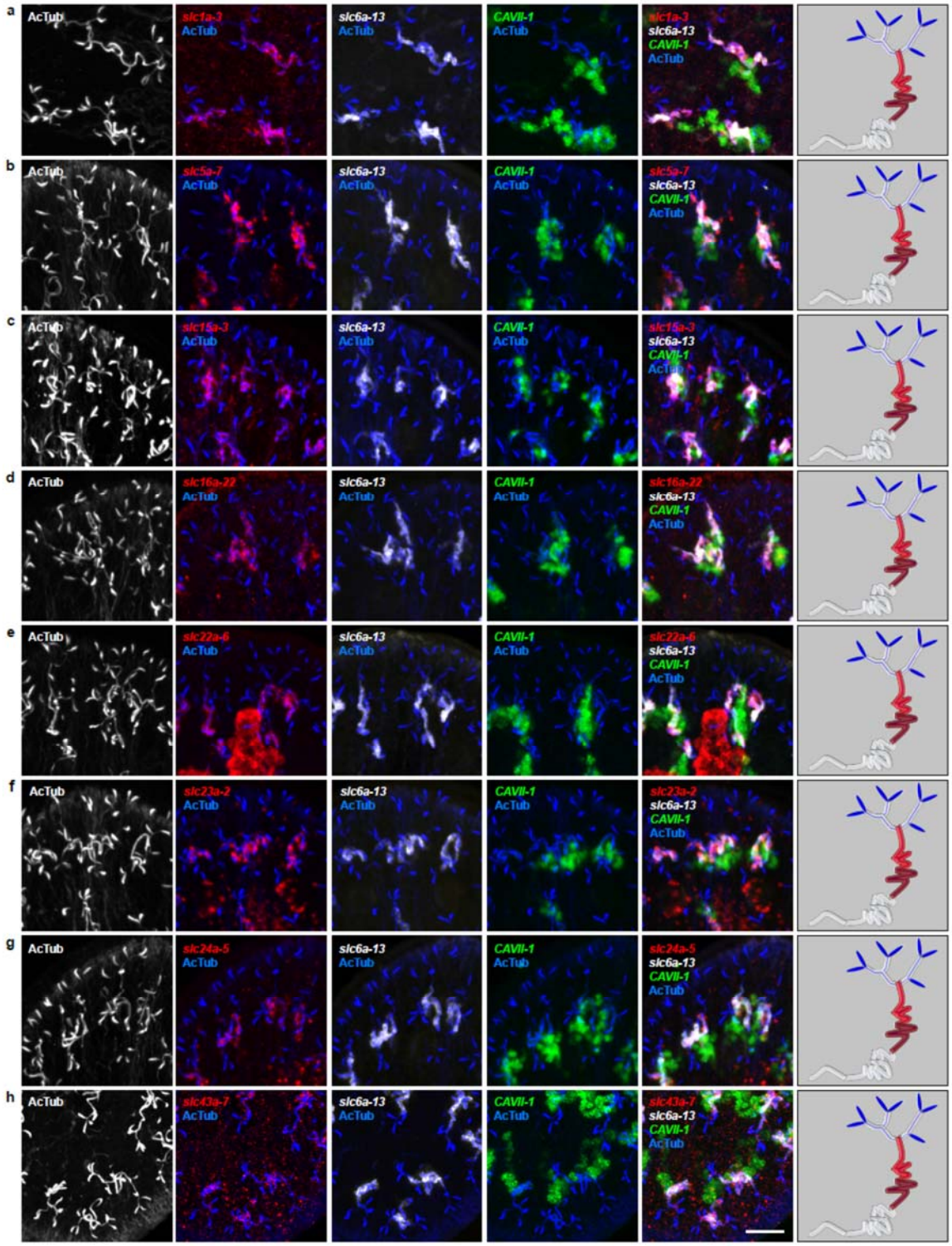
a
AcTub
slc1a-3
AcTub
slc6a-13
AcTub
CAVII-1
AcTub
slc1a-3
slc6a-13
CAVII-1
AcTub
b
AcTub
slc5a-7
AcTub
slc6a-13
AcTub
CAVII-1
AcTub
slc5a-7
slc6a-13
CAVII-1
AcTub
c
AcTub
slc15a-3
AcTub
slc6a-13
AcTub
CAVII-1
AcTub
slc15a-3
slc6a-13
CAVII-1
AcTub
d
AcTub
slc16a-22
AcTub
slc6a-13
AcTub
CAVII-1
AcTub
slc16a-22
slc6a-13
CAVII-1
AcTub
e
AcTub
slc22a-6
AcTub
slc6a-13
AcTub
CAVII-1
AcTub
slc22a-6
slc6a-13
CAVII-1
AcTub
f
AcTub
slc23a-2
AcTub
slc6a-13
AcTub
CAVII-1
AcTub
slc23a-2
slc6a-13
CAVII-1
AcTub
g
AcTub
slc24a-5
AcTub
slc6a-13
AcTub
CAVII-1
AcTub
slc24a-5
slc6a-13
CAVII-1
AcTub
h
AcTub
slc43a-7
AcTub
slc6a-13
AcTub
CAVII-1
AcTub
slc43a-7
slc6a-13
CAVII-1
AcTub

Figure 3.8. Expression of *slc* genes in the PT3 segment of the proximal tubule. Fluorescent overlay of indicated gene (in red) with PT2 and PT3 marker (*slc6a-13*), DT marker (*CAVII-1*), and AcTub staining. Images are maximum projections of confocal Z-sections. Scale bars: 50 μm. A color-coded scheme of protonephridial tubule at the end of each panel showing expression domain of indicated gene.

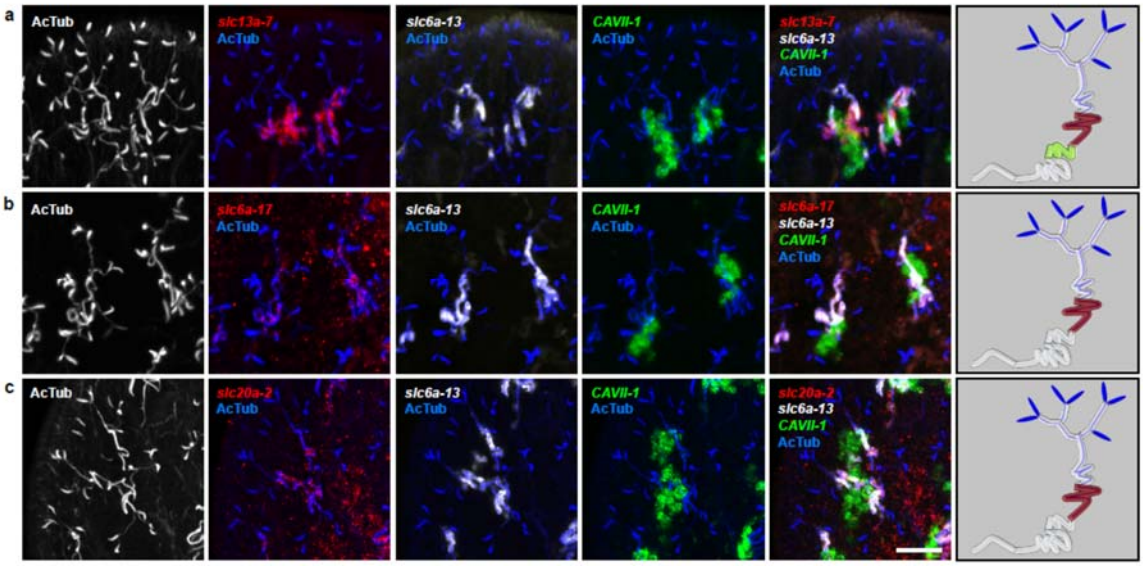
a
AcTub
slc13a-7
AcTub
slc6a-13
AcTub
CAVII-1
AcTub
slc13a-7
slc6a-13
CAVII-1
AcTub
b
AcTub
slc6a-17
AcTub
slc6a-13
AcTub
CAVII-1
AcTub
slc6a-17
slc6a-13
CAVII-1
AcTub
c
AcTub
slc20a-2
AcTub
slc6a-13
AcTub
CAVII-1
AcTub
slc20a-2
slc6a-13
CAVII-1
AcTub

Figure 3.9. Expression of *slc* genes in the distal tubule. Fluorescent overlay of indicated gene (in red) with PT marker (*slc6a-13* or *CUBN1*), DT marker (*CAVII-1*), or CD marker (*slc12a-1* or *slc24a-3*) together with AcTub staining. Images are maximum projections of confocal Z-sections. Scale bars: 50 μm. A color-coded scheme of protonephridial tubule at the end of each panel showing expression domain of indicated gene.

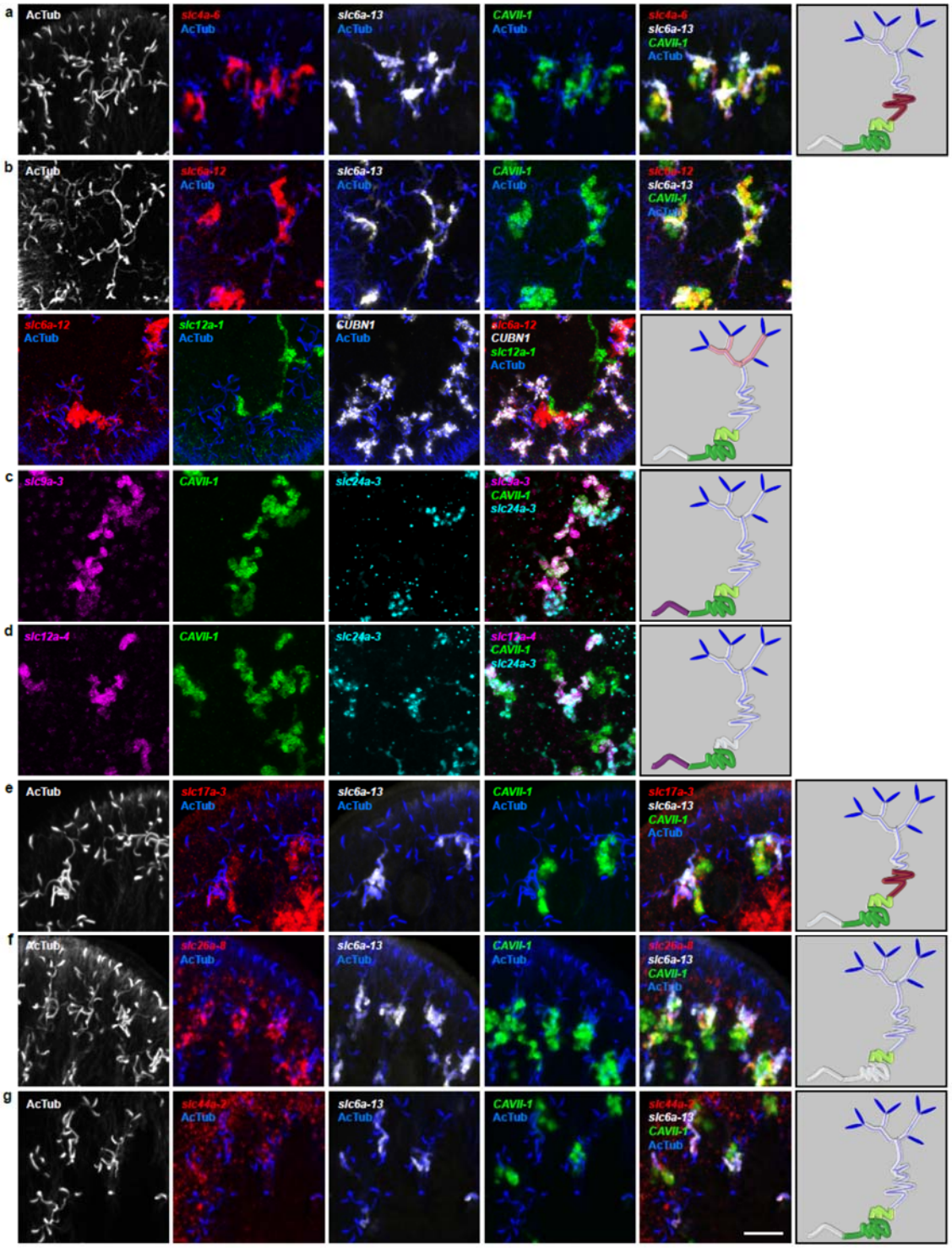
a
AcTub
slc4a-6
AcTub
slc6a-13
AcTub
CAVII-1
AcTub
slc4a-6
slc6a-13
CAVII-1
AcTub
b
AcTub
slc6a-12
AcTub
slc6a-13
AcTub
CAVII-1
AcTub
slc6a-12
slc6a-13
CAVII-1
AcTub
slc6a-12
AcTub
slc12a-1
AcTub
CUBN1
AcTub
slc6a-12
CUBN1
slc12a-1
AcTub
c
slc9a-3
CAVII-1
slc24a-3
slc9a-3
CAVII-1
slc24a-3
d
slc12a-4
CAVII-1
slc24a-3
slc12a-4
CAVII-1
slc24a-3
e
AcTub
slc17a-3
AcTub
slc6a-13
AcTub
CAVII-1
AcTub
slc17a-3
slc6a-13
CAVII-1
AcTub
f
AcTub
slc26a-8
AcTub
slc6a-13
AcTub
CAVII-1
AcTub
slc26a-8
slc6a-13
CAVII-1
AcTub
g
AcTub
slc44a-2
AcTub
slc6a-13
AcTub
CAVII-1
AcTub
slc44a-2
slc6a-13
CAVII-1
AcTub

Figure 3.10. Expression of *slc* genes in the collecting duct. Fluorescent overlay of indicated gene (in red) with PT2 and PT3 marker (*slc6a-13*), DT marker (*CAVII-1*), or CD marker (*slc24a-9*) together with AcTub staining. Images are maximum projections of confocal Z-sections. Scale bars: 50 μm. A color-coded scheme of protonephridial tubule at the end of each panel showing expression domain of indicated gene.

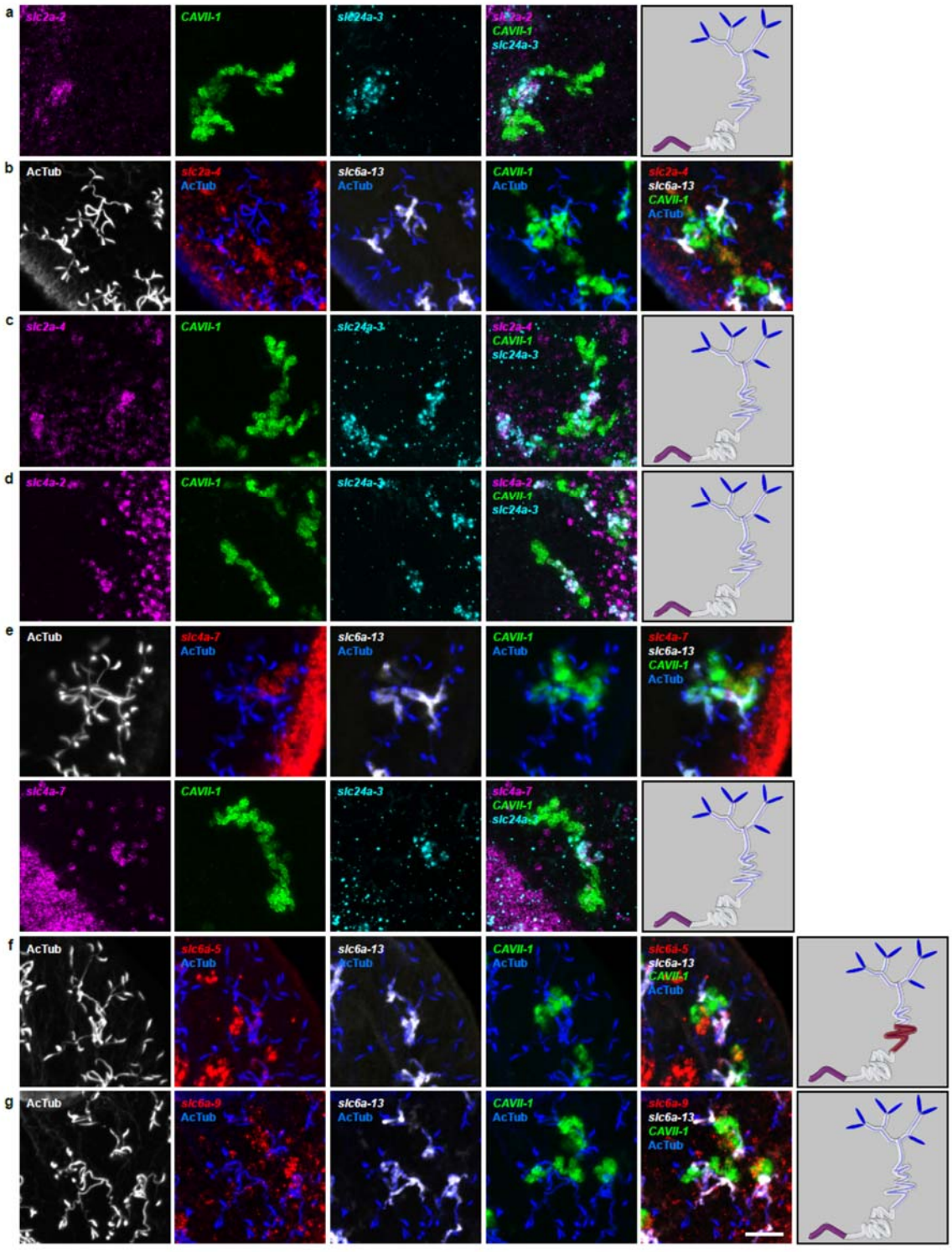
a
slc2a-2
CAVII-1
slc24a-3
slc2a-2
CAVII-1
slc24a-3
b
AcTub
slc2a-4
AcTub
slc6a-13
AcTub
CAVII-1
AcTub
slc2a-4
slc6a-13
CAVII-1
AcTub
c
slc2a-4
CAVII-1
slc24a-3
slc2a-4
CAVII-1
slc24a-3
d
slc4a-2
CAVII-1
slc24a-3
slc4a-2
CAVII-1
slc24a-3
e
AcTub
slc4a-7
AcTub
slc6a-13
AcTub
CAVII-1
AcTub
slc4a-7
slc6a-13
CAVII-1
AcTub
slc4a-7
CAVII-1
slc24a-3
slc4a-7
CAVII-1
slc24a-3
f
AcTub
slc6a-5
AcTub
slc6a-13
AcTub
CAVII-1
AcTub
slc6a-5
slc6a-13
CAVII-1
AcTub
g
AcTub
slc6a-9
AcTub
slc6a-13
AcTub
CAVII-1
AcTub
slc6a-9
slc6a-13
CAVII-1
AcTub

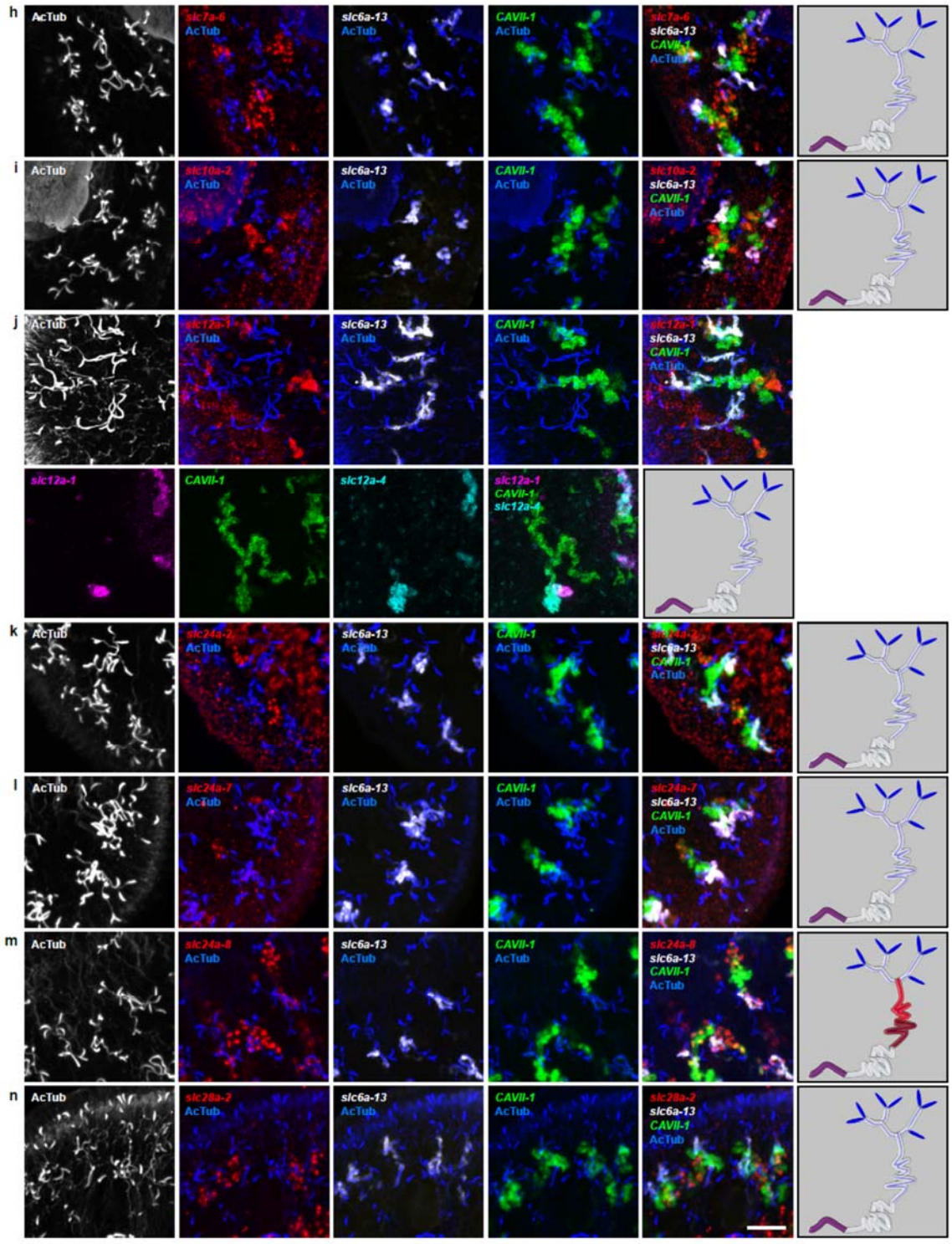

Figure 3.10. Continued

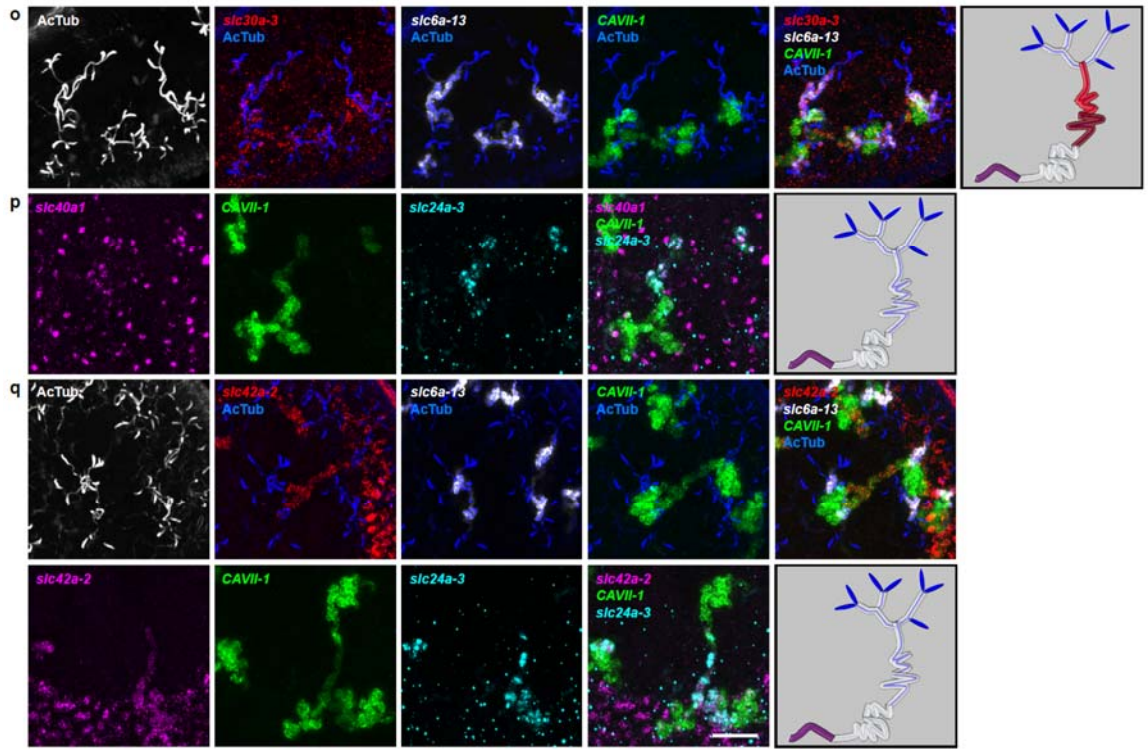

Figure 3.10. Continued

Figure 3.11. Expression of *slc* genes that weakly express in both proximal and distal tubules. Fluorescent overlay of indicated gene (in red) with PT2 and PT3 marker (*slc6a-13*), DT marker (*CAVII-1*), and AcTub staining. Images are maximum projections of confocal Z-sections. Scale bars: 50 μm. A color-coded scheme of protonephridial tubule at the end of each panel showing expression domain of indicated gene.

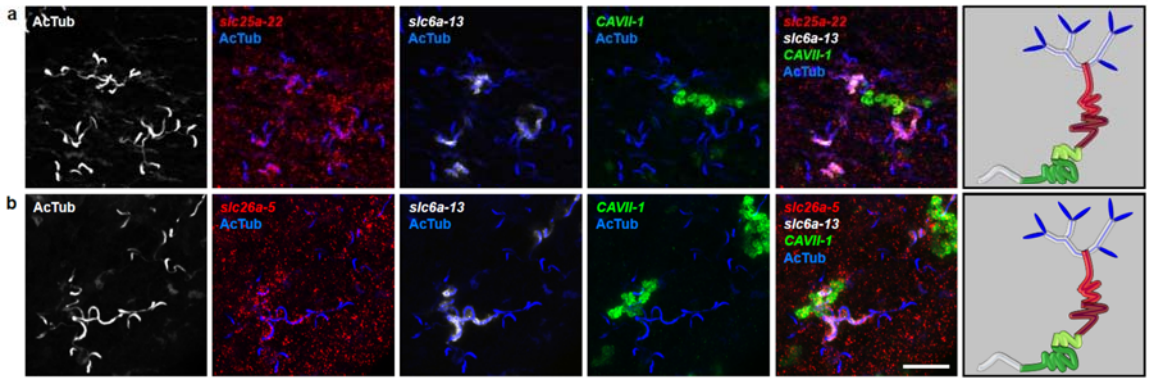
a
AcTub
slc25a-22
AcTub
slc6a-13
AcTub
CAVII-1
AcTub
slc25a-22
slc6a-13
CAVII-1
AcTub
b
AcTub
slc26a-5
AcTub
slc6a-13
AcTub
CAVII-1
AcTub
slc26a-5
slc6a-13
CAVII-1
AcTub

comparisons with the nephron. Constructing a similar map of slc expression in the rodent metanephros based on published data (Fig. 3.4j, bottom; Appendix C) revealed a striking parallel: Not only is the sequence of slc family expression very similar along the filtrate flow axis, but almost all nephron segments have clearly identifiable homologous segments in protonephridia. In vertebrates, the PT is responsible for reabsorption of more than 70% of filtered solutes from the primary urine, including inorganic/organic ions and vital nutrients (glucose, amino acids, and vitamins). The homologous *slc* expression of planarian PT1-3 and the preferential labeling of PT1-2 by injected dextran (Fig. 3.4k) provide strong evidence that the proximal protonephridial segments are likewise primarily responsible for the recovery of filtered substances. The DT plays an important role in acid-base homeostasis by reabsorbing bicarbonates and secreting protons into the urine (Carraro-Lacroix and Malnic, 2010). The corresponding expression of bicarbonate (*e.g.*, *Smed-slc4a-6*, Fig. 3.9) or proton transporters (*e.g.*, Na^+/H^+ exchanger *Smed-slc9a-3*, Fig. 3.4e) in DT1 and DT2 suggests a similar function of these protonephridial segments. Consistently, the RNAi-mediated knockdown of *slc4a-6* caused a measurable acidification of the intercellular milieu (Fig. 3.4l), thus demonstrating functionally the conserved role of DT1-2 in planarian pH homeostasis. Finally, the vertebrate collecting duct (CD) comprises distinct cortical and medullary segments and mediates the bulk of water recovery/urine concentration (Nielsen et al., 2002). The shared expression of the bicarbonate transporter *Smed-slc4a-7* and the ammonia transporter *Smed-slc42a-2* in the terminal segment (Fig. 3.4j) support a basal homology between the CD and the corresponding protonephridial segment, which is why we likewise adapt the vertebrate nomenclature. However, the large number of additional *slc* genes expressed in the protonephridial CD (Fig. 3.4a) and lack of

aquaporin expression (not shown) suggest divergent functions. The only nephron segment for which our analysis did not identify a protonephridial homologue was the intermediate tubule (IT). In terrestrial vertebrates, IT and CD have tightly linked functions in water conservation, whereby urea secretion by the IT establishes high extracellular solute concentrations that aid in water reabsorption from the CD (Pannabecker, 2012). As freshwater animals, planarian protonephridia have to clear, rather than conserve water, providing a compelling rationale for why specifically IT and CD are divergent. Such functional diversity of IT/CD segments is also observed in the pronephric kidneys of freshwater vertebrates, such as zebrafish (Wingert and Davidson, 2008). Together, our analysis reveals a striking structural and functional homology between vertebrate nephron and planarian protonephridia.

Recapitulation of Podocyte Slit-Diaphragm Pathologies in Flame Cells

We next asked whether the homologies between the nephrons and protonephridia extend to common pathologies. The striking structural similarities between the ultrafiltration sites in the two systems, podocyte foot processes (Pavenstadt et al., 2003) and flame cell filtration barriers (Fig. 3.1b), could reflect a requirement for common components. In humans, mutations in the large IgG-repeat transmembrane proteins *NPHS1* and *NEPH1* cause slit diaphragm loss and foot process effacement, resulting in proteinuria and edema (Donoviel et al., 2001; Kestila et al., 1998). Systematic sequence homology searches of the *S. mediterranea* genome identified 7 *NPHS1* homologs and 3 *NEPH* homologs (Fig. 3.12). Interestingly, *Smed-NPHS1-6* and *Smed-NEPH-3* were expressed

Figure 3.12. Slit-diaphragm components in the planarian *Schmidtea mediterranea*. a, Cartoon showing the glomerular filtration barrier. Top: A schematic view of the podocyte. The podocyte wraps around the capillary wall on the outer surface of the glomerular basement membrane with its extended interdigitating foot processes. Podocyte foot processes are then bridged by a slit diaphragm. Middle: A close-up view of the glomerular filtration barrier consisting of three components: porous endothelium, glomerular basement membrane, and podocyte foot processes with the interposed slit diaphragm. The endothelial pores are not bridged by a diaphragm. Bottom: Schematic drawing of the molecular equipment of a slit diaphragm. NPHS1 undergoes homophilic interaction on neighboring podocyte foot processes. The intercellular junction also contains the adhesion molecule NEPH-1. **b,** Homology analysis of the planarian homologs of NPHS1 and NEPH. Domains predicted by SMART for planarian and human proteins. Best reciprocal BLAST hits in human, *C. elegans*, and fly refseq protein database. **c,** Whole-mount expression patterns of NPHS1 and NEPH by *in situ* hybridization. Scale bars: 500 μm.

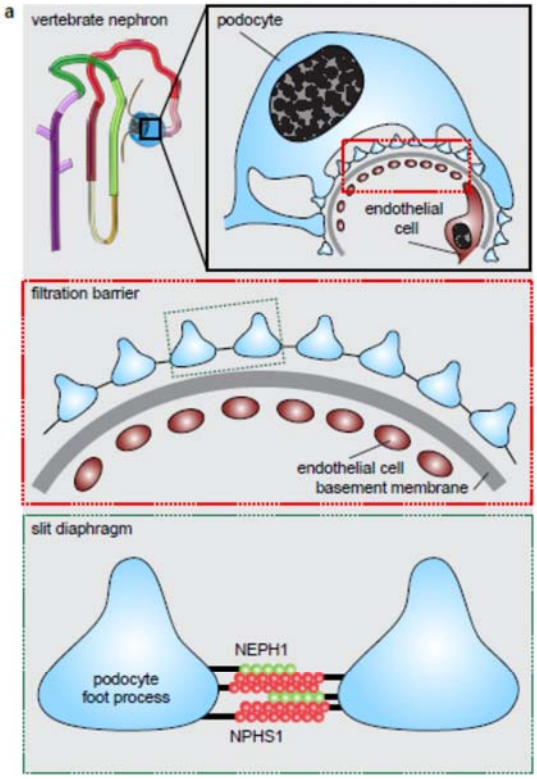

b

S. med	vs.	Best hit	E value
NPHS1-1	*H.sap.*	NPHS1	3E-18
	C.ele.	SYG-2	2E-26
	D.mel.	hbs	2E-65
NPHS1-2	*H.sap.*	NPHS1	4E-35
	C.ele.	SYG-1	1E-14
	D.mel.	sns	2E-53
NPHS1-3	*H.sap.*	NPHS1	1E-31
	C.ele.	SYG-1	8E-10
	D.mel.	hbs	3E-49
NPHS1-4	*H.sap.*	NPHS1	1E-30
	C.ele.	SYG-1	2E-10
	D.mel.	hbs	8E-44
NPHS1-5	*H.sap.*	NPHS1	3E-24
	C.ele.	SYG-1	3E-13
	D.mel.	sns	8E-29
NPHS1-6	*H.sap.*	NPHS1	3E-60
	C.ele.	SYG-2	8E-35
	D.mel.	hbs	6E-70
NPHS1-7	*H.sap.*	NPHS1	2E-13
	C.ele.	SYG-2	1E-06
	D.mel.	hbs	5E-10
NEPH-1	*H.sap.*	NEPH1	5E-17
	C.ele.	SYG-1	3E-09
	D.mel.	srt	2E-26
NEPH-2	*H.sap.*	NEPH2	3E-40
	C.ele.	SYG-1	3E-33
	D.mel.	duf	1E-43
NEPH-3	*H.sap.*	NEPH2	3E-37
	C.ele.	SYG-1	1E-28
	D.mel.	duf	5E-29

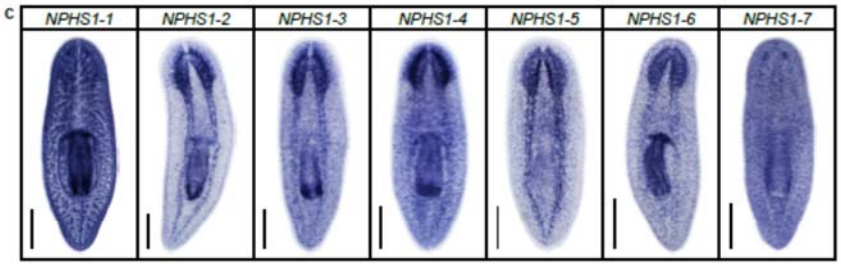

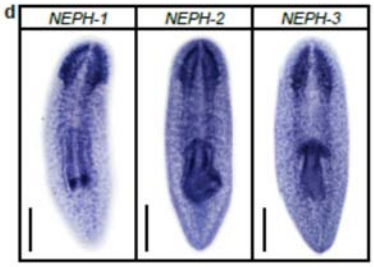

in flame cells (Fig. 3.13a-b) and RNAi of both genes produced strong bloating and partial clearing of body pigmentation (Fig. 3.13c). Both phenotypes have previously been identified as characteristic hallmarks of tissue edema (Rink et al., 2011), thus providing a strong indication that the genes are required for the function of the planarian excretory system. Since flame cell numbers appeared normal in both intact and regenerating animals (Fig. 3.14), we examined the ultrastructure of the filtration diaphragm in *NPHS1-6* and *NEPH-3(RNAi)* planarians. Wild-type flame cells display slit-shaped 35-40 nm wide fenestrae that form between 90-150nm wide foot processes (Fig. 3.1b and 3.13d). Under knockdown of either *NPHS1-6* or *NEPH-3*, the filtration diaphragm was completely absent and the foot processes underwent apparent effacement in both intact (Fig. 3.13d, Supplementary movies 2-3) and regenerating animals (Fig. 3.15) animals. Our dextran injection assay confirmed the loss of ultrafiltration capability in *NPHS1-6(RNAi)* planarians, which displayed equal uptake of small and large molecular tracers in the proximal tubule (Fig. 3.13e-f). Together, these data demonstrate that the functional homology between planarian flame cells and vertebrate podocytes extends to molecular components and thus common pathologies.

Cyst Formation in Planarian Proximal Tubules

Encouraged by these results, we extended our analysis of conserved pathologies to the protonephridial tubules. The most common class of human inherited disorders affecting the nephron are the cystic kidney diseases (CKDs). We assembled a small library of putative planarian orthologues of human CKD genes (Appendix D). This list contained nephrocystins, causative genes of nephronophthisis (NPHP), one of the most frequent

Figure 3.13. Vertebrate slit-diaphragm components are expressed in planarian flame cells and are required for the maintenance of their filtration diaphragm. a, Whole-mount expression patterns of indicated marker genes by *in situ* hybridization (NBT/BCIP development). Scale bars: 500 μm. **b,** Fluorescent overlay of indicated gene (red) with flame cell marker *EGFR-5* and AcTub staining. Images are maximum projections of confocal Z-sections. Scale bars: 50 μm. **c**, Live images showing edema in intact *NPHS1-6(RNAi)* and *NEPH-3(RNAi)* animals. Scale bars: 500 μm. **d**, TEM images showing cross section through a flame cell in intact *Control(RNAi)*, *NPHS1-6(RNAi)* and *NEPH-3(RNAi)* animals. Inset showing a high magnification of filtration diaphragm. Scale bar: 1 μm. **e-f**, Ultrafiltration assay assessing ultrafiltration capacity in *NPHS1-6(RNAi)* animals. (e) Representative images showing dextran uptake in the animals that co-injected with 10 kDa and 500 kDa fluorescently labeled dextran. Scale bar: 50 μm. (f) Quantification of small and large dextran uptake.

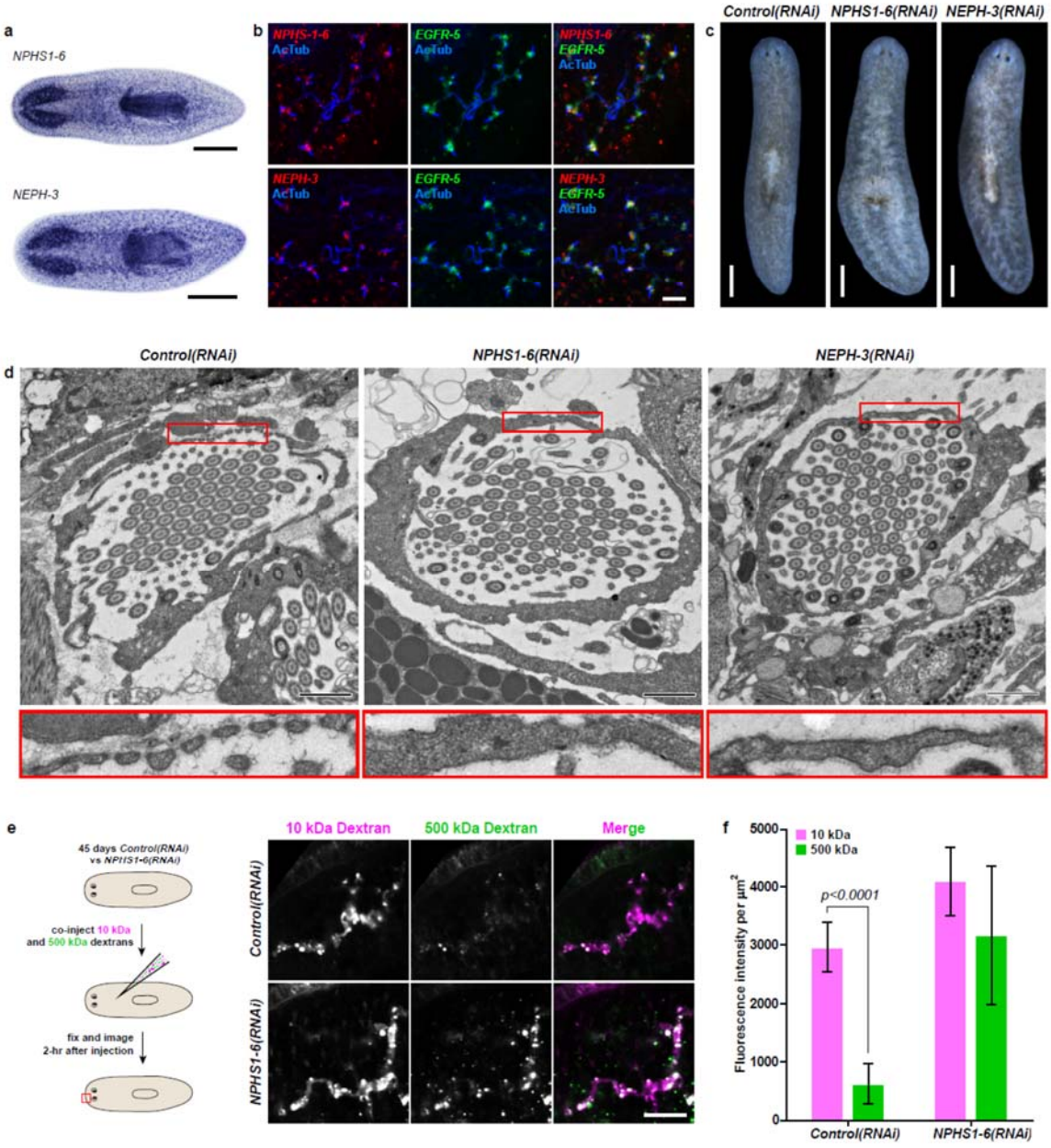
a
NPHS1-6
NEPH-3
b
NPHS1-6 AcTub
EGFR-5 AcTub
NPHS1-6 EGFR-5 AcTub
NEPH-3 AcTub
EGFR-5 AcTub
NEPH-3 EGFR-5 AcTub
c
Control(RNAi)
NPHS1-6(RNAi)
NEPH-3(RNAi)
d
Control(RNAi)
NPHS1-6(RNAi)
NEPH-3(RNAi)
e
45 days Control(RNAi) vs NPHS1-6(RNAi)
co-inject 10 kDa and 500 kDa dextrans
fix and image 2-hr after injection
10 kDa Dextran
500 kDa Dextran
Merge
Control(RNAi)
NPHS1-6(RNAi)
f
10 kDa
500 kDa
p<0.0001
Fluorescence intensity per µm²
5000
4000
3000
2000
1000
0
Control(RNAi)
NPHS1-6(RNAi)

Figure 3.14. *NPHS1-6* is not required for flame cell viability during normal homeostasis as well as regeneration. a-b, Fluorescent overlay of flame cell markers *(CXCRL* and *EGFR-5)* with AcTub staining in intact (a) and regenerating (b) *Control(RNAi)* and *NPHS1-6(RNAi)*. Images are maximum projections of confocal Z-sections. Scale bars: 50 μm.

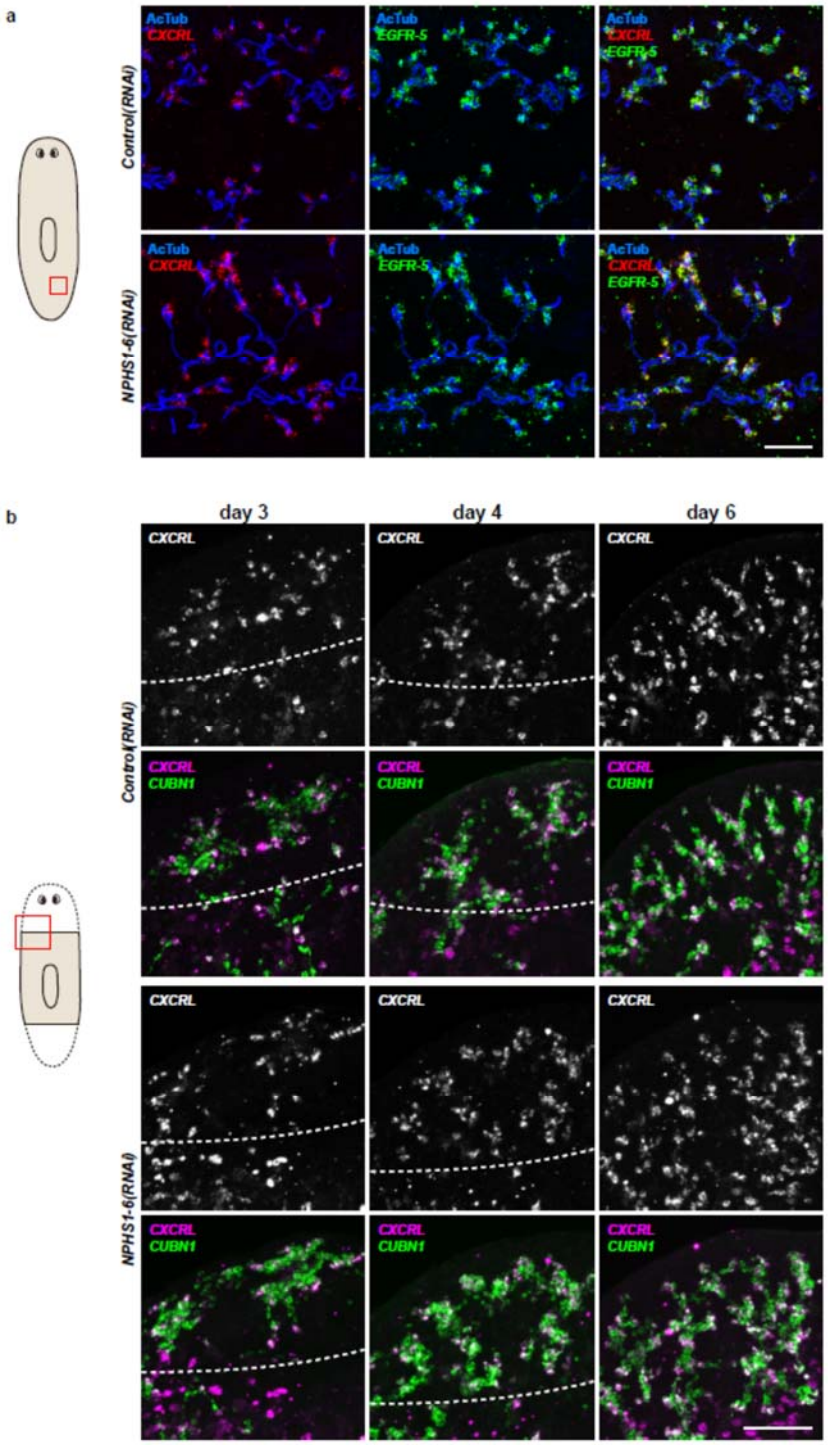
a
AcTub
CXCRL
AcTub
EGFR-5
AcTub
CXCRL
EGFR-5
Control(RNAi)
AcTub
CXCRL
AcTub
EGFR-5
AcTub
CXCRL
EGFR-5
NPHS1-6(RNAi)
b
day 3
day 4
day 6
CXCRL
CXCRL
CXCRL
CXCRL
CUBN1
CXCRL
CUBN1
CXCRL
CUBN1
Control(RNAi)
CXCRL
CXCRL
CXCRL
CXCRL
CUBN1
CXCRL
CUBN1
CXCRL
CUBN1
NPHS1-6(RNAi)

Figure 3.15. *NPHS1-6* is required for *de novo* formation of filtration diaphragm during regeneneration. TEM images showing cross section through a flame cell in regenerating *Control(RNAi)* and *NPHS1-6(RNAi)* animals. Inset showing a high magnification of filtration diaphragm. Scale bar: 1 μm.

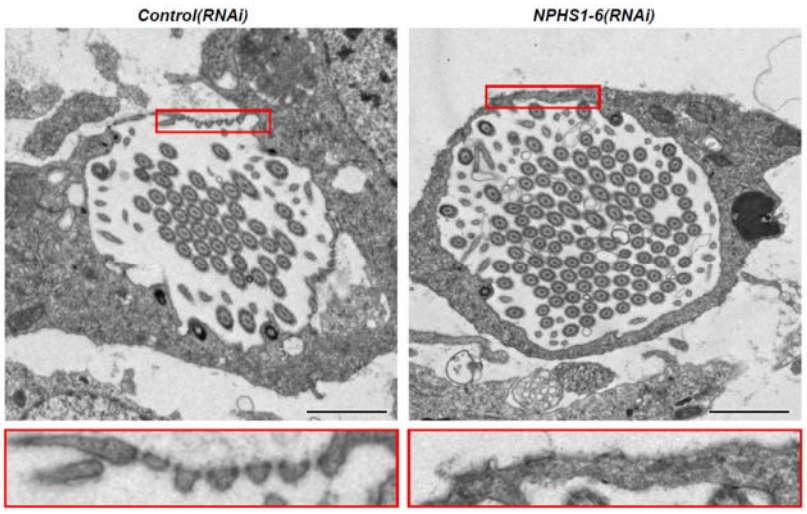
Control(RNAi)
NPHS1-6(RNAi)

genetic causes of chronic renal failure in children and young adults (Hildebrandt and Otto, 2000; Salomon et al., 2009). The *S. mediterranea* genome harbors homologs to all 9 human NPHPs, except for NPHP2 and NPHP3 (Fig. 3.16). RNAi-screening of the library revealed strong edema formation in *Smed-NPHP5*, *Smed-NPHP6*, and *Smed-NPHP8* knockdown animals (Fig. 3.17a), suggestive of a protonephridial function of these genes. Consistently, we detected severe structural alterations of protonephridial tubules in *NPHP(RNAi)* animals, particularly of the proximal segment. Instead of the fine terminal ramifications of PTs in controls, RNAi animals presented with striking clump-like accumulations of proximal marker expressing cells (Fig. 3.17a-b, Supplementary movie 4-5). High resolution imaging confirmed the presence of abnormally high numbers of densely packed proximal tubule cells (Fig. 3.18a). The protonephridial lumen was severely disorganized within such aggregates (Fig. 3.17c). Instead of strong and continuous luminal labeling throughout the coiled PT segments of controls, labeling was weak and fragmented. The weak single-line labeling outside of aggregates (Fig. 3.17c) and the much weaker cilia staining (AcTub) in *NPHP(RNAi)* animals (Fig. 3.17a) suggested general lumen defects. EM images revealed frequent basal body mislocalizations to nonluminal membrane domains and cell intrusions into the lumen, which both indicate a loss of normal tubular cell polarity (Fig. 3.19). Overall, the accumulation of morphologically abnormal tubule cells and concomitant loss of luminal connectivity present striking morphological parallels to the NPHP loss-of-function phenotype in humans, suggesting that planarian protonephridia can develop cysts.

Figure 3.16. nephrocytins in the planarian *Schmidtea mediterranea*. **a**, Homology analysis of planarian nephrocystins. Domains predicted by SMART for planarian and human proteins. Best reciprocal BLAST hits in human, *C. elegans*, and fly refseq protein database. **b**, Whole-mount expression patterns of genes encoding nephrocystins by *in situ* hybridization. Scale bars: 500 μm.

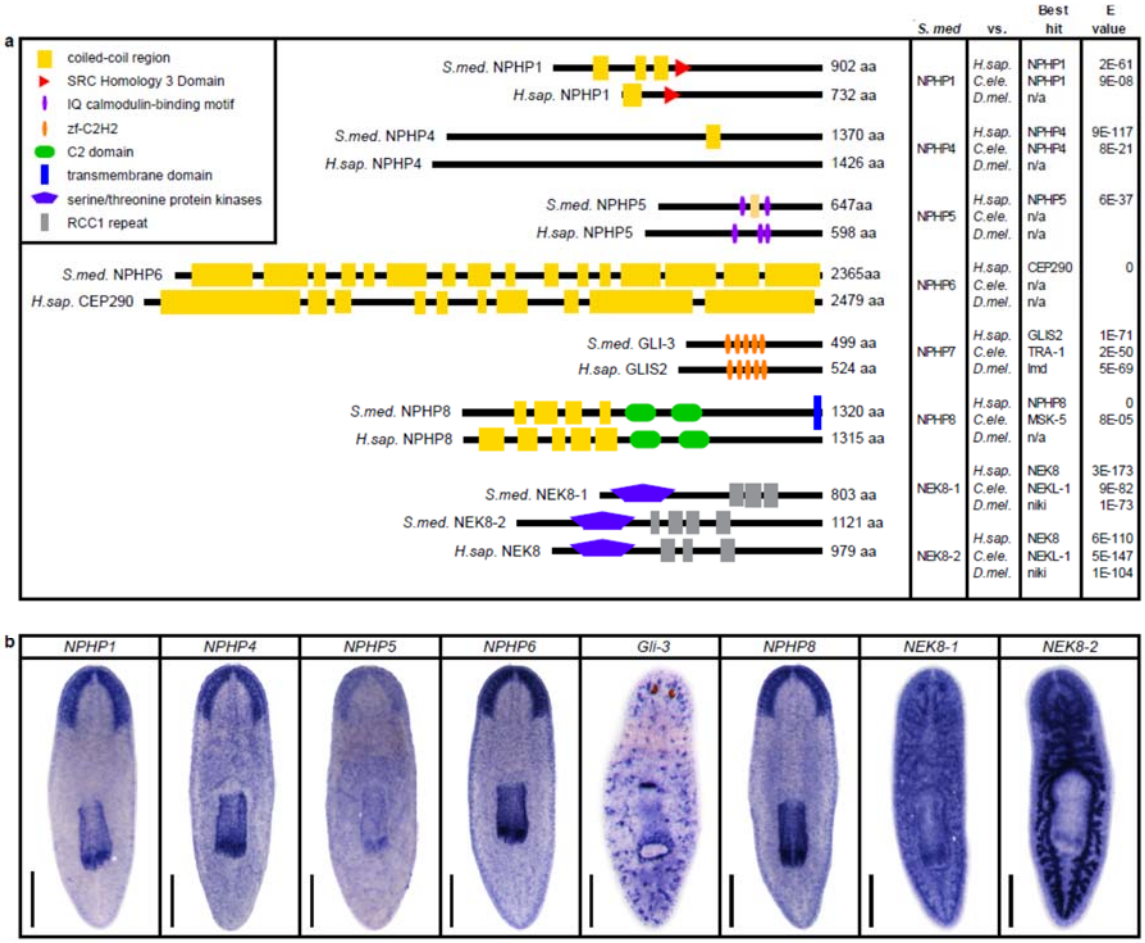
a
coiled-coil region
SRC Homology 3 Domain
IQ calmodulin-binding motif
zf-C2H2
C2 domain
transmembrane domain
serine/threonine protein kinases
RCC1 repeat
S.med. NPHP1 902 aa
H.sap. NPHP1 732 aa
S.med. NPHP4 1370 aa
H.sap. NPHP4 1426 aa
S.med. NPHP5 647aa
H.sap. NPHP5 598 aa
S.med. NPHP6 2365aa
H.sap. CEP290 2479 aa
S.med. GLI-3 499 aa
H.sap. GLIS2 524 aa
S.med. NPHP8 1320 aa
H.sap. NPHP8 1315 aa
S.med. NEK8-1 803 aa
S.med. NEK8-2 1121 aa
H.sap. NEK8 979 aa
S. med
vs.
Best hit
E value
NPHP1
H.sap. NPHP1 2E-61
C.ele. NPHP1 9E-08
D.mel. n/a
NPHP4
H.sap. NPHP4 9E-117
C.ele. NPHP4 8E-21
D.mel. n/a
NPHP5
H.sap. NPHP5 6E-37
C.ele. n/a
D.mel. n/a
NPHP6
H.sap. CEP290 0
C.ele. n/a
D.mel. n/a
NPHP7
H.sap. GLIS2 1E-71
C.ele. TRA-1 2E-50
D.mel. lmd 5E-69
NPHP8
H.sap. NPHP8 0
C.ele. MSK-5 8E-05
D.mel. n/a
NEK8-1
H.sap. NEK8 3E-173
C.ele. NEKL-1 9E-82
D.mel. niki 1E-73
NEK8-2
H.sap. NEK8 6E-110
C.ele. NEKL-1 5E-147
D.mel. niki 1E-104
b
NPHP1
NPHP4
NPHP5
NPHP6
Gli-3
NPHP8
NEK8-1
NEK8-2

Figure 3.17. Downregulation of nephrocystin members leads to the formation of cyst-like structure in protonephridia. **a**, Protonephridial defects in *NPHP5(RNAi)*, *NPHP6(RNAi)*, and *NPHP8(RNAi)* animals. Top panel: live images showing edema in intact RNAi animals. Scale bars: 500 μm; middle panel: monochrome showing AcTub staining; bottom panel: fluorescent overlay of AcTub staining with PT2 and PT3 marker (*slc6a-13*) and DT marker (*slc6a-12*). Scale bars: 50 μm. **b**, 3D rendering images showing normal tubule and cystic-like tubule in *Control(RNAi)* and *NPHP8(RNAi)* animals, respectively. 3D rendering was performed in IMARIS. Scale bars: 50 μm. **c,** Dilated lumen in enlarged protonephridial tubule. Fluorescent overlay of PT2 and PT3 marker *slc6a-13* and lumen marker in intact *Control(RNAi)* and *NPHP8(RNAi)* animals. Scale bars: 50 μm. Images in (a) and (c) are maximum projections of confocal Z-sections.

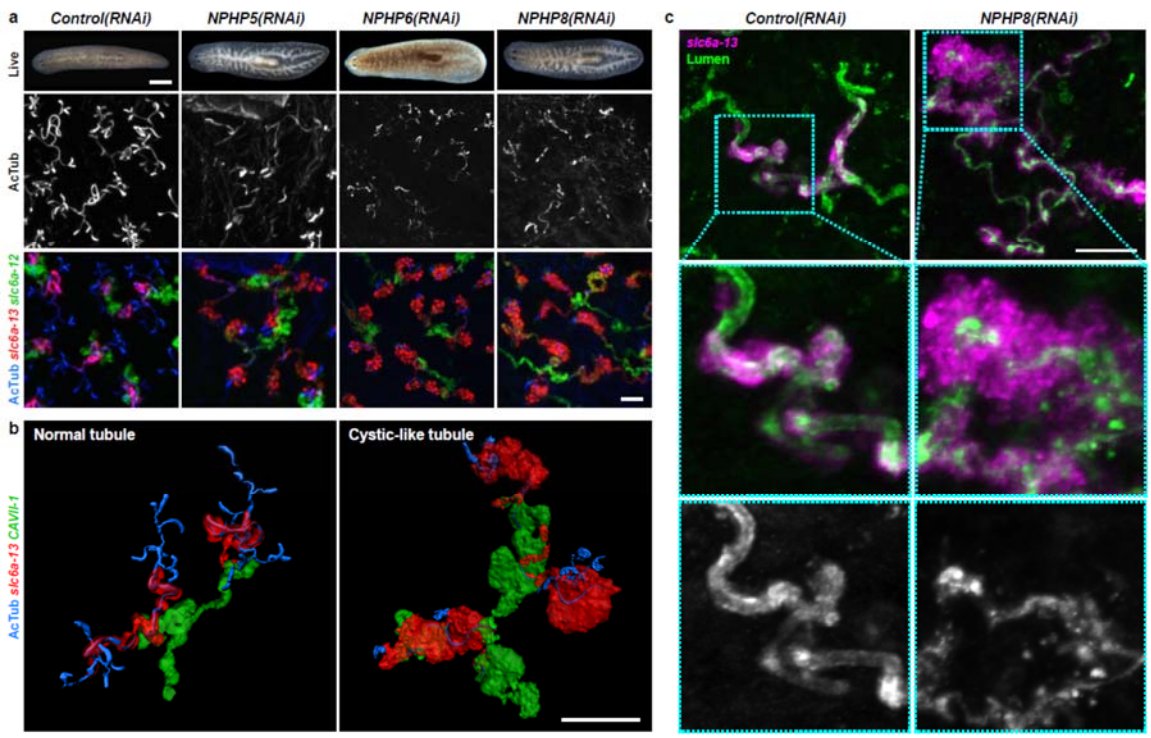
a
Control(RNAi)
NPHP5(RNAi)
NPHP6(RNAi)
NPHP8(RNAi)
Live
AcTub
AcTub slc6a-13 slc6a-12
b
Normal tubule
Cystic-like tubule
AcTub slc6a-13 CAVII-1
c
Control(RNAi)
NPHP8(RNAi)
slc6a-13
Lumen

Figure 3.18. Abnormal tubular enlargement in *NPHP8(RNAi)* animals. **a**, Fluorescent overlay of lumen marker with PT2 and PT3 marker *slc6a-13* and nuclei (DAPI) in *Control(RNAi)* and *NPHP8(RNAi)* animals. Scale bars: 25 μm. **a**, Fluorescent overlay of PT marker (*slc6a-13*) and DT marker (*CAVII-1*) in intact *Control(RNAi)* and *NPHP8(RNAi)* animals. Images are maximum projections of confocal Z-sections. Scale bars: 50 μm.

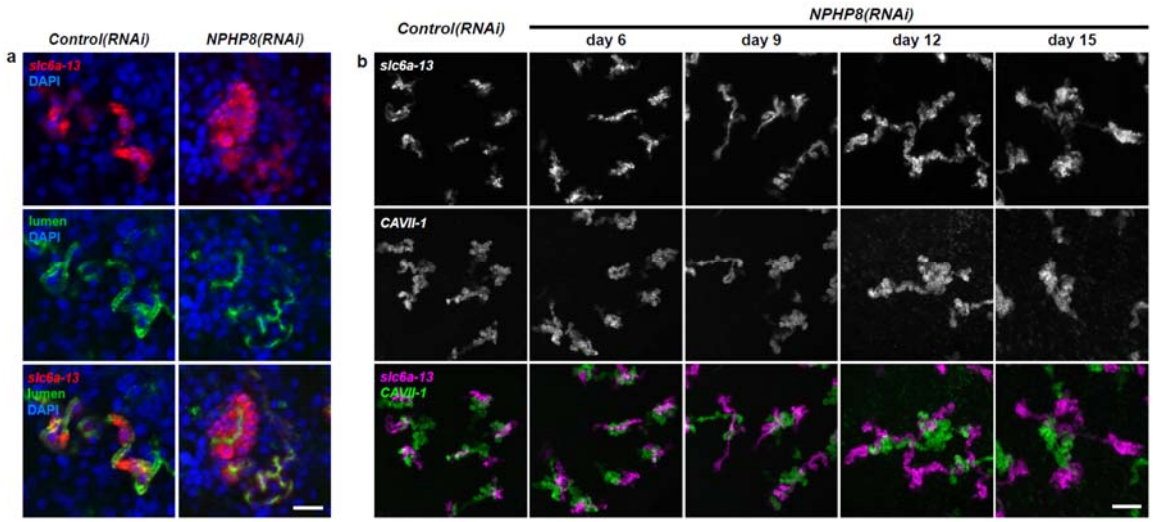
a
Control(RNAi)
NPHP8(RNAi)
slc6a-13
DAPI
lumen
DAPI
slc6a-13
lumen
DAPI
b
Control(RNAi)
NPHP8(RNAi)
day 6
day 9
day 12
day 15
slc6a-13
CAVII-1
slc6a-13
CAVII-1

Figure 3.19. Ultrastructure of the proximal tubule in *NPHP(RNAi)* animals. TEM images showing cross section through a tubule of protonephridia in indicated RNAi animals. Inset in red box showing abnormal localized basal body in indicated RNAi animals. Inset in green box showing ultrastructure of cilia. c, cilia; n, nucleus; bb, basal body; sj, septate junction; l, lumen.

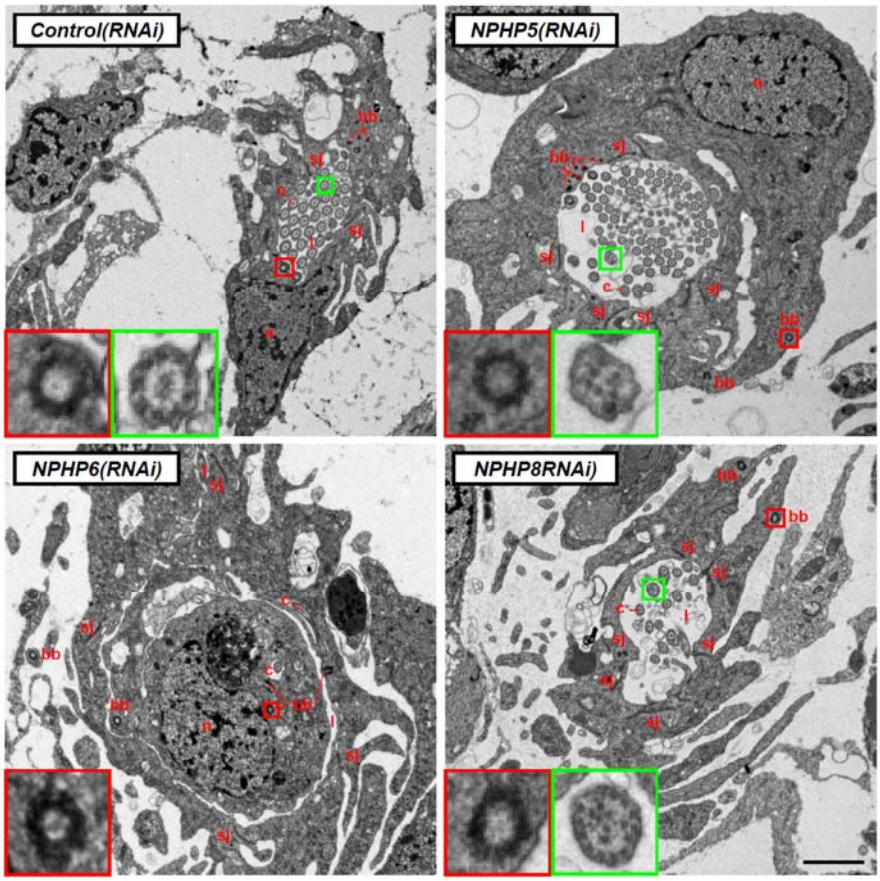
Control(RNAi)
NPHP5(RNAi)
NPHP6(RNAi)
NPHP8RNAi)
bb
sj
c
l
n

Protonephridial Cysts Originate from Direct Proliferation of Protonephridial Progenitors

Sustained cell proliferation in the renal tubules is a hallmark of cystic kidneys in humans and the severity of the phenotype correlates with the ectopic proliferation level (Wilson and Goilav, 2007). To obtain an indication of the involvement of cell proliferation in the formation of the tubule cell accumulations, we used BrdU pulse labeling (Fig. 3.20a). In controls, we found occasional cells double positive for BrdU and the protonephridial progenitor marker *Smed-POU2/3* (Scimone et al., 2011) in the vicinity of tubules (Fig. 3.20a; Fig. 3.21a), consistent with the emerging view that all planarian cell types derive from the proliferation of specific progenitor classes within the neoblast population (Adler et al., 2014; Cowles et al., 2013; Scimone et al., 2014; van Wolfswinkel et al., 2014). In *NPHP8(RNAi)* animals, the number of BrdU/*POU2/3* double-positive cells in the vicinity of cell accumulations was strongly increased (Fig. 3.20a) and further *in situ* approaches confirmed the progressive accumulation of protonephridial progenitors (Fig. 3.21c-d). To probe the magnitude of the overproliferation effect, we carried out whole-mount staining with the G2/M-phase marker phospho-Histone H3 (H3P) and found a global increase in cell proliferation in *NPHP(RNAi)* animals (Fig. 3.20b). To ask whether these effects were specific to protonephridial progenitors or globally affected all progenitor classes, we quantified the relative fraction of proliferation in protonephridial- (*POU2/3*$^{+}$*/smedwi-1*$^{+}$/H3P^{+}), neuronal- (*pax6A*$^{+}$*/smedwi-1*$^{+}$/H3P^{+}) (Scimone et al., 2014; Wenemoser et al., 2012), and intestinal (*HNF4*$^{+}$*/smedwi-1*$^{+}$/H3P^{+}) (Scimone et al., 2014; Wagner et al., 2011) progenitor classes (Fig. 3.22). Whereas the fraction of proliferating protonephridial progenitors was increased in both *NPHP5(RNAi)* and *NPHP8(RNAi)* animals, we found no

Figure 3.20. Cystogenesis in planarian protonephridia results from direct proliferation of protonephridia progenitors and requires the presence of stem cells. **a**, BrdU pulse-chase experiment showing the presence of diving protonephridial progenitors in the proximity of protonephridial tubule in *Control(RNAi)* and *NPHP8(RNAi)* animals. Yellow arrowhead showing *POU2/3*$^{+}$/BrdU^{+} cell. Scale bars: 25 μm. **b**, Increased global proliferation in *NPHP5(RNAi)* and *NPHP8(RNAi)* animals displayed by immunostaining of mitotic marker H3P. Scale bars: 500 μm. *, $p<0.05$; **, $p<0.01$; ***, $p<0.001$ versus control. **c-e**, Quantification of (c) dividing protonephridial progenitors (*POU2/3*$^{+}$/H3P^{+}), (d) diving neuronal progenitors (*pax6A*$^{+}$/H3P^{+}), and (f) diving gut progenitors (*HNF4*$^{+}$/H3P^{+}) among diving cells (H3P^{+}) in indicated RNAi animals at 18 day after last RNAi introduction. *, $p<0.05$ versus control. **f-j**, Effect of proliferation and the requirement of neoblasts on cyst formation in the planarian protonephridia. (f) Schematics showing experimental strategy for panel h-k. 7-day post RNAi feeding animals were either fed with liver to induce cell proliferation or subjected to sublethal or lethal doses of irradiation to reduce or eliminate neoblasts. Scoring live phenotype as well as measuring the average size of each protonephridial unit was used to evaluate the severity of cystic phenotype. Temporal succession of indicated phenotypes (left) and quantification of average area of each *slc6a-13*$^{+}$/*CAVII-1*$^{+}$ tubule (right) in *Control(RNAi)* and *NPHP8(RNAi)* animals under (g) basal condition (only RNAi feeding), (h) basal condition plus extra feeding with liver, (i) basal condition plus sublethal irradiation to reduce the number of neoblasts, and (j) basal condition plus lethal irradiation to completely eliminate neoblasts.

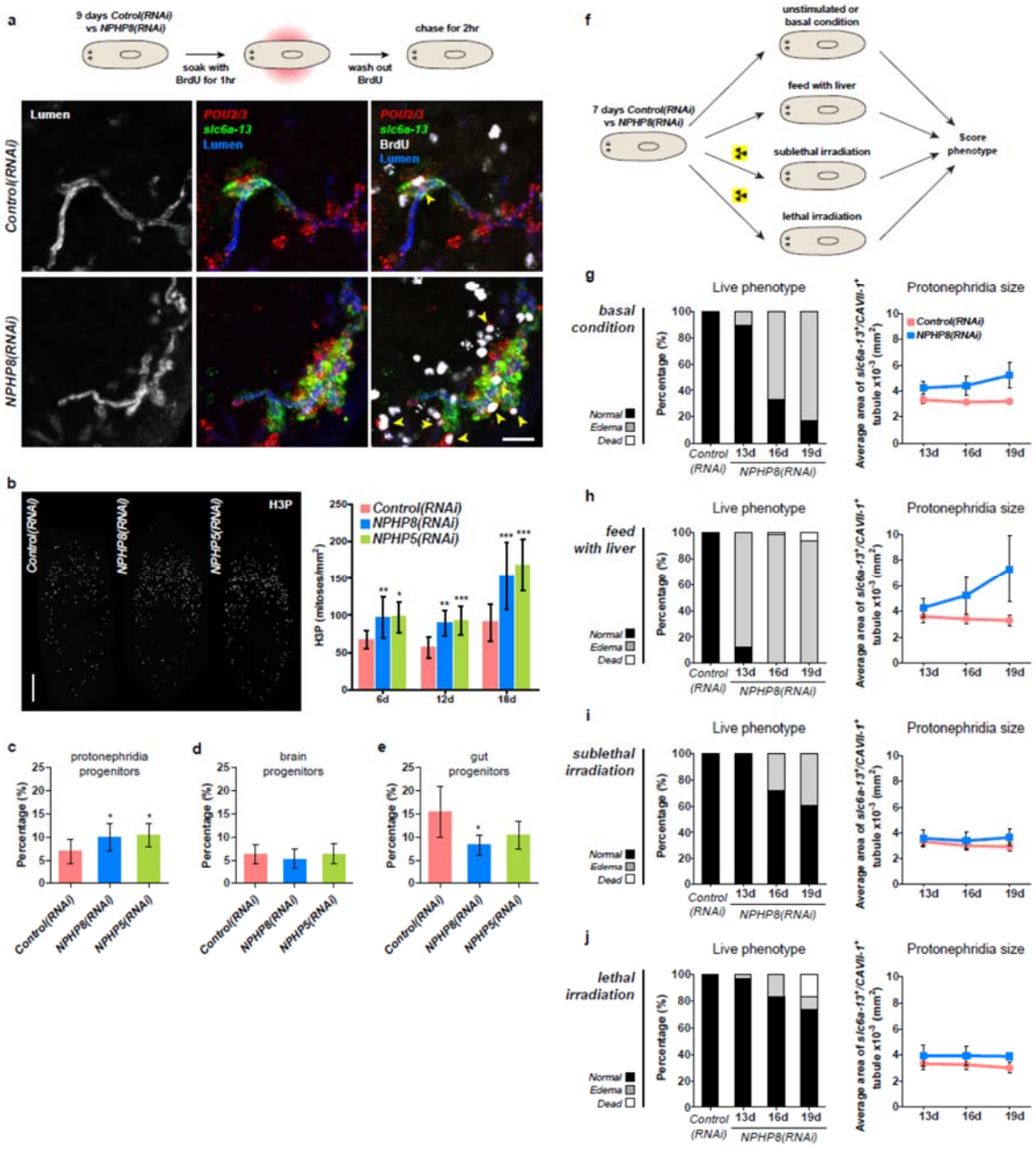
a
9 days Cotrol(RNAi) vs NPHP8(RNAi)
soak with BrdU for 1hr
wash out BrdU
chase for 2hr
Control(RNAi)
NPHP8(RNAi)
Lumen
POU2/3
slc6a-13
BrdU
b
H3P
Control(RNAi)
NPHP8(RNAi)
NPHP5(RNAi)
H3P (miloses/mm²)
6d
12d
18d
c
protonephridia progenitors
d
brain progenitors
e
gut progenitors
Percentage (%)
f
unstimulated or basal condition
feed with liver
sublethal irradiation
lethal irradiation
7 days Control(RNAi) vs NPHP8(RNAi)
Score phenotype
g
basal condition
Live phenotype
Protonephridia size
Normal
Edema
Dead
Control (RNAi)
13d
16d
19d
NPHP8(RNAi)
Average area of slc6a-13+/CAVII-1+ tubule x10⁻³ (mm²)
h
feed with liver
i
sublethal irradiation
j
lethal irradiation

Figure 3.21. Increase of protonephridial progenitors during cystogenesis in planarian protonephridia. **a**, Left: Whole-mount expression patterns of *POU2/3* by *in situ* hybridization. Scale bars: 500 μm. Right: Fluorescent overlay of *POU2/3* with DT marker *(CAVII-1)* and AcTub. Scale bar: 50 μm. **b**, Left: Whole-mount expression patterns of *six1/2-2* by *in situ* hybridization. Scale bars: 500 μm. Right: Fluorescent overlay of *six1/2-2* with DT marker *(CAVII-1)* and AcTub. Scale bar: 50 μm. **c-d**, Magnified view showing the region surrounding photoreceptor. Fluorescent overlay of *POU2/3* and *six1/2-2* with pan stem cell marker *Smedwi-1* and mitotic marker H3P. Scale bar: 50 μm. **e,** Increase of S-phase protonephridial progenitors during cystogenesis in planarian protonephridia. Intact *Control(RNAi)* and *NPHP8(RNAi)* animals were pulsed with BrdU (1 hour), followed by 2-hour chase. Fluorescent overlay of *POU2/3* with BrdU showing the abnormal increase of $POU2/3^{+}$/$BrdU^{+}$ in the head region anterior to the photoreceptors. Images are maximum projections of confocal Z-sections. Scale bar: 100 μm.

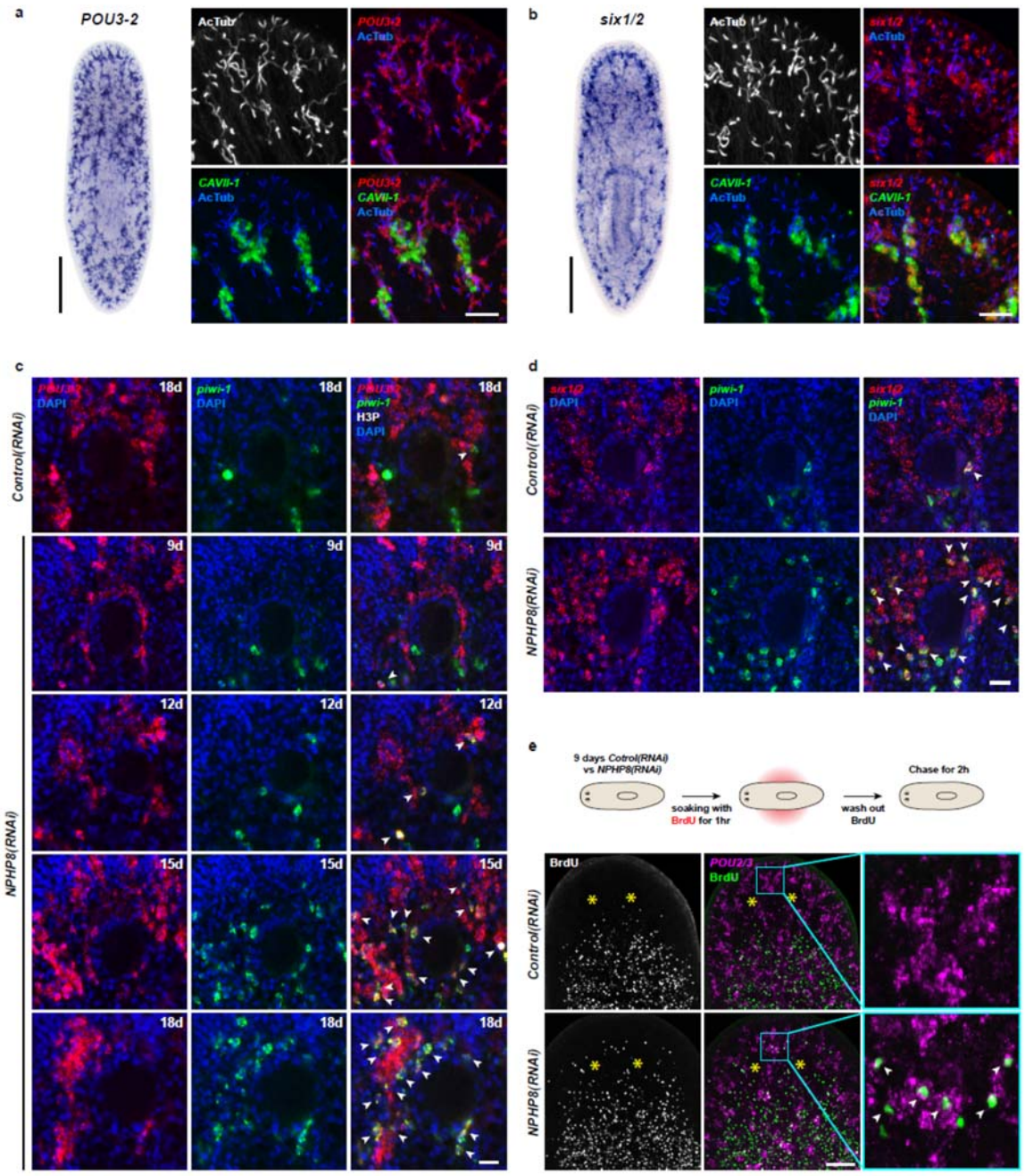
a
POU3-2
AcTub
POU3-2
AcTub
CAVII-1
AcTub
POU3-2
CAVII-1
AcTub
b
six1/2
AcTub
six1/2
AcTub
CAVII-1
AcTub
six1/2
CAVII-1
AcTub
c
Control(RNAi)
NPHP8(RNAi)
DAPI
piwi-1
H3P
18d
9d
12d
15d
d
Control(RNAi)
NPHP8(RNAi)
six1/2
piwi-1
DAPI
e
9 days Cotrol(RNAi) vs NPHP8(RNAi)
soaking with BrdU for 1hr
wash out BrdU
Chase for 2h
BrdU
POU2/3
Control(RNAi)
NPHP8(RNAi)

Figure 3.22. Gut and brain progenitors in *NPHP8(RNAi)* animals. a-b, Left panel: whole-mount expression patterns of *pax6A* (a) and *HNF4* (b) by *in situ* hybridization. Scale bars: 500 μm; Right panel: fluorescent overlay of (a) *pax6A* and (b) *HNF4* with pan stem cell marker (*Smedwi-1*) and mitotic marker (H3P). Scale bar: 50 μm. **c**, Magnified view showing the head region. Fluorescent overlay of *pax6A* and *HNF4* with pan stem cell marker *Smedwi-1* and mitotic marker H3P. Scale bar: 50 μm.

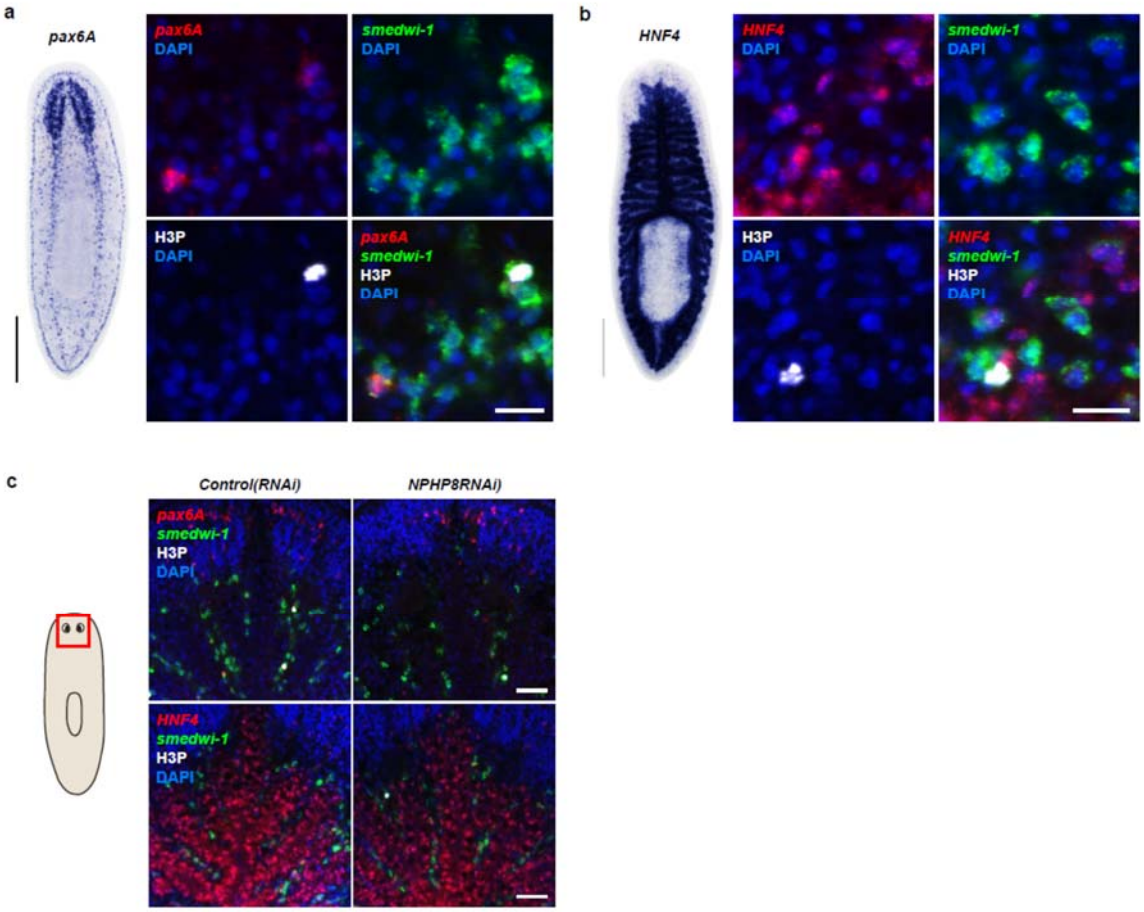
a
pax6A
pax6A
DAPI
smedwi-1
DAPI
H3P
DAPI
pax6A
smedwi-1
H3P
DAPI
b
HNF4
HNF4
DAPI
smedwi-1
DAPI
H3P
DAPI
HNF4
smedwi-1
H3P
DAPI
c
Control(RNAi)
NPHP8RNAi)
pax6A
smedwi-1
H3P
DAPI
HNF4
smedwi-1
H3P
DAPI

change in the fraction of proliferating neuronal progenitors and even a slight decrease in intestinal progenitor proliferation (Fig. 3.20c-e). The observation that all cases of ectopic BrdU-incorporation in the normally division-devoid area anterior to the photoreceptors were limited to *POU2/3*$^{+}$ protonephridial progenitors (Fig. 3.21e) further supports the protonephridial specificity of the overproliferation response. Altogether, these results demonstrated that loss of function of planarian *NPHP* genes selectively increased the proliferation of protonephridial progenitors.

To test whether like in humans, the level of proliferation determined the severity of the phenotype, we made use of the facile manipulation of global cell proliferation levels in the planarian system (Fig. 3.20f, Fig. 3.23a). Lethally or sublethally irradiated animals were used to examine the effects of abolished or reduced proliferation, respectively (Wagner et al., 2012), while animals on an increased feeding regiment provided an opportunity to examine the effects of above-baseline proliferation (Kang and Sanchez Alvarado, 2009). We found that edema development in *NPHP8(RNAi)* animals was faster and more severe under the increased proliferation condition, yet significantly diminished or even abolished under reduced or no proliferation, respectively (Fig. 3.20g-j, left). The quantification of projected area of protonephridial marker expression domains (*slc6a-13* and *CAVII-1*) as direct cell accumulation metric (Fig. 3.20g-j, right; Fig 3.23b) showed exactly the same dependency on proliferation rates, thus demonstrating that the development of planarian *NPHP* phenotypes is intimately dependent on cell proliferation.

In face of such striking morphological and ontological parallels between protonephridal and human NPHP loss of function phenotypes, we now refer to the structural alterations in planarian protonephridia as cysts.

Figure 3.23. The severity of the cystic phenotype in protonephridia depends on the rate of proliferation and requires the presence of stem cells. **a,** Quantification of mitoses in *Control(RNAi)* and *NPHP8(RNAi)* animals. Experimental paradigm is described in Fig. 3.20f. **b,** The severity of cystic phenotype in protonephridia depends on the rate of proliferation and requires the presence of stem cells. Fluorescent overlay of PT marker (*slc6a-13*) with DT marker (*CAVII-1*). Images are maximum projections of confocal Z-sections. Scale bar: 100 μm.

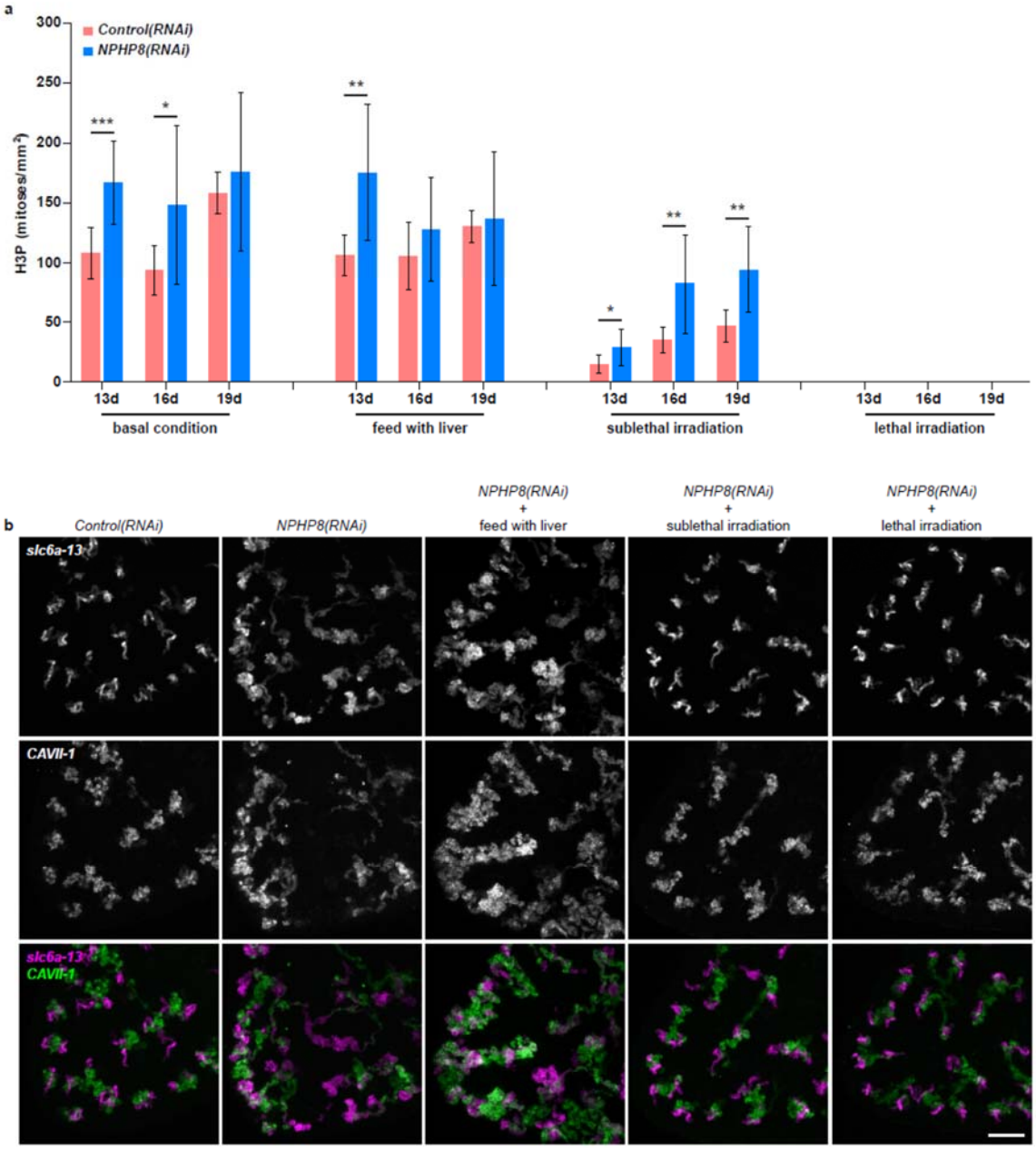
a
Control(RNAi)
NPHP8(RNAi)
H3P (mitoses/mm²)
300
250
200
150
100
50
0
***
*
**
*
**
**
13d
16d
19d
basal condition
feed with liver
sublethal irradiation
lethal irradiation
b
Control(RNAi)
NPHP8(RNAi)
NPHP8(RNAi) + feed with liver
NPHP8(RNAi) + sublethal irradiation
NPHP8(RNAi) + lethal irradiation
slc6a-13
CAVII-1

Cilia-Driven Fluid Flow Is Required for Tubular Cell Homeostasis in Planarian Protonephridia

Cilia as flow sensors play a critical role in the ontogeny of human cystic kidney disease (Hildebrandt and Otto, 2005; Hildebrandt and Zhou, 2007; Kotsis et al., 2013). *NPHP(RNAi)* planarians display severe defects in cilia-driven gliding motility (Fig. 3.24a-b), which prompted us to investigate a possible involvement of cilia in the ontogeny of planarian kidney disease. Direct visualization of axonemes in *NPHP(RNAi)* animals indeed confirmed structural cilia defects, which appeared shorter (*NPHP5(RNAi)*) or much reduced in density (*NPHP6/8(RNAi)*) (Fig. 3.24c). EM images revealed abnormal localization of centrioles as well as axoneme abnormalities in ciliated cells under *NPHP5/6/8(RNAi)* (Fig. 3.19). Together with the broad resemblance between *NPHP5/6/8* expression patterns and typical cilia genes (Glazer et al., 2010; Rink et al., 2009) (Fig. 3.16b), these data conclusively demonstrate that knockdown of planarian *NPHP*-genes causes not only protonephridial cyst formation, but also structural defects in cilia.

We therefore decided to systematically test possible mechanistic roles of cilia in planarian cyst ontogeny. If cilia were generally required for maintaining the structure/function of protonephridia, then all disruptions of cilia structure should cause cystic phenotypes. We therefore knocked down *Smed-IFT88*, a component of the intraflagellar transport machinery. As previously shown (Rink et al., 2009), *IFT88(RNAi)* animals lost their cilia-dependent gliding ability (Fig. 3.25a), developed massive tissue edema, and had severely shortened cilia (Fig. 3.24e-e'). Interestingly, *IFT88(RNAi)* animals also developed cystic protonephridia (Fig. 3.24e'') and cystogenesis in *IFT88(RNAi)* animals was also associated with the accumulation of protonephridial

Figure 3.24. Cystic phenotype in protonephridia is cilia- and fluid flow-dependent. a, Series of live images showing gliding mobility in *Control(RNAi)* and *NPHP8(RNAi)* animals. Yellow dot line provides a spatial reference to illustrate progress of animal. Scale bar: 1 mm. **b**, Quantification of translocation speed in indicated RNAi animals. Error bar, SD; ***, $p<0.001$ versus control. **c**, Fluorescent overlay of ventral cilia (AcTub) with nucleus marker (DAPI) in indicated RNAi animals. Scale bar: 10 μm. **d-g,** Live images showing bloating phenotype in *IFT88(RNAi)*, *DNAHβ-1(RNAi)*, and *LRRC50(RNAi)* animals. Scale bar: 500 μm. **d'-g',** Fluorescent overlay of ventral cilia (AcTub) with nucleus marker (DAPI) in *IFT88(RNAi)*, *DNAHβ-1(RNAi)*, and *LRRC50(RNAi)* animals. Scale bar: 10 μm. **d''-g'',** 3D rendering showing fluorescent overlay of AcTub staining with PT2 and PT3 marker (*slc6a-13*) and DT marker (*CAVII-1*) in *Control(RNAi)*, *IFT88(RNAi)*, *DNAHβ-1(RNAi)*, and *LRRC50(RNAi)* animals. Scale bar: 50 μm. **d'''-g''',** Magnified view showing fluorescent overlay of *POU2/3* with pan stem cell marker *(smedwi-1)* in the region surrounding photoreceptor. White arrowhead showing *POU2/3*$^{+}$/*smedwi-1*$^{+}$ cell. Scale bar: 25 μm. **h-i,** Abnormal cilia beating in *DNAHβ-1(RNAi)*, and *LRRC50(RNAi)* animals. (h) Left panel: live images showing cilia beating along the lateral body edge of the planarian head region; Right panel: vector map generated by STICS analysis showing velocity magnitude and beating pattern of cilia. The brightness of the vector representing the velocity magnitude of the cilia: brighter vector, stronger ciliary beating, or vice versa. (i) Quantification of ciliary velocity magnitude in indicated RNAi animals. *, $p<0.05$ versus control. **j,** Cartoon representing working model of cyst formation in the planarian protonephridia. In normal tubule, protonephridial tubular cell turnover is maintained by integration of protonephridial progenitors, originated from the neoblasts, into the tubule. During this process, cilia-driven fluid flow is required for the maintenance of tubular geometry. Obstruction of fluid flow by disrupting cilia function leads to protonephridial cystogenesis that characterized by abnormal proliferation of protonephridial progenitors, tubular enlargement, and disorganization.

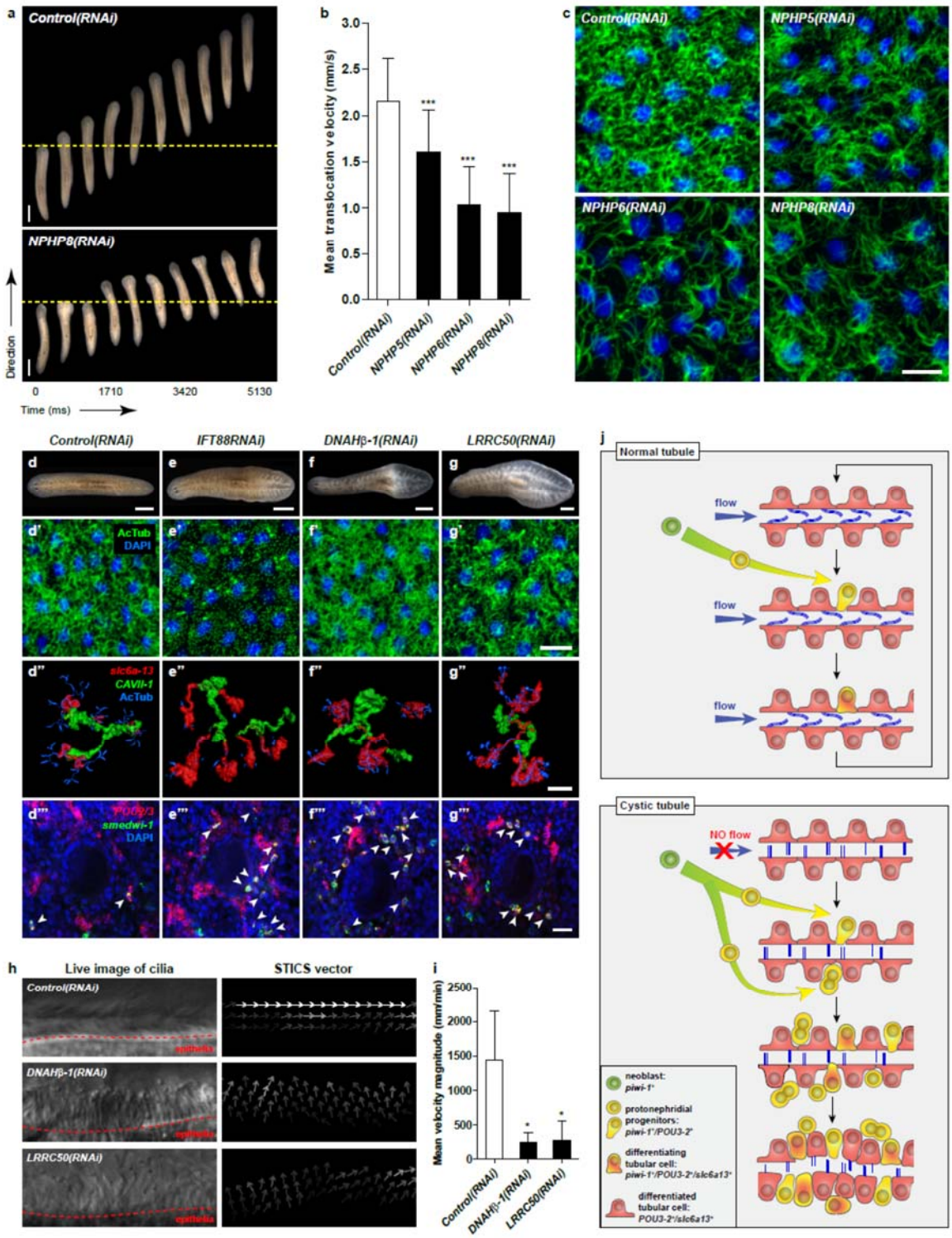
a
Control(RNAi)
NPHP8(RNAi)
Direction
0
1710
3420
5130
Time (ms)
b
Mean translocation velocity (mm/s)
3.0
2.5
2.0
1.5
1.0
0.5
0.0
***
***
***
Control(RNAi)
NPHP5(RNAi)
NPHP6(RNAi)
NPHP8(RNAi)
c
Control(RNAi)
NPHP5(RNAi)
NPHP6(RNAi)
NPHP8(RNAi)
Control(RNAi)
IFT88RNAi)
DNAHβ-1(RNAi)
LRRC50(RNAi)
d
e
f
g
d'
AcTub
DAPI
e'
f'
g'
d''
slc6a-13
CAVII-1
AcTub
e''
f''
g''
d'''
POU6/3
smedwi-1
DAPI
e'''
f'''
g'''
h
Live image of cilia
STICS vector
Control(RNAi)
DNAHβ-1(RNAi)
LRRC50(RNAi)
epithelia
i
Mean velocity magnitude (mm/min)
2500
2000
1500
1000
500
0
*
*
Control(RNAi)
DNAHβ-1(RNAi)
LRRC50(RNAi)
j
Normal tubule
flow
flow
flow
Cystic tubule
NO flow
neoblast:
piwi-1+
protonephridial
progenitors:
piwi-1+/POU3-2+
differentiating
tubular cell:
piwi-1+/POU3-2+/slc6a13+
differentiated
tubular cell:
POU3-2+/slc6a13+

progenitors (Fig. 3.24e’’’). These results therefore demonstrate that disruption of cilia is sufficient for cyst development in planarians.

To test whether cilia might be required as flow generators and/or as flow sensors, we sought to disrupt ciliary beating without gross changes in cilia length or structure. Wetherefore targeted two planarian homologues of Primary Ciliary Dyskinesia (PCD) disease genes, a rare ciliopathy causing general cilia immobility in humans (Badano et al., 2006) (Fig. 3.25b-c). Disrupting the function of *Smed-DNAHβ-1* and *Smed-LRRC50* by RNAi led to abnormal gliding ability (Fig. 3.25a) due to loss of ciliary beating (Fig. 3.24h-i; Supplementary movie 6-8), while cilia length or structure appeared unaffected (Fig. 3.24f’-g’). Interetingly, *DNAHβ-1* and *LRRC50 (RNAi)* animals also developed edema and formed protonephridial cysts (Fig. 3.24f-g, f’’-g’’, f’’’-g’’’). These results indicate that reduced ciliary beating rate without change in cilia structure is sufficient to cause the cystic phenotype in planarian protonephridia. Together, these results suggest that cilia-driven fluid flow is crucial to orchestrate tubular cell homeostasis in planarian protonephridia.

Discussion

In sum, this study provides comprehensive molecular and functional evidence demonstrating planarian protonephridia to be excretory organs in which cilia-driven ultrafiltration by flame cells is coupled with filtrate modification by a system of tubules. First, two major constituents of the podocyte slit diaphragm, *NPHS1* and *NEPH1*, are expressed in planarian flame cells. Recent studies have also demonstrated similar molecular parallels between insect nephrocytes and vertebrate podocytes (Weavers et al., 2009; Zhuang et al., 2009), suggesting that planarian flame cells, insect nephrocytes, and

Figure 3.25. PCD genes in the planarian *Schmidtea mediterranea*. **a,** Schematic drawing showing the structure of 9 + 2 motile cilia in planarians. Right panel: schematic representation of the expanded view of the ODA depicts several light, intermediate, and heavy chains. The planarian homologs of human PCD genes with the ODA defects indicated in this study are labeled in red (*DNAHβ-1* and *LRRC50*). **a'**, TEM image showing cross section through a cilium of protonephridial tubule. IDA, inner dynein arm; ODA, outer dynein arm; DHC, dynein heavy chain; LC, dynein light chain; IC, dynein intermediate chain; DC, docking complex. **b**, Whole-mount expression patterns of *DNAHβ-1* and *LRRC50* by *in situ* hybridization. Scale bars: 500 μm. **c**, Quantification of translocation speed in indicated RNAi animals. Error bar, SD; ***, $p<0.001$ versus control.

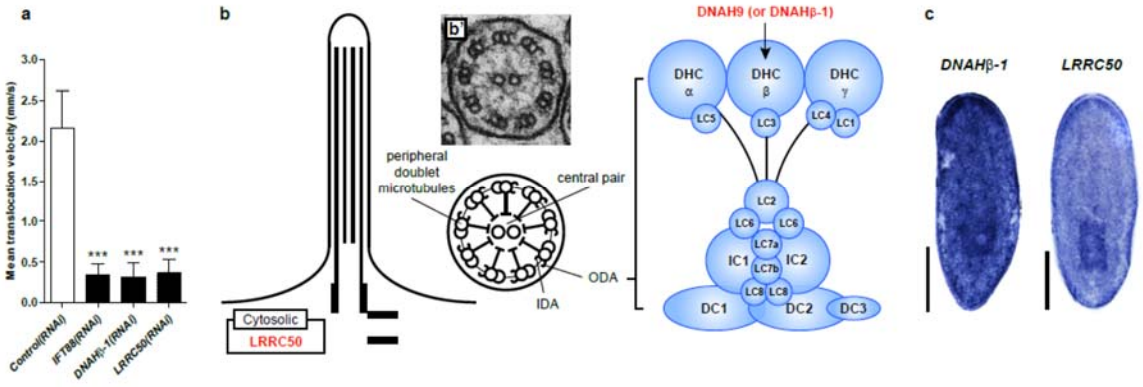
a
Mean translocation velocity (mm/s)
3.0
2.5
2.0
1.5
1.0
0.5
0.0
***
***
***
Control(RNAi)
IFT88(RNAi)
DNAHβ-1(RNAi)
LRRC50(RNAi)
b
b'
peripheral doublet microtubules
central pair
ODA
IDA
Cytosolic
LRRC50
DNAH9 (or DNAHβ-1)
DHC α
DHC β
DHC γ
LC5
LC3
LC4
LC1
LC2
LC6
LC6
LC7a
IC1
IC2
LC7b
LC8
LC8
DC1
DC2
DC3
c
DNAHβ-1
LRRC50

vertebrate podocytes are likely homologous cell types. Second, the structural and functional topology of the protonephridial tubule revealed by systematic gene expression comparisons of *slc* families bears significant resemblance to the vertebrate pronephros/metanephros. Interestingly, structural and functional similarities between planarian protonephridia and vertebrate nephrons extend even further to common pathologies, including the shared requirement of *NPHS1* and *NEPH1* in the maintenance of ultrafiltration barriers as well as of cilia/fluid flow in preventing cystogenesis in the tubules. Cumulatively, the extensive functional and structural conservation of planarian protonephridia has important evolutionary implications, suggesting the existence of cilia-driven ultrafiltration excretory organs in an urbilaterian ancestor.

If cilia-driven filtration excretory organs do exist in the urbilaterian ancestor of planarians and mammals, the observation of only immotile primary cilia in adult mammalian kidneys (Schwartz et al., 1997; Takeda and Narita, 2012) raises an interesting question: Is flow-dependent bending of cilia in human nephron an evolutionary vestige of cilia-powered filtration excretory organs? The remarkable conservation of cilia/fluid flow in the ontogeny of tubular cysts in planarians supports the aforementioned premise. We found that interruption of flow by loss of cilia after *IFT88(RNAi)* or *NPHP(RNAi)* causes cyst formation in planarian protonephridia. Immotile, but intact cilia after *DNAH-β1*- and *LRRC50(RNAi)*, interestingly, also leads to cystogenesis in the protonephridial tubules. Our data suggest that flow-dependent bending and/or flow-generating bending are required for orchestrating tubular cell homeostasis in the “primitive” kidneys. Loss of motile cilia in vertebrate kidneys has been observed in coincidence with the acquirement of a relatively high blood pressure in the birds and mammals (Marshall JR., 1934). One could therefore

postulate that with the presence of an extensively developed circulatory system in mammals, the flow-generating role of cilia to aid the propulsion of fluid into the tubules became redundant and thus lost during the course of evolution. Flow-dependent bending of immotile primary cilia in human kidneys is indeed an evolutionary remnant of cilia-powered filtration excretory organs. Fish or amphibian pronephros thus represents an interesting intermediate case to sort out flow-sensing capabilities of flow-generating cilia in the future.

Regardless, the key question now becomes: What are cilia-associated signaling pathways actually accomplishing in protonephridia? Are cilia required for orchestrating the integration of progenitors into the protonephridial tubule? Or do they instead function as gatekeepers of progenitor proliferation? Our observation that global amplification of cell division by increased feeding schedule fastens phenotypic severities of protonephridial cysts in planarians argues for the former possibility. However, we do see a global increase of mitoses due to the overproliferation of protonephridial progenitors when cilia-driven fluid flow is affected. Therefore, we propose a working model in which that cilia/flow can generate a noncell autonomously acting signal to “turn off” the production of protonephridial progenitors after protonephridia formation/maintenance is complete. Disrupting cilia/flow thus leads to overproduction of protonephridial progenitors, and subsequently cyst formation in the tubules (Fig. 3.24j). Recent identification of stem/progenitor cells in adult mammalian kidney (Angelotti et al., 2012; Rinkevich et al., 2014; Romagnani et al., 2013) is hence highly interesting because it suggests that the generation of a trans-acting signal by a tubule cell and its reception by “an exogenous division-competent population” could also be at the core of human kidney diseases.

However, formal investigation is required to confirm this speculative hypothesis. Nonetheless, the remarkable conservation of flow/cilia/proliferation axis during tubular cystogenesis between planarian protonephridia and human nephrons suggests the very likely conservation of aforementioned cilia/flow-associated signal. Future study to identify the cross-talk signaling between tubule cells and stem cells represents a key step for better understanding disease pathologies. Given the high speed and low cost of deployment, combined with robust and high-throughput RNAi screening, planarians are a highly promising invertebrate model system to study mechanisms of human kidney disease.

Materials and Methods

Planarian Maintenance and Irradiation

The CIW4 clonal line of *Schmidtea mediterranea* was maintained as described (Cebria and Newmark, 2005). 1-week starved animals were used for all experiments. For irradiation experiments, animals were exposed to 1250 or 6000 rads on a GammaCell 40 Exactor irradiator.

Gene Identification and Cloning

Human, mouse, *Xenopus*, and zebrafish protein sequences were used to find planarian homologs from *Schmidtea mediterranea* genome database via TBLASTN. Planarian homologs were then used for reciprocal BLAST against the human refseq to verify the homology. All genes were cloned from an 8-day regeneration time course cDNA library prepared as described previously (Gurley et al., 2008). Primers used for cloning are described in Appendix A and D.

Phylogenetic Analysis

The complete set of protein sequences were retrieved for human, mouse, and fly from Ensembl (release 76) (Flicek et al., 2014). The mosquito protein sequences were retrieved from Ensembl metazoa (release 23). Only the proteins corresponding to the longest isoform of each gene were considered for the analysis. The PFAM protein domains (PfamA-27.0) (Finn et al., 2014) were predicted for all those proteins from human, mouse, fly, and mosquito and the planarian homologs of solute carriers using the InterProScan (version 5.4-47.0) tool (Jones et al., 2014). The solute carrier proteins were classified into their corresponding solute carrier family or clan groups based on the presence of the corresponding PFAM protein domain as described in the literature (He et al., 2009; Hoglund et al., 2011). The predicted domain regions were extracted from those proteins and multiple sequence alignment was then performed for those extracted regions using clustalw2 (version 2.1, with default parameters) (Larkin et al., 2007). Using the sequence alignment, the bootstrapped neighbor joining trees (positions with gaps removed and corrected for multiple substitution) were constructed using clustalw2 (version 2.1) (Larkin et al., 2007).

In Situ Hybridization and Immunohistochemistry

Colorimetric and fluorescent *in situ* hybridizations were performed as previously described (King and Newmark, 2013; Pearson et al., 2009). Following fluorescent or NBT/BCIP development, animals were incubated with anti-acetylated-Tubulin antibody (1:1000, Cell Signaling), anti-H3P (1:1000, Millipore), or a rabbit antiserum recognized unknown epitope to visualize the lumen of proximal tubule (1:500). Primary antibodies

were detected with either Alexa-conjugated anti-rabbit antibodies (1:1000; Abcam) or HRP-conjugated anti-rabbit antibodies (1:1000; Jackson ImmunoResearch). NBT/BCIP developed whole-mount *in situ* specimens were mounted in mounting media containing 75% glycerol and 2M urea. Fluorescent whole-mount *in situ* specimens were mounted in modified Sca*l*eA2 containing 20% glycerol, 2.5% DABCO, and 4M urea (Hama et al., 2011). For cryosectioning, fluorescently stained whole-mounted animals were fixed overnight in 4% paraformaldehyde (in PBS) at 4^{o}C, washed three times in PBS, equilibrated in 30% sucrose, frozen in OCT, and cryosectioned (10-20 μm).

Imaging and Image Quantification

A Leica M205 Stereo Microscope was used for documenting live images, movies, and NBT/BCIP developed whole-mount *in situ* specimens. Zeiss LSM-510 VIS or LSM-700 Upright confocal microscopes were used to capture fluorescent whole-mount *in situ* specimens and image projections. To quantify the average size of each protonephridial unit and mitotic activity, individual worm was imaged and tiled on a Perkin Elmer Ultraview spinning disk microscope. Stitching and mitotic activity quantification was performed in FiJi using standard plugins (Schindelin et al., 2012). Worm area, protonephridial size, and number were measured/counted using a custom signal to noise thresholding and seeded region grow plugins. Batching was performed using macros. Movement speed quantification was performed on movie sequences (acquired at 17.5 Hz) using a custom thresholding plugin and Mtrack2 (Klopfenstein and Vale, 2004). For each tracked object, the initial position was subtracted from the final to determine an average

translocation velocity. Average velocities were computed by weighting track averages by the length of the track. Plugins and macros are available at https://github.com/jouyun.

BrdU Labeling

BrdU was administered by soaking animals in 15mg/mL BrdU and 3% DMSO (diluted in 0.1X Montjuic salts) for 1 hour as previously described (Cowles et al., 2012) and chasing for specified time. Animals were fixed and processed as *in situ* hybridization protocol except they were bleached in 6%H2O2 in PBSTx (0.5% Triton) for 3-4 hours under direct light. After *in situ* development, specimens were treated with 2N HCl for 45 minutes at room temperature, and washed 4 times with PBSTx (0.3% Triton) for 1 hour. BrdU was detected using rat anti-BrdU antibody (1:1000; Abcam, Cat. No. ab6326). Primary antibody was detected with HRP-conjugated anti-rat antibody (1:1000; Jackson ImmunoResearch).

Ultrafiltration and Reabsorption Assay

To assay ultrafiltration capacity of planarian protonephridia, 10 kDa tetramethylrhodamine-dextran (Molecular Probes, D-1817) and 500 kDa fluorescein-dextran (Molecular Probes, D-7136) at the concentration of 1 mg/mL were co-injected into the mesenchyme of the animals. After 2 hours, the animals were rinsed with an excess of 1X Montjuic salts, fixed in cold 4% paraformaldehyde (in 1X Montjuic salts), mounted in modified ScaleA2, and photographed using a Zeiss LSM-510 VIS confocal microscope. Dextran uptake was quantified by measuring the average fluorescence intensity per unit area using a standard signal to noise thresholding in Fiji (Schindelin et al., 2012). For

immunostaining, after fixation, the samples were rinsed 3-4 times with PBSTx (0.3% Triton), incubated in blocking solution containing 5% horse serum in PBSTx (0.5% Triton) for 2 hours at room temperature, and then in anti-acetylated-Tubulin antibody (1:1000, Cell Signaling). Primary antibody was detected using Alexa-conjugated anti-rabbit antibodies (1:1000; Abcam).

pHi Reporter Assay

Intracellular pH was measured using ratiometric pH dye SNARF-5F-AM (Molecular Probes, Cat. No. S-23923) at 5uM (in DMSO with 20% w/v Pluronic F-127) as previously described (Beane et al., 2011; Beane et al., 2013). Animals were soaked for 1 hour, rinsed 3 times with an excess of 1X Montjuic salts, immobilized on the glass bottom dish using the microfluidic device, and imaged at both 640 nm (pH sensitive) and 580 nm (pH insensitive) wavelengths using a LSM-700 Falcon confocal microscope. The ratio of 580/640 (used for controlling uneven dye uptake) was shown.

High-speed Video Microscopy

To visualize cilia beating along the lateral body edge of the planarian head region, live worms are immobilized on the glass bottom dish using a microfluidic device and imaged on a Zeiss Axiovert 200 microscope under DIC optics using 63X objective. Series of images were captured at 250 frames per second with pixel number of 800 x 800 (exposure time is 3.97 ms) using a ORCA-Flash4.0 V2 C11440-22CU camera from Hamamatsu. Spatiotemporal image correlation spectroscopy (STICS) was used to determine the speed of the cilia for each animal. In each time-lapse, 100 consecutive

frames were manually selected in which the animal was stationary so that no image registration was required. A region of interest was manually drawn around the cilia in each time-lapse. The area outside this region was uniformly filled with the average intensity inside the region. Spatiotemporal correlation was then carried out in 32 x 32 pixel regions with a 16 pixel overlap between the regions to allow for highly localized motions to be accurately represented using the fast Fourier transform method. The average cilia displacement within the correlation image is represented by the maximum of the spatial cross-correlation between two images separated in time. The time correlation shift was a single frame, and all velocities were converted to micrometers per minute. This method was adapted from a previous paper (Yi et al., 2011), where it was implemented with custom plugins written in Java for ImageJ, available for download at (http://research.stowers.org/imagejplugins).

Statistical Analysis

Statistical analysis of the data was carried out in Excel. P values were determined using Student's t-test.

Electron Microscopy

Specimens were prepared as following at 4^{o}C on orbital rotator: 1) fix in cold 2.5% glutaraldehyde in 0.05M or 0.1M sodium cacodylate (contained 1mM $CaCl_2$) for overnight; 2) wash in wash buffer (0.1M sodium cacodylate buffer; 1mM $CaCl_2$; and 1% sucrose) for 1 hour (3-4 exchanges); 3) fix in 1% Osmium tetroxide in 0.1M sodium cacodylate buffer (+ 1mM $CaCl_2$) for 2 hours; 4) wash in wash buffer for 1 hour (3-4 exchanges) and in

distilled water for 30 minutes (3-4 exchanges); 5) fix in 0.5% aqueous Uranyl Acetate (in dark) overnight; 6) wash in distilled water for 30 minutes (3-4 exchanges); 7) and dehydrate in acetone 30% (20 minutes), 50% (20 minutes), 70% (overnight), 90% (20 minutes, 2 times), and 100% (20 minutes, 3 times). Specimens were then embedded in epon-araldite or Spurr's resin (25% resin/acetone for 3 hours; 50% resin/acetone for 2.5 hours; 75% resin/acetone overnight; 100% resin without accelerator with microwave at 350W for 3 minutes on/3 minutes off/3 minutes on for 1 day (2 exchanges); 100% resin with accelerator with microwave at 350W for 3 minutes on/3 minutes off/3 minutes on for 1 day (2 exchanges) and placed in 60ºC oven for polymerization for 2 days. Ultra-thin 50-100 nm sections were collected using a Leica UC6 Ultramicrotome. TEM specimens were stained with Sato's lead (3minutes)/4% Uranyl Acetate in 70% methanol (4 minutes)/ Sato's lead (6 minutes) prior to imaging on a FEI Technai BioTwin at 80kV equipped with a Gatan UltraScan 1000 digital camera.

RNAi via dsRNA Feeding

RNAi feedings were performed as described previously (Gurley et al., 2008; Rink et al., 2009). Feeding and amputation schedules were tailored for each experiment and described in detail as following:

Fig. 3.24l:	5 dsRNA feedings (3 days in between)
Fig. 3.13c-d, 14a:	8 dsRNA feedings (3 days in between)
Fig. 3.13e:	9 dsRNA feedings (3 days in between)
Fig. 3.14b, 3.15:	6 dsRNA feedings (3 days in between) prior to amputation
Fig. 3.17a-c:	3 dsRNA feedings (3 days in between)

Fig. 18-23:	2 dsRNA feedings (3 days in between)
Fig. 3.24a-c:	3 dsRNA feedings (2 days in between)
Fig. 3.24d-h, 3.25:	*IFT88* and *LRRC50*: 3 dsRNA feedings (2 days in between)
	DNAHβ-1: 8 dsRNA feedings (2 days in between)

References

Adler, C.E., Seidel, C.W., McKinney, S.A., and Sanchez Alvarado, A. (2014). Selective amputation of the pharynx identifies a foxa-dependent regeneration program in planaria. Elife *3*, e02238.

Angelotti, M.L., Ronconi, E., Ballerini, L., Peired, A., Mazzinghi, B., Sagrinati, C., Parente, E., Gacci, M., Carini, M., Rotondi, M., *et al.* (2012). Characterization of renal progenitors committed toward tubular lineage and their regenerative potential in renal tubular injury. Stem Cells *30*, 1714-1725.

Badano, J.L., Mitsuma, N., Beales, P.L., and Katsanis, N. (2006). The ciliopathies: An emerging class of human genetic disorders. Annu Rev Genomics Hum Genet *7*, 125-148.

Beane, W.S., Morokuma, J., Adams, D.S., and Levin, M. (2011). A chemical genetics approach reveals h,k-atpase-mediated membrane voltage is required for planarian head regeneration. Chem Biol *18*, 77-89.

Beane, W.S., Morokuma, J., Lemire, J.M., and Levin, M. (2013). Bioelectric signaling regulates head and organ size during planarian regeneration. Development *140*, 313-322.

Bisceglia, M., Galliani, C.A., Senger, C., Stallone, C., and Sessa, A. (2006). Renal cystic diseases: A review. Adv Anat Pathol *13*, 26-56.

Buechner, M. (2002). Tubes and the single c. Elegans excretory cell. Trends Cell Biol *12*, 479-484.

Carraro-Lacroix, L.R., and Malnic, G. (2010). Acid-base transport by the renal distal nephron. J Nephrol *23 Suppl 16*, S19-27.

Cebria, F., and Newmark, P.A. (2005). Planarian homologs of netrin and netrin receptor are required for proper regeneration of the central nervous system and the maintenance of nervous system architecture. Development *132*, 3691-3703.

Cowles, M.W., Brown, D.D., Nisperos, S.V., Stanley, B.N., Pearson, B.J., and Zayas, R.M. (2013). Genome-wide analysis of the bhlh gene family in planarians identifies factors required for adult neurogenesis and neuronal regeneration. Development *140*, 4691-4702.

Cowles, M.W., Hubert, A., and Zayas, R.M. (2012). A lissencephaly-1 homologue is essential for mitotic progression in the planarian schmidtea mediterranea. Dev Dyn *241*, 901-910.

Deane, J.A., and Ricardo, S.D. (2012). Emerging roles for renal primary cilia in epithelial repair. Int Rev Cell Mol Biol *293*, 169-193.

Donoviel, D.B., Freed, D.D., Vogel, H., Potter, D.G., Hawkins, E., Barrish, J.P., Mathur, B.N., Turner, C.A., Geske, R., Montgomery, C.A., *et al.* (2001). Proteinuria and perinatal lethality in mice lacking neph1, a novel protein with homology to nephrin. Mol Cell Biol *21*, 4829-4836.

Dow, J.A., and Romero, M.F. (2010). Drosophila provides rapid modeling of renal development, function, and disease. Am J Physiol Renal Physiol *299*, F1237-1244.

Finn, R.D., Bateman, A., Clements, J., Coggill, P., Eberhardt, R.Y., Eddy, S.R., Heger, A., Hetherington, K., Holm, L., Mistry, J., *et al.* (2014). Pfam: The protein families database. Nucleic Acids Res *42*, D222-230.

Flicek, P., Amode, M.R., Barrell, D., Beal, K., Billis, K., Brent, S., Carvalho-Silva, D., Clapham, P., Coates, G., Fitzgerald, S., *et al.* (2014). Ensembl 2014. Nucleic Acids Res *42*, D749-755.

Fliegauf, M., Horvath, J., von Schnakenburg, C., Olbrich, H., Muller, D., Thumfart, J., Schermer, B., Pazour, G.J., Neumann, H.P., Zentgraf, H., *et al.* (2006). Nephrocystin specifically localizes to the transition zone of renal and respiratory cilia and photoreceptor connecting cilia. J Am Soc Nephrol *17*, 2424-2433.

Glazer, A.M., Wilkinson, A.W., Backer, C.B., Lapan, S.W., Gutzman, J.H., Cheeseman, I.M., and Reddien, P.W. (2010). The zn finger protein iguana impacts hedgehog signaling by promoting ciliogenesis. Dev Biol *337*, 148-156.

Gurley, K.A., Rink, J.C., and Sanchez Alvarado, A. (2008). Beta-catenin defines head versus tail identity during planarian regeneration and homeostasis. Science *319*, 323-327.

Hama, H., Kurokawa, H., Kawano, H., Ando, R., Shimogori, T., Noda, H., Fukami, K., Sakaue-Sawano, A., and Miyawaki, A. (2011). Scale: A chemical approach for fluorescence imaging and reconstruction of transparent mouse brain. Nat Neurosci *14*, 1481-1488.

He, L., Vasiliou, K., and Nebert, D.W. (2009). Analysis and update of the human solute carrier (slc) gene superfamily. Hum Genomics *3*, 195-206.

Hildebrandt, F., and Otto, E. (2005). Cilia and centrosomes: A unifying pathogenic concept for cystic kidney disease? Nat Rev Genet *6*, 928-940.

Hildebrandt, F., and Zhou, W. (2007). Nephronophthisis-associated ciliopathies. J Am Soc Nephrol *18*, 1855-1871.

Hoglund, P.J., Nordstrom, K.J., Schioth, H.B., and Fredriksson, R. (2011). The solute carrier families have a remarkably long evolutionary history with the majority of the human families present before divergence of bilaterian species. Mol Biol Evol *28*, 1531-1541.

Igarashi, P. (2005). Overview: Nonmammalian organisms for studies of kidney development and disease. J Am Soc Nephrol *16*, 296-298.

Jones, P., Binns, D., Chang, H.Y., Fraser, M., Li, W., McAnulla, C., McWilliam, H., Maslen, J., Mitchell, A., Nuka, G., *et al.* (2014). Interproscan 5: Genome-scale protein function classification. Bioinformatics *30*, 1236-1240.

Kang, H., and Sanchez Alvarado, A. (2009). Flow cytometry methods for the study of cell-cycle parameters of planarian stem cells. Dev Dyn *238*, 1111-1117.

Kestila, M., Lenkkeri, U., Mannikko, M., Lamerdin, J., McCready, P., Putaala, H., Ruotsalainen, V., Morita, T., Nissinen, M., Herva, R., *et al.* (1998). Positionally cloned gene for a novel glomerular protein--nephrin--is mutated in congenital nephrotic syndrome. Mol Cell *1*, 575-582.

King, R.S., and Newmark, P.A. (2013). In situ hybridization protocol for enhanced detection of gene expression in the planarian schmidtea mediterranea. BMC Dev Biol *13*, 8.

Klopfenstein, D.R., and Vale, R.D. (2004). The lipid binding pleckstrin homology domain in unc-104 kinesin is necessary for synaptic vesicle transport in caenorhabditis elegans. Mol Biol Cell *15*, 3729-3739.

Kotsis, F., Boehlke, C., and Kuehn, E.W. (2013). The ciliary flow sensor and polycystic kidney disease. Nephrol Dial Transplant *28*, 518-526.

Landowski, C. (2008). The mammalian transporter families. In Seldin and Giebisch's the kidney (fourth edition), R.A.a.S. Hebert, ed. (Academic Press), pp. 91-146.

Larkin, M.A., Blackshields, G., Brown, N.P., Chenna, R., McGettigan, P.A., McWilliam, H., Valentin, F., Wallace, I.M., Wilm, A., Lopez, R., *et al.* (2007). Clustal w and clustal x version 2.0. Bioinformatics *23*, 2947-2948.

Lodi, D., Ligabue, G., Lupo, V., and Cavazzini, F. (2012). The role of pec progenitors in adpkd progression. Int J Stem Cells *5*, 65-72.

Marshall JR., E.K. (1934). The comparative physiology of the kidney in relation to theories of renal secretion. Physiol Rev *14*, 133-159.

Mollet, G., Silbermann, F., Delous, M., Salomon, R., Antignac, C., and Saunier, S. (2005). Characterization of the nephrocystin/nephrocystin-4 complex and subcellular localization of nephrocystin-4 to primary cilia and centrosomes. Hum Mol Genet *14*, 645-656.

Murer, L., Caridi, G., Della Vella, M., Montini, G., Carasi, C., Ghiggeri, G., and Zacchello, G. (2002). Expression of nuclear transcription factor pax2 in renal biopsies of juvenile nephronophthisis. Nephron *91*, 588-593.

Nauli, S.M., Alenghat, F.J., Luo, Y., Williams, E., Vassilev, P., Li, X., Elia, A.E., Lu, W., Brown, E.M., Quinn, S.J., *et al.* (2003). Polycystins 1 and 2 mediate mechanosensation in the primary cilium of kidney cells. Nat Genet *33*, 129-137.

Nielsen, S., Frokiaer, J., Marples, D., Kwon, T.H., Agre, P., and Knepper, M.A. (2002). Aquaporins in the kidney: From molecules to medicine. Physiol Rev *82*, 205-244.

Pannabecker, T.L. (2012). Structure and function of the thin limbs of the loop of henle. Compr Physiol *2*, 2063-2086.

Pavenstadt, H., Kriz, W., and Kretzler, M. (2003). Cell biology of the glomerular podocyte. Physiol Rev *83*, 253-307.

Pearson, B.J., Eisenhoffer, G.T., Gurley, K.A., Rink, J.C., Miller, D.E., and Sanchez Alvarado, A. (2009). Formaldehyde-based whole-mount in situ hybridization method for planarians. Dev Dyn *238*, 443-450.

Praetorius, H.A., Praetorius, J., Nielsen, S., Frokiaer, J., and Spring, K.R. (2004). Beta1-integrins in the primary cilium of mdck cells potentiate fibronectin-induced ca2+ signaling. Am J Physiol Renal Physiol *287*, F969-978.

Praetorius, H.A., and Spring, K.R. (2001). Bending the mdck cell primary cilium increases intracellular calcium. J Membr Biol *184*, 71-79.

Praetorius, H.A., and Spring, K.R. (2003). The renal cell primary cilium functions as a flow sensor. Curr Opin Nephrol Hypertens *12*, 517-520.

Priolo, C., and Henske, E.P. (2013). Metabolic reprogramming in polycystic kidney disease. Nat Med *19*, 407-409.

Raciti, D., Reggiani, L., Geffers, L., Jiang, Q., Bacchion, F., Subrizi, A.E., Clements, D., Tindal, C., Davidson, D.R., Kaissling, B., *et al.* (2008). Organization of the pronephric kidney revealed by large-scale gene expression mapping. Genome Biol *9*, R84.

Rink, J.C., Gurley, K.A., Elliott, S.A., and Sanchez Alvarado, A. (2009). Planarian hh signaling regulates regeneration polarity and links hh pathway evolution to cilia. Science *326*, 1406-1410.

Rink, J.C., Vu, H.T., and Sanchez Alvarado, A. (2011). The maintenance and regeneration of the planarian excretory system are regulated by egfr signaling. Development *138*, 3769-3780.

Rinkevich, Y., Montoro, D.T., Contreras-Trujillo, H., Harari-Steinberg, O., Newman, A.M., Tsai, J.M., Lim, X., Van-Amerongen, R., Bowman, A., Januszyk, M., *et al.* (2014).

In vivo clonal analysis reveals lineage-restricted progenitor characteristics in mammalian kidney development, maintenance, and regeneration. Cell Rep *7*, 1270-1283.

Romagnani, P., Lasagni, L., and Remuzzi, G. (2013). Renal progenitors: An evolutionary conserved strategy for kidney regeneration. Nat Rev Nephrol *9*, 137-146.

Ruppert, E.E. (1994). Evolutionary origin of the vertebrate nephron. Amer. Zool *34*, 542-553.

Ruppert, E.E., and Smith, P.R. (1988). The functional organization of filtration nephridia. Biol Rev *63*, 231-258.

Schindelin, J., Arganda-Carreras, I., Frise, E., Kaynig, V., Longair, M., Pietzsch, T., Preibisch, S., Rueden, C., Saalfeld, S., Schmid, B., *et al.* (2012). Fiji: An open-source platform for biological-image analysis. Nat Methods *9*, 676-682.

Schwartz, E.A., Leonard, M.L., Bizios, R., and Bowser, S.S. (1997). Analysis and modeling of the primary cilium bending response to fluid shear. Am J Physiol *272*, F132-138.

Scimone, M.L., Kravarik, K.M., Lapan, S.W., and Reddien, P.W. (2014). Neoblast specialization in regeneration of the planarian *Schmidtea mediterranea*. Stem Cell Reports *3*, 339-352.

Scimone, M.L., Srivastava, M., Bell, G.W., and Reddien, P.W. (2011). A regulatory program for excretory system regeneration in planarians. Development *138*, 4387-4398.

Takeda, S., and Narita, K. (2012). Structure and function of vertebrate cilia, towards a new taxonomy. Differentiation *83*, S4-11.

Uhlenhaut, N.H., and Treier, M. (2008). Transcriptional regulators in kidney disease: Gatekeepers of renal homeostasis. Trends Genet *24*, 361-371.

van Wolfswinkel, J.C., Wagner, D.E., and Reddien, P.W. (2014). Single-cell analysis reveals functionally distinct classes within the planarian stem cell compartment. Cell Stem Cell.

Wagner, D.E., Ho, J.J., and Reddien, P.W. (2012). Genetic regulators of a pluripotent adult stem cell system in planarians identified by rnai and clonal analysis. Cell Stem Cell *10*, 299-311.

Wagner, D.E., Wang, I.E., and Reddien, P.W. (2011). Clonogenic neoblasts are pluripotent adult stem cells that underlie planarian regeneration. Science *332*, 811-816.

Watnick, T., and Germino, G. (2003). From cilia to cyst. Nat Genet *34*, 355-356.

Weavers, H., Prieto-Sanchez, S., Grawe3, F., Garcia-Lopez, A., Artero, R., Wilsch-Brauninger, M., Ruiz-Gomez, M., Skaer, H., and Denholm, B. (2009). The insect nephrocyte is a podocyte-like cell with a filtration slit diaphragm. Nature *457*, 322-327.

Weimbs, T. (2007). Polycystic kidney disease and renal injury repair: Common pathways, fluid flow, and the function of polycystin-1. Am J Physiol Renal Physiol *293*, F1423-1432.

Wenemoser, D., Lapan, S.W., Wilkinson, A.W., Bell, G.W., and Reddien, P.W. (2012). A molecular wound response program associated with regeneration initiation in planarians. Genes Dev *26*, 988-1002.

Wilhelmi, J. (1906). Untersuchungen über die excretionsorgane der sübwassertricladen. Z Wiss Zool *80*, 544-575.

Wilson, P.D., and Goilav, B. (2007). Cystic disease of the kidney. Annu Rev Pathol *2*, 341-368.

Wilson, R.A., and Webster, L.A. (1974). Protonephridia. Biol Rev Camb Philos Soc *49*, 127-160.

Wingert, R.A., and Davidson, A.J. (2008). The zebrafish pronephros: A model to study nephron segmentation. Kidney Int *73*, 1120-1127.

Yi, K., Unruh, J.R., Deng, M., Slaughter, B.D., Rubinstein, B., and Li, R. (2011). Dynamic maintenance of asymmetric meiotic spindle position through arp2/3-complex-driven cytoplasmic streaming in mouse oocytes. Nat Cell Biol *13*, 1252-1258.

Yoder, B.K., Hou, X., and Guay-Woodford, L.M. (2002). The polycystic kidney disease proteins, polycystin-1, polycystin-2, polaris, and cystin, are co-localized in renal cilia. J Am Soc Nephrol *13*, 2508-2516.

Zhuang, S., Shao, H., Guo, F., Trimble, R., Pearce, E., and Abmayr, S.M. (2009). Sns and kirre, the drosophila orthologs of nephrin and neph1, direct adhesion, fusion and formation of a slit diaphragm-like structure in insect nephrocytes. Development *136*, 2335-2344.

CHAPTER 4

CONCLUSIONS AND PERSPECTIVES

Through systematic molecular and functional characterization, we identify planarian protonephridia as complex epithelial excretory organs composed of two principle components. These include 1) flame cells as mediators of ultrafiltration and 2) a system of epithelial tubes accountable for filtrate modification by reabsorption and secretion. Interestingly, the flame cells and tubule system are morphologically and functionally similar to the vertebrate kidney. The conservation between planarian protonephridia and vertebrate nephrons extends even further to genetic programs governing early kidney development, as well as common pathologies. Together, from this study, we are able to not only gain incredible insights into the evolutionary history of animal excretory organs, but we also provide a substantial set of evidence to establish planarian protonephridia as a novel invertebrate model to study kidney development, diseases, and evolution.

Planarian Protonephridia – New Perspectives on the Evolutionary Origin of Vertebrate Nephrons

The evolutionary origin of organ systems poses an intriguing question in biology. However, understanding whether two organs in animals separated by hundreds of millions of years share a common evolutionary history or simply represent examples of convergent evolution can be difficult. In the case of the excretory system, this problem is confounded by the extensive diversity in forms and functions. For instance, the specific tasks of an excretory system can vary greatly based upon an animal's environment. With respect to maintaining salt and water balance, land-dwelling organisms have to conserve water and excrete superfluous solutes in as little volume as possible. In contrast, freshwater animals need to continuously excrete excess water while conserving solutes. In term of anatomical

diversity, excretory organs can range from a single excretory cell in *C. elegans* to multi-cellular excretory systems, such as Malpighian tubules in insects, protonephridia, and metanephridia in invertebrates, or kidneys in vertebrates (Buechner, 2002; Dow and Romero, 2010; Nelson et al., 1983; Ruppert, 1994; Ruppert and Smith, 1988).

Confronted with such functional and anatomical diversity, the evolutionary origin of excretory organs poses a significant challenge. Have excretory organs evolved independently in different animal lineages? Or, has a single primordial excretory organ undergone functional and anatomical diversification during the course of animal evolution? Comparative morphological data have been the primary data supporting current models for the evolution of excretory systems (detailed discussion by (Bartolomaeus and Quast; Goodrich, 1945a, b; Ruppert, 1994; Ruppert and Smith, 1988)). However, morphology alone cannot resolve this important question, as similar-looking structures can easily arise by either common descent or convergent evolution. Systematic comparisons of gene functions and expression patterns have emerged as an essential alternative to elucidate the evolutionary history of tissues and organs (Arendt, 2005, 2008). Therefore, we undertook a comprehensive molecular and functional analysis of the planarian protonephridia.

We have identified protonephridial cell types homologous to the vertebrate podocyte, which is the ultrafiltration apparatus and the renal tube that functions as a filtrate modifier. We have accomplished this by demonstrating that the planarian orthologues of two major constituents of the podocyte slit diaphragm, *NPHS1* and *NEPH1*, are expressed in planarian flame cells and are required for the formation and maintenance of their filtration diaphragms. Furthermore, we find that expression of many *slc* genes in the protonephridial tubule suggest an important role in filtrate modification by reabsorption

and secretion. Surprisingly, expression of *slc* genes in specific segments along the protonephridial tubule is also confined to the equivalent segments of the vertebrate pronephros/metanephros, demonstrating unexpected molecular and functional similarities between protonephridial segments and their vertebrate pronephric/metanephric counterparts. We also developed assays to probe the functional roles of planarian protonephridia, and provide further evidence supporting functional homology for each protonephridial compartment.

Not only are the structure and function of planarian protonephridia very similar to vertebrate nephrons, many regulatory genes that govern early kidney development are also shared between planarians and vertebrates. For instance, many members of RTK signaling pathways, including EGFR, have been reported to play an important role in guiding morphogenesis of the renal tubule (Costantini and Kopan, 2010; Ishibe et al., 2009). In this study, we show that a member of RTK signaling, *EGFR-5*, is also required for branching morphogenesis in planarian protonephridia. Furthermore, many regulatory genes that are essential for early kidney development, including *POU2/3*, *six1/2*, and *sall*, are shared between planarians and vertebrates (Fig. 4.1; and see (Scimone et al., 2011) for more information). Systematic functional characterization of these transcriptional regulators in planarian protonephridia, as well as their regulatory interactions, will be an interesting area to explore in the future for better understanding the evolutionary history of excretory systems. Nonetheless, these findings strongly suggest that the basic architecture of the nephrons evolved early in animal evolution, and the last common ancestor of vertebrates and invertebrates must have already possessed “glomerular” ultrafiltration excretory organs.

Figure 4.1. Regulatory genes controlling early kidney development are expressed in planarian protonephridia. **a**, Whole-mount expression patterns of indicated genes by *in situ* hybridization (NBT/BCIP development). Scale bars: 500 μm. **b-j,** Representative images showing expression domains of indicated genes in planarian protonephridia. Fluorescent overlay of indicated gene (red) with PT marker (AcTub) and DT marker (*CAVII-1*). A color-coded scheme of the protonephridial tubule at the end of each panel summarizes expression domain of indicated gene. Images are maximum projections of confocal Z-sections. Scale bars: 50 μm. **k**, Cartoon showing expression map of regulatory genes governing kidney development along protonephridial tubule. Abbreviations for segments of protonephridia are as follows: PT1, PT2, and PT3, segments of proximal tubule; DT1 and DT2, segments of distal tubule; CD, collecting duct.

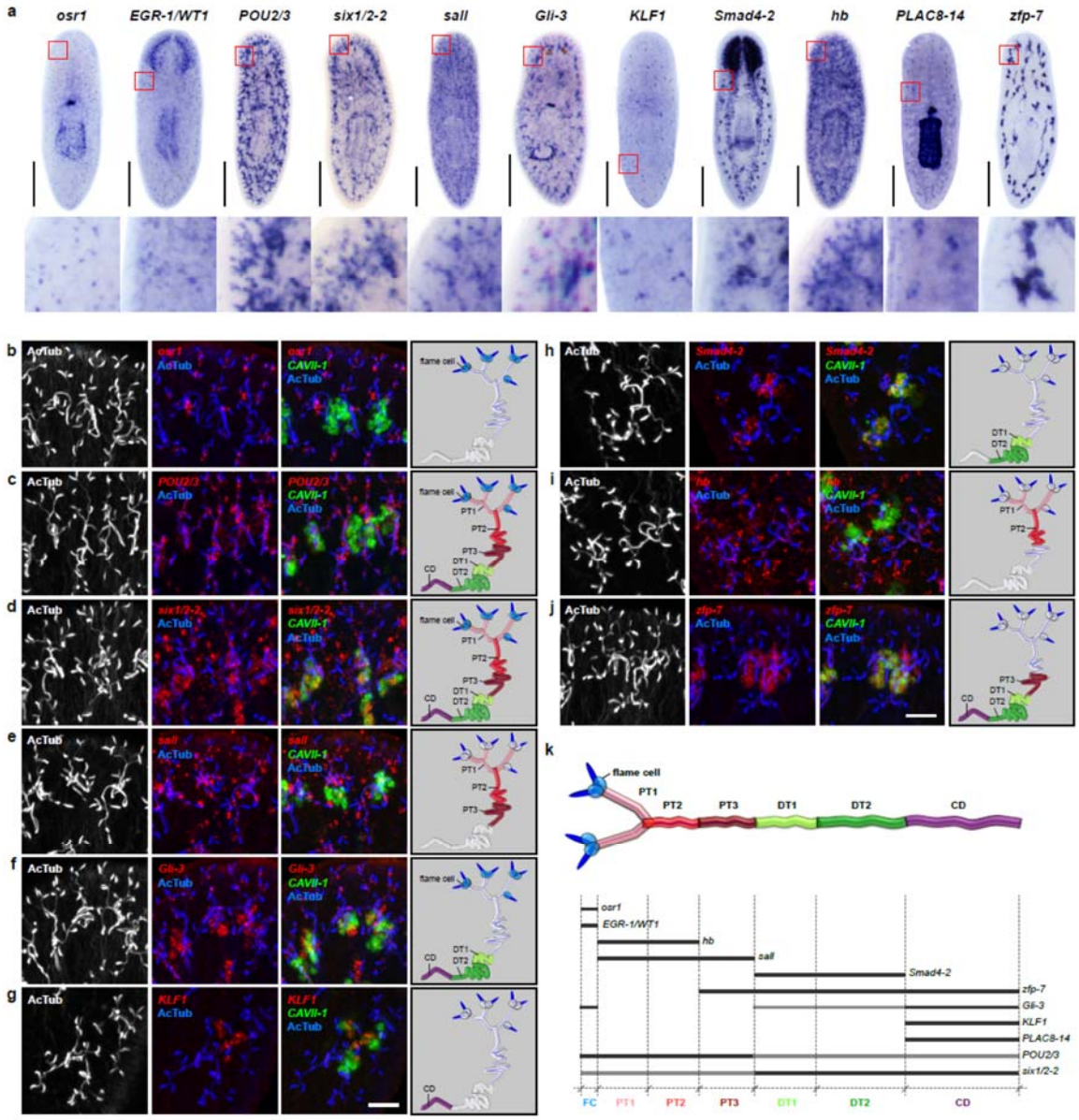
a
osr1
EGR-1/WT1
POU2/3
six1/2-2
sall
Gli-3
KLF1
Smad4-2
hb
PLAC8-14
zfp-7
b
c
d
e
f
g
h
i
j
AcTub
CAVII-1
flame cell
PT1
PT2
PT3
DT1
DT2
CD
k
FC

Planarian Protonephridia – A Novel Invertebrate Model for Better Understanding Kidney Biology

Planarians have emerged as powerful model organisms to study organ regeneration and stem cell biology (Gurley and Sanchez Alvarado, 2008; Reddien and Sanchez Alvarado, 2004; Sanchez Alvarado, 2004; Sanchez Alvarado and Newmark, 1998). Our discovery of the recapitulation of many renal defects in planarian protonephridia expands the potential of planarian protonephridia as a model system to study many important aspects of kidney biology and diseases.

Our observation of the *de novo* regeneration of planarian protonephridia reveals a high degree of similarity to early formation of the vertebrate nephrons. At the earliest stage of regeneration, we and others observe the accumulation of cells in the blastema to form the proto-tubule (Rink et al., 2011; Scimone et al., 2011). The proto-tubule then undergoes extensive branching morphogenesis and segmentation to form the mature tubule. Despite the significant increase in protonephridial progenitors and differentiated cells in the blastema during regeneration, mitotic events are rarely found in this region (Tasaki et al., 2011), indicating that branching of protonephridia is not driven by localized proliferation. Instead, branching must occur through cell migration and rearrangements, highly reminiscent of the UB branching morphogenesis during vertebrate development (Costantini and Kopan, 2010). Furthermore, we observe the tubular cells extend perpendicular to the long axis of the duct during the process of tubular elongation. This asymmetric shape is hypothesized to reflect a process of convergent extension (i.e., lateral intercalation), making the duct narrower and longer (Costantini and Kopan, 2010). These data suggest that convergent extension likely occurs to facilitate tubular elongation of

protonephridia, which is highly similar to that of the pronephric/metanephric tubules. Unfortunately, there is still so little known about cellular events and molecular control of kidney patterning and morphogenesis. Compounding this problem is the complicated architecture and inaccessibility of the mammalian metanephros. Given the simplicity, accessibility, and rapid regeneration of planarian protonephridia, together with the large-scale RNAi screening ability, planarian protonephridia hold tremendous potential for identifying and studying genes involved in nephron patterning and morphogenesis.

As mentioned previously, the process of filtrate modification to reabsorb essential nutrients and eliminate harmful substances in the nephron is restricted to specific segments of the renal tubules. Any dysregulation of patterning, segmentation, or morphogenesis of the nephron severely affects kidney function. For example, autosomal renal tubular dysgenesis (OMIM 267430) is a severe disorder characterized by lack of proximal tubule differentiation (Allanson et al., 1983). Unfortunately, molecular regulation of nephron segmentation and terminal differentiation of individual segment is not well understood. Given the significant similarity in the topologies of protonephridial and metanephric tubules, together with the substantial set of markers developed in this study, in-depth investigation of how differentiation of protonephridial segments is achieved will provide fruitful insights into understanding nephron segmentation.

Furthermore, the recapitulation of many kidney diseases in planarian protonephridia indicates their potential as a new invertebrate system for modeling these disorders. For instance, glomerular diseases are characterized by reduced filtration integrity with consequent loss of protein (proteinuria) and/or blood cells (hematuria) into the urine (Lennon et al., 2014). Many recent studies have suggested the emerging roles of

the slit diaphragm complex *NPHS1-NEPH1* as regulator of podocyte behavior, in response to stress and injury, including cell survival, polarity, and differentiation (Grahammer et al., 2013). How these functions of the slit diaphragm are related to disease pathologies is not well understood. Since planarian protonephridia also require *NPHS1* and *NEPH1* for the normal function of their filtration cells (flame cells), they provide a tantalizing new model for studying podocyte biology and diseases. Furthermore, the reduced rate of filtration and glomerular proteinuria have been shown to have negative effects on renal tubular integrity (Guo et al., 2012), yet the molecular and cellular mechanisms underlying these phenotypes are unclear. Again, this is due to the complexity and inaccessibility of vertebrate nephrons, as well as the paucity of suitable invertebrate model organisms. Along with the loss of filtration capacity of flame cells when *NPHS1* or *NEPH1* function is compromised, we observe abnormal lengthening of protonephridial tubules accompanying the increase of protonephridial progenitors in planarians (Fig. 4.2), suggesting an adaptive response of tubules for the decrease of filtration rate and/or loss of proteins. This recapitulates the phenotypes found in metanephric tubules when *NPHS1* or *NEPH1* are perturbed. Altogether, planarian protonephridia could provide a simple and tractable model to better understand the molecular mechanism of compensatory proliferation in the tubules. They might help us ascertain whether the increase in cell numbers provides an adaptive advantage by increasing the number of cells available for reabsorption of abnormally filtered proteins and other small molecules, as has been hypothesized previously.

Additionally, in the recent years, mutations in various *slc* genes have been identified as the underlying causes of various forms of familial renal diseases in humans. These mutations dampen functions that are normally confined to specific nephron segments

Figure 4.2. Abnormal tubular elongation in *NPHS1-6(RNAi)* and *NEPH-3(RNAi)* animals. a, Fluorescent overlay of PT marker (*slc6a-13*) with DT marker (*CAVII-1*). Scale bars: 50 μm. Images in are maximum projections of confocal Z-sections. **b,** Quantification of average area of each *slc6a-13*$^{+}$ tubule in *Control(RNAi)* and *NPHP8(RNAi)* animals. *** $p<0.001$ versus control. **c,** Magnified view showing the region surrounding photoreceptor. Fluorescent overlay of *POU2/3* and *six1/2-2* with pan stem cell marker *Smedwi-1* and mitotic marker H3P. Scale bar: 50 μm.

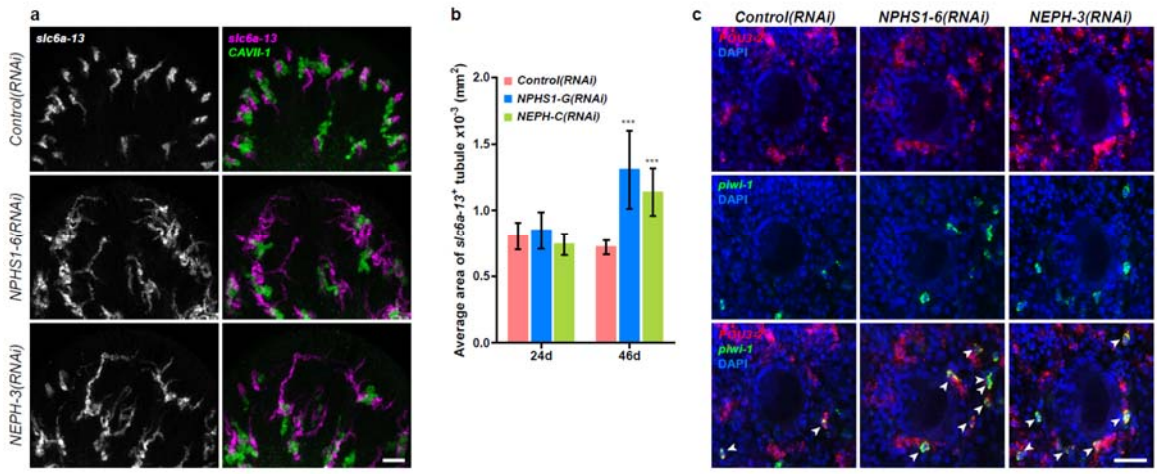
a
slc6a-13
slc6a-13
CAVII-1
Control(RNAi)
NPHS1-6(RNAi)
NEPH-3(RNAi)
b
Control(RNAi)
NPHS1-G(RNAi)
NEPH-C(RNAi)
Average area of slc6a-13+ tubule x10-3 (mm2)
2.0
1.5
1.0
0.5
0.0
***
***
24d
46d
c
Control(RNAi)
NPHS1-6(RNAi)
NEPH-3(RNAi)
Aqp3-a
DAPI
piwi-1
DAPI
Aqp3-a
piwi-1
DAPI

(Zelikovic, 2001). For instance, mutations in *slc4a1* cause renal acidosis in the distal tubule (OMIM 611590). Interesting, our systematic expression analysis of *slc* genes in planarian protonephridia show clear evidence that the planarian homologs of many *slc* genes are expressed in regions corresponding to equivalent segments of the nephron. Furthermore, downregulation of *slc* function leads to transport abnormalities in planarians. We demonstrate that RNAi of *slc4a-6* in planarians causes a global acidification of the intercellular environment (Fig. 3.4l). We therefore believe that planarian protonephridia may offer a useful biological context for exploring the basic molecular mechanisms involved in inherited human renal diseases.

Planarian Protonephridia – New Opportunities to Study Stem Cell Based Kidney Regeneration

Kidney diseases interfere with normal nephron development or cause nephron impairment, affecting millions of people worldwide. Disturbances in kidney function can lead to kidney failure, which requires patients to undergo life-long dialysis or an organ transplant. Understanding how nephrons develop and how they regenerate has received increasing attention because of the possible clinical applications.

Emerging evidence suggests the involvement of stem and progenitors cells during the development and regeneration of animal excretory systems (Becherucci et al., 2014; Blanpain et al., 2007; Davidson, 2011; Diep et al., 2011; He et al., 2009; Holmes, 2014; Romagnani, 2009, 2010; Romagnani et al., 2013; Ronconi et al., 2009; Scimone et al., 2011; Singh et al., 2007; Urbach et al., 2014). However, neogenesis of excretory organs in adults has only been observed in fish and other more basal branches of the animal

kingdom. *De novo* kidney regeneration has not been observed in mammals (Davidson, 2011; Elger et al., 2003; Reimschuessel, 2001; Reimschuessel et al., 1990; Rink et al., 2011; Romagnani, 2010; Scimone et al., 2011). Studying the regenerative strategies of more primitive animal excretory organs may prove key for understanding and modulating the regenerative capacities of the mammalian kidneys.

Planarians are a useful model system to elucidate basic regeneration phenomena (Elliott and Sanchez Alvarado, 2013; Reddien and Sanchez Alvarado, 2004), but it is currently unclear to what extent planarian regenerative processes are comparable and applicable to vertebrates. A recent study has suggested that tissue-specific progenitors are involved in protonephridial regeneration in planarians (Scimone et al., 2011), recapitulating regenerative processes of vertebrate kidneys (Romagnani et al., 2013). Fascinatingly, regulatory genes required for normal function of renal progenitor populations are highly conserved between vertebrates and planarians, suggesting deep mechanistic conservation of the regenerative strategy of the kidneys. In this study, we further demonstrate the requirement of stem and progenitor cells during cyst formation in planarian protonephridia. Interestingly, abnormal activation of renal progenitor markers in cystic kidneys has also been reported (Karafin et al., 2011; Murer et al., 2002; Senanayake et al., 2013; Stayner et al., 2006; Winyard et al., 1996). Future investigations should aim to better understand the genes involved in protonephridia regeneration and to identify the molecular signals that activate transcriptional programs producing protonephridial lineages in planarians during cystogenesis. Since these endeavors may provide fruitful insights into understanding kidney regeneration and diseases, planarian

protonephridia constitute a new and relevant model organism to study stem cell based kidney regeneration.

Conclusion: A Model for All Reasons

Altogether, our comprehensive investigation of planarian protonephridia demonstrates extensive molecular and functional homologies between protonephridia and vertebrate nephrons. Our finding supports a common evolutionary origin of animal excretory organs. Furthermore, we have shown that planarian protonephridia are relevant to a broad range of fundamental questions pertaining to emerging areas in kidney development and diseases. We present a comprehensive set of molecular markers and tools to study the planarian excretory system. Together with the high speed and low cost of performing robust and high-throughput RNAi screens in planarians, these flatworms offer an exciting new prospect for advancing our understanding of kidney development, diseases, and evolution.

References

Allanson, J.E., Pantzar, J.T., and MacLeod, P.M. (1983). Possible new autosomal recessive syndrome with unusual renal histopathological changes. Am J Med Genet *16*, 57-60.

Arendt, D. (2005). Genes and homology in nervous system evolution: Comparing gene functions, expression patterns, and cell type molecular fingerprints. Theory Biosci *124*, 185-197.

Arendt, D. (2008). The evolution of cell types in animals: Emerging principles from molecular studies. Nat Rev Genet *9*, 868-882.

Bartolomaeus, T., and Quast, B. (2005). Structure and development of nephridia in annelida and related taxa. Hydrobiologia *535-536*, 139-165.

Becherucci, F., Lazzeri, E., Lasagni, L., and Romagnani, P. (2014). Renal progenitors and childhood: From development to disorders. Pediatr Nephrol *29*, 711-719.

Blanpain, C., Horsley, V., and Fuchs, E. (2007). Epithelial stem cells: Turning over new leaves. Cell *128*, 445-458.

Buechner, M. (2002). Tubes and the single C. elegans excretory cell. Trends Cell Biol *12*, 479-484.

Costantini, F., and Kopan, R. (2010). Patterning a complex organ: Branching morphogenesis and nephron segmentation in kidney development. Dev Cell *18*, 698-712.

Davidson, A.J. (2011). Uncharted waters: Nephrogenesis and renal regeneration in fish and mammals. Pediatr Nephrol *26*, 1435-1443.

Diep, C.Q., Ma, D., Deo, R.C., Holm, T.M., Naylor, R.W., Arora, N., Wingert, R.A., Bollig, F., Djordjevic, G., Lichman, B., *et al.* (2011). Identification of adult nephron progenitors capable of kidney regeneration in zebrafish. Nature *470*, 95-100.

Dow, J.A., and Romero, M.F. (2010). Drosophila provides rapid modeling of renal development, function, and disease. Am J Physiol Renal Physiol *299*, F1237-1244.

Elger, M., Hentschel, H., Litteral, J., Wellner, M., Kirsch, T., Luft, F.C., and Haller, H. (2003). Nephrogenesis is induced by partial nephrectomy in the elasmobranch leucoraja erinacea. J Am Soc Nephrol *14*, 1506-1518.

Elliott, S.A., and Sanchez Alvarado, A. (2013). The history and enduring contributions of planarians to the study of animal regeneration. Wiley Interdiscip Rev Dev Biol *2*, 301-326.

Goodrich, E.S. (1945a). The study of nephridia and genital ducts since 1895. Q J Microsc Sci *86*, 113-301.

Goodrich, E.S. (1945b). The study of nephridia and genital ducts since 1895 (continued). Q J Microsc Sci *86*, 303-392.

Grahammer, F., Schell, C., and Huber, T.B. (2013). The podocyte slit diaphragm--from a thin grey line to a complex signalling hub. Nat Rev Nephrol *9*, 587-598.

Guo, J.K., Marlier, A., Shi, H., Shan, A., Ardito, T.A., Du, Z.P., Kashgarian, M., Krause, D.S., Biemesderfer, D., and Cantley, L.G. (2012). Increased tubular proliferation as an adaptive response to glomerular albuminuria. J Am Soc Nephrol *23*, 429-437.

Gurley, K.A., and Sanchez Alvarado, A. (2008). Stem cells in animal models of regeneration. StemBook, ed. (Cambridge: The Stem Cell Research Community).

He, S., Nakada, D., and Morrison, S.J. (2009). Mechanisms of stem cell self-renewal. Annu Rev Cell Dev Biol *25*, 377-406.

Holmes, D. (2014). Stem cells: Budding renal progenitors. Nat Rev Nephrol *10*, 4.

Ishibe, S., Karihaloo, A., Ma, H., Zhang, J., Marlier, A., Mitobe, M., Togawa, A., Schmitt, R., Czyczk, J., Kashgarian, M., *et al.* (2009). Met and the epidermal growth factor receptor act cooperatively to regulate final nephron number and maintain collecting duct morphology. Development *136*, 337-345.

Karafin, M., Parwani, A.V., Netto, G.J., Illei, P.B., Epstein, J.I., Ladanyi, M., and Argani, P. (2011). Diffuse expression of pax2 and pax8 in the cystic epithelium of mixed epithelial stromal tumor, angiomyolipoma with epithelial cysts, and primary renal synovial sarcoma: Evidence supporting renal tubular differentiation. Am J Surg Pathol *35*, 1264-1273.

Lennon, R., Randles, M.J., and Humphries, M.J. (2014). The importance of podocyte adhesion for a healthy glomerulus. Front Endocrinol (Lausanne) *5*, 160.

Murer, L., Caridi, G., Della Vella, M., Montini, G., Carasi, C., Ghiggeri, G., and Zacchello, G. (2002). Expression of nuclear transcription factor pax2 in renal biopsies of juvenile nephronophthisis. Nephron *91*, 588-593.

Nelson, F.K., Albert, P.S., and Riddle, D.L. (1983). Fine structure of the caenorhabditis elegans secretory-excretory system. J Ultrastruct Res *82*, 156-171.

Reddien, P.W., and Sanchez Alvarado, A. (2004). Fundamentals of planarian regeneration. Annu Rev Cell Dev Biol *20*, 725-757.

Reimschuessel, R. (2001). A fish model of renal regeneration and development. ILAR J *42*, 285-291.

Reimschuessel, R., Bennett, R.O., May, E.B., and Lipsky, M.M. (1990). Development of newly formed nephrons in the goldfish kidney following hexachlorobutadiene-induced nephrotoxicity. Toxicol Pathol *18*, 32-38.

Rink, J.C., Vu, H.T., and Sanchez Alvarado, A. (2011). The maintenance and regeneration of the planarian excretory system are regulated by egfr signaling. Development *138*, 3769-3780.

Romagnani, P. (2009). Toward the identification of a "renopoietic system"? Stem Cells *27*, 2247-2253.

Romagnani, P. (2010). From proteus to prometheus: Learning from fish to modulate regeneration. J Am Soc Nephrol *21*, 726-728.

Romagnani, P., Lasagni, L., and Remuzzi, G. (2013). Renal progenitors: An evolutionary conserved strategy for kidney regeneration. Nat Rev Nephrol *9*, 137-146.

Ronconi, E., Sagrinati, C., Angelotti, M.L., Lazzeri, E., Mazzinghi, B., Ballerini, L., Parente, E., Becherucci, F., Gacci, M., Carini, M., *et al.* (2009). Regeneration of glomerular podocytes by human renal progenitors. J Am Soc Nephrol *20*, 322-332.

Ruppert, E.E. (1994). Evolutionary origin of the vertebrate nephron. Amer. Zool *34*, 542-553.

Ruppert, E.E., and Smith, P.R. (1988). The functional organization of filtration nephridia. Biol Rev *63*, 231-258.

Sanchez Alvarado, A. (2004). Regeneration and the need for simpler model organisms. Philos Trans R Soc Lond B Biol Sci *359*, 759-763.

Sanchez Alvarado, A., and Newmark, P.A. (1998). The use of planarians to dissect the molecular basis of metazoan regeneration. Wound Repair Regen *6*, 413-420.

Scimone, M.L., Srivastava, M., Bell, G.W., and Reddien, P.W. (2011). A regulatory program for excretory system regeneration in planarians. Development *138*, 4387-4398.

Senanayake, U., Koller, K., Pichler, M., Leuschner, I., Strohmaier, H., Hadler, U., Das, S., Hoefler, G., and Guertl, B. (2013). The pluripotent renal stem cell regulator six2 is activated in renal neoplasms and influences cellular proliferation and migration. Hum Pathol *44*, 336-345.

Singh, S.R., Liu, W., and Hou, S.X. (2007). The adult drosophila malpighian tubules are maintained by multipotent stem cells. Cell Stem Cell *1*, 191-203.

Stayner, C., Iglesias, D.M., Goodyer, P.R., Ellis, L., Germino, G., Zhou, J., and Eccles, M.R. (2006). Pax2 gene dosage influences cystogenesis in autosomal dominant polycystic kidney disease. Hum Mol Genet *15*, 3520-3528.

Tasaki, J., Shibata, N., Nishimura, O., Itomi, K., Tabata, Y., Son, F., Suzuki, N., Araki, R., Abe, M., Agata, K., *et al.* (2011). Erk signaling controls blastema cell differentiation during planarian regeneration. Development *138*, 2417-2427.

Urbach, A., Yermalovich, A., Zhang, J., Spina, C.S., Zhu, H., Perez-Atayde, A.R., Shukrun, R., Charlton, J., Sebire, N., Mifsud, W., *et al.* (2014). Lin28 sustains early renal progenitors and induces wilms tumor. Genes Dev *28*, 971-982.

Winyard, P.J., Risdon, R.A., Sams, V.R., Dressler, G.R., and Woolf, A.S. (1996). The pax2 tanscription factor is expressed in cystic and hyperproliferative dysplastic epithelia in human kidney malformations. J Clin Invest *98*, 451-459.

Zelikovic, I. (2001). Molecular pathophysiology of tubular transport disorders. Pediatr Nephrol *16*, 919-935.

APPENDIX A

SUMMARY INFORMATION OF THE PLANARIAN HOMOLOGS OF SOLUTE CARRIER GENES

No.	Gene ID	Top Hit - *Homo sapiens*	E-value	Forward Primer	Reverse Primer
1	*Smed-slc1a-1*	excitatory amino acid transporter 1 isoform 5	7E-71	GTTGTTCCAGCATATTGGGC	TGTTCACAATTTTCATGATGGC
2	*Smed-slc1a-2*	excitatory amino acid transporter 2 isoform X2	5E-176	ATGGAGCCACACGAGAACTG	TGGTTACACAAGAAACAAGACCAC
3	*Smed-slc1a-3*	excitatory amino acid transporter 3	2E-123	TGACTTCGAACCCAAAGATTG	TCTGGATTATTCCTCCACCG
4	*Smed-slc1a-4*	excitatory amino acid transporter 2 isoform 2	3E-147	GGAGAAATGCTAATG	CCTGAACCCAAAGAATCACC
5	*Smed-slc1a-5*	excitatory amino acid transporter 2 isoform 1	0	TACGATTGCTTCTGTGGTGC	CACAAATGATCAACGATTCC
6	*Smed-slc2a-1*	solute carrier family 2, facilitated glucose transporter member 1	1E-114	AAATGTTTCAGATGACCCGC	TTTCGAAATGGGATCCAAAG
7	*Smed-slc2a-2*	solute carrier family 2, facilitated glucose transporter member 1	4E-88	GCCGTCATAAATCTTCCAGC	AATGCCAAGTCTCGAGCAAC
8	*Smed-slc2a-3*	solute carrier family 2, facilitated glucose transporter member 1	3E-67	ATGGCAGTCATCAATCTCCC	TGTGCGATTTTTCGTTTCAG
9	*Smed-slc2a-4*	solute carrier family 2, facilitated glucose transporter member 1	2E-86	GAAAAATTTCGCCCACTCTG	ATCACAGTCGTACCGAAGGC
10	*Smed-slc2a-5*	solute carrier family 2, facilitated glucose transporter member 1	5E-122	TTTGGGTATCAAACCGGC	AGGAACAGGTGAGTTTTGGG
11	*Smed-slc2a-6*	solute carrier family 2, facilitated glucose transporter member 3	8E-74	TCGGGAGAAAGAAAGCATTG	TGCAATTTCAGCAAAAGAGC
12	*Smed-slc2a-7*	solute carrier family 2, facilitated glucose transporter member 1	1E-119	CACAAACGTCCATCAAGCTG	CAATGAAATCGCGATGAAAG
13	*Smed-slc2a-8*	solute carrier family 2, facilitated glucose transporter member 3	3E-47	GGAATCATTGGAAGTGGCTG	ACCGATTCCCATTGCTACAG
14	*Smed-slc2a-9*	proton myo-inositol cotransporter	1E-79	AATTGGCGGGTTTATGTTTG	CGCGGAATAGATCCAAAATG
15	*Smed-slc2a-10*	proton myo-inositol cotransporter	1E-157	AATCCGCAACTCTCGAAGC	CCAGAATGTCCCGTATTTGG
16	*Smed-slc2a-11*	solute carrier family 2, facilitated glucose transporter member 3	3E-42	TTTTGGAGTTTGTTGTGGACC	TGGCTAAACAACCGATTTGC

No.	Gene ID	Top Hit - *Homo sapiens*	E-value	Forward Primer	Reverse Primer
17	*Smed-slc3a-1*	4F2 cell-surface antigen heavy chain isoform c	2E-19	ATGAACGACGTCCAGAAACC	TTAAAAACGTGAACCGAGCC
18	*Smed-slc4a-1*	sodium-driven chloride bicarbonate exchanger isoform X3	0	TGAACCGCCTAAGAGTGGTC	CTCGCAGAAGGAGGAATGAC
19	*Smed-slc4a-2*	sodium-driven chloride bicarbonate exchanger isoform X3	0	TTGGTCAAAGCCTCATGTTG	AGCAGTGAACAAATGGACCC
20	*Smed-slc4a-3*	anion exchange protein 2 isoform 1	5E-45	ACGCAAACCCGAGATATTTG	TCCTAGCATTGCTGACGTT
21	*Smed-slc4a-4*	sodium bicarbonate transporter-like protein 11 isoform X2	0	CCCTTAGCAATGGACGTTTC	TATGACATCTCGCTGGTTCG
22	*Smed-slc4a-5*	sodium bicarbonate transporter-like protein 11 isoform X2	2E-180	AACATTTGTCCCTTTCACCG	CTGGGAGAGAAACCAAGTGC
23	*Smed-slc4a-6*	band 3 anion transport protein	8E-84	GGAATGGGAAATTCTGAGCC	TGCCTTCATCCTTTGAATCC
24	*Smed-slc4a-7*	band 3 anion transport protein	3E-68	CCTGACTCGGAAGTAGCTGG	TTCTGCGCTGCATTAAGTTG
25	*Smed-slc4a-8*	sodium bicarbonate transporter-like protein 11 isoform 3	0	TTAAAACTTCCGTGGCTTGC	ATTTTTCGTCGATCACTCGG
26	*Smed-slc4a-9*	sodium bicarbonate transporter-like protein 11 isoform 3	3E-44	CCAGCATTTTATTTGACCCC	ACATTTCCGCATAAAAC
27	*Smed-slc4a-10*	sodium bicarbonate transporter-like protein 11 isoform 2	2E-37	GAAACATCTTTCTTCAATCAATC	ATCTTTCAGCCCAACCACAG
28	*Smed-slc5a-1*	sodium-coupled monocarboxylate transporter 1	8E-129	TCTTGCAAATCGGAAAATGG	TGTTGCGTCAATTGAACCTC
29	*Smed-slc5a-2*	sodium/glucose cotransporter 1 isoform 1	0	TGGCGGGTACTTTTTAGCAG	TTCTTGTGCTGTCAAAACCG
30	*Smed-slc5a-3*	sodium-coupled monocarboxylate transporter 1	5E-141	GGCGCTATTCCAGTAGCTTG	ATCGCACTTTGTCCTCTTGC
31	*Smed-slc5a-4*	sodium-coupled monocarboxylate transporter 2	1E-127	GCGTATGGGCTCTATTGCTC	TTCCACAGTTTTTGCAATGG
32	*Smed-slc5a-5*	high affinity choline transporter 1	0	TGTTAAGCCAAGTTCCGCTC	AAAGACATTCGTTTGGCGAG

No.	Gene ID	Top Hit - *Homo sapiens*	E-value	Forward Primer	Reverse Primer
33	*Smed-slc6a-1*	sodium- and chloride-dependent GABA transporter 1	0	TGACAAGCACAGAAGGAACG	GCTAGAAAAATTCCAATCGC
34	*Smed-slc6a-2*	sodium- and chloride-dependent taurine transporter isoform a	2E-177	TGCTATAAAAATGGCGGAGG	CATTGGTGAAATGCTCGATG
35	*Smed-slc6a-3*	sodium-dependent noradrenaline transporter isoform 2	0	TTGGAATTGGAACAAGGAGC	ATGGGTCTCCCGTTATTTG
36	*Smed-slc6a-4*	sodium-dependent serotonin transporter	0	GAATAAGCGATTCTCTG	ATCAATGGTCTCGGTTCAGG
37	*Smed-slc6a-5*	sodium- and chloride-dependent glycine transporter 2	0	ACAGCTCGTGGAAATTGGTC	CATACCGGTCGTCAATCTC
38	*Smed-slc6a-6*	sodium- and chloride-dependent glycine transporter 2	9E-169	ATGAGATGAACAGTTCCCCG	CAGACTCCTTTTGCTTTGG
39	*Smed-slc6a-7*	sodium-dependent noradrenaline transporter isoform 2	0	ACGAAACGTCTAATGGTCCG	CAGGAATTTCCAGCAGATCC
40	*Smed-slc6a-8*	sodium-dependent dopamine transporter	2E-162	TCAAATTGTCGAACAATCGC	TATTCGGTAGAGGACCACGC
41	*Smed-slc6a-9*	sodium- and chloride-dependent glycine transporter 2	1E-156	CAAAGGCTTGAGACAATCCG	TCGGAGAATAACAGCCAACC
42	*Smed-slc6a-10*	sodium- and chloride-dependent glycine transporter 2	3E-113	CACAAGACGTTGAGGCAGAC	TATGACAAAAATCGCCAACG
43	*Smed-slc6a-11*	sodium-dependent proline transporter	3E-114	CCCAATAGATTGGTGGATCG	TACGAGGGCGATGGAATAAC
44	*Smed-slc6a-12*	sodium- and chloride-dependent glycine transporter 1 isoform 3	9E-129	TCAAGAACGTGCAATGTGG	AGTAGACCTGATGCGAACCG
45	*Smed-slc6a-13*	sodium- and chloride-dependent glycine transporter 2	0	AAAAATCGATTCATGGCAGC	AAAATAAATTGGCACTGCGG
46	*Smed-slc6a-14*	sodium-dependent proline transporter	2E-106	CAAAACCTCTTGGATCTGGG	TCGGTCTTGGGAATGTATGG
47	*Smed-slc6a-15*	sodium-dependent proline transporter	3E-104	AAATGAGGATTCCCCTCCAG	TCGGGATTGGTCTAAAGCAC
48	*Smed-slc6a-16*	sodium- and chloride-dependent glycine transporter 2	4E-98	CATGTGTCGGATATGCTGTTG	TTTCGAAGACCCAATTCTGG

No.	Gene ID	Top Hit - *Homo sapiens*	E-value	Forward Primer	Reverse Primer
49	*Smed-slc6a-17*	sodium-dependent proline transporter	4E-113	TGTAAATGGGTTTTCTCCCG	ACTATTTCTCCCCAAAGCGG
50	*Smed-slc6a-18*	sodium-dependent noradrenaline transporter isoform 2	3E-80	TGCAGATGAAGACAAGGCAC	TTTCGATTTCAAAGCAAGGG
51	*Smed-slc6a-19*	sodium-dependent proline transporter	3E-82	CTCCCAAGCTCCTGTATTG	TAATGGCCGAGGAAGTGTTC
52	*Smed-slc6a-20*	sodium- and chloride-dependent GABA transporter 2 isoform 1	4E-42	GCGGTGAAAAATCTCATTG	AATATGGCCCGTAGATGTCG
53	*Smed-slc6a-21*	sodium-dependent serotonin transporter	5E-42	ACATTTTCTCGGTGCCAAAC	TCAGTGGCTTGGGATACACC
54	*Smed-slc6a-22*	sodium- and chloride-dependent glycine transporter 2	1E-61	AAATGAATGAACTCGATTGCG	ACTGGATACCACGGCTTGTC
55	*Smed-slc6a-23*	sodium- and chloride-dependent glycine transporter 2	8E-127	GGAAAATGCATAGAGTTGG	AAATCATGACTGCAAACTGACC
56	*Smed-slc6a-24*	sodium-dependent neutral amino acid transporter B(0)AT3	1E-18	CCATTGGTCGATTTTTACG	ATTCTTGGATTTGGGAGGC
57	*Smed-slc7a-1*	probable cationic amino acid transporter	4E-145	GAATCGTGTGTCATGTTGG	CTGTCGGAGAGTTCATTGCC
58	*Smed-slc7a-2*	low affinity cationic amino acid transporter 2 isoform 2	0	AATTCGGAGCTAGGGTTCC	TCGCTGGGATACATCTTTGG
59	*Smed-slc7a-3*	high affinity cationic amino acid transporter 1	9E-92	AACTCAACTGCAACACACGC	TTTTCTCTTCCGCCTTTTCC
60	*Smed-slc7a-4*	cystine/glutamate transporter	9E-124	CATCAGCGTCAAAGAACTG	TCAGACTCATCCTGGCACTG
61	*Smed-slc7a-5*	high affinity cationic amino acid transporter 1	3E-82	TTTCCCAACTGCAGACATTG	GTGCAAGTGGCATTAAAGG
62	*Smed-slc7a-6*	Y+L amino acid transporter 1	5E-153	GATCAATTATTGGGTCTGGC	ACTTTCTTTTGACTCGGG
63	*Smed-slc7a-7*	Y+L amino acid transporter 2	3E-133	CAATGAGGATAAATGCCAAC	TCAAATAAACCGGAACTGCC
64	*Smed-slc7a-8*	cystine/glutamate transporter	6E-127	ACTCCGTTGGAATGTCGATG	TTCTGTGAGATTGGTCACCG

No.	Gene ID	Top Hit - *Homo sapiens*	E-value	Forward Primer	Reverse Primer
65	*Smed-slc7a-9*	Y+L amino acid transporter 2	2E-140	GTAGCATGATTGGGTCTGG	ATTCGATTGAATGGTTTCGG
66	*Smed-slc7a-10*	Y+L amino acid transporter 2	1E-144	CCACCTGAAAATTCTTCCC	TTCGCCAATAAAGGTTGGTC
67	*Smed-slc8a-1*	sodium/calcium exchanger 3 isoform D precursor	0	CATTACCATCCCGATGGATTCAATGCGAACCTC	TCACATTTTCGAACACATTGC
68	*Smed-slc8a-2*	sodium/calcium exchanger 1 isoform D precursor	0	CATGTGGCAACCAGCAATAG	TTTAGGACCGCCAAGTTCAC
69	*Smed-slc8a-3*	sodium/calcium exchanger 3 isoform F	2E-100	TCAATTGATGAGGAAAAGTCAC	TTTTTCGGTCCTCCTAGTTCAC
70	*Smed-slc8a-4*	sodium/calcium exchanger 1 isoform B precursor	0	TGCTTCAATGAAACGGTCTG	ACCTCCGAGTTCTCCACCTC
71	*Smed-slc8a-5*	sodium/calcium exchanger 1 isoform B precursor	0	ATTCTAAATGCGTGGAAGG	GCCAAACATATGCTACTATGG
72	*Smed-slc9a-1*	sodium/hydrogen exchanger 2 precursor	2E-81	TTTAATGGTGTTCGGCTGTG	AATGCCATTGGATTTTCCTG
73	*Smed-slc9a-2*	sodium/hydrogen exchanger 6 isoform a precursor	2E-168	ATTTGTGCATGAAACGAG	AGGAATGCATCGGAACTCAC
74	*Smed-slc9a-3*	sodium/hydrogen exchanger 2 precursor	1E-61	CATTTCTGATTACCGCTGG	TTGTTGGGGGACTGAGGTAG
75	*Smed-slc9a-4*	sodium/hydrogen exchanger 1	7E-97	CATCACATGCCGAGATTGTC	CAATTGACATTTGCTGCGTC
76	*Smed-slc9a-5*	sodium/hydrogen exchanger 8 isoform 2	4E-179	AAAATGATGGGTAATTGGCG	CAAATTTGGCCCACAAAATC
77	*Smed-slc9a-6*	sodium/hydrogen exchanger 2 precursor	2E-80	CCAGTAATCCTGCCTTGAG	CATGGTGCCATATTTAGGGG
78	*Smed-slc9a-7*	sodium/hydrogen exchanger 2 precursor	2E-76	TATTTCTCTTGTCGGGTGGC	TTCTGGCTGTTGGGTGTATG
79	*Smed-slc9a-8*	sodium/hydrogen exchanger 3 isoform 1	1E-74	CATCATCGGTTTCCACATTG	CTTAGCTATTGCCTCCGCAC
80	*Smed-slc9a-9*	sodium/hydrogen exchanger 2 precursor	1E-63	TGTTTGCGACAATCATTTGC	TCATTCTGCTCATGGCTTTG

No.	Gene ID	Top Hit - *Homo sapiens*	E-value	Forward Primer	Reverse Primer
81	*Smed-slc10a-1*	P3 protein isoform 2 precursor	2E-25	AAGCATCGAATCTTTGCTCG	AGGCATTCACTTGGCTCTTC
82	*Smed-slc10a-2*	ileal sodium/bile acid cotransporter	2E-42	TTTTATTGTTACGCGAATGGC	TACGATGAGCGGCATTACAG
83	*Smed-slc10a-3*	ileal sodium/bile acid cotransporter	3E-35	AAATGAGGGAGAATCGCAAG	CTTGTGCAGCCTCATATTCC
84	*Smed-slc10a-4*	sodium/bile acid cotransporter	3E-11	GTTCAATTGTACGTGCTGCC	AAAGCCTATCTGATTCCCATC
85	*Smed-slc10a-5*	ileal sodium/bile acid cotransporter	1E-38	GAACATTGGCAGCAGTTGG	CATCACAGATCCCAAATCCC
86	*Smed-slc10a-6*	P3 protein isoform 2 precursor	3E-11	TGTTGTGACTCCTCAAACGG	GCCATTTTAGCCAGACTTG
87	*Smed-slc11a-1*	natural resistance-associated macrophage protein 2 isoform X3	0	AATCAAACTCAACTGCCGC	ACAGGAGGTAAAGGGCCAAG
88	*Smed-slc12a-1*	solute carrier family 12 member 4 isoform e	0	AGATTCGGACAACCAAAACG	CTTTGCCAGTTCCTCTGACC
89	*Smed-slc12a-2*	solute carrier family 12 member 9 isoform 1	0	TGGTGATCGCTCTTGTTCAG	TAGTCCCCTCACGAAAACG
90	*Smed-slc12a-3*	solute carrier family 12 member 9 isoform 3	2E-54	TGAAAAATCCAGAGGTTCTCAG	GACTGGGTTCTTTTCGATG
91	*Smed-slc12a-4*	solute carrier family 12 member 5 isoform 1	0	AGTTTCAGGAACCGCTTTG	ATCCAAATCACCAATCGAGC
92	*Smed-slc12a-5*	solute carrier family 12 member 8	1E-126	ACTGGTCGAAATTTGGGTTG	AAGGCAATAAATCCGTGTGG
93	*Smed-slc13a-1*	solute carrier family 13 member 3 isoform a precursor	8E-126	CCGTTGATTTTCGTTCATCC	TTCGGGAATTCATTCAGACC
94	*Smed-slc13a-2*	solute carrier family 13 member 2 isoform b	1E-118	ATCCCGATCGTTCTCTTTCC	TCCAGTCGGGAAATTCATTG
95	*Smed-slc13a-3*	solute carrier family 13 member 3 isoform a precursor	8E-60	AGCAGCATTCTGGGCATTAG	TTGAACAAAAGGTAAGCGGG
96	*Smed-slc13a-4*	solute carrier family 13 member 1	7E-105	GGATCGCTACTATTCCCG	AAACCCGACGTGACCATATC

No.	Gene ID	Top Hit - *Homo sapiens*	E-value	Forward Primer	Reverse Primer
97	*Smed-slc13a-5*	solute carrier family 13 member 3 isoform a precursor	2E-108	AACCCGGATTTCCACTATG	CAATTGCATTTGGTGGAGTG
98	*Smed-slc13a-6*	solute carrier family 13 member 5 isoform a	2E-101	AGCGAAAACTGTGGAAGAGC	CAATGACATGAACCCTTCCC
99	*Smed-slc13a-7*	solute carrier family 13 member 1	8E-118	TAGATCCAGTCAGGGATGGC	ATTTGCAGAAATCCAGTCCG
100	*Smed-slc15a-1*	solute carrier family 15 member 2 isoform a	3E-112	TTCACGACAATTATTGGGAGC	GTAACAGAAAGGGCGAGGTG
101	*Smed-slc15a-2*	solute carrier family 15 member 2 isoform a	9E-59	CAAAGCCGATCAGACCAAAC	ATAAAAATGTTCCCCAGGGC
102	*Smed-slc15a-3*	solute carrier family 15 member 1	8E-116	AAATTTCCGCTTCCATGTTG	GTCAGTTTGCTCCCAACTC
103	*Smed-slc15a-4*	solute carrier family 15 member 2 isoform a	2E-59	AAATTTCCTAAAGGAGCCGC	TATTGGGCCGACAAAAGAAC
104	*Smed-slc15a-5*	solute carrier family 15 member 4	8E-61	CTAGCGCAAATGTTAGAGCG	AAGATACCATTGGTGACCGC
105	*Smed-slc15a-6*	solute carrier family 15 member 4	5E-75	AATCTGATGCCGCAAAAGTC	TCCAACAAAATGATCCCTCC
106	*Smed-slc15a-7*	solute carrier family 15 member 4	3E-06	CTTGTGCTCGTTGATTGTGG	TTTCAAATCGGGTCATCAGC
107	*Smed-slc15a-8*	solute carrier family 15 member 4	6E-15	TGTCCAAGTGAACATCCAGG	ACCTGTGAGGAAACCGATTG
108	*Smed-slc15a-9*	PREDICTED: solute carrier family 15 member 2 isoform X3	3E-08	CCACTTTGATGACCAACACG	AGCGGCAGCAAAATAAGAG
109	*Smed-slc16a-1*	monocarboxylate transporter 12	3E-09	GAGAGCGTTTGGAAGTTTCG	CCGTCAGTCCGTTTTCTAGG
110	*Smed-slc16a-2*	monocarboxylate transporter 9	0.00002	TTTCGGCAGTTTTGTAGC	ATTCCAAATCCCATTCCTG
111	*Smed-slc16a-3*	monocarboxylate transporter 5 isoform 5	3E-10	CAATGGAACTTCGATGGTTG	AGGCGCCTTCATAGTTTTC
112	*Smed-slc16a-4*	monocarboxylate transporter 5 isoform 1	6E-27	AAATCCAAGATGGTGGCTG	GTGGCATCGAAAATGAAAC

No.	Gene ID	Top Hit - *Homo sapiens*	E-value	Forward Primer	Reverse Primer
113	*Smed-slc16a-5*	monocarboxylate transporter 9	0.00005	CTCATTCATTTCTCCCTCGG	TCAATCCAGCACCAATTCC
114	*Smed-slc16a-6*	monocarboxylate transporter 14	2E-48	TTTGTGGATCAGGATTTGGG	TGAATGAAAGAGTCGCATCG
115	*Smed-slc16a-7*	monocarboxylate transporter 12	0.006	ATCAGGAAATGACGGTTTGG	TTTAATAATCACGGGCTGGC
116	*Smed-slc16a-8*	monocarboxylate transporter 14	3E-07	AGATTCCTATGCTGCGCTC	GCCGAAATGATCAAGATTGC
117	*Smed-slc16a-9*	monocarboxylate transporter 7	1E-37	AAGAGATTGTCCCGATGGTG	AATCGCTCCTGACATTGGAG
118	*Smed-slc16a-10*	monocarboxylate transporter 9	4E-06	AGCAGTTTTCGGTGGTTTTC	TTTTGGTGTCTTGGTCAGC
119	*Smed-slc16a-11*	monocarboxylate transporter 12	6E-52	TGCGAGCTTGCTTAGTGATG	CCACCGAGAGCAATACATCC
120	*Smed-slc16a-12*	monocarboxylate transporter 5 isoform 1	1E-29	TTTGAAAACCCCACGAAAAC	AAACGGCGGTATTCAAACTG
121	*Smed-slc16a-13*	monocarboxylate transporter 14	6E-27	TATGGTTGGTCGCTTTTTCG	TTGAGATCGGGGAAACTCTG
122	*Smed-slc16a-14*	monocarboxylate transporter 5 isoform 1	4E-59	ATGATCTTGATGGAGGCTGG	CGAGGAAGAGCATTAAACCG
123	*Smed-slc16a-15*	monocarboxylate transporter 12	5E-44	ACCAAACCATTCTCTCGTGG	TCCACTGCAAATCATGAAGC
124	*Smed-slc16a-16*	monocarboxylate transporter 12	2E-60	GTCAATGTAGCAAGGCCTCC	TAGCCAGCTAAAGGTGGTCC
125	*Smed-slc16a-17*	monocarboxylate transporter 9	7E-37	ATTCCAGATGGTGGCTATGG	ATGTCAAAGATCAAACCGG
126	*Smed-slc16a-18*	monocarboxylate transporter 14	1E-26	TCACAGCTTATCCAACGCAC	CTGACAACACCATTTGGACC
127	*Smed-slc16a-19*	monocarboxylate transporter 12	2E-38	GTAATCCGAAAACGCAAACG	CAATAAATTGCGAAACCATCTC
128	*Smed-slc16a-20*	monocarboxylate transporter 12	3E-38	GTGGCTATGGATGGGTTGTC	TTTCTGAAGGTTTTCGACGC

No.	Gene ID	Top Hit - *Homo sapiens*	E-value	Forward Primer	Reverse Primer
129	*Smed-slc16a-21*	monocarboxylate transporter 5 isoform 1	8E-38	AACGAACGAGGACAACAACC	CCAATTGAAGGATTTCGTGG
130	*Smed-slc16a-22*	monocarboxylate transporter 12	4E-21	GCCAAATGGGAGATATCGAG	CATAATATTCCCGCCAGCAC
131	*Smed-slc16a-23*	monocarboxylate transporter 7	8E-39	AGCGATATATTCGGCAGTGG	AACCGCATGAAATAAACGG
132	*Smed-slc16a-24*	monocarboxylate transporter 14	1E-29	CTCATCTATCGGCCAATTCC	CAGTGCAATAATCGGTGGC
133	*Smed-slc16a-25*	monocarboxylate transporter 2	4E-06	TGTCGGCTTGTGGTATTGAC	CACCCATTGTCGATTGACTG
134	*Smed-slc16a-26*	monocarboxylate transporter 8	1E-24	AATAGCCTTGCTTGGTGGTG	AGGCATGAAAATGACCCATC
135	*Smed-slc16a-27*	monocarboxylate transporter 9	1E-32	TTTGCTGATGCAACTGGTTC	AACAGAAATGCGGGTACAGG
136	*Smed-slc16a-28*	monocarboxylate transporter 12	3E-17	CATGGAGTGTCACGATAGG	CCAAGTGCTAAAATAGCGCC
137	*Smed-slc17a-1*	vesicular glutamate transporter 2	0	TTTTTCGGAATGGTGCTAGG	TGCATTTGACACTCTCAGGG
138	*Smed-slc17a-2*	vesicular glutamate transporter 2	5E-71	AATTTCGGCTCAATCGACAC	ACTGTGTTGAAAGCGAAACG
139	*Smed-slc17a-3*	sialin isoform X1	1E-128	ATTTTTGGGATTCGCAGTC	TTTCAATTGCCCAACTTTGC
140	*Smed-slc17a-4*	vesicular glutamate transporter 2	3E-76	CTGAGATTGGGATTTTTC	TCTGACGATGCAAAAAGCAG
141	*Smed-slc17a-5*	sialin isoform X1	3E-101	CCATTGTGTAATTCCAAGCG	CACCTGCCACGTAAATGATG
142	*Smed-slc17a-6*	sialin	9E-86	CCGATTTATTTTTGCATGG	ACGGCACCGAAGAACATAAC
143	*Smed-slc17a-7*	vesicular glutamate transporter 3 isoform 1	3E-98	ACCCTTGGGAATGAGATGTG	TCCGTCAAAAATAAGCCACC
144	*Smed-slc17a-8*	vesicular glutamate transporter 2	2E-64	TGTTATTGGAATGCGCTCAG	TCATCAATTGGTGGGAAAGC

No.	Gene ID	Top Hit - *Homo sapiens*	E-value	Forward Primer	Reverse Primer
145	*Smed-slc17a-9*	sialin isoform X1	5E-88	TGTTGCGAGTCAATCTCAGTG	CAGGATCCAAGATAGCCCAC
146	*Smed-slc17a-10*	vesicular glutamate transporter 1	6E-97	CCATTTTGGATACTGACGCAC	CTGAATTCCAGTTTAGGCGG
147	*Smed-slc17a-11*	solute carrier family 17 member 9	4E-96	ATCAACGGGAATTGTGCTC	AACCACCTGATTTCCAGTGC
148	*Smed-slc17a-12*	sialin isoform X2	2E-53	TTGGGTTTTTGAGCAGTATGG	TGTGACTCCATAAGAAAATAGCG
149	*Smed-slc18a-1*	vesicular acetylcholine transporter	3E-19	TGTGATGATTGTTTGGCAGC	TGGGCCACTTGATAAGGTTC
150	*Smed-slc18a-2*	synaptic vesicular amine transporter	8E-12	TCCTCGGTATCAAGTACGCC	TAAACAAGCCATAAACGGGG
151	*Smed-slc18a-3*	synaptic vesicular amine transporter	2E-12	AATCTCTGCCAGTTCCAGC	GCGCTGATTCTACACGAAC
152	*Smed-slc18a-4*	synaptic vesicular amine transporter	2E-160	TCGGATGGGAATCACAAATC	TGCTTAAATCGTTTGAGGGC
153	*Smed-slc18a-5*	synaptic vesicular amine transporter	7E-14	CAAGCGTGATTTTCAAATGG	TTGATGAAGTGATTGAGGTTCC
154	*Smed-slc18a-6*	vesicular acetylcholine transporter	2E-149	AGCCGTGTCGAGGTAGTTC	AGGACGACTTGTTCTGTG
155	*Smed-slc18a-7*	synaptic vesicular amine transporter	2E-156	ATTGATGAAAATGGCGAACG	ATTGTACCCAACCATCGACC
156	*Smed-slc18a-8*	synaptic vesicular amine transporter	2E-19	CAATCAAACGTCGATTTCGG	ATTTGTGCCGAAAAATTGC
157	*Smed-slc20a-1*	sodium-dependent phosphate transporter 1	2E-81	TTGGCTTTTGGTATTGGTGC	ACGCCCACTTTTTGAGACAG
158	*Smed-slc20a-2*	sodium-dependent phosphate transporter 1 isoform X1	4E-72	TGATGTGGCAAATTCTTTCG	CTTATTCCTGCCGAAACTG
159	*Smed-slc21a-1*	solute carrier organic anion transporter family member 5A1 isoform 1	2E-98	TTATTTCCCCAAGTCAACCG	TCTGATTTCCTGAAAGGCTG
160	*Smed-slc21a-2*	solute carrier organic anion transporter family member 1B3	3E-60	TAACAAATCCCAAAATCGCC	GACCATACCGGCTAAAGGTG

No.	Gene ID	Top Hit - *Homo sapiens*	E-value	Forward Primer	Reverse Primer
161	*Smed-slc21a-3*	solute carrier organic anion transporter family member 1B3	1E-59	AGGCTCAAGCCTTCCAAGAG	TTTATACGTCAATGCCGTGG
162	*Smed-slc22a-1*	solute carrier family 22 member 3	9E-40	TTCAATTCAGCAGCCAAATG	GTGCTCTCATTGGTTTTC
163	*Smed-slc22a-2*	solute carrier family 22 member 5	2E-40	ATGATCTCGGTCCACAAGG	GAATGAAAGCGAAGACGAG
164	*Smed-slc22a-3*	solute carrier family 22 member 7 isoform a	2E-50	CTCGGAGGGAAGAACAAATG	AACCCCTGTCAACAAACAGC
165	*Smed-slc22a-4*	solute carrier family 22 member 5	4E-38	TTTACGGCCGGTCAAATATC	TTTCTGTGCCTTAGGAACCC
166	*Smed-slc22a-5*	solute carrier family 22 member 5	6E-48	AATGCGTTGATCCGATTTTC	TTCATTGCCTTCTTCCAAGG
167	*Smed-slc22a-6*	solute carrier family 22 member 6 isoform a	5E-31	CACCGAAACCAATTCAAAGC	CTTGGAACTTTTCCTCCACG
168	*Smed-slc22a-7*	solute carrier family 22 member 3	1E-37	ACTGTCTTTGCCAGCCTTTC	CATCAGAATCCTCTCGGTC
169	*Smed-slc22a-8*	solute carrier family 22 member 5	2E-71	TTATGTTGGCCCTTTCTGATG	TTTGAAAGTTAAGCCGCCAG
170	*Smed-slc22a-9*	solute carrier family 22 member 3	1E-42	AAAAACCTGTGGGCTGATTG	TTCACAGTAAATGGCATCGC
171	*Smed-slc22a-10*	solute carrier family 22 member 24 isoform 3	5E-07	CATTCAATCAAACCTACG	ATCGTCTCGCATCATTCCTC
172	*Smed-slc22a-11*	solute carrier family 22 member 2	1E-20	ATTTGCGGACTCTGATTGG	TGTGGTACCCTATCTAACCCG
173	*Smed-slc23a-1*	solute carrier family 23 member 1 isoform a	7E-93	TATACCAGCATGGCACTTGG	TTTGCCTGATCCTTGCTTTC
174	*Smed-slc23a-2*	solute carrier family 23 member 2	7E-100	TGACTTCAACACCCCTCCTC	GAAATTTGAGAGCTACCC
175	*Smed-slc24a-1*	sodium/potassium/calcium exchanger 5 precursor	4E-107	AGCCAACTGCTCACCAAAAG	TGATGCAGCTTTGAAAAAGG
176	*Smed-slc24a-2*	sodium/potassium/calcium exchanger 6, mitochondrial isoform X1	7E-41	TTTGATAATCGTTGGGCTCC	TTTCGCAAGAGTGACATTGG

No.	Gene ID	Top Hit - *Homo sapiens*	E-value	Forward Primer	Reverse Primer
177	*Smed-slc24a-3*	sodium/potassium/calcium exchanger 6, mitochondrial isoform X1	4E-46	TTGAAGTTTCCGTTTTTCCG	TCGGTTTTTGTGCAGTCTTG
178	*Smed-slc24a-4*	sodium/potassium/calcium exchanger 2 isoform 2	8E-82	CATAAAGCGCCACAATCAAC	TCACATGAGGAATCAGCAGC
179	*Smed-slc24a-5*	sodium/potassium/calcium exchanger 6, mitochondrial isoform X1	6E-49	TCTTCTCTTAGCAGTGGCCG	TGCAGCATAAGCGATTCTTG
180	*Smed-slc24a-6*	sodium/potassium/calcium exchanger 5 precursor	8E-122	CAACGATATTGGGGGAAAAG	GGTAAGCCAAGACCGACAAG
181	*Smed-slc24a-7*	sodium/potassium/calcium exchanger 6, mitochondrial isoform X1	1E-40	TTATTAGCGCTGGGAAATGG	CCAAGAGAATTGGCAAAAGC
182	*Smed-slc24a-8*	sodium/potassium/calcium exchanger 5 precursor	5E-130	CCAAATGATTTCATGACCAGG	TGAACCCAAGGAAACGATTG
183	*Smed-slc25a-1*	ADP/ATP translocase 3	4E-91	TTTGGTTTGAGTGGTGTTGC	AATCCTGCTAAAACGCCAG
184	*Smed-slc25a-2*	mitoferrin-1	1E-91	GTAAAGCTTTTGGCGTGAC	CCCCAACTTATTGCAGAACC
185	*Smed-slc25a-3*	calcium-binding mitochondrial carrier protein SCaMC-1 isoform 1	3E-120	GTTATGTGGATTTCTCGG	TAAATCTTTTCCCGGGCTTC
186	*Smed-slc25a-4*	hexokinase-1 isoform X3	1E-119	CCTTAATTTCAGGAATCGCC	GAAACAGAAACAACTGGAACC
187	*Smed-slc25a-5*	tricarboxylate transport protein, mitochondrial isoform a precursor	4E-129	CCTAAAAGGAATAATTGCCG	AGCAGATATTTCCACAACCAATG
188	*Smed-slc25a-6*	S-adenosylmethionine mitochondrial carrier protein isoform a	7E-57	CATAACGTCTGGTGCTGTGG	CCATTTATCTATTGACGGATTC
189	*Smed-slc25a-7*	calcium-binding mitochondrial carrier protein SCaMC-1 isoform 1	1E-167	ATGCCGATGACAAAATGAGC	TTCCCAGAAAGTGTCTTGTTTG
190	*Smed-slc25a-8*	mitoferrin-2	2E-87	CACATGATTGCTGGTTCCTG	AGCCGATATCTGGTGCTGAG
191	*Smed-slc25a-9*	calcium-binding mitochondrial carrier protein Aralar1	0	TGATGCATCGAGCAGATACAG	TTGCAAAAATAGAGACCGGG
192	*Smed-slc25a-10*	mitochondrial coenzyme A transporter SLC25A42	4E-72	TGAGCTCACAAAATCGTCAAC	CACTCGCAATCCCATGTAATC

No.	Gene ID	Top Hit - *Homo sapiens*	E-value	Forward Primer	Reverse Primer
193	*Smed-slc25a-11*	solute carrier family 25 member 51	3E-59	AGAGCACATGTTCAAAGATCAAG	TCTCACACAATTCGCAGGAG
194	*Smed-slc25a-12*	solute carrier family 25 member 48 isoform X6	1E-33	AAAAACCCGTAGGCCGTAAC	ATATCTTTGTCGACACCGGC
195	*Smed-slc25a-13*	solute carrier family 25 member 38	3E-39	AAATGGAGCTTGTAGTGGTTTTG	CTAAAATACCCACCGATGCC
196	*Smed-slc25a-14*	mitochondrial thiamine pyrophosphate carrier	4E-67	AATTCAGCAAGGGAATCTGC	ATTGGCCATCTGAACTCCTG
197	*Smed-slc25a-15*	solute carrier family 25 member 44 isoform 2	2E-64	TATTTGAATGGATTCAGCCG	ATTTACACTCTTCCGCCGTC
198	*Smed-slc25a-16*	mitochondrial thiamine pyrophosphate carrier	4E-67	ATAGCTGGTGCTTCTGGTGG	ATCGTTGGAACTCAGAATCG
199	*Smed-slc25a-17*	solute carrier family 25 member 46	1E-67	TGGTCTGAATTAGCAACAGG	CCTTTATATAAGCCGCCAG
200	*Smed-slc25a-18*	mitochondrial 2-oxoglutarate/malate carrier protein isoform 1	1E-141	TGTCATCGCAAAACATTTCC	TGAACTACCTTTCGATGGGC
201	*Smed-slc25a-19*	mitochondrial dicarboxylate carrier isoform 2	1E-92	CCCAAATGAAGAAACCTTCTG	TCCTATTCTGACAAATGCCG
202	*Smed-slc25a-20*	mitochondrial thiamine pyrophosphate carrier	9E-72	TCAGCTTTTACTGCTGGTGC	CCTTTAAACAAACCCGAAATCC
203	*Smed-slc25a-21*	mitochondrial 2-oxoglutarate/malate carrier protein isoform 1	2E-110	GGCAAAGCATTCCAATTCC	CCAAAATTCTGTATGCTTCACTC
204	*Smed-slc25a-22*	calcium-binding mitochondrial carrier protein SCaMC-2 isoform a	1E-141	TGAACCTGTGCATTTGATTTG	CCAAAGGATTATCCAATGCC
205	*Smed-slc25a-23*	mitochondrial carnitine/acylcarnitine carrier protein	1E-132	GTGGGGTTGGTGGTATATG	TATCCTAAAAAGCAAGCCGC
206	*Smed-slc25a-24*	kidney mitochondrial carrier protein 1 isoform 1	1E-94	ATTCAGGCACATTCCCAATC	TACAATGAACCGGGATGATG
207	*Smed-slc25a-25*	mitochondrial carrier homolog 1 PSAP-LL	6E-25	CTTCGAAAAGCGATAGCCTG	AGGGTTCTCCAGCACTTACG
208	*Smed-slc25a-26*	mitochondrial glutamate carrier 1	7E-116	GTGGTATTGCTGGCATTG	ATATTCGGCAACTCCGAGG

No.	Gene ID	Top Hit - *Homo sapiens*	E-value	Forward Primer	Reverse Primer
209	*Smed-slc25a-27*	phosphate carrier protein, mitochondrial isoform a precursor	3E-153	AACGACACACACAGCCATTG	CAAACATTCGAAAAACACC
210	*Smed-slc25a-28*	mitochondrial folate transporter/carrier	3E-104	TCGAACAGTTCAGTGGGAGC	ACCACTAGCTGGCGTTACAC
211	*Smed-slc25a-29*	solute carrier family 25 member 36 isoform a	2E-94	TGGAATCGGTGGAACAGTC	CACACACACACAGGTTTGAGG
212	*Smed-slc25a-30*	ADP/ATP translocase 3	2E-94	TTTGGACTCAGTGGATGTGC	TATCAAAACCAGCCAGGACAC
213	*Smed-slc25a-31*	mitochondrial dicarboxylate carrier isoform 2	6E-95	AAGTGCCTTGGCCATAAGTG	TGCAATATCACAAAATGCGG
214	*Smed-slc25a-32*	mitochondrial ornithine transporter 1	1E-68	ATGTCGGTCAACCTTTGGAC	ACACACACAGGCAAACAAGC
215	*Smed-slc25a-33*	mitochondrial dicarboxylate carrier isoform 2	4E-51	ACAAATGATCAAAAACCCCG	AATCGAGTTCGGAATTGCTC
216	*Smed-slc25a-34*	mitochondrial dicarboxylate carrier isoform 2	2E-116	TTGGTGGAGTAGCAAGTGCC	TCAAACTCAATAAAGAAGTC
217	*Smed-slc25a-35*	solute carrier family 25 member 40	2E-81	GGCAACGATTAGTCTCATCAAG	TTGTAGCAATGACAACACGC
218	*Smed-slc25a-36*	solute carrier family 25 member 35 isoform X1	4E-92	AGGAAATGATTCTCGGTG	TACGGTGTGAGGTGTCAAGC
219	*Smed-slc26a-1*	prestin isoform a	1E-126	ACGATGAAAACTCGGACGAC	TGGATCACTGGCAATTCTTG
220	*Smed-slc26a-2*	sodium-independent sulfate anion transporter	3E-112	ACGGATCTATGCACGGTGAC	TCGATTTTCTGCTTCCATTG
221	*Smed-slc26a-3*	prestin isoform a	3E-130	TACCATCACTCGTCCGACAC	CTGACGCAAAATACTGAC
222	*Smed-slc26a-4*	prestin isoform b	2E-114	TGAATTCGATGAGGATCACG	AAAGCGCTACAGTGGAATGG
223	*Smed-slc26a-5*	prestin isoform b	6E-108	ACAAGGAATGGCGTATGGAC	ACTTAGGTTATCCTCGGC
224	*Smed-slc26a-6*	solute carrier family 26 member 6 isoform 3	2E-107	CAAATTCACATTTTTCCAGC	TCCGCAGGGAATGACTTATG

No.	Gene ID	Top Hit - *Homo sapiens*	E-value	Forward Primer	Reverse Primer
225	*Smed-slc26a-7*	prestin isoform a	4E-131	CACTCCGCAATACAAAGTCG	ATCTGGGATTTCATGCCAAC
226	*Smed-slc26a-8*	prestin isoform a	1E-134	TATGGCATACGCTCACTTGG	ACGTTTTCCATTTTGCGTTC
227	*Smed-slc26a-9*	solute carrier family 26 member 6 isoform 1	6E-76	CGACACCTTTCAATGGGAAC	ATGCATTCAACACTGCATCG
228	*Smed-slc26a-10*	prestin isoform a	6E-50	ATGAAATCCCAGATGGCAAG	CAAAACTGCGTCATGGATTG
229	*Smed-slc27a-1*	long-chain fatty acid transport protein 1	0	ATTTACTGCGCATTTGGAGG	TGTTCAAAAATTGCGCTGTC
230	*Smed-slc28a-1*	solute carrier family 28 member 3	5E-126	AAATGACATAGAAAGCCGGG	TTTGCAAATCCACAAAGTGC
231	*Smed-slc28a-2*	sodium/nucleoside cotransporter 2	2E-29	CCAATTTTTGAAAGTTTCCGC	CCTATTAAAAATGCGATGGGC
232	*Smed-slc28a-3*	solute carrier family 28 member 3	2E-126	ATTAGATTGCGATTCACCCG	TGACGTTTTTGCAAGTTTGG
233	*Smed-slc29a-1*	equilibrative nucleoside transporter 1 isoform X2	5E-73	TTACGGGAATCGGAGTCTTG	GCAACTCCAAAAGCTAGTCC
234	*Smed-slc29a-2*	equilibrative nucleoside transporter 4 isoform 1	2E-75	CGAAGAAAGGCAAGAAAAAG	TGTCGTCATTAGATTCCCCG
235	*Smed-slc30a-1*	zinc transporter 9	2E-125	ATTCGAAGCAACCACCAAAG	TCAATATGTTTGACCGAAGGG
236	*Smed-slc30a-2*	zinc transporter 10 isoform X1	1E-09	TGTGTGTTTCACTCAGAAATGTG	GTTCTCTTCTTAACCCCACCG
237	*Smed-slc30a-3*	zinc transporter 2 isoform 1	1E-125	ATACTATGCTCGCGGCTTTC	TATCGGATCTGCGATTTTCC
238	*Smed-slc30a-4*	zinc transporter 5 isoform 1	2E-165	TTGTTTGACCCAGATCATCG	CACTCCACATTGACTGCTG
239	*Smed-slc30a-5*	zinc transporter 1	8E-74	AATTGCTGCCAGGCGTATAG	TGAATTTTCACACCCCCAG
240	*Smed-slc30a-6*	zinc transporter 10	6E-32	CTTTTTCGCCGAACTGATTG	ACTGACCCGACAAAGTCAGC

No.	Gene ID	Top Hit - *Homo sapiens*	E-value	Forward Primer	Reverse Primer
241	*Smed-slc30a-7*	zinc transporter 1	7E-73	TGGGAAAATACAATGGCAAG	TCATTCCCAGTTCCCAAAC
242	*Smed-slc30a-8*	zinc transporter 2 isoform 1	7E-128	AAAGCACCTGCACCCTTTC	GCGATCTGGAATCTCTGTC
243	*Smed-slc30a-9*	zinc transporter 6 isoform 4	1E-84	AGTCTTGGCGATTTTTACCG	TCGGGAGATTTGAATGGTTC
244	*Smed-slc30a-10*	PREDICTED: zinc transporter 3 isoform X7	2E-82	GAATGCAAATTCAAGTCCCC	ACGGCTTTGCTGAAGACTC
245	*Smed-slc31a-1*	high affinity copper uptake protein 1	3E-17	AATCATACCAATGGATCGTCG	ACAGTGCTCATTGGAGTCCC
246	*Smed-slc31a-2*	high affinity copper uptake protein 1	2E-25	TCAAATGAAACACGGAGCTG	AATAAGGGCTTGATAACGACAC
247	*Smed-slc31a-3*	high affinity copper uptake protein 1	1E-07	TAATAGCGAATCCAAACCGC	TGCCAAAGAATAGCTTCTTAACG
248	*Smed-slc32a-1*	vesicular inhibitory amino acid transporter	1E-45	ATATGGAAGGCAGTGTTCGG	TAATGGATCCCACCAAACC
249	*Smed-slc32a-2*	vesicular inhibitory amino acid transporter	7E-60	TTAAAAGGCAGCTGGATTGG	TTCGCAGCAAAAATCATTCC
250	*Smed-slc33a-1*	acetyl-coenzyme A transporter 1	1E-151	TTCCAGTAAATTTGGCCGTC	ATTTCCCTTGCAGTTGCTTG
251	*Smed-slc35a-1*	UDP-N-acetylglucosamine transporter isoform 1	3E-135	ACGGCTCTGGTTTTAATC	AATTCGTTGCTTGGTTTTGG
252	*Smed-slc35a-2*	probable UDP-sugar transporter protein SLC35A4	1E-44	AAATGACCAGTGACGCTACAG	AGTAATGTTGCTTGCGTG
253	*Smed-slc35a-3*	UDP-galactose translocator isoform a	2E-79	TGATGCGATATTGCAGAACAAG	ATTACACCCCGATTTCAAGC
254	*Smed-slc35a-4*	UDP-galactose translocator isoform c	1E-89	CACTCGTCCAGGAGATTTG	TTCCTGTGGAGTTTTGGAGG
255	*Smed-slc35b-1*	UDP-xylose and UDP-N-acetylglucosamine transporter	3E-35	TGTTCAACAGTTGTCAGTTTCATC	AATGGCCGTATGTTTCACAG
256	*Smed-slc35b-2*	adenosine 3'-phospho 5'-phosphosulfate transporter 2	2E-126	CACTTAAAGTTCCAAATGATCCTG	TCCTCCATTTCAAACAACACC

No.	Gene ID	Top Hit - *Homo sapiens*	E-value	Forward Primer	Reverse Primer
257	*Smed-slc35b-3*	solute carrier family 35 member B1 isoform 1	1E-89	CTTATTCGGTTGTTCATTGGG	CATTTGATCCAAAACCAGCC
258	*Smed-slc35b-4*	adenosine 3'-phospho 5'-phosphosulfate transporter 1 isoform a precursor	1E-114	AGAGGAGAATGGCGATAG	TCTGACAGAAACATGTGCCG
259	*Smed-slc35c-1*	GDP-fucose transporter 1 isoform b	5E-52	AAAGTAACCTTTCCTGTCGCTG	TGAGCACCACCAGAACAGTG
260	*Smed-slc35c-2*	GDP-fucose transporter 1 isoform b	4E-101	GTTCATTTCAATTTCTCTCGTG	CATACACCAAAGAGCCTCC
261	*Smed-slc35c-3*	solute carrier family 35 member C2 isoform X2	2E-111	GAAAATTTCACCATCTGGC	TCAATCGTTCCAAATTCCAC
262	*Smed-slc35c-4*	solute carrier family 35 member C2 isoform c	6E-64	TGGACGAAGTGCACTGTATTG	TAACGAGATTCCGAGCAAGC
263	*Smed-slc35d1*	UDP-glucuronic acid/UDP-N-acetylgalactosamine transporter	2E-75	CCGTATTCTATGGTTTTGTTTC	TATAATCTCCCGCGAAATGC
264	*Smed-slc35e1*	solute carrier family 35 member E1	3E-67	TGCCCATACGTAGAAGTCGG	TGCACCAGAAGGAAGTTGTG
265	*Smed-slc35f-1*	solute carrier family 35 member F5 isoform X1	8E-115	ATTCTTTCGGAACACAAGCG	CCTCTGAATCCGTTTCAACC
266	*Smed-slc35f-2*	solute carrier family 35 member F2	3E-75	TTTTTGTGGTCAGGTTCTCTC	TGCAACATACATTCCAACACC
267	*Smed-slc35f-3*	solute carrier family 35 member F3 isoform 1	1E-25	ATAAGGCATCTGTTGCGAGG	TATTGCCGATTTTGTGCAAC
268	*Smed-slc36a-1*	proton-coupled amino acid transporter 2	3E-51	ATGTCCCTAGACAACAGCCG	CCTCCCAAAGAACAACATCG
269	*Smed-slc36a-2*	proton-coupled amino acid transporter 1	1E-67	TTGAACTAGCTGTTCCACCG	ATCCTCATTTGTCAGATTCCAG
270	*Smed-slc36a-3*	proton-coupled amino acid transporter 1 isoform X3	5E-26	CCTGACCATCTGAACAATCG	CTGGAATTGGGCTTGGTATC
271	*Smed-slc37a-1*	sugar phosphate exchanger 2 isoform 2	1E-162	AGAAACTCCTATCGGCTGG	TTCTCCTGGCATATCCGTTC
272	*Smed-slc37a-2*	sugar phosphate exchanger 3 isoform 1	1E-146	CCTCTGAAAAATTGGAAGCG	AGCTTTTTCGCAATCATGTG

No.	Gene ID	Top Hit - *Homo sapiens*	E-value	Forward Primer	Reverse Primer
273	*Smed-slc37a-3*	sugar phosphate exchanger 2 isoform 1	2E-153	AATGCGTACTAAACCCCCAC	CAGAATGATGAACACCGTCG
274	*Smed-slc38a-1*	putative sodium-coupled neutral amino acid transporter 7	8E-62	ATATTGCAGAATCGCCTTCG	CAATTGAATGGGCGGTAGAG
275	*Smed-slc38a-2*	putative sodium-coupled neutral amino acid transporter 9 isoform 1	4E-105	TTTTCTCCTCCAGACGATGG	TGCCCTGTTTATGCATTTTG
276	*Smed-slc38a-3*	putative sodium-coupled neutral amino acid transporter 10 isoform b	7E-58	CAATTGGCGCAACACTTATG	TGCTGTCACCGAAACAGTTG
277	*Smed-slc38a-4*	putative sodium-coupled neutral amino acid transporter 11 isoform X1	4E-117	TACAGTGGCACAGAACCAGG	AGTACAGTTGACCCCTCCG
278	*Smed-slc38a-5*	putative sodium-coupled neutral amino acid transporter 7	1E-50	AAGCGGCATACAGATCCAAG	AAGCAAAATGTTCCAAG
279	*Smed-slc38a-6*	putative sodium-coupled neutral amino acid transporter 9 isoform X5	1E-73	TATGCCGTGGGCTATTCAAC	AACCACAGAATGATCCTCCG
280	*Smed-slc39a-1*	zinc transporter ZIP14 isoform X1	2E-68	TCGCGTCAGTTCTTCTGTTG	GATTTGGAATGAGCGAATC
281	*Smed-slc39a-2*	zinc transporter SLC39A7 isoform 1 precursor	3E-87	TGCAAAATATTTCGGCACAC	CACACACGCGATTCATTTTC
282	*Smed-slc39a-3*	zinc transporter ZIP1 isoform a	6E-42	AAAATTGGATTGGTGTTCGC	GGTCAATGAAGAACGAAG
283	*Smed-slc39a-4*	zinc transporter ZIP10 isoform X4	4E-49	AGTGCATTCCTTAGCTCCG	TGAAAACCACCAAAACCAGAG
284	*Smed-slc39a-5*	zinc transporter ZIP13 isoform b precursor	9E-76	TTCGTGTGAAACTATTGTGGC	AAACATGCTCTCAATCACGC
285	*Smed-slc39a-6*	zinc transporter ZIP11 isoform 2	3E-105	GGAACATTGTTTACGTGGG	TGTTGTTTGTCGTGTTGCTG
286	*Smed-slc39a-7*	zinc transporter ZIP9 isoform 1	1E-92	TTGGATGTTATTTAGCGGGC	TTGGAAAGTTCTGGGAGCAC
287	*Smed-slc39a-8*	zinc transporter ZIP3 isoform a	2E-31	TCGAAACCCTTCAGAAATCC	TCTGGCACCAGCTATCAATG
288	*Smed-slc39a-9*	zinc transporter ZIP13 isoform b precursor	1E-29	CAAAATTCACACGCTATGGG	TCACTGATGACAAAAGGCCC

No.	Gene ID	Top Hit - *Homo sapiens*	E-value	Forward Primer	Reverse Primer
289	*Smed-slc39a-10*	zinc transporter ZIP10 precursor	7E-83	AGCGATTCGAAGTGGTTCTG	TCATACAGGGCAATCAGCAG
290	*Smed-slc39a-11*	zinc transporter ZIP1 isoform a	2E-39	CTGCTGTCGTAATGCTCGTC	ACACAAGCCAGTTTTGCTCC
291	*Smed-slc39a-12*	zinc transporter ZIP14 isoform c precursor	3E-64	TTTTTCGTTGCAAAATGCTG	CCCATACAAAGCCATCAAAAG
292	*Smed-slc39a-13*	zinc transporter ZIP1 isoform a	3E-43	TGTCGAATTCATCAACGACC	TCCTTGTAAAACACCAGCGAC
293	*Smed-slc40a-1*	solute carrier family 40 member 1	2E-92	ATCCTGGGATGATCGAAGC	AGAGGGTCAAAGTTGGCTG
294	*Smed-slc41a-1*	solute carrier family 41 member 3 isoform X7	9E-33	GAGATTGGAAAACTCCGTG	TTGTTGCTACATGCTCCTGTG
295	*Smed-slc42a-1*	ammonium transporter Rh type B isoform a	5E-123	ACAGCTTCACTTCTCCAGGC	TTTCGGTATCCACCACACTG
296	*Smed-slc42a-2*	ammonium transporter Rh type A	8E-117	TGATATTTGGTTTTTGCGTGAG	AGACGTCTCTTCTGGAACGG
297	*Smed-slc43a-1*	solute carrier family 43 member 3 isoform 1	4E-20	TTGTCGCAGAAATCGAGATG	TTTTCATTCGGGGAAATTG
298	*Smed-slc43a-2*	solute carrier family 43 member 3 isoform 1	5E-29	AAATTCGACAAAAGCATGGC	TTTTAATGAAATCTGCGCCC
299	*Smed-slc43a-3*	solute carrier family 43 member 3 isoform 1	1E-36	AATGGTATGCTTCAGCGGAG	TTGGCTTCGGGATAATTTTG
300	*Smed-slc43a-4*	solute carrier family 43 member 3 isoform 1	7E-20	CTCCCAATACTGTCATCCCG	CATCCGGTAAATGATCGTCC
301	*Smed-slc43a-5*	solute carrier family 43 member 3 isoform 1	2E-25	TGTCCAATACAATTCCTGGC	ATCAATTCTTGCTTGGCCTC
302	*Smed-slc43a-6*	solute carrier family 43 member 3 isoform 1	1E-23	TTTGGTATAATTGCAGGCCC	TGAATGCCAAACATGACATACC
303	*Smed-slc43a-7*	solute carrier family 43 member 3 isoform 1	7E-12	CGGCAAATGGAATTATCAC	ACAAGGATTTCGGGGTCTTC
304	*Smed-slc44a-1*	choline transporter-like protein 1 isoform a	5E-104	CTAAGCCCAAACGACCTCAG	TCAGATCGGATGAGATTCCC

No.	Gene ID	Top Hit - *Homo sapiens*	E-value	Forward Primer	Reverse Primer
305	*Smed-slc44a-2*	choline transporter-like protein 5 isoform A	7E-149	TGGAAAGAAAAGTCCCAACG	CTTCCTTTTGATTGCATCG
306	*Smed-slc44a-3*	PREDICTED: choline transporter-like protein 2 isoform X1	1E-153	TTCTGGGCGTATTTATTCGG	CCAAGTCCTCACAGAAGCAG
307	*Smed-slc46a-1*	thymic stromal cotransporter homolog	4E-16	CCAAGGATGCTTTGGATTTG	CAAACAGGCGTCAATGTAG
308	*Smed-slc46a-2*	proton-coupled folate transporter isoform 1	1E-26	TGATAACTTGGGGACATCGC	TCCATGGAAAATTCGGAAAG
309	*Smed-slc46a-3*	solute carrier family 46 member 3 isoform a precursor	3E-19	TCTGTAATCGCACAAGTGGC	TGAATTGATGGATTCGAAGG
310	*Smed-slc46a-4*	proton-coupled folate transporter isoform 1	4E-08	AAAGACAAATCACGTTGC	ACCCAAACATCAAAAGCACC
311	*Smed-slc46a-5*	proton-coupled folate transporter isoform 1	4E-27	TGATGTCTTCCAAAAGTTACGC	AATGCAATGGAAAGCAGGAC
312	*Smed-slc47a-1*	multidrug and toxin extrusion protein 2 isoform 2	7E-70	TTTTCAGAATGCTCAACCCG	GATGCATTCAATTCCGGTTC
313	*Smed-slc47a-2*	multidrug and toxin extrusion protein 2 isoform X2	7E-61	AATTAGACGCCCCTAAACCG	AATCGGGAATGCAAGATACG
314	*Smed-slc47a-3*	multidrug and toxin extrusion protein 2 isoform X9	2E-46	TCAGCGAGAATTCAGTCTTTTG	TTAAATGGTTCGTTGGCTCC
315	*Smed-slc47a-4*	multidrug and toxin extrusion protein 1	2E-93	CCTCATGTTTATTGCATTTTCG	AAATTCAATTCCTTGCCACG
316	*Smed-slc47a-5*	multidrug and toxin extrusion protein 2 isoform 2	9E-80	AGCGTCATCCATATTTTCGG	GGACAGACGCCCAATAATTC
317	*Smed-slc47a-6*	multidrug and toxin extrusion protein 2 isoform 2	3E-68	ATCTCGAACATCAACCCCAG	TTTTCCAGATTTGTCCGAGG
318	*Smed-slc47a-7*	multidrug and toxin extrusion protein 1	1E-81	GCTTTTGCGAGAATGAAACC	TCGAAAGCGGCCAATATAAC

APPENDIX B

EXPRESSION DOMAINS OF SOLUTE CARRIER GENES IN THE PLANARIAN PROTONEPHRIDIA

Planarian solute carrier	Flame cell	Proximal tubule			Distal tubule		Collecting duct
	FC	PT1	PT2	PT3	DT1	DT2	CD
Smed-slc1a-3							
Smed-slc2a-2							
Smed-slc2a-4							
Smed-slc4a-2							
Smed-slc4a-6							
Smed-slc4a-7							
Smed-slc5a-2							
Smed-slc5a-4							
Smed-slc6a-5							
Smed-slc6a-9							
Smed-slc6a-12							
Smed-slc6a-13							
Smed-slc6a-17							
Smed-slc7a-6							
Smed-slc9a-3							
Smed-slc10a-2							
Smed-slc12a-1							
Smed-slc12a-4							
Smed-slc13a-2							
Smed-slc13a-7							
Smed-slc15a-2							
Smed-slc15a-3							
Smed-slc16a-22							
Smed-slc17a-3							
Smed-slc17a-5							
Smed-slc20a-1							
Smed-slc20a-2							
Smed-slc22a-3							
Smed-slc22a-5							
Smed-slc22a-6							
Smed-slc23a-1							
Smed-slc23a-2							
Smed-slc24a-2							
Smed-slc24a-3							
Smed-slc24a-5							
Smed-slc24a-7							
Smed-slc24a-8							
Smed-slc25a-22							
Smed-slc26a-5							
Smed-slc26a-8							
Smed-slc28a-1							
Smed-slc28a-2							
Smed-slc28a-3							
Smed-slc30a-3							
Smed-slc40a1							
Smed-slc42a-2							
Smed-slc43a-7							
Smed-slc44a-2							
Smed-slc44a-3							

APPENDIX C

EXPRESSION DOMAINS OF SOLUTE CARRIERS IN THE RODENT METANEPHROS

Solute carrier	Proximal tubule			Intermediate tubule		Distal tubule		Collecting duct		Reference(s)
	S1	S2	S3	DTL	ATL	TAL	DCT	CNT	CD	
slc6a13										(Raciti et al., 2008)
slc6a19										(Kleta et al., 2004)
slc13a1										(Lotscher et al., 1996)
slc13a2										(Chen et al., 1998)
slc13a3										(Raciti et al., 2008)
slc22a2										(Koepsell et al., 2003)
slc22a5										(Tamai et al., 2001; Tamai et al., 2004)
slc22a6										(Kojima et al., 2002; Ljubojevic et al., 2004)
slc5a1										(Lee et al., 1994; Sabolic et al., 2006)
slc5a2										(Raciti et al., 2008)
slc1a1										(Shayakul et al., 1997)
slc15a1										(Shen et al., 1999; Smith et al., 1998)
slc15a2										(Daniel and Rubio-Aliaga, 2003; Shen et al., 1999; Smith et al., 1998)
slc28a1										(Rodriguez-Mulero et al., 2005)
slc28a2										(Rodriguez-Mulero et al., 2005)
slc28a3										(Rodriguez-Mulero et al., 2005)
slc23a1										(Eck et al., 2013)
slc23a2										(Eck et al., 2013)
slc23a3										(Burzle et al., 2013)

Solute carrier	Proximal tubule			Intermediate tubule		Distal tubule		Collecting duct		Reference(s)
	S1	S2	S3	DTL	ATL	TAL	DCT	CNT	CD	
slc4a1										(Alper et al., 1989)
slc4a2										(Castillo et al., 2000)
slc4a4										(Endo et al., 2006; Raciti et al., 2008; Roussa et al., 2004)
slc12a1										(Raciti et al., 2008)
slc12a3										(Raciti et al., 2008)
slc42a3										(Eladari et al., 2002; Verlander et al., 2003)

References

Alper, S.L., Natale, J., Gluck, S., Lodish, H.F., and Brown, D. (1989). Subtypes of intercalated cells in rat kidney collecting duct defined by antibodies against erythroid band 3 and renal vacuolar h+-atpase. Proc Natl Acad Sci U S A *86*, 5429-5433.

Burzle, M., Suzuki, Y., Ackermann, D., Miyazaki, H., Maeda, N., Clemencon, B., Burrier, R., and Hediger, M.A. (2013). The sodium-dependent ascorbic acid transporter family slc23. Mol Aspects Med *34*, 436-454.

Castillo, J.E., Martinez-Anso, E., Malumbres, R., De Alava, E., Garcia, C., Medina, J.F., and Prieto, J. (2000). In situ localization of anion exchanger-2 in the human kidney. Cell Tissue Res *299*, 281-287.

Chen, X.Z., Shayakul, C., Berger, U.V., Tian, W., and Hediger, M.A. (1998). Characterization of a rat na+-dicarboxylate cotransporter. J Biol Chem *273*, 20972-20981.

Daniel, H., and Rubio-Aliaga, I. (2003). An update on renal peptide transporters. Am J Physiol Renal Physiol *284*, F885-892.

Eck, P., Kwon, O., Chen, S., Mian, O., and Levine, M. (2013). The human sodium-dependent ascorbic acid transporters slc23a1 and slc23a2 do not mediate ascorbic acid release in the proximal renal epithelial cell. Physiol Rep *1*, e00136.

Eladari, D., Cheval, L., Quentin, F., Bertrand, O., Mouro, I., Cherif-Zahar, B., Cartron, J.P., Paillard, M., Doucet, A., and Chambrey, R. (2002). Expression of rhcg, a new putative nh(3)/nh(4)(+) transporter, along the rat nephron. J Am Soc Nephrol *13*, 1999-2008.

Endo, Y., Yamazaki, S., Moriyama, N., Li, Y., Ariizumi, T., Kudo, A., Kawakami, H., Tanaka, Y., Horita, S., Yamada, H., *et al.* (2006). Localization of nbc1 variants in rat kidney. Nephron Physiol *104*, p87-94.

Kleta, R., Romeo, E., Ristic, Z., Ohura, T., Stuart, C., Arcos-Burgos, M., Dave, M.H., Wagner, C.A., Camargo, S.R., Inoue, S., *et al.* (2004). Mutations in slc6a19, encoding b0at1, cause hartnup disorder. Nat Genet *36*, 999-1002.

Koepsell, H., Schmitt, B.M., and Gorboulev, V. (2003). Organic cation transporters. Rev Physiol Biochem Pharmacol *150*, 36-90.

Kojima, R., Sekine, T., Kawachi, M., Cha, S.H., Suzuki, Y., and Endou, H. (2002). Immunolocalization of multispecific organic anion transporters, oat1, oat2, and oat3, in rat kidney. J Am Soc Nephrol *13*, 848-857.

Lee, W.S., Kanai, Y., Wells, R.G., and Hediger, M.A. (1994). The high affinity na+/glucose cotransporter. Re-evaluation of function and distribution of expression. J Biol Chem *269*, 12032-12039.

Ljubojevic, M., Herak-Kramberger, C.M., Hagos, Y., Bahn, A., Endou, H., Burckhardt, G., and Sabolic, I. (2004). Rat renal cortical oat1 and oat3 exhibit gender differences determined by both androgen stimulation and estrogen inhibition. Am J Physiol Renal Physiol *287*, F124-138.

Lotscher, M., Custer, M., Quabius, E.S., Kaissling, B., Murer, H., and Biber, J. (1996). Immunolocalization of na/so4-cotransport (nasi-1) in rat kidney. Pflugers Arch *432*, 373-378.

Raciti, D., Reggiani, L., Geffers, L., Jiang, Q., Bacchion, F., Subrizi, A.E., Clements, D., Tindal, C., Davidson, D.R., Kaissling, B., *et al.* (2008). Organization of the pronephric kidney revealed by large-scale gene expression mapping. Genome Biol *9*, R84.

Rodriguez-Mulero, S., Errasti-Murugarren, E., Ballarin, J., Felipe, A., Doucet, A., Casado, F.J., and Pastor-Anglada, M. (2005). Expression of concentrative nucleoside transporters slc28 (cnt1, cnt2, and cnt3) along the rat nephron: Effect of diabetes. Kidney Int *68*, 665-672.

Roussa, E., Nastainczyk, W., and Thevenod, F. (2004). Differential expression of electrogenic nbc1 (slc4a4) variants in rat kidney and pancreas. Biochem Biophys Res Commun *314*, 382-389.

Sabolic, I., Skarica, M., Gorboulev, V., Ljubojevic, M., Balen, D., Herak-Kramberger, C.M., and Koepsell, H. (2006). Rat renal glucose transporter sglt1 exhibits zonal distribution and androgen-dependent gender differences. Am J Physiol Renal Physiol *290*, F913-926.

Shayakul, C., Kanai, Y., Lee, W.S., Brown, D., Rothstein, J.D., and Hediger, M.A. (1997). Localization of the high-affinity glutamate transporter eaac1 in rat kidney. Am J Physiol *273*, F1023-1029.

Shen, H., Smith, D.E., Yang, T., Huang, Y.G., Schnermann, J.B., and Brosius, F.C., 3rd (1999). Localization of pept1 and pept2 proton-coupled oligopeptide transporter mrna and protein in rat kidney. Am J Physiol *276*, F658-665.

Smith, D.E., Pavlova, A., Berger, U.V., Hediger, M.A., Yang, T., Huang, Y.G., and Schnermann, J.B. (1998). Tubular localization and tissue distribution of peptide transporters in rat kidney. Pharm Res *15*, 1244-1249.

Tamai, I., China, K., Sai, Y., Kobayashi, D., Nezu, J., Kawahara, E., and Tsuji, A. (2001). Na(+)-coupled transport of l-carnitine via high-affinity carnitine transporter octn2 and its subcellular localization in kidney. Biochim Biophys Acta *1512*, 273-284.

Tamai, I., Nakanishi, T., Kobayashi, D., China, K., Kosugi, Y., Nezu, J., Sai, Y., and Tsuji, A. (2004). Involvement of octn1 (slc22a4) in ph-dependent transport of organic cations. Mol Pharm *1*, 57-66.

Verlander, J.W., Miller, R.T., Frank, A.E., Royaux, I.E., Kim, Y.H., and Weiner, I.D. (2003). Localization of the ammonium transporter proteins rhbg and rhcg in mouse kidney. Am J Physiol Renal Physiol *284*, F323-337.

APPENDIX D

SUMMARY INFORMATION OF THE PLANARIAN HOMOLOGS OF HUMAN KIDNEY DISEASE GENES

No.	Gene ID	Forward Primer	Reverse Primer
1	*Smed-NPHP1*	ATCCAACACTTGCGACGTTC	TGCAAAGGTACAAAAGAGTGCT
2	*Smed-NPHP4*	CAAACTTGCATTGGATGGTG	TTTTCCACTTGGTTTGCCTC
3	*Smed-NPHP5*	TGAACCGAAATCCTGGAAAG	ATCCAAATCCACAGGTTCC
4	*Smed-NPHP6*	TGAGATCTGTCGGCTGTACG	CTTTTCCAGCTCCTTTGTCG
5	*Smed-NPHP8*	ATACACCGAATTCTGCTCGG	AACATTGACCTTTGCGGTTC
6	*Smed-NEK8-1*	CTGTTCTCTACAGGAATGCCG	CCTCCTGCAATTCTTTACGC
7	*Smed-NEK8-2*	CGGAACTGCGGTTCTTTATC	TTCATTGAATGGCACAAACC
8	*Smed-LRRC50*	TCGGAAACTACCCCAATTTC	ACAAGTTGATCCGGCTTGAG
9	*Smed-DNAHb-1*	ACCTATTTCCAGCTCTTGATGTC	AGTCCAATATCTCTCCTGATGC
10	*Smed-NEPH-1*	GCCAGGACCAAGAGAAACTG	ACGGACGTCTGTTAAATCCG
11	*Smed-NEPH-2*	TGGGTTAAAAGTGGCTTTGG	GCATCATTTGTGTCGATTGG
12	*Smed-NEPH-3*	TGGGTAAAAGACGGATTTGG	CGGGGATCCTTTTCTCTAGG
13	*Smed-NPHS1-1*	TTTGAGTGGAGCGTCAACAG	AGAAATTGGGCCGGTAAATC
14	*Smed-NPHS1-2*	AACATTCCATTCAAGCCTCG	ATTTCGCACTTTGTCCCAAC
15	*Smed-NPHS1-3*	GTTGTCAACAATCAGCACGG	GAAAGTTTGTTCGCTGCCTC
16	*Smed-NPHS1-4*	TGTGCTACCGTCAGTTCCAG	AGTTTCGTTCCGATTGATGG
17	*Smed-NPHS1-5*	AAGTCACGATGGGTTTCGAC	TGACTGCGTTCGATTTGAAG
18	*Smed-NPHS1-6*	AATCCACCTGCGGTTGTTAG	CGAGGCAGATATTGGGAATC
19	*Smed-NPHS1-7*	AATCACAATTAAGGCTGCCG	CGTGAGGGATGAGCTTTCTC
20	*Smed-PKD1L-1*	CAATCACACTTTCACCGTGG	ACGTAGACAAATCCCGCAAC
21	*Smed-PKD1L-2*	AAATTGTGACAACCCTTCGC	ATGTCGACAGGGACTATCGC
22	*Smed-PKD1L-3*	ACAAAATGTCGGTCCAGGAG	TCCAGGCAAAAATCCTCATC
23	*Smed-PKD2-1*	AACAGCCCTTAGGGAATTGG	GAGTCATACCGCATGAACAGC
24	*Smed-PKD2-2*	ACTGCAATGGAAGATCAACA	CTATTTCGGCTTTTACCTCAGC
25	*Smed-PKD2-3*	AGACCTGAAACAAGCACTGA	TGCAGCTCAATAGATTCCATGC
26	*Smed-PKD2-4*	TACCAAGACTTAGACAGGTTCG	CCCATAGTTTCTCTGCTTCTAGC
27	*Smed-PKD2L-1*	CAAAAGGATGGTCAACTGAAG	TGCTGAGAATAACATGAGGAAT
28	*Smed-PKD2L-2*	TCGTATCGACATTGTGGGTC	TCCACCATCATTGAAAAGGC